# Control Surfaces in Confined Spaces: The optimisation of trailing edge tabs to reduce control surface hinge moments

by

Christopher Denis Jaquet

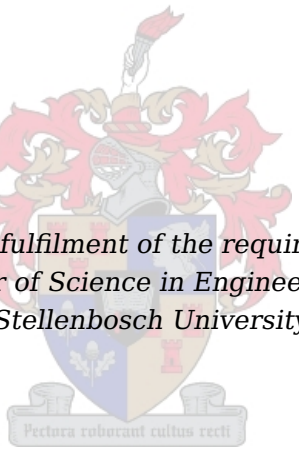


*Thesis presented in partial fulfilment of the requirements for the degree of*
*Master of Science in Engineering*
*at Stellenbosch University*

Supervisors:

Mr J.A.A. Engelbrecht  Prof T. Jones

Department Electrical and Electronic Engineering

March 2010

# Declaration

By submitting this thesis electronically, I declare that the entirety of the work contained therein is my own, original work, that I am the owner of the copyright thereof (unless to the extent explicitly otherwise stated) and that I have not previously in its entirety or in part submitted it for obtaining any qualification.

March 2010

# Abstract

This thesis describes the first project relating to the Control Surfaces in Confined Spaces (CoSICS) project at Stellenbosch University. The aim of CoSICS project is to reduce the size of control surface actuators, and this thesis considers the aileron system of commercial aircraft such as the Airbus A320 and A330. Specifically the project aims to reduce the aileron hinge moment, as this will result in smaller actuators. Possible methods are discussed where aerodynamic forces are used to reduce the aileron hinge moment through the use of a wing-aileron-tab configuration. In order to examine the use of the configuration, first order aerodynamic modelling is performed using two-dimensional thin-aerofoil theory, which is also extended to a basic three-dimensional approximation.

To determine the maximum reduction in hinge moment several optimisations are performed where only the tab chord length is varied, both tab and aileron chord lengths are varied, and finally the tab chord length and aileron span are varied. The optimisation methods used, namely the gradient-based sequential quadratic programming (SQP) and a real-encoded genetic algorithm (REGA) are discussed in detail and include general implementations which are then applied to the problem. The optimisations performed are dual-layered where optimal deflection angles are determined as well as the optimal geometry.

The results of the optimisation are tested using a roll manoeuvre in a specially developed Simulink simulation environment for this purpose.

The study produces results where new hinge moment values are an order of magnitude smaller than those of the old configuration, while maintaining suitable lift and rolling moment coefficients. The optimisation and simulation infrastructure developed in this thesis provides a platform for higher-fidelity models and components being developed in future work to provide higher fidelity results.

# Opsomming

Hierdie tesis beskryf die eerste projek in die *Control Surfaces in Confined Spaces*-projek[1] (CoSICS-projek) uitgevoer by die Universiteit Stellenbosch. Die doel van die COSICs-projek is om die grootte van beheervlak aktueerders te minimeer en hierdie tesis handel oor die aileron stelsel van kommersiële vliegtuie soos die Airbus A320 en A330. Die doel van hierdie tesisis om die skarnier draaimoment van die aileron te minimeer deur aërodinamiese kragte in te span in ’n vlerk-aileron-hulpvlak konfigurasie. Eerste-orde aërodinamiese modelle is afgelei met behulp van twee-dimensionele dunvlerkteorie en is gebruik om die konfigurasie te analiseer. ’n Eerste orde drie-dimensionele benadering is ook ontwikkel.

Om die maksimum vermindering in die skarnier draaimoment te bepaal, is verskeie optimerings uitgevoer waar eers die hulpvlak se koordlengte gevarieer word, daarna beide die aileron en hulp-vlak se koordlengtes en laastens die hulp-vlak se koordlengte en wydte. Die twee optimerings metodes wat gebruik is, nl. ’n sekwensiële kwadratiese programmerings (SKP) tegniek, en ’n reële getal-geënkodeerde genetiese algoritme (RGGA), word bespreek en ontwikkel voor hulle toegepas word op die probleem. Twee-vlak optimerings word uitgevoer waar beide die optimale defleksiehoeke en die optimale geometrie bepaal word.

Die resultate van die optimering word daarna getoets deur middel van ’n rol maneuver wat uitgevoer word in ’n Simulink simulasie omgewing wat daarvoor geskep is.

Hierdie studie lei tot goeie resultate met skarnier draaimoment waardes ’n ordegrootte kleiner as dié van die vorige stelsel, terwyl goeie waardes van rol-moment en verheffingskrag koëffisiënte behou word. Die optimering en simulasie infrastruktuur wat hier ontwikkel word verskaf ’n platform vir meer akkurate modelle en komponente wat ontwikkel word in toekomstige projekte om meer akkurate resultate te lewer.

[1] Beheervlakke in Begrensde Ruimtes

# Contents

# List of Figures

# List of Tables

# Nomenclature

### Abbreviations and Acronyms

| | |
|---|---|
| API | Application Programming Interface |
| CFD | Computation Fluid Dynamics |
| CPUT | Cape Peninsula University of Technology |
| CoSICS | Control Surfaces in Confined Spaces |
| CoX | Centre of Expertise |
| ELAC | Elevator and Aileron Computer |
| ESL | Electronic Systems Laboratory |
| GUI | Graphical User Interface |
| IP | Internet Protocol |
| KKT | Karush-Khun-Tucker (necessary conditions) |
| LMT | Lagrange Multiplier Theorem |
| LP | Linear Programming |
| NACoE | National Aerospace Centre of Excellence |
| QP | Quadratic Programming |
| REGA | Real-Encoded Genetic Algorithm |
| SMA | Shape Memory Alloy |
| SQP | Sequential Quadratic Programming |
| SUN | Stellenbosch University |
| TCP | Transmission Control Protocol |
| UCT | University of Cape Town |
| UDP | User Datagram Protocol |
| VEGA | Vector Evaluated Genetic Algorithm |
| Wits | University of the Witwatersrand |
| 2D | Two-Dimensional |
| 3D | Three-Dimensional |

### Greek Letters

| | |
|---|---|
| $\alpha$ | Angle of Attack |
| $\alpha_k$ | [SQP] Step size |
| $\beta$ | [Aircraft Dynamics] Sideslip Angle |

| | |
|---|---|
| $\beta_{n_e}$ | [REGA] Maximum Euclidean distance parameter |
| $\beta_{P_P}$ | [REGA] Perturbation deviation value |
| $\delta$ | Control surface deflection angle |
| $\epsilon$ | Maximum deviation from zero allowed to still be considered zero |
| $\epsilon_{\text{pcd}}$ | [SQP] Potential constraint deviation |
| $\epsilon_{\text{pcv}}$ | [SQP] Permissible constraint violation |
| $\epsilon_{\text{cv}}$ | [SQP] Convergence parameter |
| $\gamma$ | [SQP] Line search parameter; circulation density |
| $\rho$ | Air density |
| $\theta$ | An angle representing the position along the chord |
| $\Delta$ | Indicates a difference, e.g. $\Delta p = p_U - p_L$; incremental difference |
| $\Gamma$ | Total circulation about the aerofoil |

**Lowercase Letters**

| | |
|---|---|
| $b$ | Wing span |
| $c$ | Chord length |
| $c_{\text{mac}}$ | Mean aerodynamic chord |
| $e$ | Oswald efficiency factor |
| $h$ | An equality constraint function |
| $g$ | An inequality constraint function |
| $k_{\text{max}}$ | Maximum number of iterations [SQP] or generations [REGA] |
| $k_{s_{\text{max}}}$ | [SQP] Maximum number of simplex iterations |
| $n_e$ | [REGA] The number of chromosomes to be within $n_e$ of the most fit chromosome |
| $p$ | Sectional pressure value |
| $q_\infty$ | Dynamic air pressure ($\frac{1}{2}\rho V_\infty^2$) |
| $w$ | Weighting value |
| $x$ | Position along the chord of an aerofoil, measured from the leading edge; optimisation design variable |
| $\mathbf{x}$ | Design vector |
| $y$ | Distance from the aircraft centre-line along the $y$-axis where a particular component of the wing can be found |
| $z$ | Position perpendicular to the chord line of the aerofoil usually relating to the aerofoil's thickness |

**Uppercase Letters**

| | |
|---|---|
| $\mathit{AR}$ | Aspect Ratio |
| $A$ | Fourier coefficient |
| $C$ | Coefficient value, or stability derivative |
| $E$ | Chord lengths as a fraction of total chord length |
| $H$ | Hinge moment |

| | |
|---|---|
| $J$ | Cost value |
| $L$ | Lift |
| $M$ | Moment, usually about one of the primary aircraft axes |
| $R$ | [SQP] Penalty Parameter |
| $P_s$ | [REGA] Population Size |
| $P_E$ | [REGA] Fraction of the new generation population to be determined through elitism (pass-through) |
| $P_C$ | [REGA] Fraction of the new generation population to be determined through crossover |
| $P_P$ | [REGA] Fraction of the new generation population to be determined through perturbation mutation |
| $P_M$ | [REGA] Fraction of the new generation population to be determined through mutation |
| $V$ | Air velocity |
| $X$, $Y$, $Z$ | Aircraft forces along the $x$, $y$, and $z$-axes respectively |

**Subscripts**

| | |
|---|---|
| $\infty$ | Free-stream value |
| $a$ | Aileron |
| $i$, $j$, $k$ | Counters within summations |
| $l$ | Rolling moment |
| $m$ | Pitching moment |
| $n$ | New Value, or yawing moment |
| $o$ | Old Value |
| $t$ | Tab |
| $H$ | Hinge |
| $L$ | Lower |
| $U$ | Upper |

**Syntax and Style**

| | |
|---|---|
| $\mathbf{x}$ | The vector $\mathbf{x}$ (usually lowercase) |
| $\mathbf{A}$ | The matrix $\mathbf{A}$ (usually uppercase) |
| $\mathcal{H}\{f\}$ | The Hessian of the function $f$ |
| $\|\|\mathbf{x}\|\|$ | The Euclidean length of the vector $\mathbf{x}$ ($\sqrt{\mathbf{x}^{\mathrm{T}} \cdot \mathbf{x}}$) |
| $\mathbf{x} \bullet \mathbf{y}$ | The dot-product (scalar product) of the vectors $\mathbf{x}$ and $\mathbf{y}$ |
| $x \cdot y$ | Multiplication of $x$ and $y$. Also applicable to matrices |
| $\mathrm{d}x$ | Differential element $x$ |
| $\frac{\mathrm{d}f}{\mathrm{d}x}$ | Derivative of function, $f$, with respect to $x$ |
| $\frac{\partial f}{\partial x}$ | The partial derivative of function, $f$, with respect to $x$ |

# Acknowledgements

It would have been impossible to start, let alone complete, a project such as this without the support and assistance of a number of people who deserve my humblest thanks.

Firstly Mr Japie Engelbrecht who was thrown into the deep end of administering the Airbus projects when he arrived at Stellenbosch University in late 2008. His support, advice and guidance have been invaluable, as has been his coordination of the CoSICS team as a NACoE representative.

Secondly thanks need to go to Airbus who helped sponsor the project, and the personnel involved, specifically Keith Bohannen, David Hills, Sylvain Boye, Ian Whitehouse, Etienne Coetzee and Stéphane Boissenin who have promoted this project and provided invaluable information without which this project could not progress.

Thanks also need to go to the NACoE who also promoted and helped fund the project alongside Airbus.

Professor Christiaan Redelinghuys and Mr Chris Day of the University of Cape Town, and Mr Robert Malan of the University of the Witwatersrand deserve my thanks for their assistance regarding the aerodynamic components of this component, on which this project heavily relies.

Our colleagues at the Cape Peninsula University of Technology who provided useful information and insights regarding the smart materials are also to be thanked, especially Professors Graeme Oliver and Oscar Philander, and Messrs Lubabalo Matshoba, Velapi Msomi, Ardene Cupido and Jacques Matolla.

My thanks must go to Professor Thomas Jones and Doctor Iain Peddle whose inputs during research meetings and general discussions were very insightful.

Special thanks go to Messrs. AM de Jager and Ruan de Hart, and Miss Jeanne Marie Venter for the valuable inputs they provided during the course of the project, as well as all the members of the Electronic Systems Laboratory who created a very pleasant working environment over the last two years. Mr Marcus Collins also receives my heartfelt thanks for being a very objective proof-reader, and encouraging me continuously to “keep dominating”.

Finally I must thank my mother, Charmayne, and brother, Marc, for supporting me throughout the duration of this project.

# Chapter 1

# Introduction and Problem Description

## 1.1 Overview

This thesis forms the first part of the Control Surfaces in Confined Spaces (CoSICS) project, sponsored by Airbus and the National Aerospace Centre of Excellence of South Africa (NACoE). The aim of the CoSICS project is to examine the use of actuators for control surfaces of aircraft where the size of the actuator is limited. As a design case, the aileron and its actuator are used as a basis on which to perform the research topic.

The development of the infrastructure required to achieve the goal of minimising the aileron hinge moment which determines the size of the actuator is described. The hinge moment is caused by aerodynamic forces, which the actuator must overcome in order to deflect the control surface. A number of potential solutions are discussed where aerodynamic forces are used to reduce the aileron hinge moment, with this thesis focussing on the use of a hinged, controllable tab on the trailing edge of the aileron. The mechanisms used to actuate both the aileron and the tab are abstracted for the purpose of this study to ensure that the results are independent of the specific implementation of the actuation mechanisms.

The contents of the thesis can be divided into three main components: the aerodynamic approximations used to determine hinge moment, lift and (with further approximations) rolling moment coefficients; the optimisation techniques used to determine the optimal tab geometry (chord and later span); and finally the simulation environment used to test a given geometry or configuration.

The aerodynamic component makes use of two-dimensional thin aerofoil theory with the required equations being derived for use with the aileron-tab configuration, providing the hinge moments of both the aileron and the tab, as well as, the lift coefficient. These non-linear equations are then linearised in order to provide easily determinable first order derivatives. These equations are then compared with results obtained using existing software to verify accuracy, which is seen to be suitably accurate for this initial analysis. A rough three-dimensional approximation is developed where rolling moment can be obtained, based on the assumption that the aerofoil has the same cross-sectional shape, scaled according to the chord length.

The optimisation aims to determine the optimal geometry of the tab as a fraction of the total wing chord. It is a pre-requisite that any solution be capable of similar performance to the aileron-only system. The measures of this performance are determined to be the sectional lift coefficient in two-dimensional cases and the rolling moment coefficient in three dimensional cases. While endeavouring to maintain the same lift or rolling moment characteristics, it is also desired to minimise the aileron hinge moment and prevent very large tab hinge moments. These aspects are taken into account during the optimisation.

The optimisation process follows a dual-layer approach, where an outer optimisation varies the geometry, while the inner optimisation determines the best combination of aileron and tab deflections to obtain the required performance characteristics. The optimisation process used is that of a multi-point, multi-objective optimisation. A number of points in the operating range of the aircraft (defined by angle of attack and original aileron deflection) are evaluated, with the aforementioned performance characteristics forming the multi-objective function.

The optimisation is implemented using a sequential quadratic programming (SQP) technique where the linearised thin aerofoil theory is used, and also as a real-encoded genetic algorithm (REGA) which does not require gradient information. The results for both techniques are similar when used with the linearised

theory. Only the REGA can be used with the non-linear theory.[1] The optimisation is applied to several cases with various combinations of linear and non-linear thin aerofoil theory, with the non-linear theory producing much more satisfactory results in regions where the assumptions made during linearisation no longer hold. A technique for distributed processing of the optimisation is also discussed.

Results are obtained in all optimisation cases. The case where only the tab chord length is varied produces satisfactory results, except for extreme deflections. The results of the case where both tab and aileron chord lengths are varied produces less satisfactory results than those of the previous case, but still suggests viable solutions. The reason for this is explained in Chapter 5. The final case where span of the aileron and tab are varied, as well as the tab chord length, produces very satisfactory results in terms of performance, however, parameter modifications are required to produce physically feasible results.

A simulation environment, built using Simulink, is also developed as a means to test configurations. It is possible to program certain sizing manoeuvres required for certification using this model and this is demonstrated with a rolling manoeuvre. Results produced are satisfactory and promising.

The conclusion of the thesis indicates that actively controlled tabs as a means of continuously reducing hinge moments of control surfaces during operation appears to be viable, though this is limited by the accuracy of the aerodynamic models used in both the simulations as well as the optimisations. Drag needs to be taken into account to provide more definitive results, as well as the actual dynamics of any potential actuator replacements. It is also concluded that optimisations need to be carefully planned as they can be very time consuming.

## 1.2 Background

Since the invention of the first successful heavier-than-air craft at the beginning of the twentieth century, much time and many resources have been devoted to improving these vehicles, making them more efficient, more comfortable and easier to use. The use of aircraft as a commercial enterprise whereby freight, passengers and mail are transported over distances ranging from hundreds to thousands of kilometres, including intercontinental flights, resulted in a rapid evolution of aircraft designs during the twentieth century.

Typical fixed wing aircraft make use of various *control surfaces* in order to direct their flight. Control surfaces come in many shapes and sizes, and these control surfaces are usually found as portions of aerofoils, or in the case of canards and the horizontal stabiliser of some aircraft, the whole aerofoil, which can be positioned through a rotary action to manipulate the airflow in such a way that the entire aircraft changes direction.

Over the years fixed-wing aircraft have taken on a reasonably standard form with minor variations which usually depend on the size of the aircraft. This basic design, illustrated in Figure 1.1, includes the following main components, Stinton [2]:

- *Fuselage* – The fuselage is used to carry the payload of the aircraft, such as freight or passengers, as well as house the cockpit from which the pilot controls the aircraft. The fuselage is designed to minimise drag by having components such as a rounded nose-cone and tapered tail-section, but otherwise plays no real role as a lift-generating device (except for blended wing-body configurations and for some fighter aircraft where the fuselage can account for up to $50\,\%$ of the lift).
- *Main Wing* – The main wing is the primary lift-generating device on the aircraft. Wings come in many shapes ranging from simple rectangular to elliptical and swept-back wings, each design with its own advantages and disadvantages.
- *Horizontal Stabiliser* – The horizontal stabiliser is similar to the main wing, but its main purpose is to provide longitudinal stability, as the name implies. It is usually located at the tail section of the aircraft.
- *Fin* or *Vertical Stabiliser* – The fin is the only aerofoil on the aircraft which is asymmetrical in span about the fuselage. Its purpose is to provide lateral stability.

[1] This is not strictly true since only gradient information is required to make use of the SQP. In the case of the non-linear theory this gradient information is difficult to obtain, and linearisation around the operating point would negate the benefit of using the non-linear theory. This is discussed further in Chapter 5 and alternatives are noted in Chapter 7.

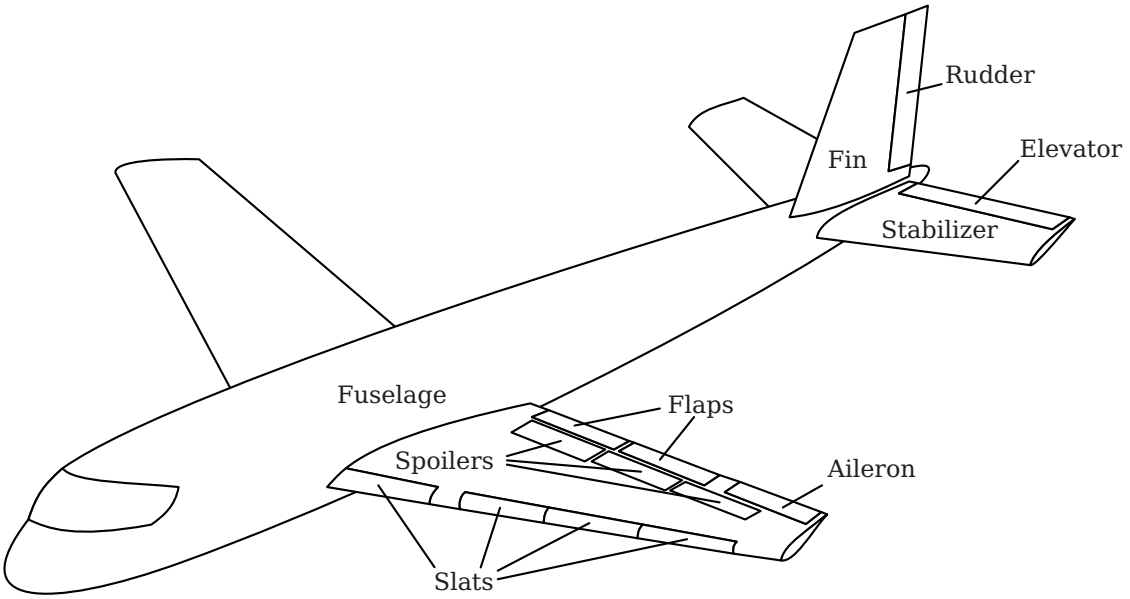


**Figure 1.1** – An aircraft with the typical control surfaces marked.

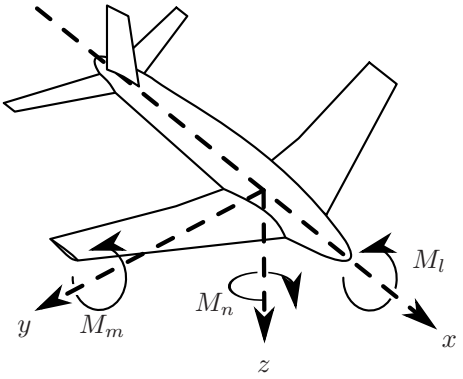


**Figure 1.2** – Definition of the aircraft body axes.

- *Ailerons* – Ailerons are used to induce a rolling moment ($M_l$) about the $x$-axis of the aircraft. These are typically controlled differentially (i.e. when one is deflected upwards, the corresponding surface on the opposite wing is deflected downwards.) Some aircraft (such as the *Airbus A330*) have a more than one set of ailerons. These extra pairs may be used independently or differentially according to their purpose (load alleviation, etc.). The ailerons are located on the trailing edge of the main wing and are usually the most outboard control surfaces on the main wing. The aircraft body axes are shown in Figure 1.2.

- *Elevator* – The elevator is used to develop a pitching moment ($M_m$) about the $y$-axis of the aircraft. It is located on the trailing edge of the horizontal stabiliser.

- *Rudder* – A yawing moment ($M_n$) about the $z$-axis of the aircraft is induced by the rudder. This control surface is located on the trailing edge of the fin, and there may be multiple rudders (such as on the Concorde).

- *Flaps* – Flaps are located on the trailing edge of the main wing inboard of the ailerons. These control surfaces are used to increase the maximum lift coefficient, especially for take off and landing. They also increase drag resulting in a steeper glide slope which is useful during landing.

- *Spoilers* – Spoilers are located on the upper sides of the main wings. These are used for roll-control, where torsional aero-elasticity is important, though the disadvantage of spoilers is the negative influence on lift, Stinton [3].

- *Slats* – Slats are also used primarily at lower speeds to increase the maximum lift coefficient. They are typically located in the upper leading edge of the main wing.

The control surfaces mentioned above all need to be actuated by some means. Initially this was done solely by using mechanical wire-and-pulley mechanisms where the pilot exerted a force on a control rod or foot pedal in the cockpit and the system of wires, pulleys and pushrods transferred this force directly to the control surface being controlled. This design relies heavily on the physical ability of the pilot, although clever selections of moment arms and hence adjustment of leverage does reduce the problem somewhat. This method was used for a number of years where the aircraft themselves were fairly small and moved at relatively low speeds and is still used in smaller aircraft today.

As the design of aircraft evolved resulting in larger, faster and more powerful craft, the physical limitations of the pilot become a large problem, especially with regards to control. Larger aircraft require larger control surfaces in order to achieve the same satisfactory performance. This means the pilot physically has to move larger and heavier control surfaces. Since these control surfaces are larger, they have larger surface areas exposed to the airflow when deflected during flight, which means that very large aerodynamic forces are applied to the control surfaces.

Modern aircraft make use of hydraulic systems which can be used to overcome the physical limitations of the pilots. This has become common practice since about the second world war, however, smaller craft still use the wire-and-pulley mechanism, Phillips [4]. Hydraulic systems have the capability of producing very large forces at the command of the pilot, and with the advent of complex fly-by-wire systems, this has been reduced to the equivalent of pushing a button. The advantages of fly-by-wire systems include the tailoring of flying qualities, advanced control modes and automatic departure avoidance, as well as simpler integration of auto-pilot systems, since physical strength no longer plays a major role. A distinct disadvantage of fly-by-wire systems is the lack of feedback the pilot would gain from a physical system, though this can be remedied artificially using feedback amplifiers, Phillips [4].

Some other disadvantages of hydraulic systems include: oily fluid mixtures used in the hydraulic systems are typically not environmentally friendly and since these systems work under high pressure, any leak could rapidly lead to a large spillage. They also require a complex layout of piping, reservoirs and pumps within the aircraft structure to transfer the fluid to the various hydraulic systems in the aircraft's extremities. Large aircraft also make use of redundancy to provide levels of security (in terms of safety) which means that there is often more than one system of hydraulics leading to the same general location in the aircraft, although usually to different control surfaces (the blue, green and yellow systems as used in the Concorde and Airbuses, Briere, et al [5]).

Figure 1.3 shows a symbolic comparison between the mechanical and electrical flight controls used in aircraft.

## 1.3 Control Surfaces in Confined Spaces Project

*Airbus* and the *National Aerospace Centre of Excellence* (NACoE) of South Africa formed an agreement with each other and various universities in South Africa (initially with only *Stellenbosch University* (SUN) and the *Cape Peninsula University of Technology* (CPUT)), to consider alternative means of actuating control surfaces on commercial aircraft such as the *Airbus* A320 and A330. This collaboration has been broadly termed the *Control Surfaces in Confined Spaces* (CoSICS) project.

As the name implies, the goal of this project is to examine the actuation of control surfaces in small spaces, where space constraints (brought on due to structural limitations, etc.) may not allow large, bulky actuators to be used. Another consideration is the reduction of drag. Many of the control surfaces on aircraft (consider the rudder actuators on the Concorde shown in Figure 1.4) require large actuators that may not fit inside the wing to which the control surface is attached. These actuators are given better aerodynamic characteristics by encasing them in fairings, but any extrusion from the aerofoil (in Concorde's case the fin) results in additional drag.

Airbus and NACoE have provided the universities mentioned with funding in order to examine potential designs which could result in smaller actuators that could potentially reduce the size of these fairings, or reduce the structural restrictions caused by large actuators. Additional information is being provided through the NACoE by students from the University of Cape Town (UCT), as well as the University of the Witwatersrand (Wits).

Due to the multi-disciplinary and complex nature of the project the project will make use of a so-called "crawl-walk-run" iterative approach where basic understanding is first achieved using simple, low-order models and approximations before increasing the fidelity of the solutions using more complex and accurate

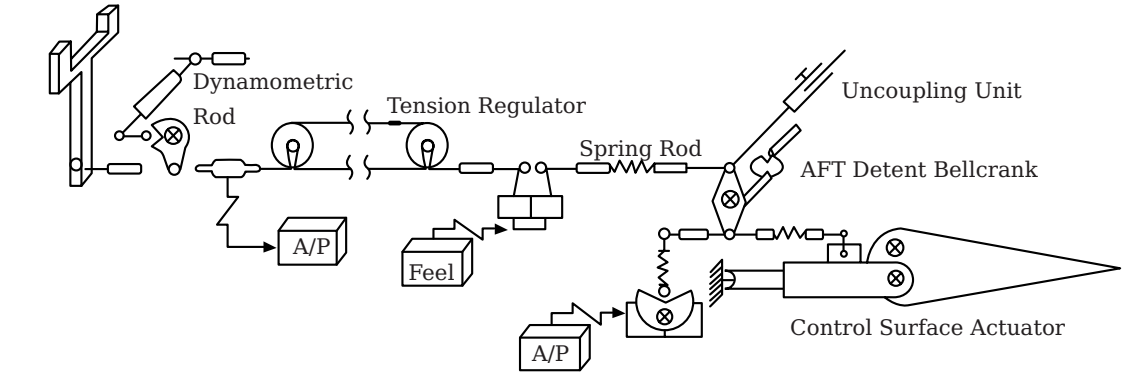


(a) Mechanical

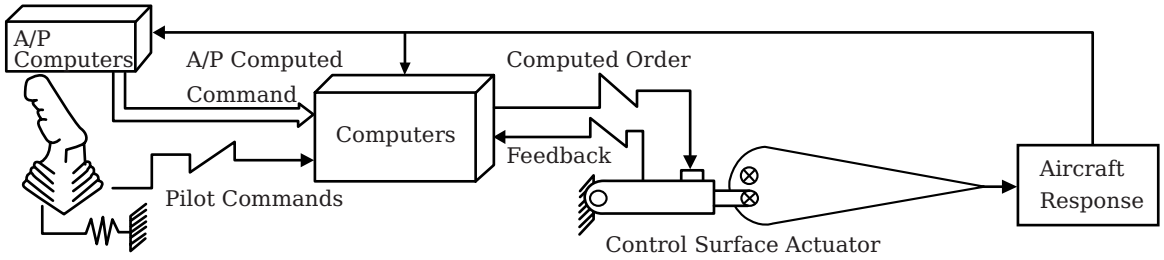


(b) Electro-hydraulic

**Figure 1.3** – Symbolic comparison between the mechanical and electro-hydraulic flight control systems used in aircraft. (Source: Briere, et al [5])


(a) Alfa Bravo at Heathrow. (Source: Wikimedia Commons)

(b) Alfa Foxtrot at Filton.

**Figure 1.4** – The tail sections of two Concordes, clearly showing the rudder actuator fairing on the fin.

models. This builds a better overall understanding of the project as a whole, as well as providing insights into the effects the various components have on the project.

The analysis of each sub-component within the project will follow similar development processes. Another advantage of this approach is the ability to gain insight in less time than when using the more complex components, such as resource-intensive analyses (e.g. computational fluid dynamics), and it allows the intelligent adjustment of various parameters based on the results from and observations made while using the lower-order models. Potential problems may also be identified before committing time and resources to complex simulations.

## 1.4 Multiple Disciplines

Due to the nature of the study, the project is interdisciplinary, consisting of several distinct engineering aspects which can be roughly grouped into the following categories: aerodynamics, control, structures

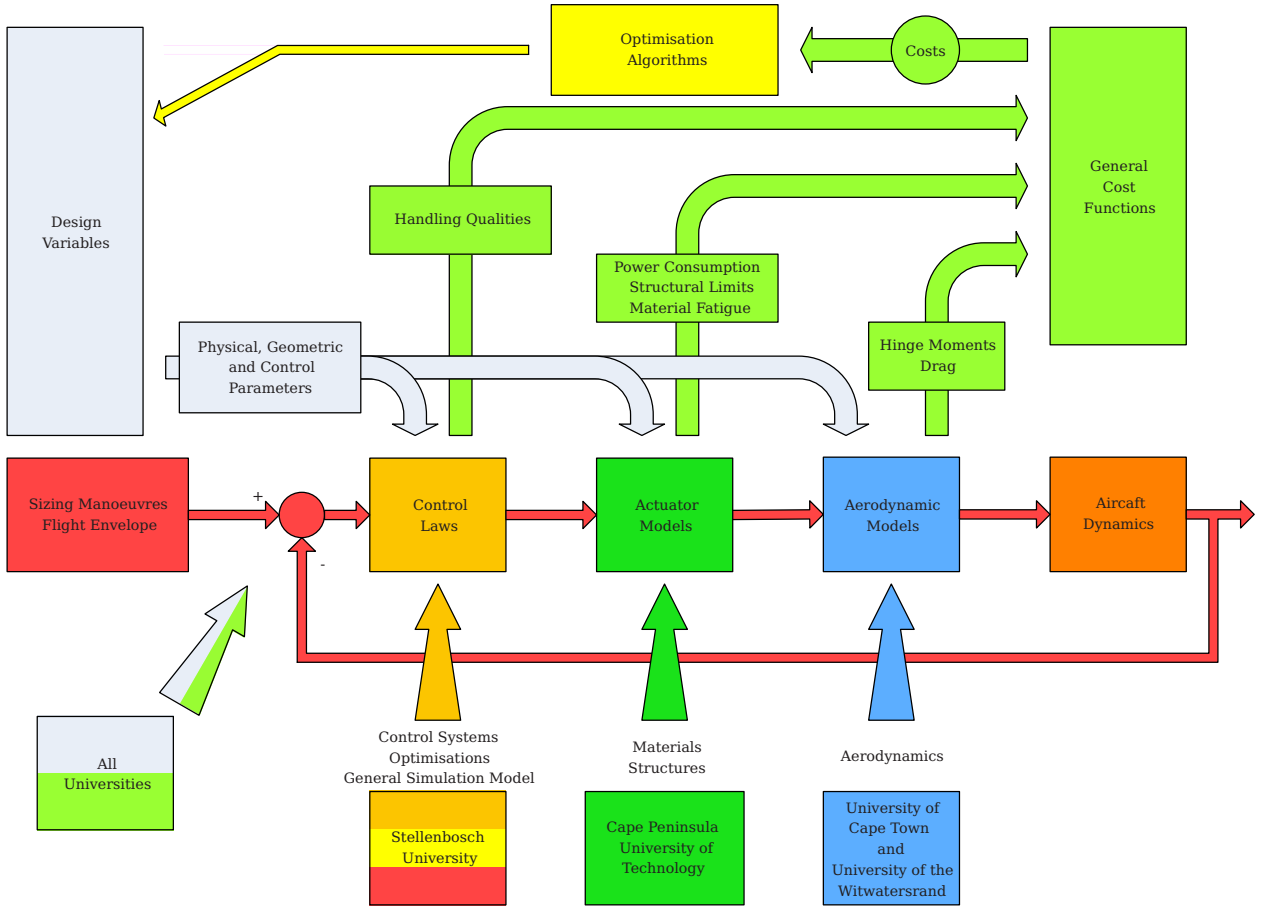


**Figure 1.5** – A block diagram indicating the relationship between the various engineering disciplines, and the various universities' roles within the project. (Modified from an original by Mr. JAA Engelbrecht.)

and optimisation. The general relation between these disciplines is shown in Figure 1.5 and described below.

The aerodynamics aspect considers the aerodynamic effects of the various potential designs that will be conceived and aim to create a suitable mathematical or simulation model in order to determine the dynamic effects of the designs while moving through the air. The structures component examines and characterises the materials that are being considered for the project, specifically looking at the dynamics of the materials as they are used as actuators. The control aspect looks at the possible techniques that could be used for the effective control of any possible solution, taking into account the aerodynamics, as well as the dynamics of the actuators, in order to provide an overall satisfactory response during operation.

The optimisation component aims to calculate the best physical dimensions of any particular solution or design in an effort to minimise aspects such as drag. While optimal control could also be considered a form of optimisation, this is classified under the control aspect.

The roles of the institutions mentioned earlier in this section depend on their specialisations which generally falls into one or more of the classifications described above. CPUT's role in the project is to undertake the analysis of the structures component of the project, while students at SUN are examining the control and optimisation components. As neither the groups at CPUT or SUN possess the required experience with the aerodynamic component of the project it was decided to consult with UCT and Wits through through the NACoE. As can be seen in Figure 1.5, there is a distinct reliance of the various disciplines on each other – the project would be unable to provide satisfactory results without the inputs from any of the institutions mentioned.

## 1.5 The Aileron

While the overall aim of the CoSICS project is to consider actuators in confined spaces in general, this definition is too vague to provide a well-defined goal in the context of a master's project. In order to

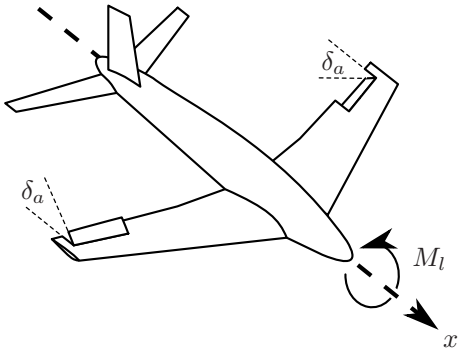


**Figure 1.6** – Diagram showing how the deflection of the ailerons result in a rolling moment about an aircraft's longitudinal ($x$) axis. Note that a negative deflection angle (as shown) results in a positive rolling moment.

reduce the range over which the project is defined, a specific case was decided upon which fits in well with the larger, more general goal.

The component thus considered for study in this masters project is the case of the *aileron actuator*. Airbus provided a large amount of information regarding the aileron actuator as well as usage for the Airbus A320, with the idea that this aircraft, which is well understood by experts at Airbus, could be used as a test base for any potential solutions regarding the reduction in actuator size.

While only this specific case is considered by the institutions, the research being performed is applicable to control surface actuators in general, and it is expected that the work being performed, especially regarding the structures, can be used for applications other than control surface actuation.

## 1.6 Problem Definition

With the aileron as the specific test case which this masters project is considering, it is necessary to redefine the goals in terms of what is expected from this project.

In alignment with the CoSICS project the aim of this thesis would be to reduce the size of the aileron actuator. However, since there are many factors which contribute to the dimensions of a physical actuator, and because this project forms part of the "crawl" phase of the CoSICS project, rather than considering the physical actuator itself, the primary *factor* used to determine the size of the actuator is examined. In order to find this factor, the purpose of the actuator is examined.

The aileron actuator's purpose is to deflect the aileron to which it is attached under all operating conditions. This is done by the applying a force to the control surface in such a way that *a moment is induced about the hinge point of the actuator which is large enough to overcome the aerodynamic forces acting on the control surface and to position the aileron as effectively as possible in the air-stream such that sufficient rolling moment is induced about the fuselage of the aircraft as is necessary to perform the commanded manoeuvre.*

From the preceding paragraph the following key phrases are highlighted: "moment ... about the hinge"; "aerodynamic forces" and "sufficient rolling moment".

The purpose of ailerons, as mentioned in §1.2, is to induce a rolling moment about the longitudinal axis of the aircraft. This is shown in Figure 1.6. This means that when considering the aileron system, it is necessary to take the rolling moment into account as a measure of the performance of the aileron system.

The rolling moment is induced when the ailerons are deflected into the air stream flowing over the primary aerofoil, or wing. The deflection of the aileron aims to re-direct the air flow sufficiently to produce a force on the main wing in such a way that the aircraft rolls. This indicates that the ability of the actuator to redirect these aerodynamic forces is also an important measure of the effectiveness of the aileron actuator.

The final highlighted phrase considers the moment about the hinge of the aileron. A diagram showing how a typical aileron actuator may be connected to the aileron, is shown in Figure 1.7. It can be seen from the figure that as the aileron actuator (a hydraulic piston) is extended, the aileron is deflected upwards (negative deflection) and as it is retracted the aileron is deflected downwards (a positive deflection). A free-body-diagram is shown in Figure 1.8 in which the aileron moment arm is represented by the bold line. In order to achieve the deflection, a moment ($M_H$) is induced about the hinge point ($H$) through a force from the actuator ($F_H$). The airflow produces a counter force which also induces a moment about

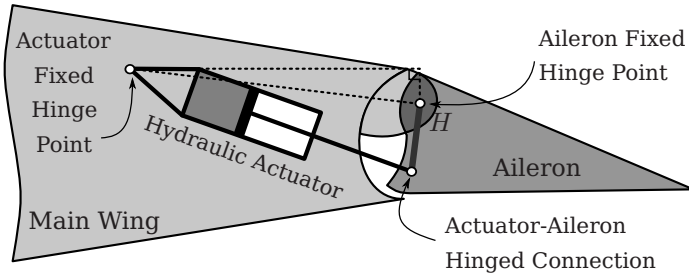


**Figure 1.7** – The aileron actuator connected to the aileron. This shows the right wing looking outboard towards the wing tip. A positive aileron deflection is shown as well as the reference direction of the hinge moment.

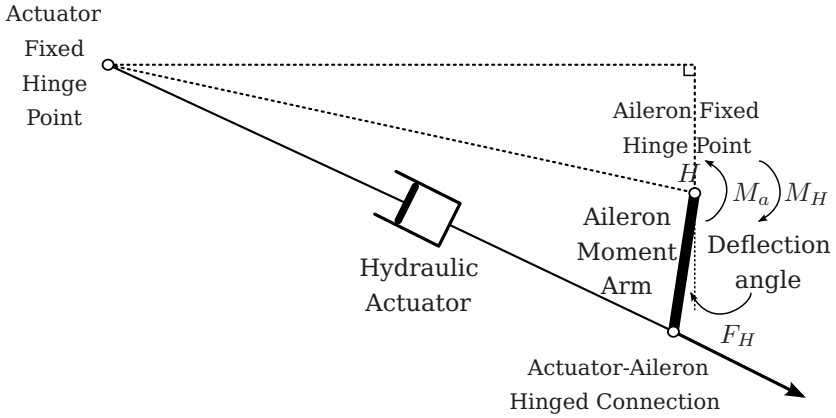


**Figure 1.8** – A free-body-diagram of Figure 1.7 (not to scale). The aileron moment arm is represented by the bold line.

the hinge point ($M_a$). In order for the control surface to be deflected, the moment induced by the actuator needs to overcome the aerodynamically induced moment. This equates to the *control hinge moment* that originally had to be exerted physically by pilots.

Ideally a drop-in replacement design is desired. A drop-in replacement would constitute removing the current aileron system, and replacing it with a new design without needing to modify the rest of the aircraft (e.g. the wing geometry) extensively. At the same time it is necessary that the replacement system be able to perform as effectively as the original system. In other words, the pilot would be unaware that the aileron system being used is different from the traditional hydraulic jack actuated aileron system in terms of the control and performance of the aircraft.

This would have the added benefit in that if the new system is indistinguishable from the old, the chances of being able to perform the same sizing manoeuvres required for certification is much higher. This aspect is considered throughout the project. While it is noted that a drop-in system is not simple to implement physically since various sub-systems (hydraulic, hinges, etc.) will more than likely need to be replaced/removed, the idea is to minimise extensive structural changes to the aircraft while maintaining the same wing geometry. In simulation models a drop-in module is much simpler to realise and equates to the replacement of a Simulink block.

*This masters project thus considers a means to determine and reduce the aerodynamic aileron hinge moment that must be overcome by the aileron actuator, as this hinge moment is the primary factor used in determining the size of the actuator.* Decreasing the aileron hinge moment thus *indirectly* results in a decrease in the size of the aileron actuator, as is desired by the CoSICS project, even though the actuator itself is not examined directly in this thesis.

It should be noted that in this initial study, dynamic effects are not taken into consideration. All analyses are considered as static points in equilibrium. As a result, actual actuators will typically have to produce *larger* hinge moments in order to overcome the inertia of both the aileron and the air mass moving over it in flight in such a way that the aileron can be deflected with sufficient speed to perform the required manoeuvres. Other aspects which are ignored in this first iteration are specific aerodynamic effects such as drag and compressibility since the complex aerodynamic models are still being developed by a partner institution, and it is believed taking these aspects into account at this early stage introduces too great

a complexity. All these aspects will need to be taken into account in future work in order to provide a definitive, accurate result.

Since this masters project is initiated simultaneously with those at other institutions, it will serve to achieve four goals:

1. The first is to lay the groundwork for the entire project, providing the necessary infrastructure that can be used as the project is executed over a number of years. This groundwork includes establishing the necessary interfaces between the various components and creating a suitable simulation environment in which a design can be tested, with the ability for this environment to be upgraded as higher fidelity components become available.
2. The second goal is to develop an initial aerodynamic approximation which can be used to determine hinge moments of control surfaces,
3. with the third goal being to implement suitable optimisation algorithms that can be used for the physical optimisation of a given design, while keeping the algorithms general enough to not be limited to any specific case.
4. The final goal is to make use of the aerodynamic approximation as well as the optimisation techniques developed to perform a first order feasibility analysis of a chosen design in the context of hinge moment reduction in order to reduce actuator size.

## 1.7 Thesis Layout

Having introduced the topic of the thesis in the preceding sections, the layout of the thesis is provided.

A consideration of potential solutions is provided in Chapter 2, as well as the selection of the solution to be used throughout the remainder of the project. Since the aerodynamics play a major role, the preliminary aerodynamic models developed are provided in Chapter 3 where the methods used are described and developed for use with the optimisation and simulation components of the project.

Chapter 4 provides the theory of the optimisation techniques used in the project as well as some of the implementation details, including a gradient based method as well as an implementation of a genetic algorithm using real-value encoding. Both methods are tested using a common example in order to validate the methods, while in Chapter 5 the two optimisation methods developed in Chapter 4 are applied to the specific design case.

Chapter 5 also provides a discussion of the dual-layered technique used to take into account the operating region and provides the results of a number of simulation cases including optimisations using the linear and non-linearised aerodynamics as well as three geometric optimisation cases.

The Simulink simulation model developed to test sizing manoeuvres is described in Chapter 6 with more details of the simulation model, including interface definitions provided in Appendix C. The results for one manoeuvre are also provided in Chapter 6 for two of the geometric optimisations.

The thesis concludes with the recommendations and deductions provided in Chapter 7 in which the potential of the project is discussed as well as recommendations regarding future work.

# Chapter 2

# Potential Designs and Solutions

It has been established that the goal of this project is to reduce hinge moments in the context of the aileron and the actuator used to deflect it. In the case of this project concepts such as redundancy are not treated as these aspects should be considered at a later design stage rather than during the preliminary analysis performed in this project.

While the aim of the project is to reduce the hinge moments of the ailerons it needs to be noted that, as with typical engineering problems, there will be some form of trade-off. In this case it is expected that with a decrease in hinge moment, there will be an associated decrease in the aileron's ability to produce the same rolling moment. Since this is an undesired consequence, it is necessary to take it into account during the optimisation process in such a way that the reduction in hinge moment does not out weigh the ability of the aileron system to perform its function satisfactorily. More details of this are discussed in Chapters 3 and 5.

The primary purpose of this chapter is to consider the current aileron system, as well as potential alternatives, or modifications, that could be used to achieve the goal of the project. The chosen design is also discussed as well as the design philosophy that is to be used.

## 2.1 The Current System

The current system in use on commercial aircraft, such as the Airbus A320 and A330, makes use of a fly-by-wire system similar to that depicted in Figure 2.1. The diagram shows the key components of the system. Commands are generated by the pilot or auto-pilot which are then processed by various control computers which determine the required command signals to be sent to the the control surface actuators. The actuators deflect the relevant control surfaces which result in aerodynamic forces acting on

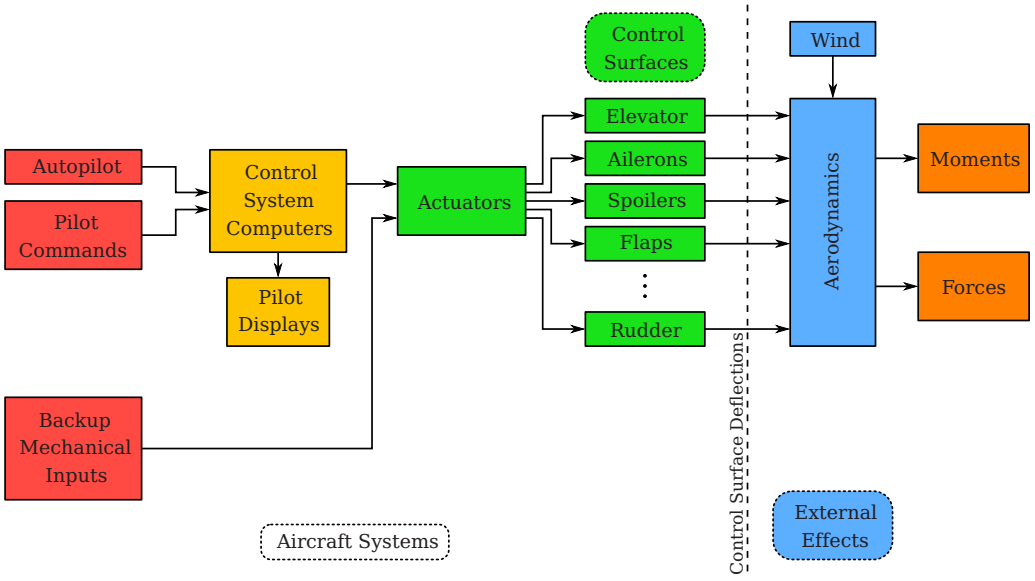


**Figure 2.1** – Block diagram showing the broad idea of the fly-by-wire system used on commercial aircraft.

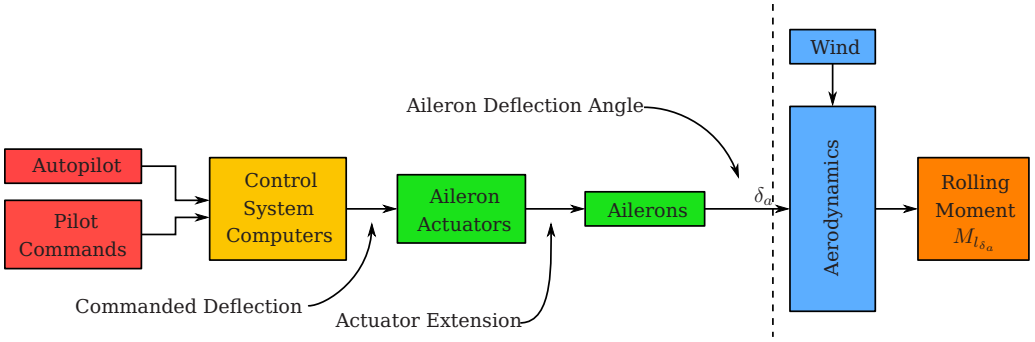


**Figure 2.2** – The aileron portion of Figure 2.1.

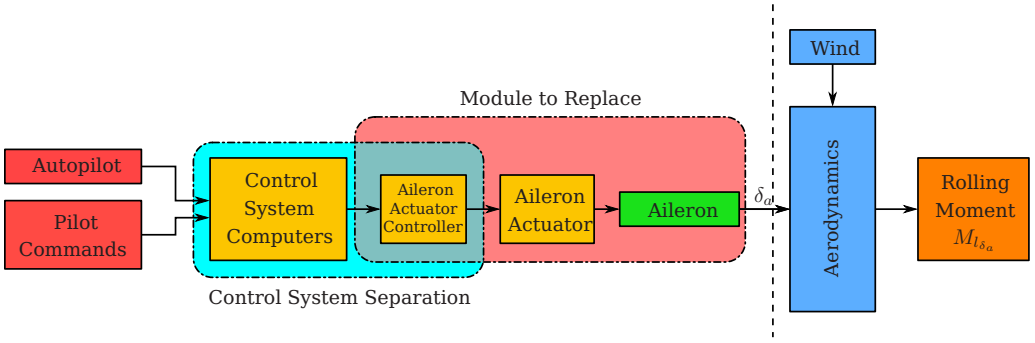


**Figure 2.3** – The components of Figure 2.2 (with the hydraulic jack controller separated) which will be replaced with alternative solutions.

the aircraft inducing moments and forces on the aircraft, causing it to perform the necessary manoeuvres required during flight.

Figure 2.1 shows all the control surfaces, but the focus for this project is on the aileron system. The relevant portion of the diagram is shown in Figure 2.2. The diagram shows how the inputs to the controllers produce the primary effect of the ailerons: rolling moment due to ailerons, $M_{l_{\delta_a}} = \frac{\partial M_l}{\partial \delta_a}$. Non-ideal effects, such as adverse yaw due to aileron ($\frac{\partial M_n}{\partial \delta_a}$) and side force due to aileron ($\frac{\partial F_Y}{\partial \delta_a}$) [6], are ignored for simplicity in this initial study.

## 2.2 The Modular Approach

The aim of the project is to examine and adapt the aileron system of the aircraft, and since it can be easily isolated from the remainder of the aircraft, as shown in Figure 2.2, a modular approach is developed whereby the aileron system is considered separately from the rest of the aircraft system.

This separation includes the controllers necessary for the aileron system, all actuators as well as the aerodynamic effects induced by the ailerons. This also eliminates the need to modify the currently used fly-by-wire system directly, since the commanded aileron deflection can be translated using an intelligent control system to provide the necessary actuation of any solution to provide the same effect as the original aileron system, in effect creating the so-called drop-in replacement of §1.6. Figure 2.3 shows the module that will be replaced with alternative potential solutions.

The modular approach allows various alternatives to the aileron system to be implemented and tested with ease, and without having to modify the entire aircraft model.

## 2.3 Potential Solutions

Having isolated the aileron system from the rest of the aircraft in §2.2 it is now possible to consider suitable replacements for the system. While this section does not provide a complete list of all possible alternatives, it does group the main classifications and provides a general idea regarding the types of solutions that can be considered.

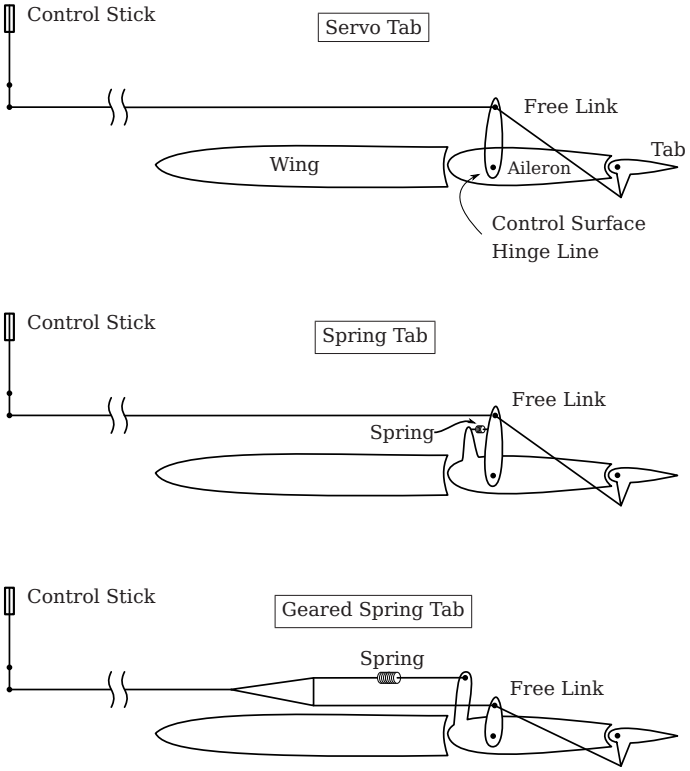


**Figure 2.4** – Various types of tab mechanisms. (Source: Phillips [4])

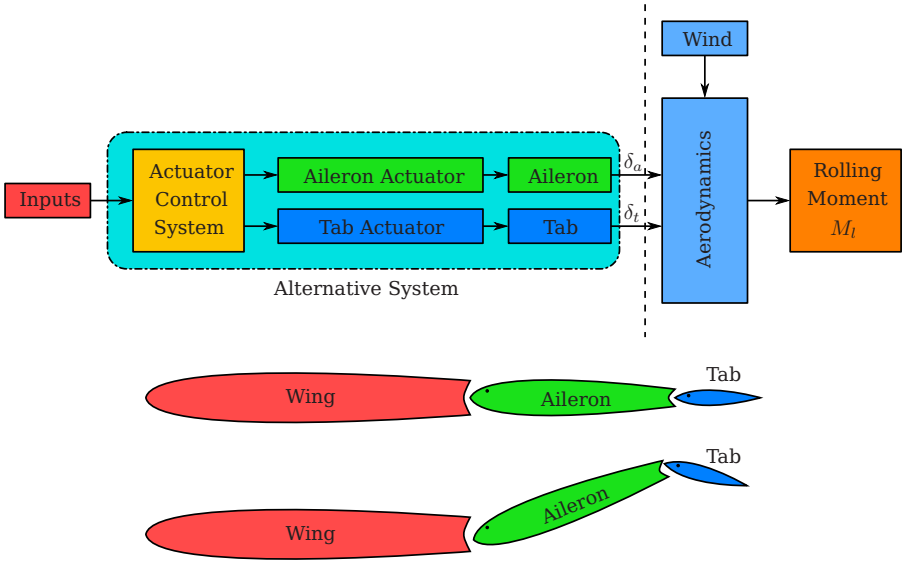


**Figure 2.5** – The tab-system module as a potential replacement for the original aileron system.

The first suggestion makes use of a *trailing edge tab*. Here a portion of the aileron chord length is made a separate hinged flap which can be actuated. The concept is widely used in the form of *trim tabs* where the tab deflection angle is set before a flight and maintained (relative to the aileron) for the duration of the flight. In this case it is used to eliminate imbalances in the control surfaces which would affect the stick-free stability, Cook [6] and Etkin [7].

Other forms of tabs have been used over the decades as a means to assist the pilot in deflecting the control surfaces. These tabs are typically named according the method in which they are actuated. Some examples are provided in Figure 2.4. Traditionally in the case of servo tabs, only the tab is actuated directly by the pilot, which then deflects the control surface to which it is attached. In the case of this project, unless stated otherwise, it is assumed that it is still necessary to deflect both the aileron and the tab.

This leads to the replacement system shown in Figure 2.5. In this case both the tab and the aileron are

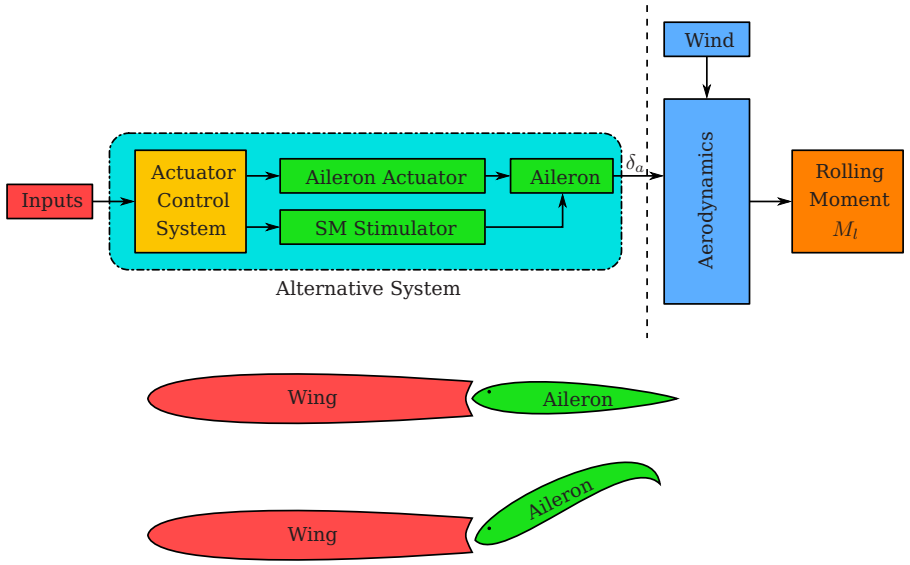


**Figure 2.6** – The deforming aileron module as a potential replacement for the original aileron system.

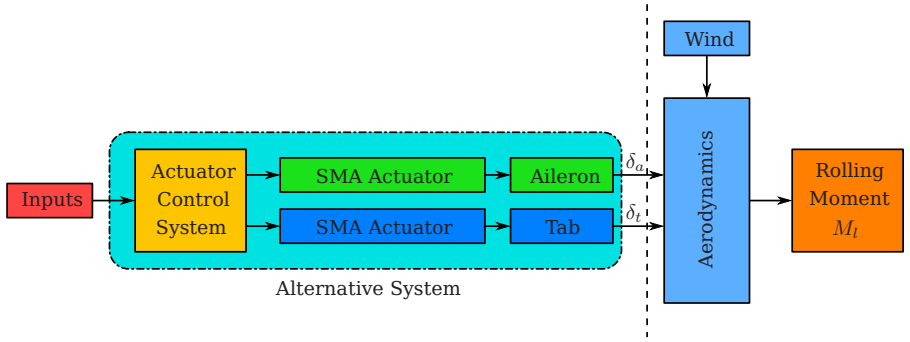


**Figure 2.7** – The smart actuators used to deflect both the aileron and the tab as a potential replacement for the original aileron system.

actuated and the controller determines the best deflections and deflection rates to achieve the same effect as the original aileron system.

The second solution makes use of a deforming aileron. In the case of any flap on an aerofoil, the deflection of the flap changes the effective camber of the control surface. The deforming aileron approach eliminates the direct need for a hinged addition to the aileron by adjusting the camber of the aileron directly. This can be done by using smart materials such as *shape memory alloys (SMAs)* and *piezoelectric materials*. This is shown diagrammatically in Figure 2.6.

Another solution considers replacing the aileron actuators directly, or making use of a serially hinged flap system such as the tab system and ensuring that the moments required to deflect each of the control surfaces is small enough that alternative actuation means can be used rather than the current hydraulic system.

This results in the so called *smart actuator*. CPUT is examining the potential use of piezoelectric devices and SMAs as potential actuators. While not incorporated into this project, at the time of writing extensive work had been done by CPUT in creating demonstratable applications on a small scale for this application. It is expected that in future iterations of the project that this work will be incorporated as the modelling of the dynamics of these systems becomes better understood. An example of the replacement module is given in Figure 2.7

## 2.4 The Chosen Configuration

For the purpose of this project the first option mentioned in §2.3 is chosen, viz. the use of a trailing edge tab, as shown in Figure 2.5. This considers the combination of the aileron and tab, each with an actuator of suitable size and speed to deflect the aileron and tab to their respective deflections within a reasonable

amount of time. This allows the project to focus on the aerodynamics and the optimisation, without being overwhelmed by the mechanics of the actuator.

The reason this configuration is chosen is due to the fixed number of components used: only the wing, aileron and tab need be considered. The techniques developed in this thesis can, however, be expanded to include any number of serially-hinged flaps, which in turn can be used to approximate the variable camber of the morphing aileron. Additional reasons for making use of the trailing edge tab can be found in Harris [8] where it was determined that inset tabs provide good results in decreasing control surface hinge moments, and the effects of these tabs can be added to those of other types (e.g. paddle-horn and frise).

Mungall [9] also indicates that there is a strong possibility that tabs can be used, even when rapid deflections are required to good effect, and that the negative effects can be eliminated using damper systems, though these are not considered in this thesis. Finally Bland and Marley [10] indicates that tabs can be used to good effect where Mach numbers are below $1{,}1$, which is above the cruise speed of the Airbus A320 and A330, though in the case of the article, the wing had a large ($45\,^\circ$) sweep-back angle. [10] also indicates practical results which correlate well with thin aerofoil theory, which is used by this project.

In future projects it is intended to incorporate the smart actuators once sufficient progress has been made in this sector, but the aerodynamics and optimisation strategies developed in this project will still be applicable. The control component will be required to incorporate the effects of the actuators, but is also not treated in this preliminary optimisation. The optimisation structure is developed in such a way that it can easily be adapted to include new information (such as higher order aerodynamic models) without much modification.

With this choice in mind, the aerodynamics discussed in Chapter 3 focus on the two-dimensional analysis of the wing-aileron-tab system where the effect of deflecting both the aileron *and* the tab are examined. The optimisation process of Chapter 5 then considers the parameters that can be optimised for this case, including the chord length, and later the span of both the aileron and tab, for reasons which will be explained in that chapter.

## 2.5 Previous Work Relating to Trailing Edge Tabs

In order to further motivate the choice of using trailing edge tabs, a summary of previous work done on the topic is now provided.

The goal of this project, as stated in Chapter 1, is to reduce the aerodynamic hinge moment of the aileron. This is not the first time that reducing the control surface hinge moments has been necessary. In §1.2 it was noted that when aircraft were first flown, the pilot had to deliver all the required forces to deflect the control surfaces, and that even though clever configurations using pulleys and were used, the aerodynamic forces eventually became too great for the pilot to overcome satisfactorily.

It thus became necessary to examine other methods of actuating the control surfaces. While researching alternative methods of actuating control surfaces without making use of hydraulic systems, it was found that there was much material available from the around the 1930's to the late 1950's, but with very little beyond this date. The most likely cause of the cessation of research is due the acceptance of the use of hydraulic systems on board commercial aircraft, thus invalidating the need for these techniques. An examination of patents issued regarding the subject also reinforced this conclusion with many patents being issued over the period described above, and very few after this time.

The problem is discussed in Phillips [4] where the author discusses the "quest for reduced control forces" during the second world war (late 1930's and early 1940's). Here aerodynamic balancing was used to reduce control forces, typically by allowing a portion of the aerofoil ahead of the hinge line to be in the air stream for positive deflections, negative deflections, or both. Other options mentioned include fixed external aerofoil balances, balancing tabs and horn balances. The author notes that the largest problem with these balancing mechanisms was the large degree of non-linearity in hinge moments associated with the control surface deflections and various speeds and angles of incidence.

A popular recurring consideration was the use of *trailing edge tabs*, attached to the various control surfaces, and much research was performed, especially during the second world war and shortly thereafter regarding the use of tabs of various forms.

Two documents (Wight [11] and [12]), published by the Aeronautical Research Council of the United Kingdom in 1952 and 1955, discuss a wing-aileron-tab system, and provide measured results of the damping

and stiffness derivatives for a 1541 section aerofoil where $20\,\%$ consists of the aileron and $4{,}2\,\%$ is tab. In 1951, Trebble and Holford [13] considers tab hinge moment characteristics of a tab on an elevator taking into account aspects such as the effect of nose balances and the hinge gap between the tab and elevator. This article re-inforces the non-linear nature of tab hinge moments stated in [4] with measured results.

Perring [14], in one of the earlier papers published (1928), considers the theoretical relationships for an aerofoil with a multiply hinged flap system. The theory described by this document is referred to and expanded upon by Kueth and Chow [15] and Moran [16] along with Allen [17] published in 1938, which considers the chord-wise load distribution over these aerofoils. The problem of reducing control forces is discussed by Harris [8], and again discusses the various types of possible tab linkages. Another aspect which is considered is the effect of angular velocities, which will need to be taken into account when dynamic effects are included. These effects are outside the scope of this thesis.

A technical report from NACA (Mungall [9]), dated 1948, discusses the use of servo tabs on an all-movable horizontal tail plane when combined with geared unbalancing tabs, with good performance at both gradual and rapid deflection rates. A NACA research memorandum from 1953 (Bland [10]) also considers the effectiveness of inset tabs to relieve aileron hinge moments in the transonic and supersonic range of Mach number.

Purser and Cook [18], in 1947, collects and analyses hinge moment data on plain, unbalanced control-surface tabs, but states that insufficient data were available to determine the differences between sectional and finite span theory. In 1946 Crandall and Murray [19] analyses then-currently available data to determine the effects of tabs on control-surface hinge moments and lists the effects of a number of considerations (gap sizes, aerofoil conditions, trailing edge angles, etc.) on the hinge moment of the control surface.

Another NACA technical report, White and Klampe [20] from 1945, develops a number of equations relating to the force and moment coefficients for a thin aerofoil with flap and tab such that they can be easily used for stability and control calculations, which becomes important when the dynamics of the configuration are considered.

In recent years the analysis of aerodynamic balancing using tabs has been re-considered by Soinne in two documents dated 2000 and 2001 ([21] and [22] respectively) The former is a collection of publications by the author on the topic of aileron characteristics performed during the late 1990's, and includes work relating to various tab configurations. The latter document describes how various static analyses can be used in certain cases (steady side-slip manoeuvres and steady roll manoeuvres) but emphasis the need for unsteady aerodynamic theory where unsteady manoeuvres are performed. While not directly related to this thesis, this promotes the use of the "crawl-walk-run" approach previously described, where the fidelity of the aerodynamic models will be increased to result in more accurate results.

Trim tabs are used in conjunction with history-dependant aerodynamic forces as described in a 2007 publication, Iosilevskii [23], where the trim-tab is used to control the surface. This focusses again on dynamics of control of the surface, but serves to emphasis the use of tabs as a means of control. The publication also examines the effect of an abrupt breakage on the control and derives numerous dynamic equations relating to the forces and moments about a three-segment wing section.

While not directly related to fixed-wing aircraft, work is also being performed on tabs on rotorcraft. One such example considers the effect of aerodynamic influences on helicopter composite blade trailing edge tabs, Kostić [24], while another considers the piezo-electric servo-flap actuator for helicopter rotor control, Pretchl [25].

A number of patents relating to the design and control of trailing edge tabs were also found and these are listed with their abstracts in Appendix E. It is noted that the number of patents relating to the topic has decreased remarkable since the first half of the 20th century with only approximately ten listed (in the appendix) for the period proceeding the 1960's.[1]

Having now described the various existing research related to trailing edge tabs, the following chapter examines the aerodynamic modelling used to determine the hinge moments of both the tab and the aileron.

[1] This does not mean that there are not more, but merely serves to indicate that there is less active research than before the 1960's.

# Chapter 3

# Aerodynamics

## 3.1 Introduction

The overall goal of the project is to reduce the size of the hydraulic aileron actuators, or to eliminate the need for these actuators completely, by reducing or eliminating the aileron hinge moments. Any control surface actuator is used to overcome the aerodynamic forces on their respective control surfaces, thus it is necessary to have a rudimentary understanding of these aerodynamic forces in the context of deflecting control surfaces.

This chapter aims to provide an introduction to the concept of hinge moments and thin aerofoil theory, before developing the necessary equations that will be used during the optimisation process. An important aspect to note is that no *dynamic effects* are taken into account. It is assumed that the actuators available are capable of deflecting the relevant control surfaces at all times, and that no transitional effects are present. This is obviously not the case in practice, though the static analyses being examined here still provide much useful insight.

## 3.2 Hinge Moment

Hinge moment, typically called *control hinge moment*, is a *measure of the force required to be exerted by the pilot in order to overcome the aerodynamic forces that prevent a control surface from being deflected*, as defined by Etkin [7]. Originally this force had to be applied through a mechanical series of pulleys, wires and linkages; but in modern commercial aircraft, which are typically fly-by-wire, this moment is overcome by the (usually hydraulic) actuator(s) attached to the control surface. Light aircraft (such as the Piper Cherokee 180) still make use of mechanical linkages for control surface actuation.

The hinge moment is calculated about the hinge of the control surface being considered and is determined from the aerodynamic forces acting only on the surface. For simplicity it will be assumed that the hinge always lies on the camber line (halfway between the upper and lower surfaces of the aerofoil). In practice this is often not the case, but to take into account the discontinuities in the camber line that would be caused by rotation about a point not on the camber line would over-encumber the use of the thin-aerofoil theory which assumes symmetrical flaps. Another, more notable aspect which is also ignored is the effect of gaps between the control surfaces, which is expected to have a more dominant role than the location of the hinges.

In order to determine the hinge moment to overcome, it is necessary to examine the aerodynamics about the wing. The field of aerodynamics is a large and complicated field with many areas that can be examined. As was mentioned in §1.6, the CoSICS project will consist of a number of successive projects with models of higher fidelity being incorporated as they are developed. As such a low fidelity, easily understood model was used and implemented for this first phase. The aerodynamic technique is derived from general fluid mechanics and is known as *thin aerofoil theory*.

## 3.3 Notation

For convenience some notation is now provided:

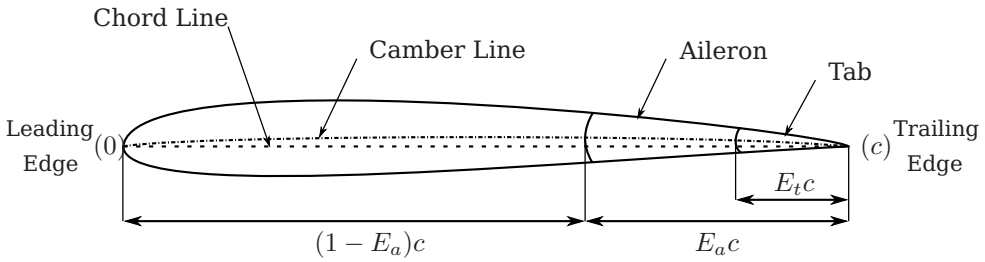


**Figure 3.1** – Side view of aerofoil with flaps neutral defining $E_a$ and $E_t$. L.E. is the leading edge and T.E. is the trailing edge.

| | |
|---|---|
| $x$ | Position along the chord measured from the leading edge of the aerofoil. |
| $c$ | The total chord length of the aerofoil with zero tab and aileron deflection. |
| $E_a$ | The fraction of the total chord that makes up the length from the aileron hinge point to the trailing edge. |
| $E_t$ | The fraction of the total chord that makes up the length from the tab hinge point to the trailing edge. |
| $\theta$ | An angle representing the position along the chord (to be defined in Equation 3.4.14). |

A side view of a typical wing-aileron-tab configuration with some of the above parameters marked is provided in Figure 3.1:

## 3.4 Thin Aerofoil Theory

There are many texts on thin aerofoil theory in the literature, of which the five primarily referred to here are Katz [26], Kueth and Chow [15], Moran [16], McCormick [27] and Anderson [28]. These texts all have detailed aerodynamic information, of which only a small portion is discussed below.

*Thin aerofoil theory* makes use of the concept of *small-disturbance flow* over two dimensional aerofoils [26]. (The three-dimensional variant is known as *slender wing theory* [26].) It is important to note that the theory discussed here is for *inviscid, incompressible flow*. Since viscosity is ignored, problems due to boundary layer effects (such as transition and separation) are ignored. The negative effect is that useful drag values also cannot be determined (see §3.5.1 for further information).

Compressibility effects can be seen from around Mach $0{,}3$ with localised supersonic regions of flow (causing shocks) being found between Mach $0{,}6$ and Mach $0{,}85$, dependant on the geometry of the aerofoil. It is noted that, due to these limitations, thin airfoil theory is not actually applicable to large commuter aircraft in cruise flight, although this initial step is useful for a preliminary analysis in accordance with the crawl-walk-run approach being followed by the CoSICS project.

A *two dimensional aerofoil* is an aerofoil with thickness and camber characteristics, but with *infinite* span. This simplifies the problem since fuselage and wing-tip effects can be ignored. A *thin* aerofoil is one where the maximum thickness is small relative to the chord length, as is the maximum camber. For two-dimensional aerofoils, it is also assumed that airflow is in the plane of the aerofoil cross-section, thus only angle of attack is taken into account, and the maximum angle of attack should also be kept small for the mathematics to be valid. Swept-back wings also result in significant span-wise flow which will need to be modelled in future projects. This is also ignored in the two-dimensional theory.

Remembering that a moment about an axis is calculated by multiplying the (resultant) force causing the moment by the perpendicular distance between the axis and line of action of the force [29], it is necessary to have a force acting on the control surface with which to calculate the moment. In the case of aerofoils, the most prominent force is that due to the air-pressure differences between the upper and lower surfaces of the aerofoil, which is used to determine the *lift* of the aerofoil.

From McCormick [27], Equations 3.4.1 and 3.4.2 are provided for the sectional lift ($L$) and moment about the leading edge ($M_{\text{LE}}$) of a two-dimensional aerofoil in terms of the pressure above ($p_U$) and below ($p_L$) the aerofoil:

$$L = \int_0^c (p_L - p_U)\ \mathrm{d}x \tag{3.4.1}$$

$$M_{\text{LE}} = -\int_0^c x\,(p_L - p_U)\ \mathrm{d}x \tag{3.4.2}$$

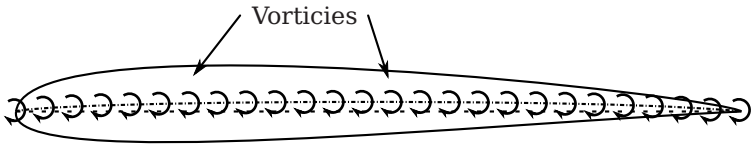


**Figure 3.2** – Vortex sheet along the aerofoil camber line with airflow to the right.

which can be expressed in terms of the the dimensionless sectional coefficients:

$$C_L = \frac{L}{q_\infty c} = \frac{1}{q_\infty c}\int_0^c (p_L - p_U)\ \mathrm{d}x \tag{3.4.3}$$

$$C_{M_{\mathrm{LE}}} = \frac{M_{\mathrm{LE}}}{q_\infty c^2} = -\frac{1}{q_\infty c^2}\int_0^c x\,(p_L - p_U)\ \mathrm{d}x \tag{3.4.4}$$

where $q_\infty$ is dynamic pressure, $C_L$ is the sectional lift coefficient, $C_{M_{\mathrm{LE}}}$ is the sectional moment coefficient about the leading edge and $\mathrm{d}x$ is a differential element along the chord length. Similarly the sectional hinge moment and its coefficient can be calculated as an integral from hinge point to the trailing edge of the *wing*:

$$M_H = -\int_{x_H}^c (x - x_H)\,(p_L - p_U)\ \mathrm{d}x \tag{3.4.5}$$

$$C_H = \frac{M_H}{q_\infty c^2} = -\frac{1}{q_\infty c^2}\int_{x_H}^c (x - x_H)\,(p_L - p_U)\ \mathrm{d}x \tag{3.4.6}$$

where $x_H$ is the position of the hinge along the chord. In all cases the *entire* wing chord length, $c$, is used.

For convenience the pressure difference is termed $\Delta p$:

$$\Delta p = p_L - p_U \tag{3.4.7}$$

It must be reinforced here that $p_L$, $p_U$, $L$, $M_{\mathrm{LE}}$ and hence $C_L$ and $C_{M_{\mathrm{LE}}}$ are all sectional values, i.e. *per unit length*, and are all functions of the chord position, $x$. Unless stated otherwise, for the remainder of the text, only the sectional coefficients will be referred to.

In Equations 3.4.1 and 3.4.2 and the relation $q_\infty = \frac{1}{2}\rho V_\infty^2$ (where $\rho$ is air density and $V_\infty$ is free-stream air velocity), assume that $\rho$, $V$ and $c$ are known, then the only unknown is $\Delta p$.

Before continuing it can be seen that $\Delta p$ is also the *lift per unit area* for the aerofoil. This can be seen from Equation 3.4.1 which gives the lift *per unit span*, and can be re-written as

$$L = \int_0^c \Delta p\ \mathrm{d}x$$

The total lift can also be related to the total *circulation* about the aerofoil through the *Kutta-Joukowski theorem* which gives (Moran [16] and Kueth and Chow [15]):

$$L = \rho V_\infty \Gamma \tag{3.4.8}$$

with $\rho$ the air density, $V_\infty$ the free-stream air velocity and $\Gamma$ the total circulation about the aerofoil.

$\Gamma$ is determined by integrating the *circulation density*, $\gamma$, about the aerofoil [16]:

$$\Gamma = \int_0^c \gamma(x)\ \mathrm{d}x \tag{3.4.9}$$

The circulation density is calculated for thin aerofoils by placing a *vortex sheet* on the aerofoil camber line. This is shown in Figure 3.2. The strength of the circulation $\gamma$ is defined as a limiting form of Stokes' theorem as stated in Kueth and Chow [15]:

$$\gamma = \lim_{\Delta s \to 0}\left[\frac{1}{\Delta s}\oint \mathbf{V}\cdot\mathrm{d}\mathbf{l}\right] \tag{3.4.10}$$

where $\Delta s$ is the width of the sheet enclosed by the contour, $\mathbf{V}$ is the velocity vector of the fluid evaluated at a point on the contour and $\mathrm{d}\mathbf{l}$ is the incremental vector tangent to the contour at that point. The contour is shown in Figure 3.3.

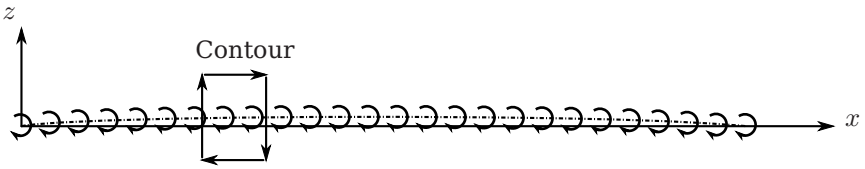


**Figure 3.3** – Contour for evaluating Stoke's theorem over the vortex sheet with airflow to the right.

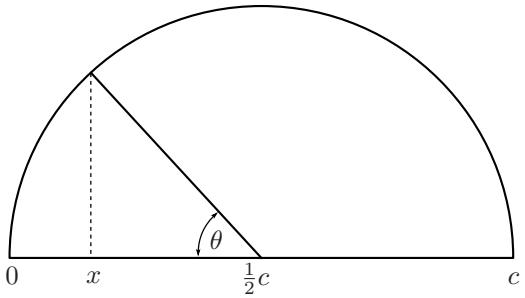


**Figure 3.4** – The definition of $x$ and $\theta$.

The Stokes' theorem integral needs to satisfy the the following boundary conditions:

$$\gamma(c) = 0 \tag{3.4.11}$$

$$\frac{1}{2\pi}\int_0^c \frac{\gamma\,\mathrm{d}x}{x_0 - x} = V_\infty\left[\alpha - \left(\frac{\mathrm{d}z}{\mathrm{d}x}\right)_0\right] \tag{3.4.12}$$

where $\alpha$ is the angle of attack of the aerofoil, and $\left(\frac{\mathrm{d}z}{\mathrm{d}x}\right)_0$ is the slope of the camber line evaluated at the chordwise element $x_0$, some arbitrary position on the chord. Equation 3.4.11 is the Kutta condition stating that there must be no circulation at the trailing edge of the aerofoil, and Equation 3.4.12 is the condition where there is zero flow normal to the camber line. It should be noted that Equation 3.4.12 is applied along the chord, not along the mean camber line. This is due to the assumption that a thin aerofoil is being analysed, and as such it is reasoned that lying the vortex sheet along the chord line will have little effect on the result [28]. This approximation is known as the *planar wing approximation*, [15].

Since it is assumed that the airfoil and camber is small relative to the chord length, it is noted that large flap deflections (such as those found later in this thesis) tend to lead to less accurate results as the deflection results in a camber large relative to the chord length of the airfoil. The results are, however, deemed suitable for this initial study.

### 3.4.1 The Unflapped, Cambered Aerofoil

Typical texts on thin aerofoil theory proceed to develop the necessary equations for a symmetrical aerofoil, before determining those for a cambered aerofoil. These steps are omitted here for expediency but can be found in Kueth and Chow [15].

The vorticity distribution for the *unflapped, cambered* aerofoil is given in this section. The term *unflapped* refers to an aerofoil with no control surfaces, but is the same for an aerofoil with all control surfaces in their neutral positions (no deflections) as shown in Figure 3.1. A flap in this context is the general term for control surfaces which can be deflected (thus changing the camber of the wing), and not just the low-speed lift generation devices used for take-off and landing.

From [15] and [16] we start by considering the position $x$ along the length of the chord of the aerofoil, but it is more convenient to make use of the transformation in Equation 3.4.13 to simplify the mathematics:

$$x = \frac{1}{2}c\,(1 - \cos\theta) \tag{3.4.13}$$

Rearranging gives

$$\theta = \arccos\left(1 - 2\frac{x}{c}\right) \tag{3.4.14}$$

This can be visualised in Figure 3.4

For convenience we now take the derivative Equation 3.4.13 with respect to $\theta$:

$$\mathrm{d}x = \frac{1}{2} c \sin\theta \, \mathrm{d}\theta \tag{3.4.15}$$

Substituting the transformation Equation 3.4.13 into the boundary conditions of Equations 3.4.11 and 3.4.12 the following are obtained:

$$\gamma(\pi) = 0 \tag{3.4.16}$$

$$\frac{1}{2\pi} \int_0^\pi \frac{\gamma \sin\theta \, \mathrm{d}\theta}{\cos\theta - \cos\theta_0} = V_\infty \left[ \alpha - \left( \frac{\mathrm{d}z}{\mathrm{d}x} \right)_0 \right] \tag{3.4.17}$$

As stated in Kueth and Chow [15], and Allen [17], Glauert has shown that, for a cambered, unflapped aerofoil a solution of Equation 3.4.10 subject to Equations 3.4.16 and 3.4.17 is the Fourier sine series:

$$\gamma(\theta) = 2V_\infty \left[ A_0 \frac{1 + cos\theta}{\sin\theta} + \sum_{n=1}^{\infty} A_n \sin n\theta \right] \tag{3.4.18}$$

Substituting Equation 3.4.18 into Equation 3.4.17 leads to

$$\frac{1}{\pi} \int_0^\pi \frac{A_0(1 + \cos\theta)}{\cos\theta - \cos\theta_0} \, \mathrm{d}\theta + \frac{1}{\pi} \int_0^\pi \sum_{n=1}^{\infty} \frac{A_n \sin n\theta \sin\theta}{\cos\theta - \cos\theta_0} \, \mathrm{d}\theta = \alpha - \left( \frac{\mathrm{d}z}{\mathrm{d}x} \right)_0$$

which can be rearranged (using trigonometric identities) to give

$$\frac{\mathrm{d}z}{\mathrm{d}x} = (\alpha - A_0) + \sum_{n=1}^{\infty} A_n \cos n\theta \tag{3.4.19}$$

which is the Fourier cosine expansion of $\frac{\mathrm{d}z}{\mathrm{d}x}$, the gradient of the mean camber line for a given aerofoil as a function of $\theta$.

The Fourier coefficients for the unflapped, cambered aerofoil are:

$$A_{0_u} = \alpha - \frac{1}{\pi} \int_0^\pi \frac{\mathrm{d}z}{\mathrm{d}x} \, \mathrm{d}\theta \tag{3.4.20}$$

$$A_{n_u} = \frac{2}{\pi} \int_0^\pi \frac{\mathrm{d}z}{\mathrm{d}x} \cos(n\theta) \, \mathrm{d}\theta \tag{3.4.21}$$

Note that these are also the same results for the case of a flaps neutral aerofoil with any number of flaps.

Substituting the Fourier coefficients Equations 3.4.20 and 3.4.21 into Equation 3.4.18 gives a complete expression for $\gamma$, and hence it is now possible to solve the integral Equation 3.4.9 which can be substituted into Equation 3.4.8. From the aforementioned equations, it is now possible to see the relation between the circulation density and $\Delta p$:

$$\Delta p = \rho V_\infty \gamma \tag{3.4.22}$$

Since $\Delta p$ is the lift per unit area, it is also representative of the force normal to the chord at any given point. This will be important when the above theory is extended for deflected flaps in §3.4.2.

Making use of Equations 3.4.7 and 3.4.22 as well as the lift and moment equations of Equations 3.4.1 to 3.4.6 leads to the following:

$$L = \rho V_\infty \int_0^c \gamma \, \mathrm{d}x \tag{3.4.23}$$

$$M_H = -\rho V_\infty \int_{x_H}^c \gamma \, (x - x_H) \, \mathrm{d}x \tag{3.4.24}$$

For the specific case of the aileron, consider (as shown in Figure 3.1) the aileron of length $E_a c$ whose hinge is located at

$$x_a = c\,(1 - E_a)$$

and converted using the transformation of Equation 3.4.14 to

$$\theta_{H_a} = \arccos\left( 1 - \frac{2c(1 - E_a)}{c} \right) = \arccos(2E_a - 1) \tag{3.4.25}$$

From the general hinge moment equation of Equation 3.4.24 the following is obtained

$$M_H = -\rho V_\infty \int_{c(1-E_a)}^{c} \gamma \left(x - c\left(1 - E_a\right)\right)\, \mathrm{d}x \tag{3.4.26}$$

and, making use of Equations 3.4.14 and 3.4.15, this becomes

$$\begin{aligned} M_{H_a} &= -\rho V_\infty \int_{\theta_{H_a}}^{\pi} \gamma \left(\frac{1}{2}c\left(1 - \cos\theta\right) - c(1 - E_a)\right) \frac{1}{2}c \sin\theta \, \mathrm{d}\theta \\ &= -\frac{\rho V_\infty c^2}{4} \int_{\arccos\left(2E_a - 1\right)}^{\pi} \gamma \sin\theta \left((2E_a - 1) - cos\theta\right)\, \mathrm{d}\theta \end{aligned} \tag{3.4.27}$$

And when normalised with dynamic pressure and chord length squared, the moment coefficient per unit span is given by

$$C_{H_a} = -\frac{\rho V_\infty}{4q_\infty} \int_{\arccos\left(2E_a - 1\right)}^{\pi} \gamma \sin\theta \left((2E_a - 1) - \cos\theta\right)\, \mathrm{d}\theta \tag{3.4.28}$$

Following a similar process with

$$x_t = c\left(1 - E_t\right)$$

and

$$\theta_{H_t} = \arccos\left(2E_t - 1\right) \tag{3.4.29}$$

the tab hinge moment coefficient is obtained:

$$C_{H_t} = -\frac{\rho V_\infty}{4q_\infty} \int_{\arccos\left(2E_t - 1\right)}^{\pi} \gamma \sin\theta \left((2E_t - 1) - \cos\theta\right)\, \mathrm{d}\theta \tag{3.4.30}$$

The lift coefficient is similarly obtained:

$$C_L = \frac{\rho V_\infty}{q_\infty c} \int_0^c \gamma \, \mathrm{d}x = \frac{\rho V_\infty}{2q_\infty} \int_0^\pi \gamma \sin\theta \, \mathrm{d}\theta \tag{3.4.31}$$

The $\gamma$ used in the above equations is only valid if neither of the control surfaces are deflected. §3.4.2 takes control surface deflections into account.

### 3.4.2 Flap Contributions – the Aileron and Tab

In §3.4.1 it was shown how to determine $\Delta p$ and hence the normal force distribution across the chord of a cambered unflapped aerofoil. This section examines the effects of using a portion of the wing as a deflectable control surface such as the aileron. The aileron is a trailing edge flap, as is the tab, thus the analysis will be limited to this case. Moran [16] suggests a method of considering leading edge flaps in a manner similar to the method described below.

The primary principle used in this section is the concept of *superposition*. When examining a cambered aerofoil with aileron and tab, it is possible in the case of thin aerofoil theory to separate the the contributions into the following components: contributions due to unflapped, cambered aerofoil; contributions due to a symmetrical aerofoil with zero angle of attack with only the aileron deflected; and contributions due to a symmetrical aerofoil with only the tab deflected. This is represented graphically in Figure 3.5. Allen [17] makes use of this concept with regards to determining the total chordwise load distribution over aerofoil sections with serially hinged trailing-edge flaps, which Kueth and Chow [15] expand upon.

Allen [17] considers the case of a single flap initially before generalising the technique to any number of serially hinged flaps. Using Figure 3.6 as reference, [17] states that the total *normal force distribution* is due to the summation of the distribution due to the cambered aerofoil and an *incremental* contribution due to the deflection of the deflected flap. For convenience the normal forces are plotted against the flap-neutral chord in order to better see the effect of the contribution. The process described in Figure 3.6 can be repeated for every deflected flap.

Similarly, Kueth and Chow [15] and Moran [16] develop the concept of an *incremental* lift and moment contribution due to the deflection of the various control surfaces. This equates to an incremental *pressure distribution* over the chord of the aerofoil for *each* control surface deflected.

It is necessary to follow the same process as was followed with the unflapped, cambered aerofoil in §3.4.1 in order to determine the Fourier coefficients used to calculate $\gamma$. Since the deflection of the flaps only

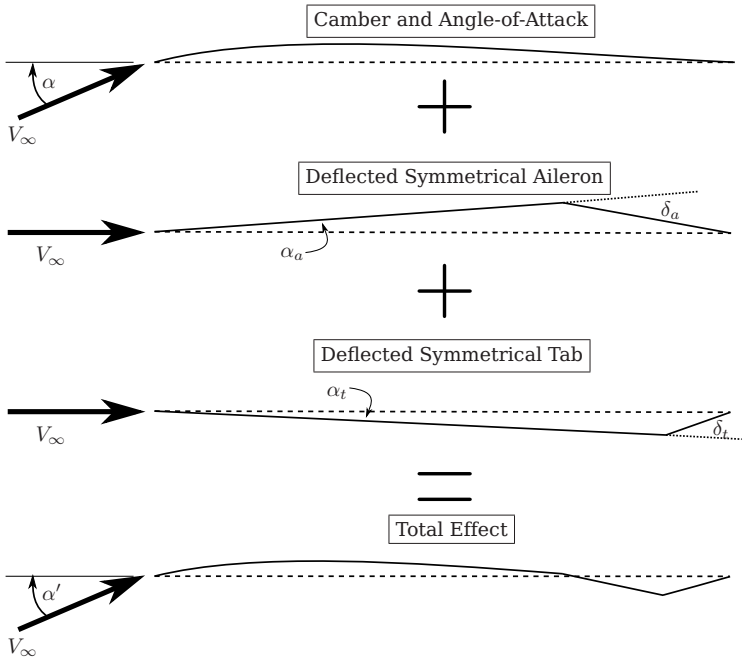


**Figure 3.5** – Components which are superimposed to provide the result of complete aerofoil with deflected flaps. The dashed line indicates the chord line from leading edge to trailing edge. In the aileron and tab cases, there is an effective angle of attack due to the camber caused by deflecting each individual surface.

provide an incremental value, the angle of attack is taken as zero [15]. It can be reasoned that the contribution due to the whole aerofoil's angle of attack is taken into account in Equations 3.4.20 and 3.4.21 already.

Considering Figure 3.7, some geometrical definitions are provided for the flapped case. Since a deflection of a flap results in a change in camber of the aerofoil, a new chord is defined from the leading edge of the aerofoil to the trailing edge of the control surface. Since it is convenient to work with a horizontal chord length, the entire aerofoil has been rotated anti-clockwise by the angle $\alpha_f$, along with the freestream velocity vector $V_\infty$. $\alpha_f$ is the new angle of attack for flap configuration, and this angle is typically very small where $E_f$ and the flap deflection angle, $\delta_f$, are small.

In order to determine $\alpha_f$, some intermediate values are required:

$$\begin{aligned} A &= (1 - E_f)\, c \\ B &= E_f c \\ C &= \sqrt{A^2 + B^2 + 2AB\cos\delta_f} = c\sqrt{(1-E_f)^2 + E_f^2 + 2E_f\,(1-E_f)\cos\delta_f} \end{aligned}$$

which is used to determine

$$\alpha_f = \arcsin\left(\frac{B}{C}\sin\delta_f\right) = \arcsin\left(\frac{E_f \sin\delta_f}{\sqrt{(1-E_f)^2 + E_f^2 + 2E_f\,(1-E_f)\cos\delta_f}}\right) \tag{3.4.32}$$

Since a symmetrical aerofoil is assumed, the camber line is now divided into two parts: that belonging to the wing (with a gradient relative to the chord of $m_{f_1}$) and that of the flap (gradient $m_{f_2}$). The position of the hinge along this new chord is given by $x'_f$ and a similar conversion as used in Equation 3.4.13 is used to determine $\theta'_a$, the hinge position in terms of $\theta$:

$$\begin{aligned} x'_f &= c(1 - E_f)\cos\alpha_f \\ \theta'_{H_f} &= \arccos\left(1 - 2\frac{(1-E_f)\cos\alpha_f}{\sqrt{(1-E_f)^2 + E_f^2 + 2E_f\,(1-E_f)\cos\delta_f}}\right) \\ m_{1_f} &= \tan\alpha_f \\ m_{2_f} &= \tan\left(\alpha_f - \delta_f\right) \end{aligned} \tag{3.4.33}$$

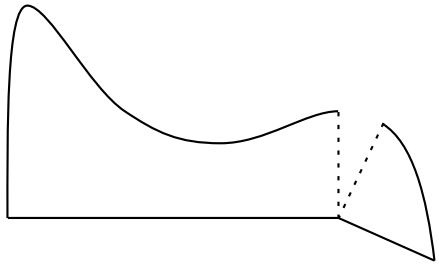

(a) Normal-force distribution for flap deflected.

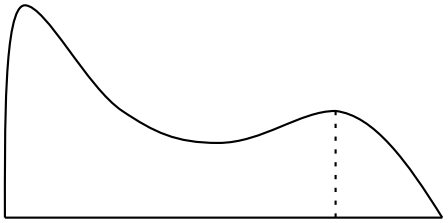

(b) Normal-force distribution for flap deflected ($p_t$) plotted against the flap neutral chord.

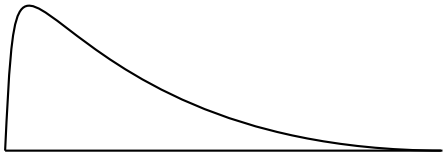

(c) Normal-force distribution ($p_u$) for flap neutral.

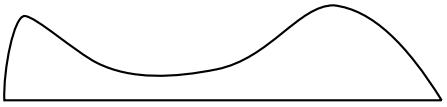

(d) Normal-force contribution ($p_f$) due to the deflected flap plotted against the flap neutral chord.

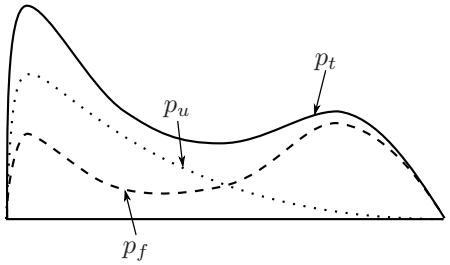


(e) The summation of the distributions in 3.6(c) and 3.6(d) to give 3.6(b).

**Figure 3.6** – Normal-force distributions over the chord of the aerofoil (based partially on a diagram from Allen [17]).

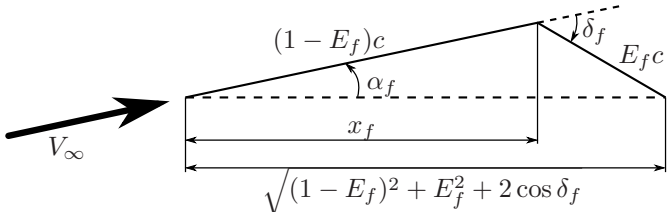


**Figure 3.7** – Geometry used for determining the incremental contribution of a flap to the pressure distribution.

Equation 3.4.20 and Equation 3.4.21 are now used and the integration is performed in two parts: from the leading edge to the hinge point ($\theta'_{H_f}$) and then from the hinge point to the trailing edge. The results for the aileron are provided below:

$$A_{0_a} = \alpha_a - \frac{1}{\pi}\left[m_{1_a}\theta'_{H_a} + m_{2_a}\left(\pi - \theta'_{H_a}\right)\right] \tag{3.4.34}$$

$$A_{n_a} = \frac{2}{n\pi}\sin\left(n\theta'_{H_a}\right)\left(m_{1_a} - m_{2_a}\right) \tag{3.4.35}$$

and similarly for the tab:

$$A_{0_t} = \alpha_t - \frac{1}{\pi}\left[m_{1_t}\theta'_{H_t} + m_{2_t}\left(\pi - \theta'_{H_t}\right)\right] \tag{3.4.36}$$

$$A_{n_t} = \frac{2}{n\pi}\sin\left(n\theta'_{H_t}\right)\left(m_{1_t} - m_{2_t}\right) \tag{3.4.37}$$

Now the circulation density contribution for each case is calculated starting with the unflapped, cambered

aerofoil:

$$\begin{aligned}\gamma_u &= 2V_\infty \left[ A_{0_u} \frac{1+cos\theta}{\sin\theta} + \sum_{n=1}^{\infty} A_{n_u} \sin n\theta \right] \\ &= 2V_\infty \left[ \left( \alpha - \frac{1}{\pi} \int_0^\pi \frac{\mathrm{d}z}{\mathrm{d}x}\, \mathrm{d}\theta \right) \left( \frac{1+cos\theta}{\sin\theta} \right) + \sum_{n=1}^{\infty} \left( \frac{2}{\pi} \int_0^\pi \frac{\mathrm{d}z}{\mathrm{d}x} \cos(n\theta)\ \mathrm{d}\theta \right) \sin n\theta \right]\end{aligned}$$

The incremental circulation density due to aileron deflection:

$$\begin{aligned}\gamma_a &= 2V_\infty \left[ A_{0_a} \frac{1+cos\theta}{\sin\theta} + \sum_{n=1}^{\infty} A_{n_a} \sin n\theta \right] \\ &= 2V_\infty \left[ \left( \alpha_a - \frac{1}{\pi} \left( m_{1_a} \theta_{H_a} + m_{2_a} (\pi - \theta_{H_a}) \right) \right) \left( \frac{1+cos\theta}{\sin\theta} \right) \right. \\ &\quad \left. + \sum_{n=1}^{\infty} \left( \frac{2}{n\pi} \sin(n\theta_{H_a}) \left( m_{1_a} - m_{2_a} \right) \right) \sin n\theta \right]\end{aligned}$$

The incremental circulation density due to tab deflection

$$\begin{aligned}\gamma_t &= 2V_\infty \left[ A_{0_t} \frac{1+cos\theta}{\sin\theta} + \sum_{n=1}^{\infty} A_{n_t} \sin n\theta \right] \\ &= 2V_\infty \left[ \left( \alpha_t - \frac{1}{\pi} \left( m_{1_t} \theta_{H_t} + m_{2_t} (\pi - \theta_{H_t}) \right) \right) \left( \frac{1+cos\theta}{\sin\theta} \right) \right. \\ &\quad \left. + \sum_{n=1}^{\infty} \left( \frac{2}{n\pi} \sin(n\theta_{H_t}) \left( m_{1_t} - m_{2_t} \right) \right) \sin n\theta \right]\end{aligned}$$

The total circulation density is thus given by:

$$\begin{aligned}\gamma &= \gamma_u + \gamma_a + \gamma_t \\ &= 2V_\infty \left[ A_{0_u} \frac{1+cos\theta}{\sin\theta} + \sum_{n=1}^{\infty} A_{n_u} \sin n\theta \right] + 2V_\infty \left[ A_{0_t} \frac{1+cos\theta}{\sin\theta} + \sum_{n=1}^{\infty} A_{n_t} \sin n\theta \right] \\ &\quad + 2V_\infty \left[ A_{0_t} \frac{1+cos\theta}{\sin\theta} + \sum_{n=1}^{\infty} A_{n_t} \sin n\theta \right]\end{aligned}$$

or in terms of the Fourier coefficients

$$\gamma = 2V_\infty \left[ \left( A_{0_u} + A_{0_a} + A_{0_t} \right) \left( \frac{1+cos\theta}{\sin\theta} \right) + \sum_{n=1}^{\infty} \left( A_{n_u} + A_{n_a} + A_{n_t} \right) \sin n\theta \right] \tag{3.4.38}$$

$\gamma$ given in Equation 3.4.38 provides the circulation density for the general case of an aerofoil with aileron and tab, regardless of the deflection angles of the two control surfaces. This can now be used to write general equations for the 2D lift and aileron hinge moments. First define $A_0 = (A_{0_u} + A_{0_a} + A_{0_t})$ and $A_n = (A_{n_u} + A_{n_a} + A_{n_t})$. Substituting the combined Fourier coefficients, $A_0$ and $A_n$, into Equation 3.4.38, which is, in turn, substituted into Equation 3.4.31 to provide the complete lift coefficient equation:

$$C_L = \frac{\rho V_\infty^2}{q_\infty} \int_0^\pi \left[ A_0 \left( \frac{1+cos\theta}{\sin\theta} \right) + \sum_{n=1}^{\infty} A_n \sin n\theta \right] \sin\theta\ \mathrm{d}\theta$$

and into Equations 3.4.28 and 3.4.30 to provide the tab and aileron hinge moment coefficient equations:

$$\begin{aligned}C_{H_a} &= -\frac{\rho V_\infty^2}{2q} \int_{\arccos(2E_a - 1)}^{\pi} \left[ A_0 \left( \frac{1+cos\theta}{\sin\theta} \right) + \sum_{n=1}^{\infty} A_n \sin n\theta \right] \sin\theta \left( (2E_a - 1) - \cos\theta \right)\ \mathrm{d}\theta \\ C_{H_t} &= -\frac{\rho V_\infty^2}{2q} \int_{\arccos(2E_t - 1)}^{\pi} \left[ A_0 \left( \frac{1+cos\theta}{\sin\theta} \right) + \sum_{n=1}^{\infty} A_n \sin n\theta \right] \sin\theta \left( (2E_t - 1) - \cos\theta \right)\ \mathrm{d}\theta\end{aligned}$$

and with $q_\infty = \frac{1}{2}\rho V_\infty^2$, these simplify to functions independent of $V_\infty$:

$$C_L = \frac{\rho V_\infty^2}{q_\infty}\int_0^\pi \left[A_0\left(\frac{1+cos\theta}{\sin\theta}\right) + \sum_{n=1}^{\infty} A_n \sin n\theta\right]\sin\theta \ \mathrm{d}\theta \tag{3.4.39}$$

$$C_{H_a} = -\int_{\arccos(2E_a-1)}^{\pi} A_0\left(1+cos\theta\right)\left((2E_a-1)-\cos\theta\right) + \sum_{n=1}^{\infty} A_n \sin n\theta \sin\theta\left((2E_a-1)-\cos\theta\right)\ \mathrm{d}\theta \tag{3.4.40}$$

$$C_{H_t} = -\int_{\arccos(2E_t-1)}^{\pi} A_0\left(1+cos\theta\right)\left((2E_t-1)-\cos\theta\right) + \sum_{n=1}^{\infty} A_n \sin n\theta \sin\theta\left((2E_t-1)-\cos\theta\right)\ \mathrm{d}\theta \tag{3.4.41}$$

## 3.5 Linearisation of the Coefficients

The equations developed in §3.4.2, specifically Equations 3.4.39 to 3.4.41, provide a non-linear approximation of the lift and control surface hinge moments. Many stability and control texts ([7], [6]) regarding aerodynamic flight use linearised equations of the form

$$C_x = C_{x_0} + C_{x_\alpha}\alpha + C_{x_{\delta_a}}\delta_a + C_{x_{\delta_t}}\delta_t \tag{3.5.1}$$

where $C_x$ is any of $C_L$, $C_{H_a}$ and $C_{H_t}$. $C_{x_0}$ is the constant contribution due to the shape (camber and thickness) of the aerofoil, $C_{x_\alpha} = \frac{\partial C_x}{\partial \alpha}$ is a derivative providing the contribution to $C_x$ due to angle of attack, $C_{x_{\delta_a}} = \frac{\partial C_x}{\partial \delta_a}$ is the derivative providing the contribution due to aileron deflection and $C_{x_{\delta_t}} = \frac{\partial C_x}{\partial \delta_t}$ is the derivative providing the contribution due to tab deflection.

Since this is a convenient form with which to work, the linearised forms of Equations 3.4.39 to 3.4.41 are provided in this section with a more complete derivation in Appendix A. Texts discussing thin aerofoil theory (Anderson [28], Kueth and Chow [15], and Moran [16]) simplify the analysis by ignoring the higher order components ($n > 2$) in the Fourier series expansions (which fall away in any case for symmetric aerofoils). Following the same route here, and making use of small angle approximations regarding the control surface deflections and angle of attack, it is possible to re-write Equations 3.4.39 to 3.4.41 in the form of Equation 3.5.1, where the dependencies on $\alpha$, $\delta_a$ and $\delta_t$ are separated.

It is also useful to define the parameter, $\Psi$, which provides a convenient means to generalise the hinge moment coefficient equation for both the tab and the aileron.For the aileron hinge moment coefficient:

$$\Psi = (2E_a - 1)$$

and for the tab hinge moment coefficient

$$\Psi = (2E_t - 1)$$

After making use of the above generalisation and small angle approximations, the hinge moment coefficient equation becomes

$$\begin{aligned}
C_H \quad = \quad & -\int_{\arccos\Psi}^{\pi} \left\{\left[-\frac{1}{\pi}\int_0^\pi \frac{\mathrm{d}z}{\mathrm{d}x}\ \mathrm{d}\theta\right](1+cos\theta) + \sum_{n=1}^{\infty}\left[\frac{2}{\pi}\int_0^\pi \frac{\mathrm{d}z}{\mathrm{d}x}\cos(n\theta)\ \mathrm{d}\theta\right]\sin n\theta\sin\theta\right\}(\Psi-\cos\theta) \\
& +\alpha\left(1+cos\theta\right)(\Psi-\cos\theta) \\
& +\delta_a(\Psi-\cos\theta)\left\{\left[1-\frac{1}{\pi}\arccos(2E_a-1)\right](1+cos\theta) + \sum_{n=1}^{\infty}\left[\frac{2}{n\pi}\sin(n\arccos(2E_a-1))\right]\sin n\theta\sin\theta\right\} \\
& +\delta_t(\Psi-\cos\theta)\left\{\left[1-\frac{1}{\pi}\arccos(2E_t-1))\right](1+cos\theta) + \sum_{n=1}^{\infty}\left\{\frac{2}{n\pi}\sin(n\arccos(2E_t-1))\right\}\sin n\theta\sin\theta\right\}\mathrm{d}\theta
\end{aligned}$$

where it can be seen that the terms related to $\alpha$, $\delta_a$, $\delta_t$ are grouped. Taking the Fourier coefficients $A_0$, $A_1$ and $A_2$ only, reduces the equation to

$$C_H = b_0 + b_1\alpha + b_2\delta_a + b_3\delta_t \tag{3.5.2}$$

where the functions describing $b_0$, $b_1$, $b_2$ and $b_3$ are provided in Appendix A. Also by setting the parameter $\Psi$ appropriately, the above coefficients can be used to determine either the tab, or the aileron sectional hinge moment coefficient.

A similar process is followed for the lift coefficient (also derived in Appendix A).

From Equation A.2.1 it can be seen that it is possible to get the lift coefficient in the form:

$$C_L = a_0 + a_1\alpha + a_2\delta_a + a_3\delta_t \tag{3.5.3}$$

The functions $a_0$, $a_1$, $a_2$ and $a_3$ are derived in a similar manner to $b_0$, $b_1$, $b_2$ and $b_3$, with the results given below:

$$a_0 = C_{L_0} = 2\int_0^\pi \frac{\mathrm{d}z}{\mathrm{d}x}\mathrm{d}\theta + 2\int_0^\pi \frac{\mathrm{d}z}{\mathrm{d}x}\cos\theta\mathrm{d}\theta$$

which is due only to the camber of the flaps-neutral aerofoil,

$$a_1 = C_{L_\alpha} = 2\pi$$

which is entirely independent of any properties of the aerofoil,

$$a_2 = C_{L_{\delta_a}} = 2[\pi - \arccos(2E_a - 1) + \sin(\arccos(2E_a - 1))]$$

which only depends on the aileron chord length, and finally the only tab chord length dependent parameter

$$a_3 = C_{L_{\delta_t}} = 2[\pi - \arccos(2E_t - 1) + \sin(\arccos(2E_t - 1))]$$

Note that the lift is determined for the entire aerofoil, and thus is not dependent on the parameter $\Psi$.

### 3.5.1 A Note Regarding Drag

As may have been noticed, the effects of drag are not included. Thin aerofoil theory which in this case is only applicable to incompressible, inviscid flow does not provide a means to determine the total drag of the aerofoil. It provides a metric to determine the sectional *induced drag* coefficient, which is drag caused during the production of lift [30], and is directly related to the square of lift:

$$C_{D_i} = \frac{C_L^2}{\pi \mathcal{AR}} \tag{3.5.4}$$

which indicates that greater lift results quadratically in greater drag. Equation 3.5.4 is valid for both as a sectional value as well as for three-dimensional wings with an elliptical lift distribution. An additional factor, known as the *Oswald efficiency factor*, $e$, is included for non-elliptical lift distributions. This factor is also known as the *span efficiency factor* for wings with finite span [30]. This leads to

$$C_{D_{i_{3D}}} = \frac{C_L^2}{\pi \mathcal{AR}e}$$

for finite-span aerofoils. The value of $e$ is typically larger than 1, since this value represents the theoretical minimum induced drag for a finite aerofoil.

Dommasch et al, [30], lists the various types of drag:

- Form or pressure drag
- Skin-friction drag
- Induced drag
- Wave drag

The skin-friction and form drag of an aerofoil are often summed together and termed the *profile drag* of the aerofoil. For sub-sonic flight, the total wing drag is given by summing the profile drag and the induced drag, while for transonic flight wave drag must be added as well.

As has been stated already, this iteration of the project only examines sub-sonic flight, and the theory developed thus far is based on this assumption, hence wave drag is ignored.

The total sectional drag coefficient for the wing is thus given by Koen [31] as

$$C_D = C_{D_0} + C_{D_i}$$

Induced drag has already been discussed, but it is necessary to briefly discuss form drag and skin-friction drag. These two components form what is known as *parasitic drag* ($C_{D_0}$).

Skin-friction drag is an effect of the viscosity of air, where air particles adhere "to the surface of any body moving through the air [and] results in the formation of a boundary layer and a given amount of drag", Dommasch [30].

Form drag is another result of the viscosity of a fluid. It is also termed pressure drag, since it is related to the normal *pressure* distribution along the body moving through the fluid. Since form drag is difficult to predict, experimental data is typically required to provide some sort of accurate measure [27].

Since both the components of the profile drag are reliant on the fluid being viscous, it is not possible to determine the effect of these two components of drag due to the shape of the aerofoil with the inviscid methods described in this chapter.

## 3.6 Thin Aerofoil Theory Validation with *X-Foil*

In order to verify the above derivations, an external program, written by Professor Mark Drela of MIT, called *XFoil* was used. Some results are provided in Appendix D as Tables D.1 and D.2 for comparison. In all cases the analysis is inviscid, and the NACA 23012 aerofoil was used. Since X-Foil makes use of a normalised chord length, $c$ was chosen to have a length of $1\,\mathrm{m}$.

The results provided in Table D.1 show the values obtained using the various methods, namely those from X-Foil, the non-linear thin aerofoil theory and linearised thin aerofoil theory. These results are then reworked to percentage deviations from the X-Foil value in Table D.2.

On examining the values provided in these tables, it is possible to see that the various methods correspond reasonably with each other with the non-linear theory providing results closer to those of X-Foil. Regarding the lift coefficients the linear and non-linear thin aerofoil theories correspond well with each other, with deviations of at most $2\,\%$ for the cases shown in the tables. These results compared with those provided by X-Foil also correspond well, with the largest deviation being approximately $37\,\%$ that of X-Foil's values and the average deviation being approximately $10\,\%$.

The aileron hinge moment coefficient values are seen to have a larger deviation with the non-linear theory corresponding better with X-Foil than the linear theory. The largest deviation is $144\,\%$ associated with large angle of attack and control surface deflections. For the remainder the non-linear theory is on average within $10\,\%$ of the X-Foil values. The linearised thin aerofoil theory does not perform as well, with deviations upwards of $20\,\%$ being found, especially for large angles of attack and deflection angles.

The tab hinge moment coefficient values correspond less well for both the linear and non-linear theory. The reason for this is explained as a result of the large deflections angles violating the constraints of the thin aerofoil theory. Another aspect is that is ignored is that of out-of-plane effects where large deflection angles are present, as well as the thickness conditions for the thin aerofoil theory no longer being satisfied.

Though there are discrepancies, the low order aerodynamic models developed within this chapter still provide suitable results to provide valuable insights. The determination of the aileron hinge moment coefficients is deemed accurate enough to allow the use of the thin aerofoil theory, though, as the values of the tab coefficients are less reliable, more advanced theories and models developed in the future will be necessary to accurately determine the tab actuator requirements. This will not pose a problem for the study performed in this thesis as primarily the aileron hinge moment is being considered.

## 3.7 A Three-Dimensional Approximation

While the two-dimensional thin aerofoil theory provides sectional coefficients, and assumes an infinitely long wing, it is possible to construct a first approximation of a *three-dimensional* wing. This can be done by considering a general wing profile as shown in Figure 3.8. As can be seen from the figure, some extra parameters can now be included relating to the span of the aerofoil and the control surfaces:

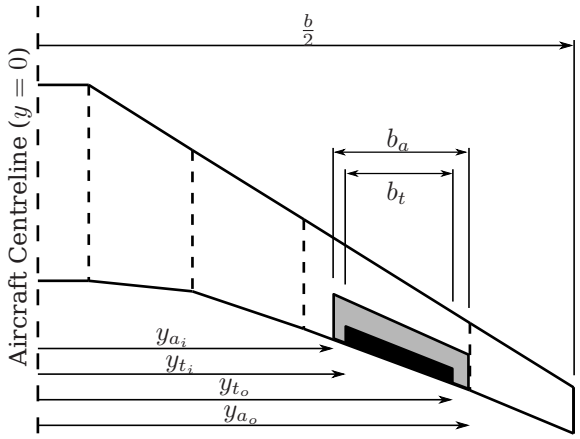


**Figure 3.8** – Plan view of a typical aerofoil showing the aileron and tab.

| | |
|---|---|
| $b$ | The span of the wing. |
| $b_a$ | Span of the aileron. |
| $b_t$ | Span of the tab. |
| $y_{a_i}$ | The $y$ position of the inboard edge of the aileron. |
| $y_{t_i}$ | The $y$ position of the inboard edge of the tab. |
| $y_{a_o}$ | The $y$ position of the outboard edge of the aileron. |
| $y_{t_o}$ | The $y$ position of the outboard edge of the tab. |

At any position along the span of the wing, it is possible to take a cross-sectional cut of the wing which provides the aerofoil's profile at that position. This can be broken up into a number of sections which have the *same* profile:

| | |
|---|---|
| $0 \leq y < y_{a_i}$ | From the wing root to the inboard edge of the aileron: wing only. |
| $y_{a_i} \leq y < y_{t_i}$ | From the inboard edge of the aileron to the inboard edge of the tab: wing and aileron. |
| $y_{t_i} \leq y < y_{a_o}$ | From the inboard to the outboard edges of the tab: wing, aileron and tab. |
| $y_{a_o} \leq y < y_{t_o}$ | From the outboard edge of the tab to the that of the aileron: wing and aileron. |
| $y_{t_o} \leq y \leq \frac{b}{2}$ | From the outboard edge of the aileron to the wing tip: wing only. |

In addition, it is assumed that the same flaps-neutral profile is used along the entire span of the wing, and only scaled according to the chord length. Since the planar wing profile has no "jump discontinuities" this assumption is deemed sufficient for this preliminary analysis.

By making use of the combination of the cross-sectional and planar profile information, it is now possible to determine the total lift coefficient the aerofoil will generate, along with the hinge moment coefficients of *each* aileron and tab. In addition the 3D geometry allows the computation of the *rolling moment*. This is an important parameter since it ties in directly with the performance characteristics of the aircraft that are required to be met.

Bearing in mind that the chord length used to eliminate the unit varies with the span in this case, pseudo-coefficients are calculated before determining the actual coefficients. These pseudo coefficients are marked with a caret:

All of the above is achieved through the process of integration over the span of the wing, from wing tip ($-\frac{b}{2}$) to wing tip ($\frac{b}{2}$):

$$\hat{C}_L = \int_{-\frac{b}{2}}^{\frac{b}{2}} c(y) C_L(y) \, \mathrm{d}y \tag{3.7.1}$$

and for the moment

$$\hat{C}_{M_l} = \int_{-\frac{b}{2}}^{\frac{b}{2}} y c^2(y) C_L(y) \, \mathrm{d}y \tag{3.7.2}$$

The hinge moment pseudo-coefficients are determined using a similar method for each of the control surfaces, with *right* aileron

$$\hat{C}_{H_a} = \int_{y_{a_i}}^{y_{a_o}} c^2(y) C_{H_a}(y) \, \mathrm{d}y \tag{3.7.3}$$

**Table 3.1** – The A330's planar wing dimensions for the right wing. Units are in metres. Source: [1]

| **Tuple #** | 0 | 1 | 2 | 3 | 4 | 5 |
|---|---|---|---|---|---|---|
| $y$ | 0 | 2,7970 | 8,3991 | 14,3932 | 23,3932 | 29,0 |
| $x_{\mathrm{LE}}$ | −0,003 | −0,003 | −3,4959 | −7,2349 | −12,8487 | −16,3465 |
| $x_{\mathrm{TE}}$ | −10,5628 | −10,5628 | −11,1513 | −13,1673 | −16,5066 | −18,8255 |

and right tab

$$\hat{C}_{H_t} = \int_{y_{t_i}}^{y_{t_o}} c^2(y) C_{H_t}(y)\, \mathrm{d}y \tag{3.7.4}$$

Each of these dimensional pseudo-coefficients can now be converted to the standard (not sectional) coefficient through the division of $S$, the wing surface area, and in the case of the moments, also with $c_{\mathrm{mac}}$:

$$C_{L_{3\mathrm{D}}} = \frac{\hat{C}_L}{S} \tag{3.7.5}$$

and the moment coefficients:

$$C_{M_{3\mathrm{D}}} = \frac{\hat{C}_{M_{3\mathrm{D}}}}{S c_{\mathrm{mac}}} \tag{3.7.6}$$

$$C_{H_{a_{3\mathrm{D}}}} = \frac{\hat{C}_{H_{a_{3\mathrm{D}}}}}{S c_{\mathrm{mac}}} \tag{3.7.7}$$

$$C_{H_{t_{3\mathrm{D}}}} = \frac{\hat{C}_{H_{t_{3\mathrm{D}}}}}{S c_{\mathrm{mac}}} \tag{3.7.8}$$

which are now the traditional coefficients and can be used to determine the lift, rolling moment and hinge moments. From Equations 3.7.5 to 3.7.8:

$$L = \frac{1}{2}\rho V_\infty^2 S C_{L_{3\mathrm{D}}} \tag{3.7.9}$$

$$M = \frac{1}{2}\rho V_\infty^2 S c_{\mathrm{mac}} C_{M_{3\mathrm{D}}} \tag{3.7.10}$$

$$H_a = \frac{1}{2}\rho V_\infty^2 S c_{\mathrm{mac}} C_{H_{a_{3\mathrm{D}}}} \tag{3.7.11}$$

$$H_t = \frac{1}{2}\rho V_\infty^2 S c_{\mathrm{mac}} C_{H_{t_{3\mathrm{D}}}} \tag{3.7.12}$$

For the purpose of numerical calculation the wing is defined by a series of tuples of the format ($y$, $x_{\mathrm{LE}}$, $x_{\mathrm{TE}}$), which can be used to define the aerofoil in segments where each segment has the same leading and trailing edge sweep angles. Sample information is provided in Table 3.1. The wing is assumed symmetrical, but asymmetrical aerofoils such as the rudder are also handled easily. A view of the complete wing is shown in Figure 3.9. The wing is then divided into a number of discrete "slices" of constant chord along the span as shown in Figure 3.10. This allows the use of a summation in order to determine the coefficient values (where $r = \frac{b}{\Delta y}$):

$$\hat{C}_L = \sum_{i=1}^{r} C_L \Delta y c \tag{3.7.13}$$

and for the moment

$$\hat{C}_{M_l} = \sum_{i=1}^{r} \left[\Delta y \left(i - \frac{1}{2}\right) - \frac{b}{2}\right] c^2 C_L \Delta y \tag{3.7.14}$$

$$\hat{C}_{H_a} = \sum_{i=1}^{r} c^2 C_{H_a} \Delta y \tag{3.7.15}$$

$$\hat{C}_{H_t} = \sum_{i=1}^{r} c^2 C_{H_t} \Delta y \tag{3.7.16}$$

where $c$, $C_L$, $C_{H_a}$ and $C_{H_t}$ are evaluated for $y = \left[\Delta y \left(i - \frac{1}{2}\right) - \frac{b}{2}\right]$.

It should be noted that this is very low-order approximation of the three dimensional effects of the aerodynamics. Aspects such as those due to sweep angle, wing-tip vortices, fuselage-effects, span-wise flow etc. are not taken into account. Better approximations for wings of finite span include the slender wing theory (the logical successor to thin aerofoil theory) [26], panel methods (Katz [26] and Moran [16]), vortex lattice methods (such as those used by Mark Drela's AVL Software) and lifting line theory ([16]).

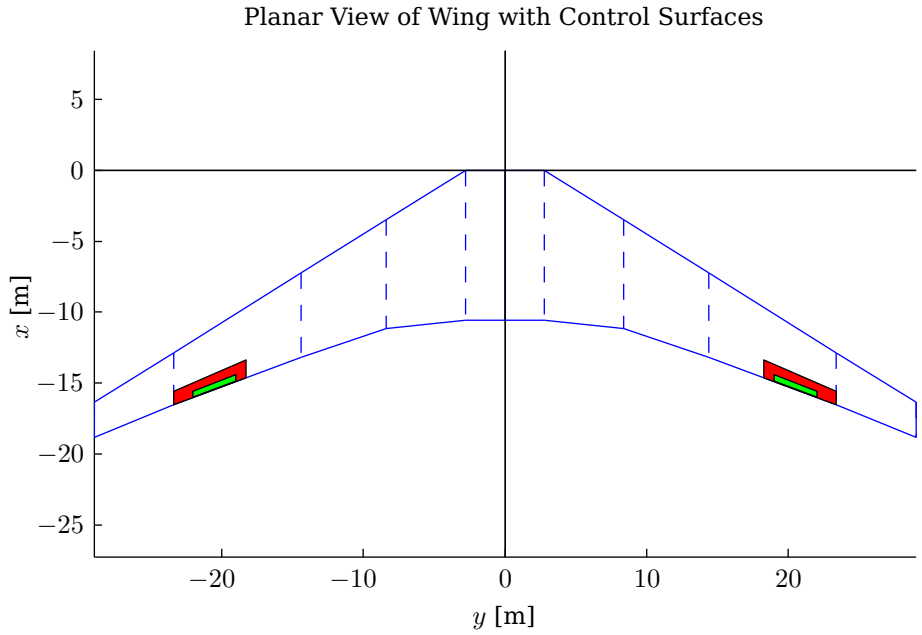


**Figure 3.9** – The planar view of the wing describe in Table 3.1. The aileron (shown in red) parameters are $y_{a_i} = 18{,}2896\,\text{m}$ and $y_{a_o} = 23{,}3932\,\text{m}$, and for the tab (shown in green) $y_{t_i} = 19\,\text{m}$ and $y_{t_o} = 22\,\text{m}$. These values are negated for the left side.

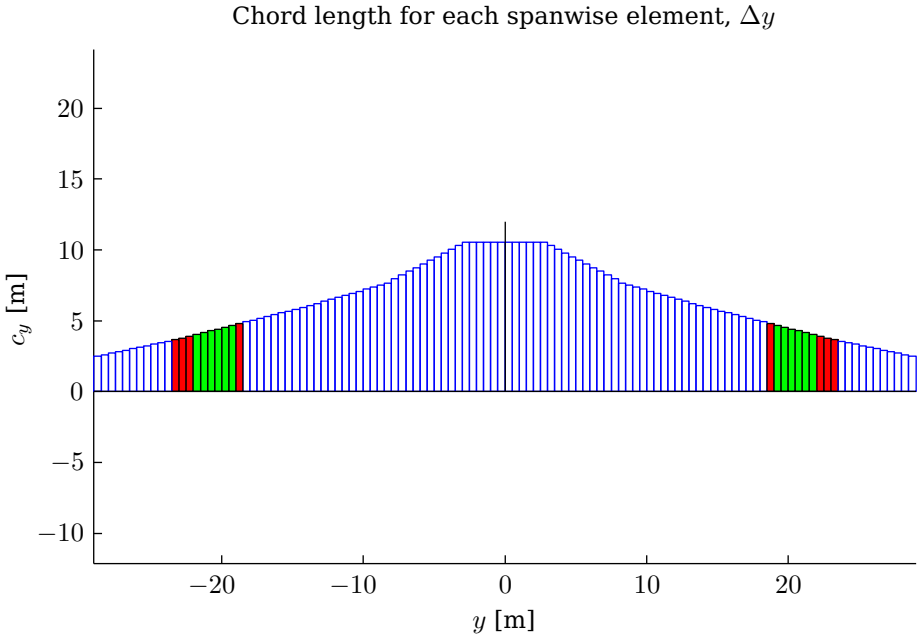


**Figure 3.10** – The planar view of the wing which has been discretised into a number of "slices", each with span $\Delta y$. Note that since no longitudinal analyses are performed, the position of each of the slices in the $x$-direction is irrelevant. The colours again indicate where the control surfaces are with red being aileron and green being aileron and tab.

## 3.8 The Effect of the Tab

Having developed the equations that are used to determine the lift and various hinge moments, it is appropriate to consider the effects of adding a tab, as well as the potential limitations due to the use of the tab. The discussion begins with the two-dimensional case.

It is assumed at all times that the actuators available to actuate the control surfaces (aileron and tab) are sufficient to position the surfaces as required. The reader is also reminded that these are static analyses, which do not take into account the dynamic effects during the act of deflecting the actuator.

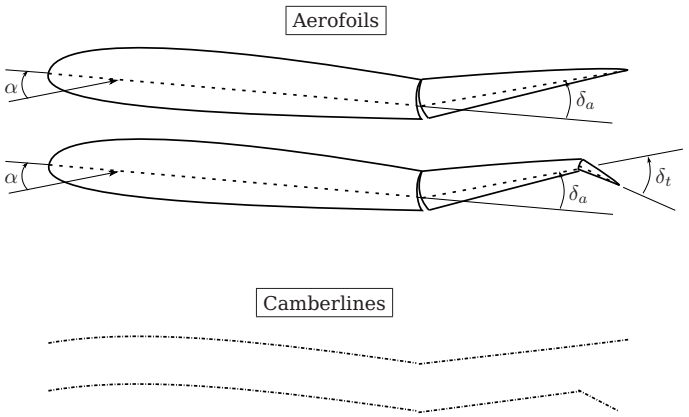


**Figure 3.11** – The effect on the camber line by deflecting the tab for a constant aileron deflection.

It is given that the both the aileron and tab chord lengths are provided as fractions of the total wing chord length with symbols $E_a$ and $E_t$ respectively. Logically the tab chord length can never exceed the aileron chord length and with these considerations in mind the following paragraphs deal with various cases where the tab and aileron chord lengths are varied.

Initially it is attempted to replace the current aileron system with an aileron-tab system which does not exceed the geometry of the current aileron system. Considering the linearised sectional aileron hinge moment coefficient equation of the form of Equation 3.5.2:

$$C_{H_a} = b_{0_a} + b_{1_a}\alpha + b_{2_a}\delta_a + b_{3_a}\delta_t$$

it can be seen that for a given angle of attack and *original aileron deflection* it is possible (at least mathematically) to eliminate the aileron hinge moment completely by choosing a suitable tab deflection for a given tab length:

$$\begin{aligned} C_{H_a} = 0 &= b_{0_a} + b_{1_a}\alpha + b_{2_a}\delta_a + b_{3_a}\delta_t \\ \delta_t^* &= -\frac{1}{b_{3_a}}\left(b_{0_a} + b_{1_a}\alpha + b_{2_a}\delta_a\right) \end{aligned} \tag{3.8.1}$$

It is, however, important to realise that if aileron hinge moment is considered on its own and a suitable tab deflection is determined, there are undesired consequences which need to be taken into account.

Considering that part of the aileron is now used for the tab, it makes sense that there will be an effect on the lift, which may lead to less satisfactory performance. Noting that for the original system the tab can be considered to have zero deflection, it is possible to determine the effect on the lift by examining the equation for the lift coefficient, Equation 3.5.3. This equation gives, for the old configuration at a specific aileron angle and angle of attack, the following sectional lift coefficient expression:

$$C_{L_o} = a_0 + a_1\alpha + a_2\delta_a$$

Now if the tab deflection is added, the following new lift coefficient is obtained:

$$C_{L_n} = a_0 + a_1\alpha + a_2\delta_a + a_3\delta_t^* \tag{3.8.2}$$

Since the first three terms on the LHS of Equation 3.8.2 are the same as the preceding equation, it is possible to see that

$$C_{L_n} - C_{L_o} = a_3\delta_t^*$$

In order to reduce the hinge moment, the tab deflection's sign is opposite to that of the aileron deflection. If one compares the camber lines of the old and new configuration shown in Figure 3.11, it is possible to note that the overall camber of the aerofoil has been changed. With this change comes the associated, undesired loss (or gain) of lift, thus the aerofoil no longer performs (in terms of lift and thus rolling moment) as expected with the original aileron deflection angle. From the figure it is also possible to see that by deflecting the aileron further it would be possible to increase the camber to a value closer to the original, thus restoring the lift. Unfortunately, the tab must now also deflect further since additional hinge moment has been generated on the hinge. This then results in an optimisation problem where the best tab

and *new* aileron deflection angles need to be determined such that the lift is not negatively affected. This is the subject of Chapter 5.

It can also be seen however that there are inherent limits due to the geometry of the system which place limitations on the maximum aileron and tab deflections. These become constraints on the optimisation problem, and also makes it clear that for certain combinations of original angle of attack and aileron deflection, it is *not* possible to achieve the exact same lift coefficient value with the aileron-tab system as with the aileron system.

If, however, more parameters can be adjusted than simply the tab chord length, for example the aileron chord length as well, it would seem possible to extend the region over which the conditions described above can be met. For the three-dimensional case it is also possible that the span of the aileron and/or tab could be varied, to result in better performance over the *entire* angle of attack and old aileron deflection region of operation.

*One final consideration is that of the tab hinge moment.* An actuator is *also* required to actuate the tab, and it would not be useful if the aileron actuator is eliminated only to be replaced by a similar actuator for the tab. There is thus a trade-off between the various goals that are desired to be obtained: reduce aileron hinge moment, maintain the lift *and* keep the tab hinge moment as small as possible.

These considerations will be looked into in Chapter 5 after the various optimisation techniques are described in Chapter 4.

# Chapter 4

# Optimisation – The Process and Algorithms

## 4.1 Introduction

Having now developed a number of aerodynamic equations in Chapter 3, it is possible to formulate the optimisation problem that needs to be solved. In order to do this, a brief introduction to the field of optimisation is provided in this chapter, before going into the specifics related to this project.

For any optimisation problem, the aim is to determine some optimal set of parameters to achieve a specific goal. In this case the parameters are related to the geometry of the aircraft, while the goals are related to the size of the aileron actuator (amongst others). Where optimisation is concerned, it is typically desired to maximise some sort of profit, or minimise some sort of cost. These terms are easily related to the world of finance (or economics) where their meanings are self-explanatory.

Optimisation problems come in many forms, and have many methods available to solve them, though choosing the most suitable method is rarely a straightforward task, Walsh [32]. Optimisation problems can be classified into two main categories, viz. constrained and unconstrained problems, Arora [33], which in turn can be broken into two subcategories: continuous and discrete. Both of these classifications have to do with the design variables, or rather the set of valid values of these design variables. For discrete optimisation problems, the selection of valid values for the parameters is limited to a (typically) fixed number of options (for example: nut and bolt sizes), whereas for continuous optimisation problems, the parameters are usually sets of ranges of real numbers (e.g. $\{\mathbf{x} \in \mathbb{R}\}$).

The simpler of the two classification of optimisation problems, unconstrained optimisation problems, have no limitations on the optimisation parameters, whereas constrained optimisation problems impose limits on the ranges of valid values of these parameters. As such, constrained optimisation problems are usually more difficult to solve than unconstrained optimisations, though most constrained solutions are derived from unconstrained solutions through various transformations or mappings [33]. A large advantage of constrained optimisations is that typically the design space is limited, whereas for unconstrained problems determining the global minimum/maximum could be difficult over the infinitely large design space.

### 4.1.1 Standard Format

The optimisation problem being examined for this project as a multiple-objective, constrained optimisation problem, the general form of which is stated below (Seireg and Rodriguez [34] and Arora [33]):

Find a *design vector*

$$\mathbf{x} = (x_1, x_2, \ldots, x_n) \tag{4.1.1}$$

which minimises (or maximises) the multiple-objective function

$$\mathbf{f}(\mathbf{x}) = (f_1(\mathbf{x}), f_2(\mathbf{x}), \ldots, f_k(\mathbf{x})) \tag{4.1.2}$$

subject to the *equality constraints*

$$h_i(\mathbf{x}) = 0 \qquad i = 1 \text{ to } p \tag{4.1.3}$$

and the *inequality constraints*

$$g_j(\mathbf{x}) \leq 0 \qquad j = 1 \text{ to } m \tag{4.1.4}$$

where $n$ is the number of design variables, $k$ is the number of individual objective functions, $p$ is the number of equality constraints and $m$ is the number of inequality constraints.

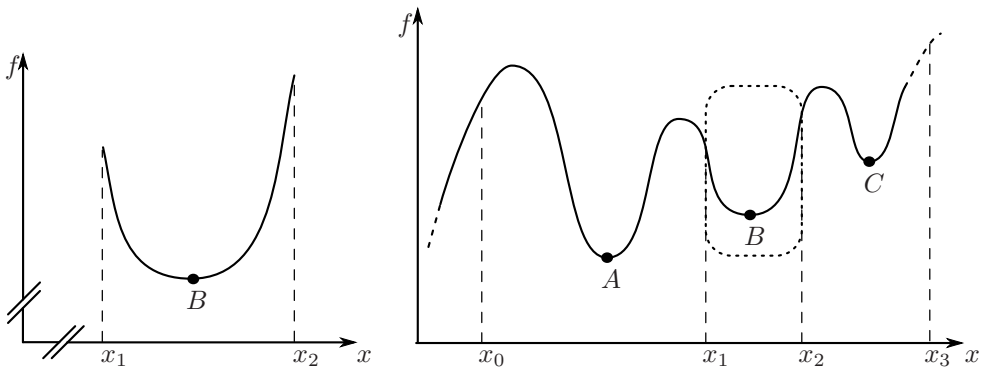


**Figure 4.1** – Graph showing the difference between a local and global minimum.

### 4.1.2 Definitions

The *design vector* is the vector of parameters used to specify a specific design. A given $\mathbf{x}$ in conjunction with the objective function, $f(\mathbf{x})$, gives the effectiveness of the specific design. The *objective function* returns a scalar value (the cost or fitness) of the particular design thus allowing different design parameters to be compared with one-another. If the objective function returns a cost value, it is desired to find the design that produces the least cost, but for an objective function that returns a profit or fitness value, it is desired to find the most profitable design.

The set of possible values for $\mathbf{x}$ is called the *design space*, i.e. it is the set containing all possible combinations of the design variables. Linked to this is the *feasibility space* which is a subset of the design space where all the constraints of the optimisation are satisfied. The idea behind the optimisation is to find some value for $\mathbf{x}$ in the feasible space which minimises (or maximises) the objective function, $f$.

The analysis performed in this project makes use of a cost function, thus the discussion in this chapter concerns finding the minimum value of the cost function. The terms objective function and cost function will be used interchangeably from this point forth. Note that the techniques discussed can be used for both minimisation and maximisation problems, and that any maximisation problems can be converted to a minimisation problem (and vice versa) by setting the new objective function to the negative of the original ($f_n(\mathbf{x}) = -f_o(\mathbf{x})$).

### 4.1.3 Local versus Global Minima

When working with certain mathematical functions it is possible to find several distinct minima, as shown in Figure 4.1. This figure also shows how the range (of $x$) over which we examine the graph is also important. If we only consider values of $x$ between $x_1$ and $x_2$, we can clearly see the minimum $B$, and would assume that this is the absolute minimum. If we consider the range $x_0$ to $x_3$, we find two other minima at $A$ and $C$. Thus when considering the minima of the graph, $f$, it is necessary to specify the ranges which are important for the application. $A$, $B$ and $C$ are all *local* minima in small regions around these points. If $f$ is only defined between $x_0$ and $x_3$, then $f$ can be said to have three local minima, and one *global* (or *absolute*) minimum at $A$.

It is thus important when performing an optimisation to consider whether the result that is delivered from the optimisation process is the desired globally optimal result. This is unfortunately not a trivial exercise and much devotion has gone into the analysis of this particular problem (see Pardalos and Romeijn [35], Horst and Pardalos [36] and Wilde [37] for further information), though the *Weierstrauss Theorem* (Haug, et al [38] and Arora [33]) states the necessary conditions for the *existence* of a global minimum – *If the objective function $f(\mathbf{x})$ is continuous on a non-empty feasible set $S$ that is closed and bounded, then $f$ has a global minimum in $S$.*

### 4.1.4 Optimality Conditions for Unconstrained Optimisation Problems

In order for a design to be considered optimal, certain conditions need to be met. For functions of a single variable most calculus texts discuss the subject of maxima and minima. For functions of a single variable, Stewart [39] provides the following necessary conditions (which are also summarised in Arora [33]):

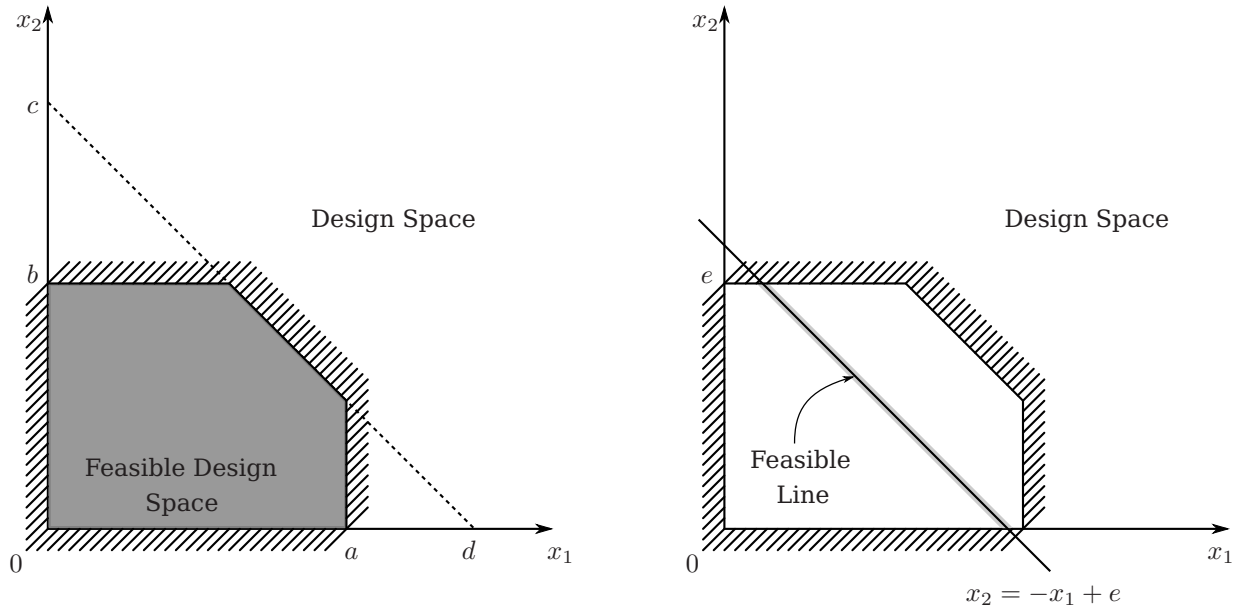


**Figure 4.2** – How constraints influence the feasible design space.

- *First order necessary condition – Fermat's Theorem* (from [39]): "If $f$ has a local maximum or minimum at $x_c$, and if $\frac{\mathrm{d}f}{\mathrm{d}x}\Big|_{x_c}$ exists, then this derivative is zero."
- *Second order necessary condition* – For a local minimum, the second derivative evaluated at $x_c$ must be: $\frac{\mathrm{d}^2 f}{\mathrm{d}x^2}\Big|_{x_c} \geq 0$ and for a local maximum $\frac{\mathrm{d}^2 f}{\mathrm{d}x^2}\Big|_{x_c} \leq 0$. These become sufficiency conditions if the relation is strictly greater- or less-than respectively in conjunction with the necessary condition.

Arora [33] also provides the optimality conditions for a function of several variables which is an extension on the above:

- *First order necessary condition* – for the multivariate function $f(\mathbf{x})$, it is necessary that $\nabla f = \mathbf{0}$.
- *Second order necessary condition* – For a local minimum, the Hessian matrix $\mathbf{H}(\mathbf{x}_c) = \left[\frac{\partial^2 f}{\partial x_i \partial x_j}\right]_{(n\times n)}$ must be at least positive semidefinite and for a local maximum must be at least negative semidefinite. If $\mathbf{H}$ is positive or negative definite these become the second order sufficiency conditions respectively.

### 4.1.5 Constraints

The conditions discussed in §4.1.4 apply to unconstrained optimisation problems, however, the standard form described in §4.1.1 has a series of functions $h_i$ (in Equation 4.1.3) and $g_j$ (in Equation 4.1.4) which are the equality and inequality constraint equations respectively.

The left side of Figure 4.2 shows how the feasible space (shaded) for the two design variables ($x_1$ and $x_2$) is defined by the three inequality constraints:

1. $0 \leq x_1 \leq a$
2. $0 \leq x_2 \leq b$
3. $x_2 \leq -x_1 + c$, or equivalently: $x_1 \leq -x_2 + d$ (Note that the numerical values of $c$ and $d$ are the same.)

By adding the equality constraint, $x_2 = -x_1 + e$, this region is reduced to only the shaded part of the constraint line in the right side of Figure 4.2.

In §4.1.1 we see that constraints are specified in a standard form. The equality constraints of Equation 4.1.3 have the form $h(\mathbf{x}) = 0$ and the inequality constraints have the form $g(\mathbf{x}) \leq 0$. It is thus desirable to convert all the specified constraints to these formats for use in the optimisation process.

The equality constraint from above is now converted to the standard format:

$$\begin{aligned} x_2 &= -x_1 + e \\ x_1 + x_2 - e &= 0 \end{aligned}$$

Similarly the third inequality in the list above is converted:

$$\begin{aligned} x_2 &\leq -x_1 + c \\ x_1 + x_2 - c &\leq 0 \end{aligned}$$

or

$$\begin{aligned} x_1 &\leq -x_2 + d \\ x_1 + x_2 - d &\leq 0 \end{aligned}$$

The inequality constraints numbered 1 and 2, however, both have *two* inequalities in them, thus they need to be broken up into two components first:

$$0 \leq x_1 \leq a \qquad\qquad 0 \leq x_2 \leq b$$

become

$$0 \leq x_1 \text{ and } x_1 \leq a \qquad\qquad 0 \leq x_2 \text{ and } x_2 \leq b$$

which can be written in the standard form:

$$-x_1 \leq 0 \text{ and } x_1 - a \leq 0 \qquad\qquad -x_2 \leq 0 \text{ and } x_2 - b \leq 0$$

which shows how the three inequality constraints originally listed have now become five constraints when in standard form, each of which only contains one inequality.

All the constraints need to be written in terms of the design vector, $\mathbf{x}$ (with $\mathbf{x} = (x_1,\ x_2)$ in the examples above), including those that indirectly affect the vector. The constraints relevant to the various optimisations will be expanded upon in the applicable subsection, though are divided into two groups: the first group of constraints are limitations on the physical dimensions of the optimised structure (chord length, distances from centreline, etc.) and the other type is related to the deflection angles used with the new geometry (aileron and tab deflection angles).

It should be noted that while the preceding discussion used examples of constraints which are directly applied to the design variables, this need not be the case. It is possible to include constraints which are only indirectly influenced by the design variables that need to be satisfied for the optimisation to be successfully completed.

### 4.1.6 Optimality Conditions for Constrained Optimisation Problems

Since the addition of the constraints now limits the values allowed for the design vector, the necessary and sufficiency conditions are no longer strictly applicable, since one or more constraints may cause the optimal point to not be the global or even necessarily a local minimum of the objective function. In order to remedy this problem we make use of another technique from calculus called the *Lagrange Multiplier Theorem*, Stewart [39]. Making use of these multipliers leads to the *Karush-Kuhn-Tucker (KKT) necessary conditions*. All optimal designs must satisfy these conditions (Walsh [32], Arora [33], Marler, et al [40]).

Associated with each equality constraint is a Lagrange multiplier, which "can be interpreted as the force required to impose the constraint" [33].

Before stating the Lagrange Multiplier Theorem, the concept of a *regular point* needs to be discussed. A regular point is a point in the feasible set where all the equality constraints are satisfied ($h_i = 0 \,\forall\, i = 1$ to $p$) and if $f$ is evaluated at this point it is differentiable. Also the gradient vector of all constraints evaluated at a regular point are linearly independent.

#### 4.1.6.1 The Lagrange Multiplier Theorem (LMT)

Arora [33] defines the *Lagrange Multiplier Theorem* as:

> For a regular point, $\mathbf{x}^*$, which is a local minimum for the minimisation of $f(\mathbf{x})$ subject to the equality constraints Equation 4.1.3, there exists unique Lagrange multipliers, $v_j^*,\ j = 1 \text{ to } p$, such that
>
> $$\frac{\partial f(\mathbf{x}^*)}{\partial x_i} + \sum_{j=1}^{p} v_j^* \frac{\partial h_j(\mathbf{x}^*)}{\partial x_i} = 0; \qquad i = 1 \text{ to } n \tag{4.1.5}$$
>
> $$h_j(\mathbf{x}^*) = 0; \qquad j = 1 \text{ to } p$$

The theorem of Equation 4.1.5 can be re-written as

$$\nabla L(x^*,\ v^*) = \mathbf{0}, \qquad \text{with} \qquad L(\mathbf{x},\ \mathbf{v}) = f(\mathbf{x}) + \sum_{j=1}^{p} v_j h_j(\mathbf{x}) = f(\mathbf{x}) + \mathbf{v}^{\mathrm{T}}\mathbf{h}(\mathbf{x}) \tag{4.1.6}$$

The function $L(\mathbf{x},\ \mathbf{v})$ is known as the *Lagrange Function*.

#### 4.1.6.2 Karush-Kuhn-Tucker Necessary Conditions

Extending the LMT of §4.1.6.1 to include the inequality constraints results in the *Karush-Kuhn-Tucker* conditions.

In order to achieve this it is necessary to convert the inequality constraints into equality constraints. This makes use of variables known as slack variables:

$$g_i(k) \leq 0 \quad \Rightarrow \quad g_i(k) + s_i^2 = 0; \qquad i = 1 \text{ to } m \tag{4.1.7}$$

with $s_i$ the slack variable associated with each inequality constraint ($s_i^2 \geq 0$). If the inequality constraint is satisfied for a design vector $\mathbf{x}$, but is *inactive*, then $s_i^2 > 0$. If the constraint is *active* then $s_i^2 = 0$ and if the constraint is *violated*, $s_i^2 < 0$ (the inequality is not satisfied).

These modified inequality constraints also have associated Lagrange multipliers, however, the values of these multipliers have an additional necessary condition [33]. Defining the Lagrange multiplier for the $i$th inequality as $u_i$, the necessary condition is stated as

$$u_i \geq 0; \qquad i = 1 \text{ to } m \tag{4.1.8}$$

or in words: the Lagrange multipliers associated with the inequality constraints must be non-negative. Inactive constraints have a zero-valued multiplier.

The *Karush-Kuhn-Tucker Optimality Conditions* are stated as follows from Arora [33]:

> If $x^*$ is a regular point and local minimum of $f(\mathbf{x})$ subject to the $p$ equality constraints $h_i(\mathbf{x}) = 0;\ i = 1$ to $p$ and the $m$ inequality constraints $g_j(\mathbf{x}) \leq 0;\ j = 1$ to $m$; then there exist Lagrange multipliers $\mathbf{v}^*$ ($p$-vector) and $\mathbf{u}^*$ ($m$-vector) such that the Lagrangian function is stationary with respect to $x_k$, $v_i$, $u_j$ and $s_j$ at the point $\mathbf{x}^*$.

A stationary point of a function is where the gradient of the function becomes zero, indicating a maximum, minimum or inflection point, Weisstein [41].

> The *Lagrangian function* is given by
>
> $$\begin{aligned} L(\mathbf{x},\ \mathbf{v},\ \mathbf{u},\ \mathbf{s}) &= f(\mathbf{x}) + \sum_{i=1}^{p} v_i h_i(\mathbf{x}) + \sum_{j=1}^{m} u_j \left(g_j(\mathbf{x}) + s_j^2\right) \\ &= f(\mathbf{x}) + \mathbf{v}^{\mathrm{T}}\mathbf{h}(\mathbf{x}) + \mathbf{u}^{\mathrm{T}}\left(\mathbf{g}(\mathbf{x}) + \mathbf{s}^2\right) \end{aligned} \tag{4.1.9}$$

The *gradient conditions* are given by

$$\begin{aligned}
\frac{\partial L}{\partial x_k} &= \frac{\partial f}{\partial x_k} + \sum_{i=1}^{p} v_i^* \frac{\partial h_i}{\partial x_k} + \sum_{j=1}^{m} u_j^* \frac{\partial g_j}{\partial x_k} = 0; \qquad k = 1 \text{ to } n \\
\frac{\partial L}{\partial v_i} &= 0 \Rightarrow h_i(\mathbf{x}^*) = 0; \qquad i = 1 \text{ to } p \\
\frac{\partial L}{\partial u_j} &= 0 \Rightarrow \left(g_j(\mathbf{x}^*) + s_j^2\right) = 0; \qquad j = 1 \text{ to } m
\end{aligned} \tag{4.1.10}$$

The *feasibility check* for inequalities:

$$s_j \geq 0; \text{ or equivalently } g_j \leq 0; \qquad j = 1 \text{ to } m \tag{4.1.11}$$

The *switching conditions*:

$$\frac{\partial L}{\partial s_j} = 0 \Rightarrow 2u_j^* s_j = 0; \qquad j = 1 \text{ to } m \tag{4.1.12}$$

*Non-negativity of inequality Lagrange multipliers*:

$$u_j^* \geq 0; \qquad j = 1 \text{ to } m \tag{4.1.13}$$

*Regularity Check* - The gradients of active constraints should be linearly independent. ■

The optimality conditions described in the preceding sections will be used in the development of the various optimisation techniques.

## 4.2 Multi-Objective and Multi-Point Optimisation

Up to now we have been referring to a *multi-objective optimisation*, and $\mathbf{f}$ in Equation 4.1.2 is this multi-objective cost function. A multi-objective optimisation is an optimisation process where there are a number of distinct objectives, all of which are desired to be met. These multiple objectives can all be described in terms of individual objective functions ($f_1,\ f_2,\ \ldots\ f_k$), where $k$ is the number of objectives that are desired to be met.

A *multi-point optimisation* is not related to the number of objective functions, but rather concerns the concept of an *operating point*. An operating point is a set of parameters that defines under what conditions the optimisation is being performed. In the case of aerodynamic optimisations, the operating point can be defined as the trim point of an aircraft in flight.

### 4.2.1 Multi-Point Optimisation

Usually an optimisation is performed under a specific set of operating conditions (for example, the cruise speed of an aircraft) since it is at this specific point where the aircraft will be spend most of its operating time, and hence where it needs to be the least costly (most efficient). Thus the losses due to a non-optimal design at other operating points will just have to be accepted.

There are, however, cases where there may be more than one point where satisfactory performance is required (say two), and thus the optimisation needs to be performed at each of these operating points. It may happen however, that each of the two designs are very inefficient at the other operating point, and thus neither are suitable for the final design. A relative weighting of these two operating points can then be chosen, and a compromise design reached where performance is satisfactory at both operating points, even though it is not as good as for the individual optimisations.

This type of optimisation is a *multi-point* optimisation – where an optimisation is performed by taking into account multiple points of operation, and these points are weighed relatively to each other. Nemec, et al [42] shows a good example of how an aerofoil's shape is optimised to provide suitable drag characteristics over a range of Mach numbers. Similar multi-point optimisations have been performed (also for wing shape optimisation) in Zing and Elias [43], Huyse and Lewis [44] and Li, et al [45] to great effect.

### 4.2.2 Multi-Objective Optimisation

There are a number of methods for dealing with multi-objective optimisations. Marler and Arora provide a useful comparative survey of various methods that have been developed over the years in [40]. These methods can be classified into three categories: *priori*, *posteriori* and *no* articulation of preferences.

The *priori* methods rely on the designer having pre-defined set of preferences, or ideas on what components of the optimisation are important relative to others. In this case the optimisation process takes these preferences into account during the optimisation process and thus the final result will be the optimum based on these preferences. Some *priori* methods include:

1. Weighted global criterion method
2. Weighted sum method
3. Lexicographic method
4. Weighted min-max method
5. Exponential weighted criterion method
6. Weighted product method
7. Goal programming methods
8. Bounded objective function methods, and
9. Physical programming methods

With *posteriori* based methods, the optimisation is executed, and delivers a series of possible solutions. The designer then chooses from these the design most suitable for his application. In this case the cost associated with all the optimal designs is the same, but there are multiple results from which the designer can choose to achieve this minimum. Some *posteriori* methods are

1. Physical programming methods
2. Normal boundary intersection method
3. Normal constraint method

Finally the methods where there are no articulation of preferences. In this case the designer's requirements may not be quantifiable, or be firmly defined. Some examples:

1. Global criterion methods:
    a) Technique for order of preference by similarity to ideal solution
    b) Objective sum method
    c) Min-max method
2. Nash Arbitration and objective product method
3. Rao's method.

Refer to Marler and Arora [40] for in-depth discussions regarding these methods. Genetic algorithms are also used to solve multi-objective optimisation problems. This topic will be discussed in §4.4.

#### 4.2.2.1 Pareto Optimality

Where multiple objectives are concerned, it may result in numerous solutions that satisfy the overall optimisation objective, in other words: there may not be a unique global minimum. This is a result of the two objective functions having different *feasible regions*.

Even though the constraints are the same for each of the objective functions for an optimisation problem, it is possible that the feasible region for each problem differs greatly. The feasible region of the complete problem is thus the *intersection* of the feasible regions of the individual objective functions.

This can be represented in terms of the *criterion space*, which is merely an alternative representation of the optimisation problem where the values of the *objective functions* are varied, rather than the design variables. Where the feasible regions of the objective functions intersect in the criterion space, the *feasible criterion space* is obtained for the optimisation problem.

The *utopia point* is the point in the criterion space (not necessarily feasible) where all the objective functions have their minimum values. If this point is attainable (all constraints are satisfied in the design space) this is the optimal solution to the problem.

The term *optimal* when referring to a multi-objective problem is defined in terms of *Pareto Optimality*. Marler and Arora [40] provides the following concise definitions of the various types of Pareto Optimality ($\mathbf{X}$ is the feasible design space):

> **Pareto Optimal** *A point $\mathbf{x}^* \in \mathbf{X}$, is Pareto optimal if, and only if, there does not exist another point, $\mathbf{x} \in \mathbf{X}$, such that $\mathbf{f}(\mathbf{x}) \leq \mathbf{f}(\mathbf{x}^*)$, and $f_i(\mathbf{x}) \leq f_i(\mathbf{x}^*)$ for at least one sub-objective function.*

In other words, there cannot be another point where any of the individual cost function minimum values can be reduced without increasing at least one other objective function's minimum value.

> **Weakly Pareto Optimal** *A point $\mathbf{x}^* \in \mathbf{X}$, is Pareto optimal if, and only if, there does not exist another point, $\mathbf{x} \in \mathbf{X}$, such that $\mathbf{f}(\mathbf{x}) < \mathbf{f}(\mathbf{x}^*)$.*

If there is no other point that can improve *all* the objective functions simultaneously, then the point is said to be weakly Pareto optimal.

#### 4.2.2.2 Method of Weighted Sums

This is the most common means of solving multi-objective optimisations, according to [40].

The method of weighted sums was chosen for use in this project due to its popularity in shape optimisations (see the references listed in §4.2.1), and since it is easy to implement. The need to consider separate objectives is also eliminated since the method combines all objectives into a single objective function which is a function of the design vector, yet it is still possible to relate the importances of the various sub-objectives by choosing suitable weightings.

The objective function is described as

$$J(\mathbf{x}) = \sum_{i=1}^{k} w_i f_i(\mathbf{x}) \tag{4.2.1}$$

Choosing the weightings, $w_i$, correctly is very important for the results of the optimisation to be valid. Typically the sum of the weightings should total one: $\sum_{i=1}^{k} w_i = 1$, though if the objective functions are not normalised, this need not be the case as will be seen in Chapter 5.

Regarding the Pareto optimality of the weighted sums method, according to Marler, et al [40] and Arora [33], if a minimum can be found, and all the weightings $w_i$ are positive, then the minimum is Pareto optimal.

## 4.3 Sequential Quadratic Programming – A Gradient Based Optimisation Algorithm

It has already been mentioned that there are many optimisation methods available. This section discusses an implementation of a gradient-based method used to solve constrained optimisation problems.

Gradient based methods require continuous functions with continuous first and second derivatives. A full discussion of this can be found in Arora [33].

The method used for the purposes of this project is the *Sequential Quadratic Programming (SQP)* algorithm. Arora [33] and Boggs and Tolle [46] both provide a lengthy discussions on the SQP algorithm and it is on these discussions that the algorithm used by this project is based.

The SQP is based on the steepest descent method used for unconstrained problems where the gradient of the objective function is used to determine a step direction as well as a step size that will result in suitable convergence rates.

In [46] Boggs and Tolle make an important remark regarding the SQP: It is not necessary for the initial guess of an optimal solution to be feasible. Since there are constraints that need to be taken into account, the design space and the feasible space are not necessarily the same. Naturally a well-chosen starting point will result in a faster convergence rate.

The steepest descent and SQP methods are all iterative methods. This means that for each iteration the following is calculated with regards to the design vector:

$$\mathbf{x}^{(k+1)} = \mathbf{x}^{(k)} + \Delta\mathbf{x}^{(k)} \tag{4.3.1}$$

with

$$\Delta\mathbf{x}^{(k)} = \alpha_k \mathbf{d}^{(k)} \tag{4.3.2}$$

where $k$ indicated the current or $k$th iteration, $\Delta\mathbf{x}$ is the change in the design vector, $\alpha_k$ is the step size and $\mathbf{d}$ is the direction vector in which the step will occur.

### 4.3.1 The Quadratic Programming Sub-problem

Most algorithms used to solve non-linear optimisation problems make use of linearisation at the design point currently being examined in the optimisation process. When constraints are also taken into account, it is also necessary to linearise these constraints. These combine to give a new *linearised* constrained optimisation problem that is used to solve for the step direction vector, $\mathbf{d}^{(k)}$ and step size, $\alpha_k$.

The problem with a linearisation is that for many problems, this technique is not very robust, thus a *quadratic programming* sub-problem with linear constraints is solved each iteration. The quadratic sub-problem is strictly convex, thus if it has a minimum, it is global and unique, Arora [33].

The quadratic programming sub-problem is defined below as in Arora [33] and Boggs and Tolle [46]:

$$\min_{\mathbf{x}} q(\mathbf{x}) = \mathbf{c}^{\mathrm{T}}\mathbf{x} + \frac{1}{2}\mathbf{x}^{\mathrm{T}}\mathbf{H}\mathbf{x} \tag{4.3.3}$$

subject to the equality and inequality constraints

$$\mathbf{N}^{\mathrm{T}}\mathbf{x} = \mathbf{e} \tag{4.3.4}$$

$$\mathbf{A}^{\mathrm{T}}\mathbf{x} \leq \mathbf{b} \tag{4.3.5}$$

with non-negative variables:

$$\mathbf{x} \geq 0 \tag{4.3.6}$$

The definition of the QP sub-problem in Equation 4.3.3 to Equation 4.3.6 are related to the original problem given in Equation 4.1.1 to Equation 4.1.4 as follows:

Derivative of the cost function, and its Hessian matrix (for $i = 1$ to $n,\ j = 1$ to $n$):

$$\mathbf{c} = [c_i]_{(n\times 1)} = \left[\frac{\partial f(\mathbf{x}^{(k)})}{\partial x_i}\right] \tag{4.3.7}$$

$$\mathbf{H} = [h_{ij}]_{(n\times n)} = \left[\frac{\partial^2 f}{\partial x_i \partial x_j}\right] = \frac{\partial^2 f}{\partial \mathbf{x}\partial \mathbf{x}} \tag{4.3.8}$$

The equality constraints and their derivatives (for $i = 1$ to $n,\ j = 1$ to $m$):

$$\mathbf{N} = [n_{ij}]_{(n\times p)} = \left[\frac{\partial h_j(\mathbf{x}^{(k)})}{\partial x_i}\right] \tag{4.3.9}$$

$$\mathbf{e} = [e_j]_{(p\times 1)} = -\mathbf{h}(\mathbf{x}^{(k)}) \tag{4.3.10}$$

The inequality constraints and their derivatives (for $i = 1$ to $n,\ j = 1$ to $m$):

$$\mathbf{A} = [a_{ij}]_{(n\times m)} = \left[\frac{\partial g_j(\mathbf{x}^{(k)})}{\partial x_i}\right] \tag{4.3.11}$$

$$\mathbf{b} = [b_j]_{(m\times 1)} = -\mathbf{g}(\mathbf{x}^{(k)}) \tag{4.3.12}$$

■

As stated in Boggs and Tolle [46], in order to take the non-linearities in the constraints while still using linearised constraints, the SQP method will make use of a quadratic form of the Lagrangian defined in Equation 4.1.9 using a Taylor series expansion:

$$L_{\mathrm{QP}}(\mathbf{x},\ \mathbf{v},\ \mathbf{u},\ \mathbf{s}) \approxeq L(\mathbf{x},\ \mathbf{v},\ \mathbf{u},\ \mathbf{s}) + \nabla L(\mathbf{x},\ \mathbf{v},\ \mathbf{u},\ \mathbf{s})^{\mathrm{T}}\mathbf{x} + \frac{1}{2}\mathbf{x}^{\mathrm{T}}\mathcal{H}\{L(\mathbf{x},\ \mathbf{v},\ \mathbf{u},\ \mathbf{s})\}\mathbf{x} \tag{4.3.13}$$

where $\mathcal{H}\{\cdot\}$ indicates the Hessian. Examining Equation 4.1.9, Equation 4.3.13 becomes

$$L = \mathbf{c}^{\mathrm{T}}\mathbf{x} + \frac{1}{2}\mathbf{x}^{\mathrm{T}}\mathbf{H}\mathbf{x} + \mathbf{u}^{\mathrm{T}}\left(\mathbf{A}^{\mathrm{T}}\mathbf{x} + \mathbf{s} - \mathbf{b}\right) + \mathbf{v}^{\mathrm{T}}\left(\mathbf{N}^{\mathrm{T}}\mathbf{x} - \mathbf{e}\right) \tag{4.3.14}$$

with the slack variables, $\mathbf{s}$, introduced for the inequality constraints as follows:

$$\mathbf{A}^{\mathrm{T}}\mathbf{x} + \mathbf{s} = \mathbf{b} \qquad \text{with} \qquad \mathbf{s} \geq \mathbf{0}$$

Note that in Arora [33] there is an additional component due to the non-negativity of the design vector as stated in Equation 4.3.6, however, since this restriction is removed in subsequent steps, it is ignored.

The KKT conditions of §4.1.6.2 are now written as:

$$\frac{\partial L}{\partial \mathbf{x}} = \mathbf{c} + \mathbf{H}\mathbf{x} + \mathbf{A}\mathbf{u} + \mathbf{N}\mathbf{v} = \mathbf{0} \tag{4.3.15}$$

$$\mathbf{A}^{\mathrm{T}}\mathbf{x} + \mathbf{s} - \mathbf{b} = \mathbf{0} \tag{4.3.16}$$

$$\mathbf{N}^{\mathrm{T}}\mathbf{x} - \mathbf{e} = \mathbf{0} \tag{4.3.17}$$

$$u_i s_i = 0 \qquad i = 1 \text{ to } m \tag{4.3.18}$$

$$u_i,\ s_i \geq 0 \qquad \text{for } i = 1 \text{ to } m \tag{4.3.19}$$

which need to be solved for $\mathbf{x}$, $\mathbf{u}$, $\mathbf{v}$ and $\mathbf{s}$.

In order to solve for these unknowns, a method taken from *linear programming* (LP) will be used, called the *simplex method*.

### 4.3.2 The Simplex Method for Solving the QP Sub-problem

A detailed discussion of the simplex method (and its derivation) for linear programming is provided in Chapter 6 of Arora [33] and will not be repeated here, except for some of the terminology and operations performed.

The simplex algorithm is used to solve the system of $m \times n$ linear equations of the form $\mathbf{A}\mathbf{x} = \mathbf{b}$. It makes used of a process of *Gauss-Jordan Elimination* in order to reduce the system of equations into the canonical form $\mathbf{I}_{(m)}\mathbf{x}_{(m)} + \mathbf{Q}\mathbf{x}_{(n-m)} = \mathbf{b}$. Arora [33] also defines the concepts of *basic* and *non-basic* variables. The canonical form described above provides a general solution in the form $\mathbf{x}_{(m)} = \mathbf{b} - \mathbf{Q}\mathbf{x}_{(m-n)}$ where $\mathbf{x}_{(m)}$ are dependant variables and $\mathbf{x}_{(m-n)}$ are independent variables. If the independent variables are set to zero, the resulting vector $\mathbf{x}_{(m)}$ of the dependant variables are said to be *basic*. The variables making up $\mathbf{x}_{(m-n)}$ are then called *non-basic variables*.

The information required to solve the optimisation problem is laid out in a *tableau* as defined in Table 4.1. The table shows the list of current basic variables in the first column, and $m \times m$ identity matrix in the following $m$ columns, the coefficients of the $\mathbf{A}$ matrix in the next $n$ columns and finally the $\mathbf{b}$ vector in the final column. The last row of the tableau is a the cost function written in the format $\mathbf{c}^{\mathrm{T}}\mathbf{x} = f$. It must be noted that the cost function is always written in terms of *only* the *non-basic* variables.

For ease of implementation Table 4.1 will be rearranged such that the basic and non-basic column groups are swapped as shown in Table 4.2. The $\mathbf{A}$ matrix is generated from the inequality constraints with an additional non-negative slack variable per constraint. If there are two design variables ($n = 2$) and three constraints ($m = 3$) there will be two non-basic variables and three basic variables, since three slack

**Table 4.1** – The simplex tableau.

| *Basic Variable* | $x_1$ | $x_2$ | $\cdots$ | $x_m$ | $x_{(m+1)}$ | $x_{(m+2)}$ | $\cdots$ | $x_{(m+n)}$ | **b** |
|---|---|---|---|---|---|---|---|---|---|
| $x_1$ | 1 | 0 | $\cdots$ | 0 | $a_{1,m+1}$ | $a_{1,m+2}$ | $\cdots$ | $a_{1,m+n}$ | $b_1$ |
| $x_2$ | 0 | 1 | | 0 | $a_{2,m+1}$ | $a_{2,m+2}$ | | $a_{2,m+n}$ | $b_2$ |
| $\vdots$ | $\vdots$ | | $\ddots$ | | $\vdots$ | | $\ddots$ | | $\vdots$ |
| $x_m$ | 0 | 0 | | 1 | $a_{m,m+1}$ | $a_{m,m+2}$ | | $a_{m,m+n}$ | $b_m$ |
| Cost Function | 0 | 0 | 0 | 0 | $c_1$ | $c_2$ | $\cdots$ | $c_n$ | $f$ |

**Table 4.2** – The rearranged simplex tableau.

| *Basic Variable* | $x_1$ | $x_2$ | $\cdots$ | $x_n$ | $x_{(n+1)}$ | $x_{(n+2)}$ | $\cdots$ | $x_{(n+m)}$ | **b** |
|---|---|---|---|---|---|---|---|---|---|
| $x_{(n+1)}$ | $a_{11}$ | $a_{12}$ | $\cdots$ | $a_{1n}$ | 1 | 0 | $\cdots$ | 0 | $b_1$ |
| $x_{(n+2)}$ | $a_{21}$ | $a_{22}$ | | $a_{2n}$ | 0 | 1 | | 0 | $b_2$ |
| $\vdots$ | $\vdots$ | | $\ddots$ | | $\vdots$ | | $\ddots$ | | $\vdots$ |
| $x_{(n+m)}$ | $a_{m1}$ | $a_{m2}$ | | $a_{mn}$ | 0 | 0 | | 1 | $b_m$ |
| Cost Function | $c_1$ | $c_2$ | $\cdots$ | $c_n$ | 0 | 0 | 0 | 0 | $f$ |

variables need to be added, and initially all the slack variables are basic. As an example consider if one of the inequality constraints was $x_1 + x_2 \leq 15$. This would be converted to the equality by making use of slack variable $x_3$: $x_1 + x_2 + x_3 = 15$. This same process is followed for all the inequality constraints.

Once the tableau has been set up, a series of *pivot* operations are performed. A pivot operation involves a selection of an element in the cost row corresponding to one of the non-basic variables. A row is selected based on some criteria (see Step 7 in §4.3.5) and then the pivot operation is executed.

The pivot operation entails examining the selected *pivot element* (the element where the selected row and column cross) and determining the linear multiples of this row such that the other elements in the selected column are reduced to zero, and the pivot element is reduced to 1. This is the same set of operations performed in *row reduction* of Gauss-Jordan elimination in linear algebra (see Chapter 1.2 of Lay [47]). In the process the non-basic variable corresponding to the column becomes basic, and the basic variable corresponding to the row becomes non-basic.

A notable problem with the traditional simplex algorithm, is the need for an *initial basic feasible solution*. Typically one is not readily available, thus the simplex method was augmented to first determine a suitable basic feasible solution, before restarting the traditional simplex algorithm with the newly calculated initial solution in order to determine the actual optimal solution for the LP. This method is known as the *two-phase method*, where the first phase determines a basic feasible solution and the second phase determines the optimal solution. It is actually the first phase of this two-phase algorithm that will be used to solve the quadratic sub-problem.

The premise on which the two-phase method is based is that of artificial variables. Artificial variables are introduced as a means of handling constraints of the $\geq$ and $=$ types. This allows these constraints to be written in the following format:

$$\sum_{j=1}^{n} a_{ij}x_j + x_{n+i} = b_i \tag{4.3.20}$$

The aim in this case is to reduce all artificial variables to zero. In order to eliminate the artificial variables, an *artificial cost function* is defined, and minimised. This artificial cost function is simply the sum of all the artificial variables:

$$w = x_{n+1} + x_{n+2} + \cdots + x_{n+m} = \sum_{i=1}^{m} x_{n+i} \tag{4.3.21}$$

Combining Equation 4.3.20 and Equation 4.3.21 we get the artificial cost function in terms of the non-basic variables:

$$w = \sum_{i=1}^{m} b_i - \sum_{j=1}^{n}\sum_{i=1}^{m} a_{ij}x_j \tag{4.3.22}$$

with new (reduced) cost coefficients

$$c'_j = -\sum_{i=1}^{m} a_{ij} \tag{4.3.23}$$

**Table 4.3** – The tableau for the first phase of the two-phase simplex algorithm with the artificial cost function.

| *Basic Variable* | $x_1$ | $x_2$ | $\cdots$ | $x_n$ | $x_{(n+1)}$ | $x_{(n+2)}$ | $\cdots$ | $x_{(n+m)}$ | $\mathbf{b}$ |
|---|---|---|---|---|---|---|---|---|---|
| $x_{(n+1)}$ | $a_{11}$ | $a_{12}$ | $\cdots$ | $a_{1n}$ | 1 | 0 | $\cdots$ | 0 | $b_1$ |
| $x_{(n+2)}$ | $a_{21}$ | $a_{22}$ | | $a_{2n}$ | 0 | 1 | | 0 | $b_2$ |
| $\vdots$ | $\vdots$ | | $\ddots$ | | $\vdots$ | | $\ddots$ | | $\vdots$ |
| $x_{(n+m)}$ | $a_{m1}$ | $a_{m2}$ | | $a_{mn}$ | 0 | 0 | | 1 | $b_m$ |
| Artificial Cost Function | $c'_1$ | $c'_2$ | $\cdots$ | $c'_n$ | 0 | 0 | 0 | 0 | $w - \sum_{i=1}^{m} b_i$ |

The tableau is now set up as shown in Table 4.3 where the variables $x_{m+i}$ $i = 1$ to $n$ are the artificial variables. Solving the LP described in the tableau of Table 4.3 involves applying the simplex algorithm until the value of the artificial cost function is zero ($w = 0$). At this point a viable initial basic feasible solution has been found.

If the aim was to find the minimum of the original objective function, the second phase of the simplex method would now be used, however for the purpose of solving the QP, it is not necessary, and will thus not be described further. An important note is that all artificial variables must become zero and can thus be eliminated from the remaining table for the remainder of the algorithm.

The use of the simplex method, or simplex-like methods have been well-documented in the literature (see Lemke [48], Rusin [49], Wolfe [50] and Wolfe [51]). All of these references make use of the simplex method to solve QP problems with equality constraints, though [51] also discusses inequality constraints.

In order to use the simplex method to solve the QP sub-problem the KKT conditions (of Equations 4.3.15 to 4.3.19) need to be modified slightly and are written in matrix format. The first modification comes as a result of the simplex method only being able to handle non-negative values of the components of $\mathbf{x}$, both for the original and artificial variables. This means that all sign-free variables need to be broken up into two components which are sign restricted.

The variables that need to be converted include the design vector, $\mathbf{x}$ and the Lagrange multipliers associated with the equality constraints, $\mathbf{v}$:

$$\mathbf{x} = \mathbf{x}^+ - \mathbf{x}^- \tag{4.3.24}$$

$$\mathbf{v} = \mathbf{v}^+ - \mathbf{v}^- \tag{4.3.25}$$

where all of $\mathbf{x}^+$, $\mathbf{x}^-$, $\mathbf{v}^+$, and $\mathbf{v}^-$ are non-negative. If a component of $\mathbf{x}$, say $x_i$ is negative, then $x_i^+ < x_i^-$ but both $x_i^+,\ x_i^- \geq 0$.

Now Equations 4.3.15 to 4.3.17 are put into matrix form, taking into account Equations 4.3.24 and 4.3.25:

$$\begin{bmatrix} \mathbf{H} & -\mathbf{H} & \mathbf{A} & \mathbf{0} & \mathbf{N} & -\mathbf{N} \\ \mathbf{A}^{\mathrm{T}} & -\mathbf{A}^{\mathrm{T}} & \mathbf{0} & \mathbf{I} & \mathbf{0} & \mathbf{0} \\ \mathbf{N}^{\mathrm{T}} & -\mathbf{N}^{\mathrm{T}} & \mathbf{0} & \mathbf{0} & \mathbf{0} & \mathbf{0} \end{bmatrix} \begin{bmatrix} \mathbf{x}^+ \\ \mathbf{x}^- \\ \mathbf{u} \\ \mathbf{s} \\ \mathbf{v}^+ \\ \mathbf{v}^- \end{bmatrix} = \begin{bmatrix} -\mathbf{c} \\ \mathbf{b} \\ \mathbf{e} \end{bmatrix} \tag{4.3.26}$$

Equation 4.3.26 is a set of linear equations, thus rearranging the matrix will not have an effect on the solution. Equation 4.3.26 is thus rearranged as follows to make the implementation of the algorithm simpler:

$$\begin{bmatrix} \mathbf{H} & -\mathbf{H} & \mathbf{N} & -\mathbf{N} & \mathbf{A} & \mathbf{0} \\ \mathbf{N}^{\mathrm{T}} & -\mathbf{N}^{\mathrm{T}} & \mathbf{0} & \mathbf{0} & \mathbf{0} & \mathbf{0} \\ \mathbf{A}^{\mathrm{T}} & -\mathbf{A}^{\mathrm{T}} & \mathbf{0} & \mathbf{0} & \mathbf{0} & \mathbf{I} \end{bmatrix} \begin{bmatrix} \mathbf{x}^+ \\ \mathbf{x}^- \\ \mathbf{v}^+ \\ \mathbf{v}^- \\ \mathbf{u} \\ \mathbf{s} \end{bmatrix} = \begin{bmatrix} -\mathbf{c} \\ \mathbf{e} \\ \mathbf{b} \end{bmatrix} \tag{4.3.27}$$

which is of the form $\mathbf{BX} = \mathbf{D}$, which means the KKT conditions are reduced to finding the vector $\mathbf{X}$ as a solution of this linear system and ensuring that Equation 4.3.18 (the complementary slackness conditions) and Equation 4.3.19 (the non-negativity conditions) are satisfied.

The final step that needs to be done before describing the steps used by the simplex algorithm is to define the artificial cost function in the context of the QP sub-problem.

Again artificial variables are introduced such that the system $\mathbf{BX} = \mathbf{D}$ is written as

$$\mathbf{BX} + \mathbf{Y} = \mathbf{D} \tag{4.3.28}$$

where $\mathbf{Y}$ is a vector of artificial variables – one for each row of the system. Again the artificial cost function is the sum of the artificial variables

$$\begin{aligned} w &= \sum_{i=1}^{n+p+m} Y_i && (4.3.29)\\ &= \sum_{i=1}^{n+p+m} D_i - \sum_{j=1}^{2(n+p+m)} \sum_{i=1}^{(n+p+m)} B_{ij} X_j \\ &= w_0 + \sum_{j=1}^{2(n+p+m)} C_j X_j && (4.3.30) \end{aligned}$$

with

$$C_j = \sum_{i=1}^{n+m+p} B_{ij} \quad \text{and} \quad w_0 = \sum_{i=1}^{n+m+p} D_i \tag{4.3.31}$$

The complete simplex algorithm is now described below:

**Step 1: Initialisation** Initially create the preliminary matrices

$$\mathbf{B}_p = \begin{bmatrix} \mathbf{H} & \mathbf{N} & \mathbf{A} & \mathbf{0} \\ \mathbf{N}^{\mathrm{T}} & \mathbf{0} & \mathbf{0} & \mathbf{0} \\ \mathbf{A}^{\mathrm{T}} & \mathbf{0} & \mathbf{0} & \mathbf{I} \end{bmatrix} \qquad \mathbf{D}_p = \begin{bmatrix} -\mathbf{c} \\ \mathbf{e} \\ \mathbf{b} \end{bmatrix}$$

As of yet sign-free variables are not taken into account. Note that $\mathbf{X} = \begin{bmatrix} \mathbf{x}^{\mathrm{T}} \mathbf{v}^{\mathrm{T}} \mathbf{u}^{\mathrm{T}} \mathbf{s}^{\mathrm{T}} \end{bmatrix}^{\mathrm{T}}$ at this stage.

**Step 2: Eliminate as many sign-free variables as possible** It is possible to write some of the sign-free variables in terms of the remaining variables. Doing so reduces the size of the problem greatly, thus decreasing the number of iterations required to solve a problem. These eliminated variables can then be reconstructed once the other unknowns are determined. It is thus necessary to record the rows as they are eliminated. For every sign-free variable eliminated, a row and column of the $\mathbf{B}_p$ matrix falls away and a row of the $\mathbf{D}_p$ matrix falls away. There are now $n'$ sign-free variables remaining related to the design vector, and $m'$ relating to the inequality constraints.

**Step 3: Create $\mathbf{B}$ matrix** Now that as many of the sign-free variables have been eliminated it is necessary to construct the $\mathbf{B}$ matrix in the format of Equation 4.3.27.

$$\mathbf{B} = \begin{bmatrix} \mathbf{H}' & -\mathbf{H}' & \mathbf{N}' & -\mathbf{N}' & \mathbf{A} & \mathbf{0} \\ \mathbf{N'}^{\mathrm{T}} & -\mathbf{N'}^{\mathrm{T}} & \mathbf{0} & \mathbf{0} & \mathbf{0} & \mathbf{0} \\ \mathbf{A}^{\mathrm{T}} & -\mathbf{A}^{\mathrm{T}} & \mathbf{0} & \mathbf{0} & \mathbf{0} & \mathbf{I} \end{bmatrix} \qquad \mathbf{D} = \begin{bmatrix} -\mathbf{c}' \\ \mathbf{e}' \\ \mathbf{b} \end{bmatrix}$$

It can be seen that only the components relating to the Design variables and inequality constraints are affected. It is also necessary now to examine the components of $\mathbf{D}$. If any of these components are negative, the component and the row associated with this component in $\mathbf{B}$ need to be negated ($D_i \to -D_i$ and $B_{ij} \to -B_{ij}$ $j = 1$ to the number of columns in $\mathbf{B}$).

**Step 4: Create the artificial cost function** The artificial cost-function is constructed by summing the columns of the $\mathbf{B}$ and $\mathbf{D}$ matrix, and taking their negatives. This equates to Equation 4.3.31

**Step 5: Augment $\mathbf{B}$ with the artificial variables** For every row in the $\mathbf{B}$ matrix, an artificial variable needs to be added. This results in the system being augmented by an identity matrix of dimension $n' + m' + p$. The system now has the following form:

$$\begin{array}{cc|c} \mathbf{B}_{(n'+m'+p)\times(2n'+2m'+p)} & \mathbf{I}_{(n'+m'+p)\times(n'+m'+p)} & \mathbf{D}_{(n'+m'+p)\times 1} \\ \hline \mathbf{C}_{1\times(2n'+2m'+p)} & \mathbf{0}_{1\times(n'+m'+p)} & w_0 \end{array}$$

**Step 6: Find the pivot column** Find the most negative element in the *cost* row which is related to a *non-basic* variable. This will be the pivot column ($c_p$). If there is no negative element, then go to Step 9. If any element in the pivot column of the augmented $\mathbf{B}$ is non-negative ($\geq 0$) then the solution is unbounded.

**Step 7: Find the pivot row** In order to determine the pivot row, the following operation is performed:

$$T_i = \frac{D_i}{B_{i,c_p}}$$

from which we find the index ($r_p$) of the smallest positive value of $\mathbf{T}$. In order to reduce the possibility of *cycling* (where a series of pivot operations results in an unchanged tableau), if there are multiple indices with the same smallest value, choose the index relating to the basic variable with the lowest index.

**Step 8: Perform row-reduction** The scaling factor is found at the position ($r_p$, $c_p$) in the augmented $\mathbf{B}$ matrix. The pivot row is now divided by this value, resulting in the pivot point having a value of $1$. Now multiples of this row are subtracted from all the other rows (including the cost row) such that all other positions in the pivot column become zero. Now the non-basic variable (indicated by the column position) has been swapped with the basic variable indicated by the row. Go to Step 6.

**Step 9: Reconstruct the vectors** Once all the row operations have been completed and all artificial variables have been reduced to zero (the cost $w = 0$) it is necessary to determine the values of the basic variables, and from these determine the values of the sign-free variables eliminated in Step 2. If any of the artificial variables are non-zero then there is no solution. From Arora [33], this could be due to an over-constrained or improperly formulated problem. In the case of a standard two-phase simplex procedure, this equates to there being no feasible solution for the original design problem.

The basic variables listed in the first column of the simplex tableau are equated with the corresponding value of the last column. Now these values are used to reconstruct the vector

$$\mathbf{X}' = \begin{bmatrix} \mathbf{x}'^{+} \\ \mathbf{x}'^{-} \\ \mathbf{v}'^{+} \\ \mathbf{v}'^{-} \\ \mathbf{u} \\ \mathbf{s} \end{bmatrix}$$

Now the values of $\mathbf{x}'$ and $\mathbf{v}'$ are determined by taking

$$\mathbf{x}' = \mathbf{x}'^{+} - \mathbf{x}'^{-} \qquad \text{and} \qquad \mathbf{v}' = \mathbf{v}'^{+} - \mathbf{v}'^{-}$$

From these values it is possible to reverse the process described in Step 2 in order to reconstruct the values of the eliminated sign-free variables. Once this process has been completed, the original $\mathbf{X}$ has been calculated, thus given the values of the design vector, $\mathbf{x}$, the Lagrangian multipliers, $\mathbf{u}$ and $\mathbf{v}$, and the slack variable vector, $\mathbf{s}$.

The quadratic programming sub-problem has been solved.

While the derivation above was performed using the design vector, $\mathbf{x}$, the QP sub-problem is actually used to determine the step direction vector, $\mathbf{d}$.

### 4.3.3 Line Search

The previous section allows the calculation of the step *direction*, however, a step *size* is also necessary. This problem is less complex than that of determining the step direction since it is a one-dimensional problem. This allows line-search techniques to be used to determine the step size. Traditional line-search techniques such as the golden-ratio search and the equal interval search cannot be used directly since they do not take into account the constraints, and could determine a step size which would take the test point out of the feasible region. The concept of a descent function is thus used to alleviate this problem.

The combination of a suitable descent function and the *inaccurate line search* (sometimes called the inexact line search, or Armijo line search) is used for the purposes of this project. The line search proposed by Arora [33] is discussed below.

Given a succession of trial step sizes defined as

$$t_j = \left(\frac{1}{2}\right)^j \tag{4.3.32}$$

where $j$ is the current iteration of the line search algorithm and initialised to zero and a descent function:

$$\mathbf{\Phi}_k = f_k + RV_k \tag{4.3.33}$$

with $R$ a *penalty parameter* related to constraint violations, and $V^{(k)}$ is the value of the *maximum constraint violation* or zero if no constraints are violated, for the current SQP iteration; the *inaccurate line search algorithm* aims to satisfy the *descent condition*

$$\mathbf{\Phi}_{(k+1),j} \leq \mathbf{\Phi}_k - t_j\beta_k \tag{4.3.34}$$

Re-writing Equation 4.3.34 with all the variables for the current line search iteration on the left gives

$$\mathbf{\Phi}_{(k+1),j} + t_j\beta_k \leq \mathbf{\Phi}_k \tag{4.3.35}$$

The parameter $\beta$ in Equation 4.3.35 is defined using the search direction vector, $\mathbf{d}^{(k)}$ for the $k$th SQP iteration:

$$\beta_k = \gamma||\mathbf{d}||^2 \tag{4.3.36}$$

with $\gamma$ a user selected constant[1].

The line search algorithm thus starts with by determining $\mathbf{\Phi}_k$, $\beta_k$ and setting $j = 0$. Thereafter Equation 4.3.33 is calculated each iteration in the form

$$\mathbf{\Phi}_{(k+1),j} = f_{(k+1),j} + RV_{(k+1),j}$$

with trial design point

$$\mathbf{x}_{(k+1),j} = \mathbf{x}_k + t_j\mathbf{d}_k$$

until Equation 4.3.35 is satisfied, with each iteration resulting a trial step size half that of the previous iteration. Once the descent condition was satisfied, the step size $\alpha_k$ was set to the current $t_j$.

The *penalty parameter*, $R$, is initially selected by the user, but as the line search progresses, it must satisfy the following necessary condition:

$$R \geq r_k \tag{4.3.37}$$

where $r_k$ is the summation of all the Lagrange multipliers, for the current iteration:

$$r_k = \sum_{i=1}^{p} |v_{i_k}| + \sum_{i=1}^{m} |u_{i_k}| \tag{4.3.38}$$

In order to satisfy the necessary condition of Equation 4.3.37, the value of $R$ is set to

$$R = \max\{R_k,\, r_k\} \tag{4.3.39}$$

In other words, choose the maximum between the summation of the Lagrange multipliers and the value of $R$ used during the previous SQP iteration.

In order to take the constraints into account the parameter $V_k$ is chosen as

$$V_k = \max\{0;\ |h_1|, |h_2|, \ldots, |h_p|;\ g_1, g_2, \ldots, g_m\} \tag{4.3.40}$$

which relates it to the maximum constraint violation. If no constraints are violated (all $g$ are negative, and all $h$ are zero), it is set to zero.

[1] See §4.3.4. During implementation for the application of this project, a non-zero value of $\gamma$ resulted in very poor performance. This was due to the approximate Hessian not converging rapidly enough, which meant the step sizes were too small.

### 4.3.4 Hessian Approximation

The final component required for the SQP algorithm is the Hessian matrix. The Hessian matrix (given in Equation 4.3.8) is very time-consuming and processing intensive to determine, thus an approximation technique will be used, as described in Arora [33].

This algorithm, used to approximate the Hessian, is known as the *Quasi-Newton Hessian Approximation*. This implementation makes use of the *Broyden-Fletcher-Goldfarb-Shanno (BGFS) method*, which has been modified for the case of constrained optimisations. The algorithm as given in Arora [33] is now provided where for each iteration, the following is determined:

First the design change vector:

$$\mathbf{s}_k = \alpha_k \mathbf{d}_k$$
$$\mathbf{z}_k = \mathbf{H}_k \mathbf{s}_k$$

The difference in the gradients of the Lagrangian at two points:

$$\mathbf{y}_k = \nabla L\left(x_{(k+1)},\, u_k,\, v_k\right) - \nabla L\left(x_k,\, u_k,\, v_k\right)$$

Some scalars:

$$\xi_1 = \mathbf{s}_k \cdot \mathbf{y}_k$$
$$\xi_2 = \mathbf{s}_k \cdot \mathbf{z}_k$$
$$\theta = 1 \text{ if } \xi_1 \geq 0{,}2\xi_2, \text{ else } \theta = \frac{0{,}8\xi_2}{(\xi_2 - \xi_1)}$$

A vector and scalar:

$$\mathbf{w}_k = \theta \mathbf{y}_k + (1-\theta)\mathbf{z}_k$$
$$\xi_3 = \mathbf{s}_k \cdot \mathbf{w}_k$$

Correction matrices:

$$\mathbf{D}_k = \frac{1}{\xi_3}\mathbf{w}_k \mathbf{w}_k^{\mathrm{T}}$$
$$\mathbf{E}_k = \frac{1}{\xi_2}\mathbf{z}_k \mathbf{z}_k^{\mathrm{T}}$$

Hessian Update:

$$\mathbf{H}_{(k+1)} = \mathbf{H}_k + \mathbf{D}_k - \mathbf{E}_k$$

■

During the implementation of this component of the algorithm, it was noted that the performance of the line search described in §4.3.3 was very poor. This is due to the initial Hessian approximations not being accurate enough, which resulted in very small ($1 \times 10^{-9}$) step sizes during the initial phases of the optimisation which caused the iteration limits chosen to be exceeded.

The parameter, $\gamma$ in Equation 4.3.36 was thus chosen as $0$. This modification resulted in much faster convergence in the line search algorithm since the step direction (which is determined based on the Hessian approximation) is only taken into account once in the descent function. It was found that non-zero values of $\gamma$ did not produce the desired convergence rates.

### 4.3.5 The Complete SQP Algorithm

All the required components have now been developed. All that remains is to list the complete SQP algorithm as was implemented.

**Step 1: Initialisations** Perform the initialisation of all variables used in the optimisation:

- Zero the iteration counter, $k = 0$
- Choose an initial design vector, $\mathbf{x}_0$ and initial Lagrangian multipliers, $\mathbf{u}_0$ and $\mathbf{v}_0$
- Set the initial Hessian approximation to the identity matrix, $\mathbf{H}_0 = \mathbf{I}_{(n\times n)}$
- Choose a *permissible constraint violation* value, $\epsilon_{\text{pcv}}$
- Choose a *convergence parameter* value, $\epsilon_{\text{cv}}$
- Choose an initial *penalty parameter* value, say $R_0 = 1$.
- Choose a minimum allowable step size, $\epsilon_{\alpha_{min}}$

**Step 2: Evaluate Cost and Constraint Functions, and Update the Hessian** For the current design vector, determine the values of the cost and constraint functions. Also determine the maximum constraint violation $V_k$ and update the Hessian using the method described in §4.3.4. Note that the Hessian should only be updated where $k \geq 1$, since it makes use of the previous iterations values of $\mathbf{u}$ and $\mathbf{v}$ as determined by solving the QP sub-problem.

**Step 3: Define and Solve the QP Sub-problem** Set up and solve the quadratic programming sub-problem as described in §4.3.1 and §4.3.2 respectively to obtain $\mathbf{d}_k$, $\mathbf{u}_{\text{QP}}$ and $\mathbf{v}_{\text{QP}}$.

As a means of increasing performance, only include inequality constraints that are active or could potentially become active in the $\mathbf{A}$ matrix and $\mathbf{b}$. This is known as the *potential constraint strategy* where only inequality constraints whose values are within $\epsilon_{\text{pcd}}$ of being active (or violated) are included. Equality constraints are always included since they must always be satisfied.

**Step 4: Evaluate Stopping Criteria** Examine the stopping criteria to determine if the optimisation is complete. There are two conditions to consider:

1. Stopping criteria: $||\mathbf{d}_k|| \leq \epsilon_{\text{cv}}$
2. Constraint violation criteria: $V_k \leq \epsilon_{\text{pcv}}$

Both of these conditions must be met in order for the optimisation to be considered complete. An additional exit condition that could be considered is that of the step size. If a certain minimum change in the design has been found to occur between two successive steps, then the design could be considered converged. Note that this is invalid while the Hessian approximation is still converging to the actual Hessian since this could result in very small step sizes initially causing premature completion, with a non-optimal design.

**Step 5: Update the Penalty Parameter** Determine the sum of the Lagrange multipliers and update the value of the penalty parameter as done in equations Equations 4.3.38 and 4.3.39.

**Step 6: Determine Step Size** Use the line search method described in §4.3.3 to determine $\alpha_k$.

**Step 7: Update and Continue** Use the step size, $\alpha_k$, and direction vector, $\mathbf{d}_k$, to determine the value of the next trial design vector as given in Equations 4.3.1 and 4.3.2:

$$\mathbf{x}_{(k+1)} = \mathbf{x}_k + \alpha_k \mathbf{d}_k$$

Also update the Lagrange multipliers using the formulae recommended by Boggs and Tolle [46]:

$$\mathbf{u}_{(k+1)} = \mathbf{u}_k + \alpha_k \mathbf{d}_{u_k}$$
$$\mathbf{v}_{(k+1)} = \mathbf{v}_k + \alpha_k \mathbf{d}_{v_k}$$

where

$$\mathbf{d}_{u_k} = \mathbf{u}_{\text{QP}} - \mathbf{u}_k$$
$$\mathbf{d}_{v_k} = \mathbf{v}_{\text{QP}} - \mathbf{v}_k$$

with $\mathbf{u}_{\text{QP}}$ and $\mathbf{v}_{\text{QP}}$ the optimal Lagrange multipliers determined in Step 3. Now proceed to Step 2.

## 4.4 Real-Encoded Genetic Algorithm – A Non-Gradient Based Optimisation Algorithm

The gradient-based sequential quadratic programming algorithm for optimisation was discussed in §4.3. This algorithm requires at least first derivative information to function. This derivative information is not always available, and in the case of this project, where a dual optimisation will be performed (see §5.3), this is the case. Gradient-based methods also do not function for objection functions where there are discontinuities in the first-derivative, thus a method of optimisation which does not require gradient information is desirable.

There are a number of optimisation methods which do not require gradient information. Some of these, viz. *genetic algorithms* (GAs), *particle swarm optimisations* (PSOs) and the *dividing into rectangles* (DIRECT) algorithm, are introduced and compared in Shutte [52]. Other methods mentioned include *simulated annealing*, *tabu searching*, *clustering methods* and *statistical optimisations* – all of which are stochastic methods.

To achieve the goals of this project the *genetic algorithm* was chosen, and will be discussed in this section. Genetic algorithms form part of a family of optimisation techniques that make use of the *Darwinian principle* of *survival of the fittest*, or *natural selection* Smith [53]. A genetic algorithm is an *evolutionary algorithm* making use of a series of successive generations of a population chosen according to the afore-mentioned principles. They have been in use for some time and "are now a well developed field of computing" [53], which is one of the reasons that a GA was chosen for the application to this project.

Other reasons for using a genetic algorithm are:

- *The relatively simple implementation* – GAs do not have a complex structure and can be quickly implemented in most programming languages.
- *The ease of understanding* – The lack of a complex structure and use of simple operators make GAs easy to understand in principle. They are far less abstract than a method such as the SQP and its sub-components.
- *Parallelisable nature* – The structure of the GA allows several computations to be performed simultaneously if suitable infrastructure exists. This is the topic of §4.6.
- *Easy to apply constraints* – Constraints are easily handled since there are no degrees of violation. The cost is also only computed if no constraints are violated, though inequality constraints may be active or inactive.
- *Larger range of applications* – Since no gradient information is necessary, a larger range of problem types can be solved, including discrete problems. There are restrictions such as the requirement that a minimum/maximum exists but these are far fewer than for gradient based methods. Since gradient information is not required, external programs and solvers can be used to determine cost values, though this may come with a performance trade-off.
- *Ability to find the global minimum* – Genetic algorithms can be used to find the global minimum, if one exists.
- *Representation of the design space* – Various encoding techniques exist for various types of data. This project makes used of real-value encoding since the design vector consists of real numbered values.
- *Well researched* – There is much published material on the uses of GAs for various applications.

### 4.4.1 Terminology

Due to the origins of GAs, much of the terminology stems from biological origins. At the lowest level, there are *genes*. A gene is "a unit of inheritance that [ferries] a characteristic from parent to child", Pearson [54]. A complete collection of genes is called a *chromosome*. In the case of the genetic algorithm, an individual gene represents a single design variable in the design vector, and a chromosome is a complete design vector. Thus a chromosome can be used to describe a design completely.

During evolution, a specific *population* is considered. A population is a collection of chromosomes (design points), usually of a fixed number called the *population size*. A *generation* is an iteration of the optimisation algorithm. Each generation has its own population which "evolves" into the next generation.

The concept of the *fitness* of a specific chromosome is related to how well it performs, and its suitability to be kept for the next generation. It is desired to only keep chromosomes which have high fitness values (relative to other chromosomes in the population). Since the discussion thus far has to do with minimising costs, we now define the fitness of a specific chromosome as the inverse of cost. The higher the *fitness* ($F$) a chromosome is, the *lower its cost* ($f$) when substituted into the objective function:

$$F(\mathbf{x}) = -f(\mathbf{x})$$

During the implementation of the algorithm *maximum fitness* was treated as *minimum cost*.

The evolution process itself is described by the a set of actions performed on the chromosomes in the population of each generation Holst and Pulliam [55]:

1. *Selection* – A process whereby individual chromosomes are selected from the current population. This selection process favours individuals with higher fitness values and eliminates those with lowest fitness values. The chromosomes chosen for selection make up the pool on which the other operators are applied.

2. *Passthrough or Elitism* – A certain percentage of the fittest chromosomes (the elite) are *passed through* directly to the next generation, unmodified.

3. *Crossover* – During the application of this operator some attributes (genes) of two chromosomes are exchanged creating two new offspring which are then inserted into the next generation.

4. *Mutation* – In order to prevent the stagnation of the generation where only existing genes are reused, random mutation allows the creation of new genes (and hence new chromosomes) or the mutation (modification) of existing genes to provide diversity in the generation. This step is important to prevent the convergence of the optimisation to a local minimum, rather that the global.

### 4.4.2 Encoding

In order for genetic algorithms to be used, the design variable(s) need to be written (or encoded) in such a way that the operators described in §4.4.1 can be applied. Traditional genetic algorithms make use of *binary coding*, Arora [33], where chromosomes are represented as a string of ones and zeros. This makes a great deal of sense since computers are inherently binary and can thus perform efficiently on binary representations of design variables.

Herrera, et al [56] points out, however, that binary coding presents problems when examining *continuous search spaces* since the binary representation can only represent a discrete number of points to some maximum resolution (results in low accuracy). [56] also states that problems may occur when search spaces have large dimensions.

A logical continuation of the problem occurs when the various design variables within the design vector have differing ranges. Using the same encoding technique for all design variables could result in loss of accuracy or range on some of the variables (consider, for instance, lengths in metres versus deflection angles in radians).

*Real-number encoding* makes use of *real* ($\mathbb{R}$), or floating-point, numbers to represent genes, and chromosomes thus become vectors of real numbers. The chromosome is thus simply the design vector, $\mathbf{x}$. Since most engineering design applications make use of real numbers, this seems a logical choice. The accuracy of each design variable is thus limited to that of the computer used to perform the optimisation.

The ranges of these real numbers might be limited, though this can be taken into account during the optimisation process through intelligent selection of design points based on these ranges, and adding constraints to the optimisation problem.

Other advantages of using a real-number encoding technique are provided by Herrera, et al [56]: it is now possible to use large domains, take into account the graduality of functions (small changes in parameters result in small changes of the function value), and eliminate the time-consuming coding and decoding of parameters to and from the binary representation.

### 4.4.3 Operators

The genetic algorithm operators listed in §4.4.1 are now explained in more detail. Most of the implementations of these operators are based on those discussed in Holst and Pulliam [55].

#### 4.4.3.1 Selection

The selection process examines the fitness of the current generation. As stated previously the main idea is to eliminate the chromosomes with low fitness and promote those with higher fitness.

A new selection of chromosomes is created from the current generation based on the following algorithm (from Holst and Pulliam [55]):

$i = 0$
**while** $i < P_s$ **do**
  **for** $j = 1$ to $P_s$ **do**
    **if** Rank($G_n(j)$) $\leq j$ **then**
      $G_s(i) = G_n(j)$
      $i = i + 1$
    **end if**
    **if** $i > P_s$ **then**
      stop
    **end if**
  **end for**
**end while**

where $P_s$ is the population size, $G_n$ is the population vector for the $n$th generation of the optimisation algorithm, and $G_s$ is the generation selection vector. The Rank() operator provides the position of the chromosome provided as parameter if all the chromosomes in the generation were to be arranged from most to least fit. It returns an integer value on the closed interval $[1, P_s]$.

Examination of this process shows how the fittest chromosomes are included multiple times while the least fit individuals are not included at all.

#### 4.4.3.2 Passthrough and Elitism

Here the best (most fit) chromosomes are chosen from the selection pool, $P_s$, and inserted directly into the next generation vector $G_{n+1}$. Typically a certain percentage of the population size is chosen, and is labeled $P_E$.

#### 4.4.3.3 Crossover

There are a number of ways of performing crossover. Herrera, et al [56] provides several crossover operators, such as *flat crossover*, *simple crossover*, *arithmetical crossover*, *BLX-$\alpha$*, *linear crossover* and others.

The method used by this project is a straightforward *random average crossover*. Here two chromosomes are chosen randomly from the selection pool, and a new (single) chromosome is created where each gene in the new chromosome is determined using the formula

$$x_i^N = \frac{1}{2}\left(x_{i_1} + x_{i_2}\right) \qquad \text{for } i = 1 \text{ to } n$$

where $x_{i_1}$ and $x_{i_2}$ are the $i$th genes of the first and second randomly selected chromosomes respectively, $x_i^N$ is the $i$th gene of the new chromosome, and $n$ is still the number of design variables (and also the total number of genes in a chromosome).

Crossover, like the previously mentioned operators, again determines a certain percentage of the new generation. This percentage is represented by $P_C$

#### 4.4.3.4 Perturbation Mutation

There are two types of mutation that take place. The first is a localised mutation where some of the chromosomes in the selection pool are perturbed randomly to obtain new chromosomes. This so-called *perturbation mutation* functions under the assumption that some of the chromosomes in the selection pool are fairly close to the optimum point, and simply perturbs them about their current points in an attempt to get a fitter chromosome.

The original implementation suggested by Holst and Pulliam [55] selects random chromosomes from the selection pool and adjusts a *single* gene in the chromosome by a small random value. During experimentation with the algorithm, it was found that better results were obtained by perturbing *all* the genes in the chromosome. The perturbation of each gene is provided by the following formula

$$x_i^N = x_i^O + \beta\,(x_{i_{\max}} - x_{i_{\min}})\,\mathrm{rand}(0,\,1) \qquad \text{for } i = 1 \text{ to } n$$

where $x_i^N$ is the new gene value, $x_i^O$ is the old gene value, $x_{i_{\max}}$ and $x_{i_{\min}}$ are the minimum and maximum allowable values for this gene, and $\mathrm{rand}(0,\,1)$ indicates a random number chosen on the closed interval $[0,\,1]$. $\beta$ is the perturbation value is also on the closed interval $[0,\,1]$, and represents a percentage of the gene's range.

The percentage of chromosomes in the next generation to be made up from this process is $P_P$.

#### 4.4.3.5 Mutation

The second mutation is used to ensure that the algorithm does not converge on a local minimum by introducing new "genetic material". In this case entirely new chromosomes are generated using the formula

$$x_i^N = (x_{i_{\max}} - x_{i_{\min}})\,\mathrm{rand}(0,\,1) \qquad \text{for } i = 1 \text{ to } n$$

which calculates a new value for each gene in a chromosome. This chromosome is then added to the next generation until a percentage $P_M$ of the next generation is generated.

The summation of all the components described in §4.4.3.2 to §4.4.3.5 should total one:

$$P_E + P_C + P_P + P_M = 1$$

which results in the next generation having $P_s$ chromosomes, as with the current generation.

### 4.4.4 The Use of the REGA in Multi-Objective Optimisation

The use of genetic algorithms in a multi-objective optimisation environment is discussed in the survey of multi-objective optimisation performed by Marler and Arora in [40]. The topic is also raised in Fonseca and Fleming [57]. Both references yield multiple methods of performing the optimisation where there are several distinct objectives.

As has been previously mentioned, the lack of the need for gradient information is a distinct advantage of genetic algorithms since this allows a wider range of functions to be used as objective functions. Another advantage is that genetic algorithms converge on the *Pareto optimal set*, Arora [33], rather than just a single point, when the optimisation has multiple objectives (dependant on the problem formulation).

Arora [33], Marler, et al [40] and Fonseca and Fleming [57] all mention the *vector evaluated genetic algorithm* (VEGA) as one means of evaluating multiple objectives. In this case the fitness measures are a vector of values (obtained from the individual objective functions), rather than a single value as with the traditional genetic algorithm. This results in a number of sub-populations being created during fitness evaluation (one for each objective). The disadvantage of this method as described in [33] and [40] is that *species* tend to develop. A species occurs when the optimisation begins to favour a specific objective, thus resulting in "clusters" of chromosomes around the individual objective function minima, [33].

Various methods have been suggested by Marler and Arora [40] to overcome this difficulty (ranking, Pareto-set filter, tournament selection, niche techniques, and fitness sharing), though an alternative to the VEGA is also provided. This alternative resolves the fitness *vector* back into a *scalar*, using techniques already mentioned in §4.2.2. These techniques include the

1. Weighted global criterion method

2. Weighted sum method
3. Lexicographic method
4. Weighted min-max method
5. Goal programming methods

A concise comparison of these methods is provided in Arora [33] in tabular form.

The method chosen for the project is that described in §4.2.2.2, the *weighted sum method*. The following remark is added from Arora [33]: "Even with the use of some of the methods discussed in literature for determining weight[ings], a satisfactory a priori selection of weight[ings] does not guarantee that the final solution will be acceptable". This does not mean that the point is not Pareto optimal, only that the result is not the desired result. It is thus often necessary to vary the weight[ings] manually and re-run the optimisation until a suitable optimal point is found.

The reasons for making use of the weighted sum method are the same as those described in §4.2.2.2,

### 4.4.5 The Complete Real-Encoded Genetic Algorithm

This section describes the entire REGA in a step-by-step manor as was implemented for the application to this project.

**Step 1: Initialisation** The initial generation of $P_s$ chromosomes is generated by randomly selecting chromosomes over the design space, or is provided by the user if desired. If random selection is used, this is done by following the process as described in the mutation section (§4.4.3.5) for each chromosome.

The generation counter, $k$, is set to zero. If necessary normalise the values of $P_E$, $P_C$, $P_P$ and $P_M$ by creating the vector

$$\mathbf{P}_{\text{all}} = (P_E,\, P_C,\, P_P,\, P_M)$$

and performing the operation

$$\mathbf{P}_{\text{all}_{\text{norm}}} = \frac{P_{\text{all}}}{P_E + P_C + P_P + P_M}$$

**Step 2: Determine population fitness** Now that the generation population has been assembled, it is necessary to evaluate the fitness of each chromosome. As mentioned in §4.4.1, this project makes use of cost functions which need to be minimised, thus the chromosome with the greatest fitness has the value closest to zero.

An aspect that has not been considered up to now is the concept of constraints. During the optimisation process the constraints need to be taken into account. The simplest way of doing this is to modify the fitness (or cost) associated with a specific chromosome. There are no degrees of violation of constraints. Either a constraint is active, violated or inactive. Equality constraints can only be active or violated.

If a constraint is active or inactive the fitness of the chromosome is not modified since the design point is within the feasible region and is thus valid. If any of the constraints are violated, the *cost* of the chromosome is set to infinity, or the fitness is set to the lowest possible (zero). It is thus theoretically possible for *all* the chromosomes to be associated with infinite costs.

If this is the case, the problem may need to be reformulated, though the mutation step will typically remedy the problem if there are feasible design points, though convergence to the final result may take longer.

An important code optimisation should be noted here: For many optimisation problems (especially in aerodynamics-based problems) external programs or codes are called to evaluate the fitness of a specific chromosome or design vector. This could be a very time-consuming process in the case of flow-solvers and other complex programs, thus it is advised by the author that the constraints be evaluated before the fitness. This will allow the opportunity to only evaluate the fitness of chromosomes that are not in violation of the design constraints, which could potentially save a great deal of execution time, especially in the first few generations.

**Step 3: Ranking** Once the fitness calculations have been completed it is necessary to sort the chromosomes according to fitness from most to least fit. This order is stored in a vector known as the *rank vector* which indicates the rank of each of the chromosomes in the generation.

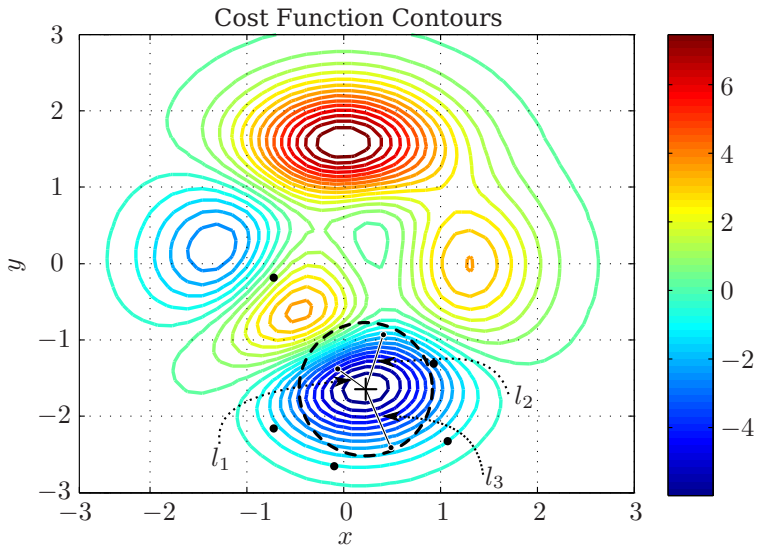


**Figure 4.3** – How the convergence is determined using the *Euclidean distance* between the fittest chromosome and the next three chromosomes ($p = 3$). In this case the lengths $l_1$, $l_2$, and $l_3$ are all less than the convergence parameter (indicated by the dashed circle), thus the optimisation will terminate with point 1 as the optimum. The $+$ symbol is the optimum point.

**Step 4: Evaluate termination conditions** Before creating the next generation, examine the current generation in order to determine whether the solution has converged.

The most common method of determining whether the optimum solution has been reached is to keep a history of the most fit individual of each generation and examine the most fit individuals until the difference in fitness between two successive generations is less than some convergence value. An alternative method is now suggested for the purposes of this project.

Instead of examining the fitness value, the convergence is determined based on the values of the chromosomes themselves. This can be done since the chromosomes are the design vectors of the system in the case of this REGA. In order to achieve this, the *Euclidean* distance is calculated between a certain number of chromosomes in the generation.

This is based on the assumption that as the optimisation progresses, clustering will occur around the optimum point as less fit chromosomes are eliminated. Care must be taken when choosing the number of chromosomes to compare since there is still an element of randomness (in the two mutation steps) that may cause the optimisation to never converge.

The convergence parameter now specifies the maximum Euclidean distance allowed between the most fit chromosome and the next $P_e - 1$ fittest chromosomes, where $P_e$ is a number chosen by the designer. This is illustrated for the case of two design variables in Figure 4.3.

**Step 5: Selection** Here the selection process is followed as described in §4.4.3.1 to generate the selection pool $G_s$ of $P_s$ chromosomes. Note that the function makes use of the *unsorted* list of chromosomes in the current generation. Once the process is completed a new rank vector is determined for the selection pool and sorted.

**Step 6: Passthrough and elitism** The top $P_E$ percent of individuals in the selection pool are transferred directly to the next generation's population, $G_n$, as described in §4.4.3.2. In the implementation used in this project Steps 5 and 6 were swapped around.

This prevents premature, false convergence due to the possibility that the fittest individual is inserted into the new generation sufficient times that convergence is indicated as described in Step 4. Premature convergence could occur regardless of which of the two convergence evaluation techniques described in Step 4 are used.

**Step 7: Crossover** The crossover process is executed as described in §4.4.3.3 on $P_C$ percent of $G_s$.

**Step 8: Perturbation mutation** The perturbation mutation process of §4.4.3.4 is applied to $P_P$ percent of $G_s$. The performance of the algorithm can be improved slightly by applying the perturbation mutation to the top $P_P$ fittest chromosomes of $G_s$ under the assumption that the fittest individuals are closest to the optimal point.

**Step 9: Mutation** New genetic material is introduced here by randomly generating new chromosomes for the remaining $P_M$ percent of the new population. See also §4.4.3.5.

**Step 10: Update generation** The new population $G_n$ has now been compiled and needs to be transferred to the general population before proceeding to Step 2.

## 4.5 Comparison Between SQP and REGA

Having now fully described the two optimisation procedures that will be used in the remainder of this document, it seems prudent to compare the two algorithms. In order to do this, a known, analytic, twice-continuously-differentiable function is used. This is the same function used to generate the "peaks" plot in MATLAB:

$$f(x,\, y) = \frac{3(x-1)^2}{\mathrm{e}^{(x^2+(y+1)^2)}} + \frac{(10x^3 - 2x + 10y^5)}{\mathrm{e}^{(x^2+y^2)}} - \frac{1}{3\mathrm{e}^{((x+1)^2+y^2)}} \tag{4.5.1}$$

with partial derivatives:

$$\frac{\partial f}{\partial x} = 2\mathrm{e}^{-(x^2+y^2)}\left[\frac{3\left(2x^2 - x^3 - 1\right)}{\mathrm{e}^{(2y+1)}} + \frac{(x+1)}{3\mathrm{e}^{(2x+1)}} + 10xy^5 + 17x^2 - 10x^4 - 1\right] \tag{4.5.2}$$

$$\frac{\partial f}{\partial y} = \frac{2y}{3\mathrm{e}^{\left((x+1)^2+y^2\right)}} - \frac{6\,(y+1)\,(x-1)^2}{\mathrm{e}^{\left((y+1)^2+x^2\right)}} - \frac{2y\left(10y^5 - 25y^3 + 10x^3 - 2x\right)}{\mathrm{e}^{(x^2+y^2)}} \tag{4.5.3}$$

A three-dimensional plot of Equation 4.5.1 function and some of its contours are shown in Figure 4.4.

For the purpose of the optimisation, the design vector is set up as $\mathbf{x} = (x,\, y)$. Constraints are limitations only on the range of the design variables (inequality constraints):

$$g_1(\mathbf{x}) = -(x+3) \leq 0 \tag{4.5.4}$$

$$g_2(\mathbf{x}) = x - 3 \leq 0 \tag{4.5.5}$$

$$g_3(\mathbf{x}) = -(y+3) \leq 0 \tag{4.5.6}$$

$$g_4(\mathbf{x}) = y - 3 \leq 0 \tag{4.5.7}$$

Equations 4.5.4 and 4.5.5 are for the constraint $-3 \leq x \leq 3$, and Equations 4.5.6 and 4.5.7 are for the constraint $-3 \leq y \leq 3$.

The derivatives of the constraints are:

$$\frac{\partial g_1}{\partial x} = -1 \qquad \frac{\partial g_1}{\partial y} = 0 \tag{4.5.8}$$

$$\frac{\partial g_2}{\partial x} = 1 \qquad \frac{\partial g_2}{\partial y} = 0 \tag{4.5.9}$$

$$\frac{\partial g_3}{\partial x} = 0 \qquad \frac{\partial g_3}{\partial y} = -1 \tag{4.5.10}$$

$$\frac{\partial g_4}{\partial x} = 0 \qquad \frac{\partial g_4}{\partial y} = 1 \tag{4.5.11}$$

Now that a sample problem has been defined, it can be used to compare the the *sequential quadratic programming* and *real-encoded genetic algorithms*. The parameters that can be adjusted for the algorithms are given in Tables 4.4 and 4.5 for the SQP and REGA respectively.

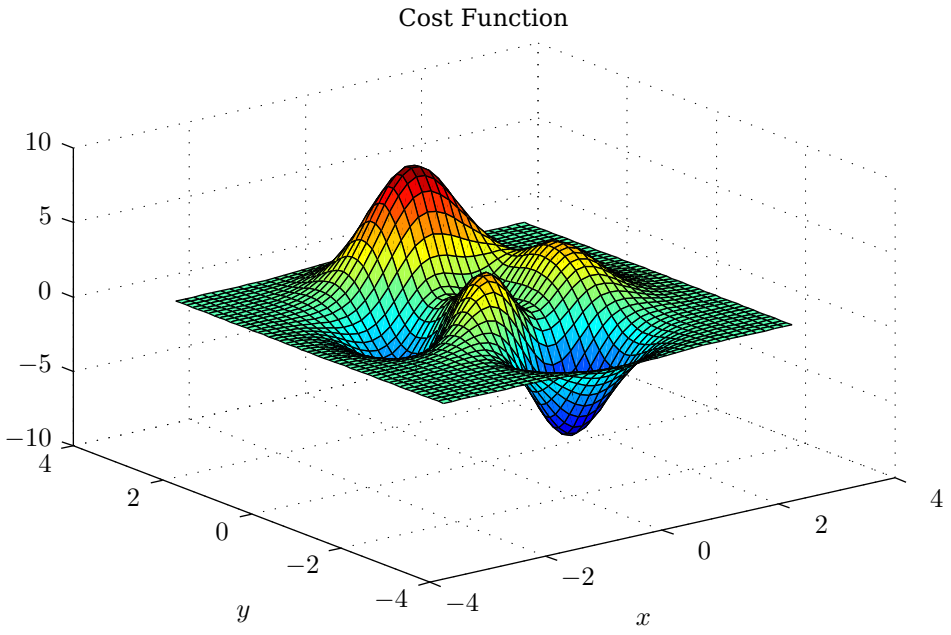


(a)

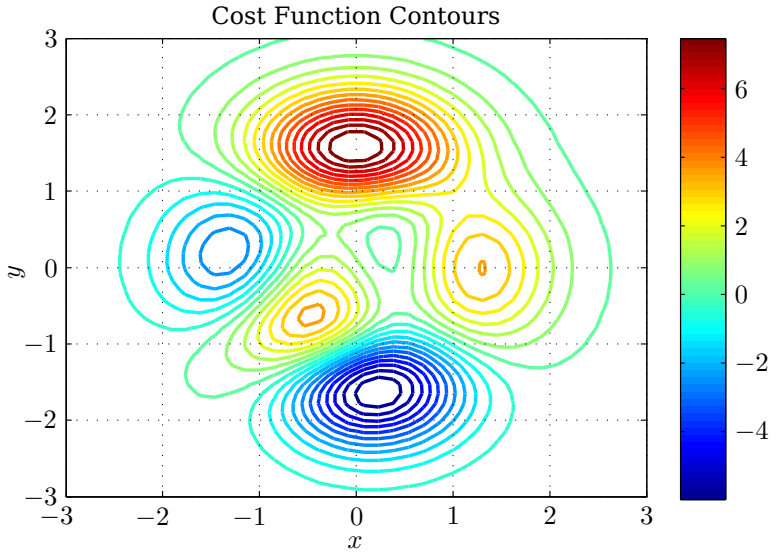


(b)

**Figure 4.4** – The plot of Equation 4.5.1 with the three-dimensional surface shown in 4.4(a) and some contour plots in 4.4(b).

### 4.5.1 SQP Results

The parameters were used for the SQP algorithm are given below:

$$k_{\max} = 100 \qquad k_{s_{\max}} = 20$$
$$R = 1 \times 10^{-15} \qquad \epsilon_{\text{pcd}} = 5 \times 10^{-3}$$
$$\epsilon_{\text{pcv}} = 1 \times 10^{-7} \qquad \epsilon_{\text{cv}} = 1 \times 10^{-7}$$
$$\gamma = 0$$

The initial design vector is chosen randomly on the intervals $-3 \leq x \leq 3$ and $-3 \leq y \leq 3$ with the initial values of the Lagrange multipliers set to zero. The results of one of the runs is given as both a surface and a contour plot (in Figures 4.5 and 4.6). Successive results will only be plotted on contour plots. In this case the optimisation converged to the global optimum ($\mathbf{x} = [0{,}2283, -1{,}6255]^{\text{T}}$), with minimum cost $J = -6.5511$. For clarification, the coordinates of the design vector are provided in Table D.3 and the

**Table 4.4** – Parameters for the SQP algorithm for the optimisation of Equation 4.5.1

| Parameter Description | Symbol | See |
|---|---|---|
| Maximum number of iterations | $k_{\max}$ | |
| Maximum number of simplex iterations | $k_{s_{\max}}$ | |
| Penalty parameter initial value | $R$ | §4.3.3 |
| Potential constraint deviation | $\epsilon_{\text{pcd}}$ | §4.3.5 |
| Permissible constraint violation | $\epsilon_{\text{pcv}}$ | §4.3.5 |
| Convergence parameter | $\epsilon_{\text{cv}}$ | §4.3.5 |
| Line search parameter | $\gamma$ | §4.3.3 |

**Table 4.5** – Parameters for the REGA for the optimisation of Equation 4.5.1

| Parameter Description | Symbol | See |
|---|---|---|
| Maximum number of generations | $k_{\max}$ | |
| Population size | $P_s$ | §4.4.5 |
| Elitism percentage | $P_E$ | §4.4.3.2 |
| Crossover percentage | $P_C$ | §4.4.3.3 |
| Perturbation percentage | $P_P$ | §4.4.3.4 |
| Perturbation deviation value | $\beta_{P_P}$ | §4.4.3.4 |
| Mutation percentage | $P_M$ | §4.4.3.5 |
| Number of elements to determine the Euclidean distance of | $n_e$ | §4.4.5 |
| Maximum Euclidean distance allowed for convergence | $\beta_{n_e}$ | §4.4.5 |

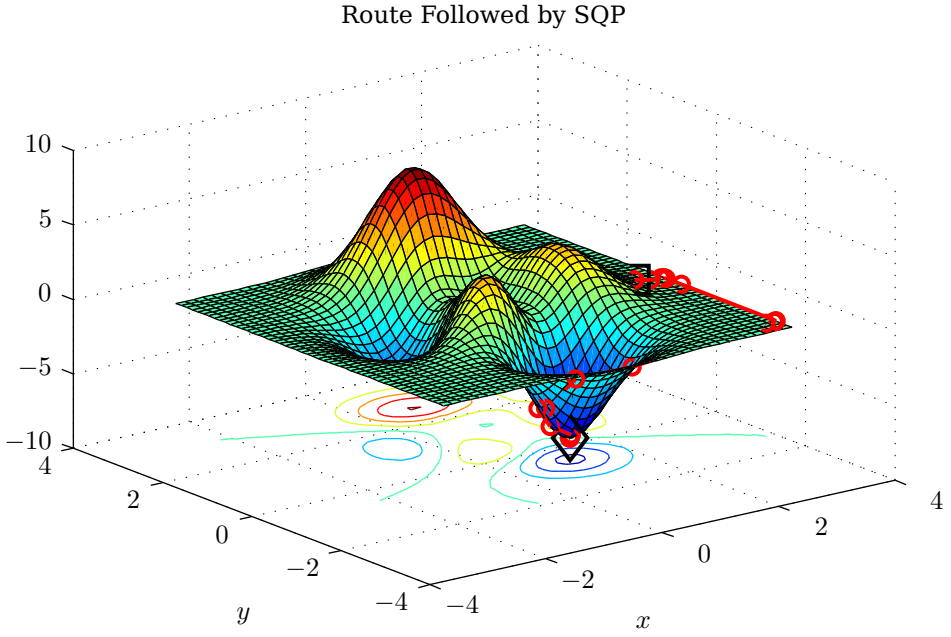


**Figure 4.5** – The progression of the design vector in three dimensions as the optimisation progressed for the SQP with the parameters described in the text. The □ indicates the starting point, and the ◇ is the final design vector.

direction vector and step sizes for each iteration are listed in Table D.4, both of which can be found in Appendix D.

Since the algorithm is very dependant on the starting position, some further plots are provided in Figures 4.7 and 4.8 to show some possible routes where the parameters remain the same as those listed above. As before, in each of the design progressions □ indicates the initial (guessed) design vector and ◇ indicates the final design vector.

A summary of the results is given in Table 4.6. As can be seen from both the figures in Figures 4.7 and 4.8, and the summarised results of Table 4.6, there are a number of cases where the global minimum is reached, a number of cases where a local minimum is reached and finally a number of cases where the result is on the constraints boundary. This indicates the importance of choosing a good initial value for the

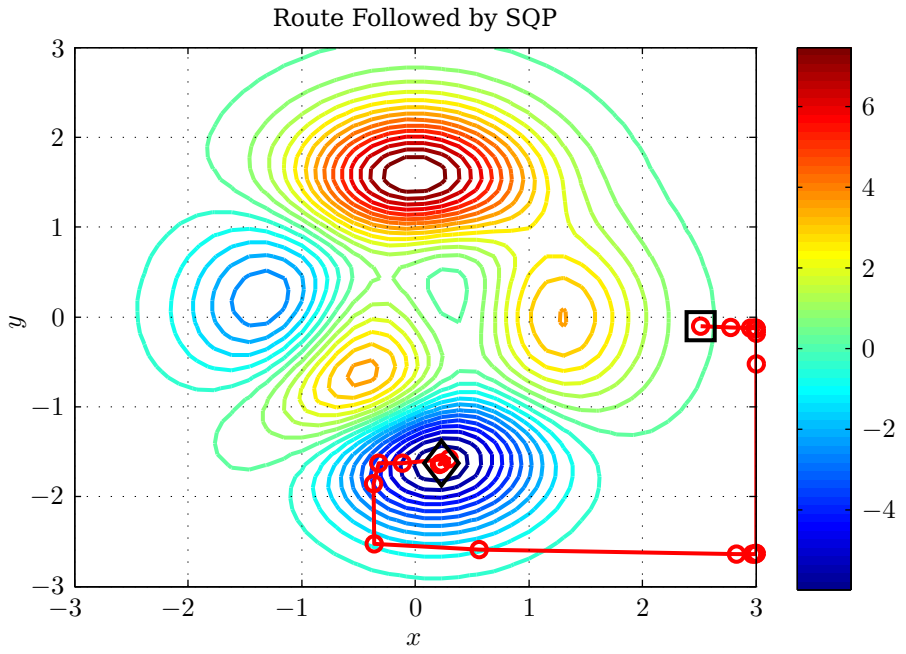


**Figure 4.6** – The progression of the design vector in two dimensions as the optimisation progressed for the SQP with the parameters described in the text. The □ indicates the starting point, and the ◇ is the final design vector.

**Table 4.6** – Summary and comparison of the results of the various test cases for the SQP algorithm.

| Case | Initial x | | Final x | | Iterations | Minimum Cost |
|---|---|---|---|---|---|---|
| | $x$ | $y$ | $x$ | $y$ | | |
| 1 | 2,5153 | −0,104 51 | 0,228 28 | −1,6255 | 24 | −6,5511 |
| 2 | −0,646 91 | 0,295 13 | 0,228 28 | −1,6255 | 10 | −6,5511 |
| 3 | 1 | 1 | 0,228 28 | −1,6255 | 36 | −6,5511 |
| 4 | 0,811 16 | 0,605 96 | −1,3474 | 0,204 52 | 12 | −3,0498 |
| 5 | −0,189 47 | 0,083 43 | 3 | 3 | 18 | $4{,}103 \times 10^{-5}$ |
| 6 | 1,193 | −0,127 63 | −3 | −3 | 18 | $6{,}6713 \times 10^{-5}$ |
| 7 | 1,2363 | −2,809 | 0,228 28 | −1,6255 | 12 | −6,5511 |
| 8 | −2,4172 | 1,9407 | −1,3474 | 0,204 52 | 21 | −3,0498 |
| 9 | −2,2 | 2,5 | −3 | 3 | 15 | $3{,}2235 \times 10^{-5}$ |

SQP algorithm, as it will converge to some local minimum, but not necessarily the global minimum.

This is due to the algorithm making use of local gradient information about the current evaluation point (for both the cost function, and the constraint functions). The step size also plays a major role. The algorithm always takes the largest step that satisfies the descent condition. This can sometimes result in large jumps between minima regions, but the jump to a global minimum is not guaranteed.

Examining each of the graphs shown in Figures 4.7 and 4.8 for Cases 2 through 9, and the contour graph for Case 1 shown in Figure 4.6 the following behaviour is noted:

- Cases 1, 2, 3 and 7 all converge to the *global* minimum.
- Cases 1 and 3 both reach the boundaries determined by the constraints described above, causing them to slide along the boundaries for a number of iterations.
- Case 2 started converging on the local minimum, before the descent condition and direction vector caused a jump toward the global minimum, to which it converged.
- Case 4 converged to the local minimum. It can be reasoned this is due to none of the direction vectors being in the direction of the global minimum, resulting in step sizes which were small enough to keep it in the local minimum region.
- Case 5 did not converge to either the global, or local minimum. Instead, once it reached the positive $y$ boundary, it converged on the *boundary* minimum at $(3, 3)$.

- A similar effect occurred in Case 6 where the direction vector resulted in the optimisation converging on the boundary at $(-3, -3)$.
- Case 7 shows a simple global convergence where the initial design vector was close to the global minimum.
- Case 8 also shows a boundary slide and converges to the local minimum.
- Case 9 indicates how a small change in the starting point (versus that in Case 8) can result in a completely different solution, in this case on the boundary at $(-3, 3)$.
- Comparing the starting points Case 3 and Case 4 also exhibit similar behaviour, where slight variations in the initial value can result in different answers. In this case the difference between the local and global minima. This is mainly caused by the gradient information available at the starting points.

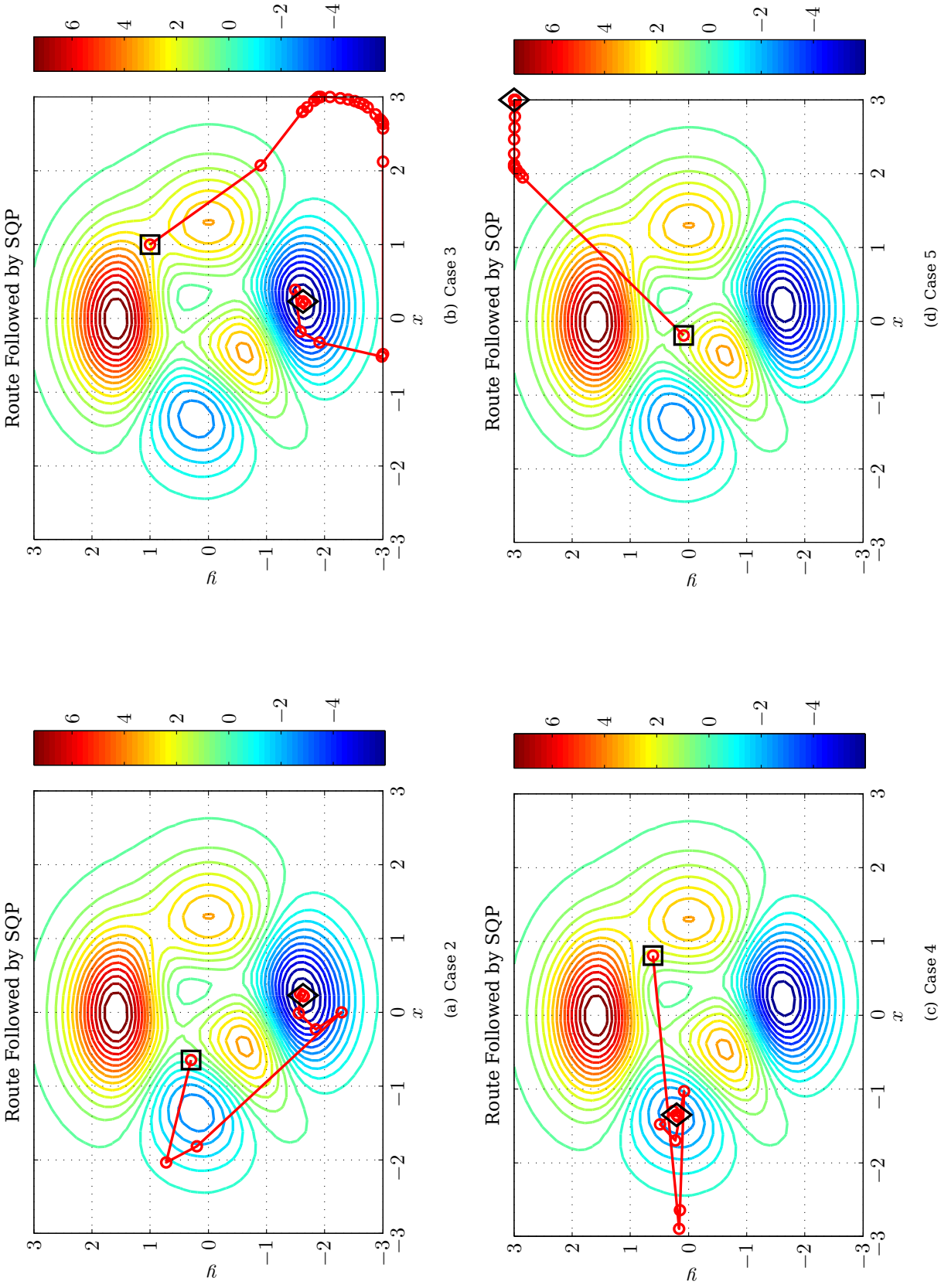


**Figure 4.7** – The progression of the design vector using the SQP algorithm for a number of cases (Part I).

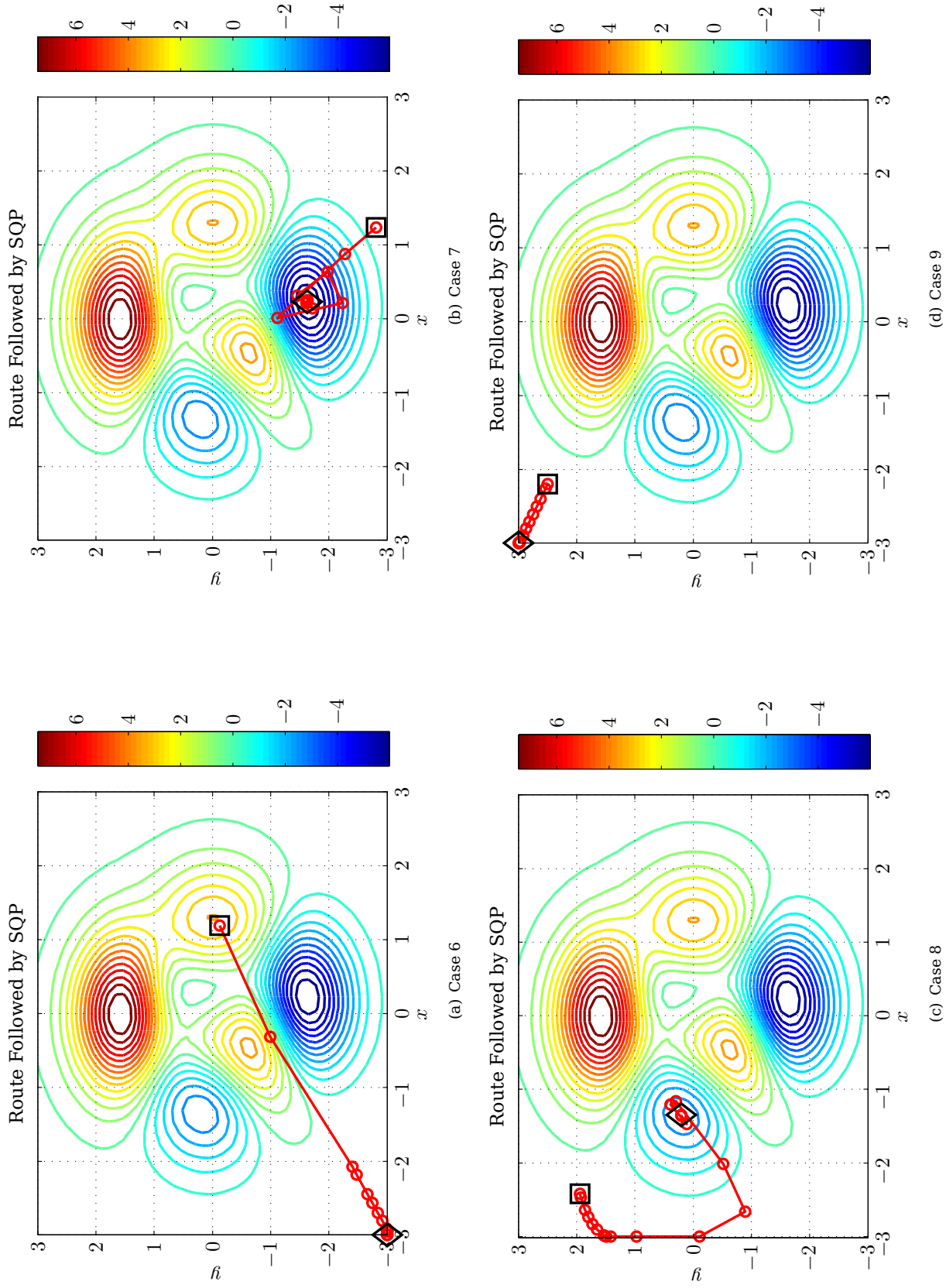


**Figure 4.8** – The progression of the design vector using the SQP algorithm for a number of cases (Part II).

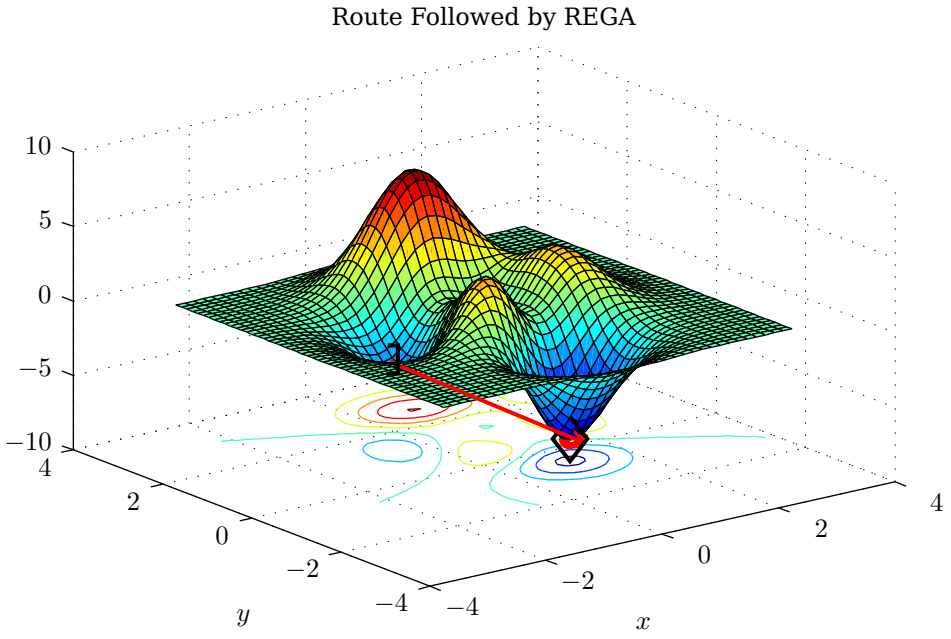


**Figure 4.9** – The evolution of the design vector in three dimensions as the optimisation progressed for the REGA with the parameters described in the text. The □ indicates the starting point, and the ◇ is the final design vector.

### 4.5.2 REGA Results

Having examined the SQP, it is necessary to look at the REGA for solving the same problem. The optimisation used to illustrate the process has the following parameters:

$$
\begin{aligned}
k_{\max} &= 300 & P_s &= 20 \\
P_E &= 0{,}2 & P_C &= 0{,}25 \\
P_P &= 0{,}4 & \beta_{P_P} &= 0{,}05 \\
P_M &= 0{,}15 & & \\
n_e &= 5 & \beta_{n_e} &= 0{,}01
\end{aligned}
$$

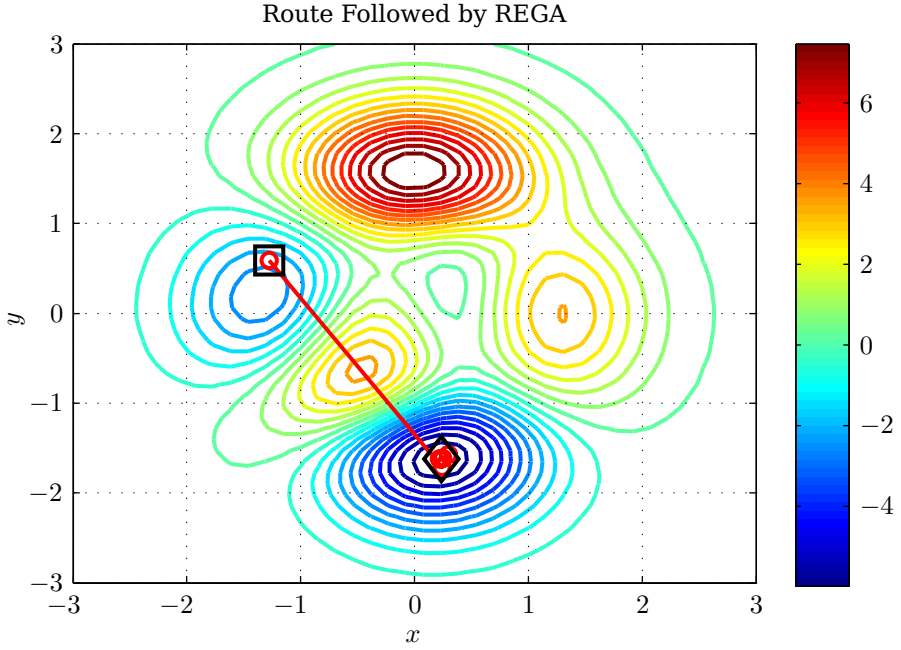


**Figure 4.10** – The evolution of the design vector in two dimensions as the optimisation progressed for the REGA with the parameters described in the text. The □ indicates the starting point, and the ◇ is the final design vector.

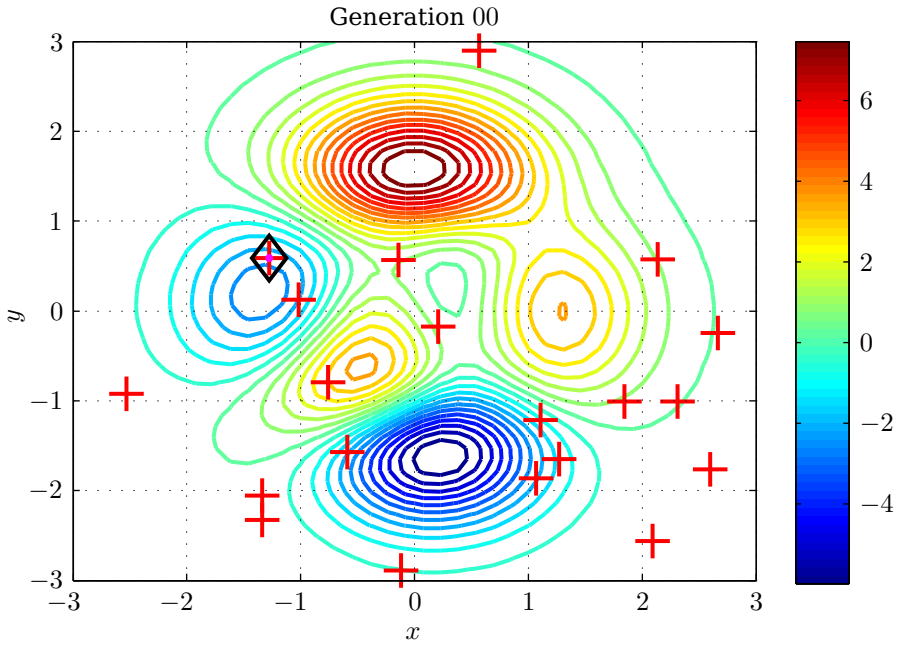


**Figure 4.11** – Initial, randomly generated population for the REGA example.

In this case the Euclidean evaluation distance was chosen fairly large in order to achieve a convergence within a reasonable number of iterations to be shown here. The evolution of the optimum design variable is shown in 3D in Figure 4.9 and in 2D in Figure 4.10.

The initial population, which is randomly chosen over the design space, is shown in Figure 4.11 with the remaining eight generations shown in Figures 4.12 and 4.13. In all cases the ◇ indicates the fittest individual of the generation.

It can be seen from Figure 4.11 that the initial population is distributed randomly over the design space. This is the reason that genetic algorithms make good global optimisers. This randomness allows the algorithm to explore the entire design space in an endeavour to find the global minimum. During each successive iteration as shown in Figures 4.12 and 4.13, clustering can be seen as the evolution process takes place.

In each of the successive generations there are still chromosomes that do not form any clusters. This is due to the mutated component of each generation. It can be seen that there are typically two or three ($15\,\%$ of $P_s = 20$) chromosomes that display this characteristic.

From Generation $1$ (Figure 4.12(b)) it can be seen that the most optimal design vector of each generation is very close to the optimal. Generation $1$ shows some clustering. This is due to the *perturbation* mutation. It soon becomes apparent that only a single cluster evolves around the global minimum as the less fit chromosomes are removed from the population.

This cluster gets successively smaller until the convergence criterion is reached, i.e. where the top $n_e$ fittest chromosomes are less than $\beta_{n_e}$ from the most fit chromosome. This chromosome is then chosen as the optimum design.

The numerical evolution for this example is summarised in Table D.5 in Appendix D.

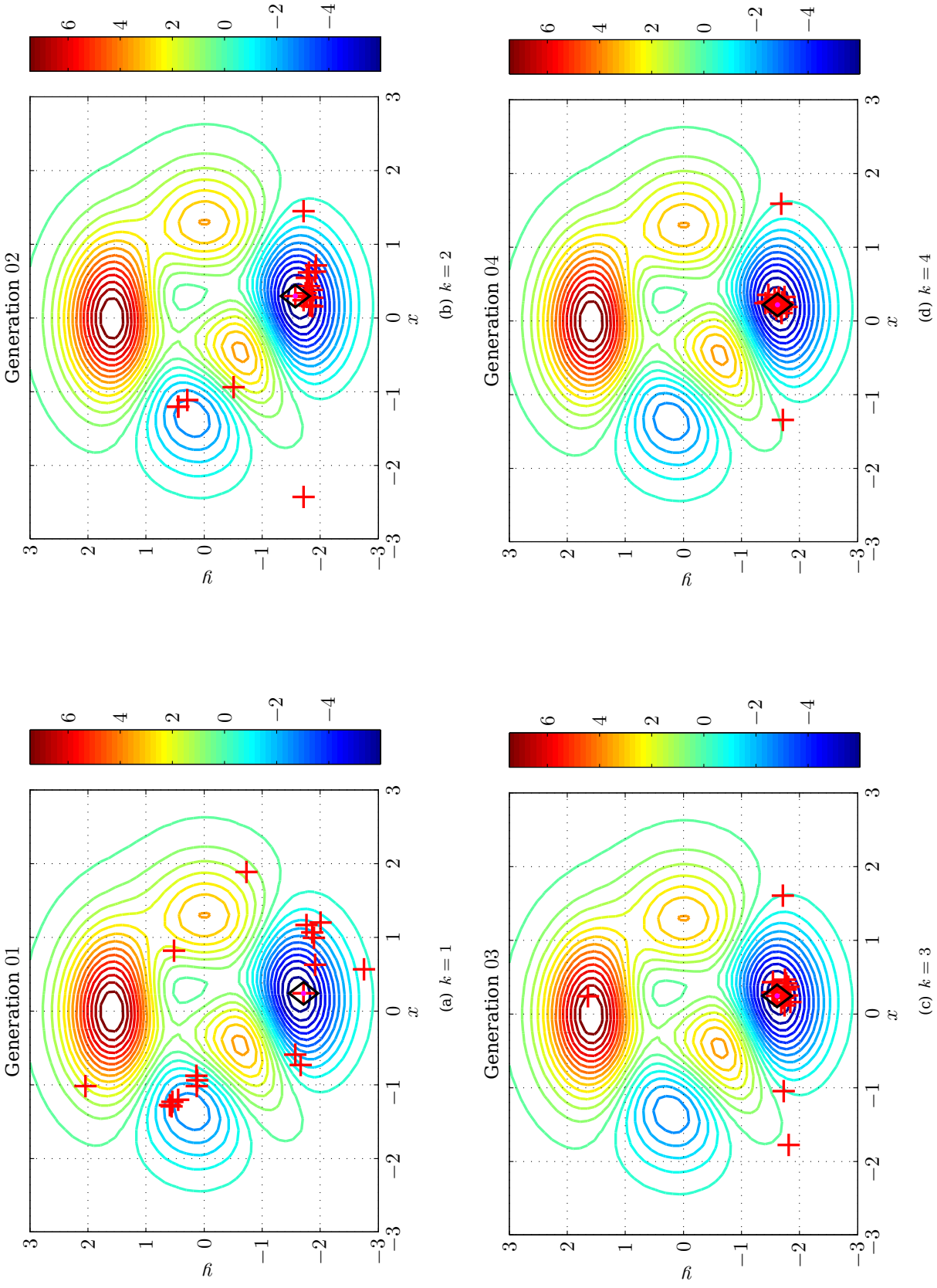


(a) $k = 1$ (b) $k = 2$ (c) $k = 3$ (d) $k = 4$

**Figure 4.12** – The chromosomes making up the population for each generation (Part I).

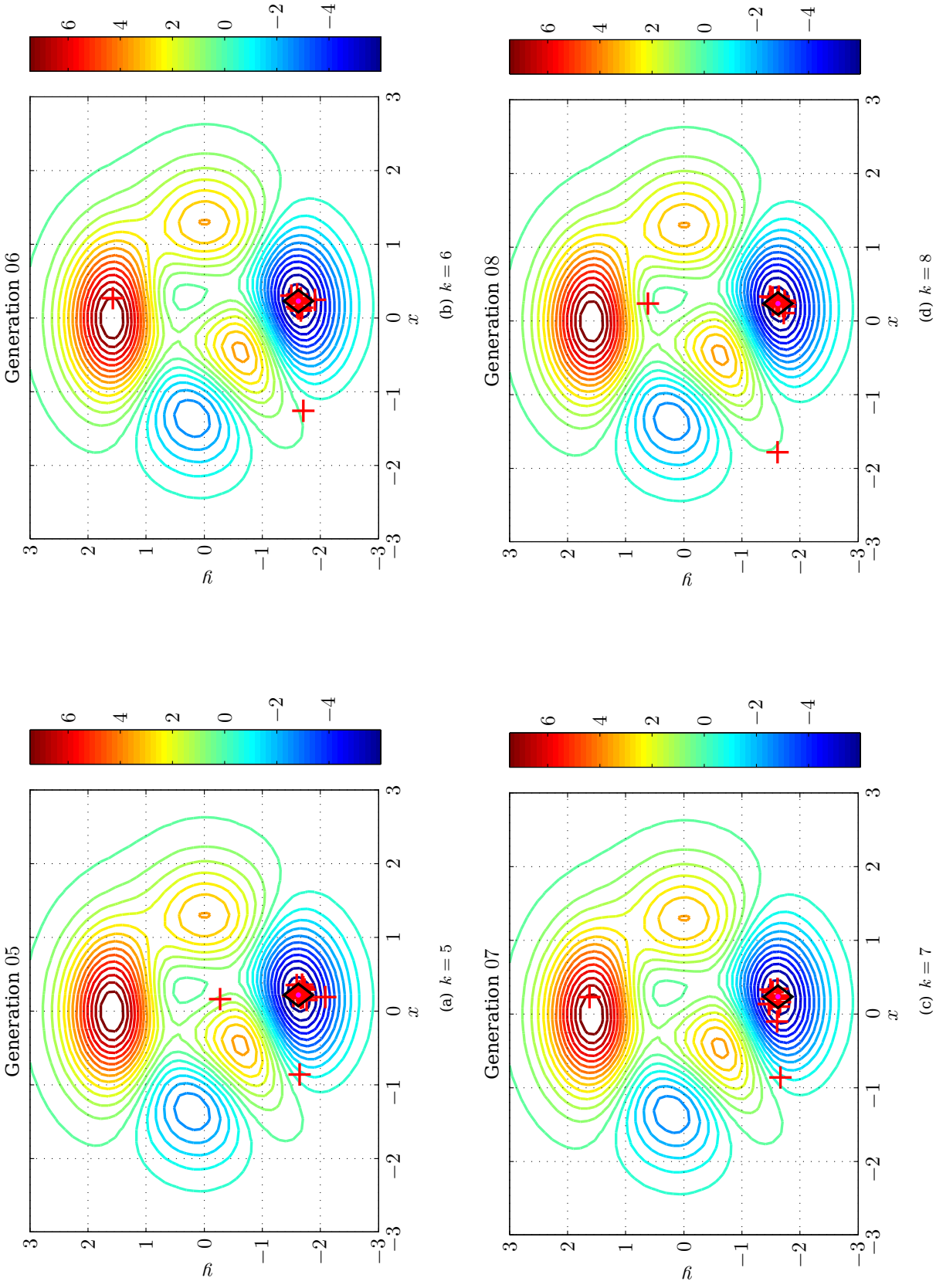


(a) $k = 5$ (b) $k = 6$ (c) $k = 7$ (d) $k = 8$

**Figure 4.13** – The chromosomes making up the population for each generation (Part II).

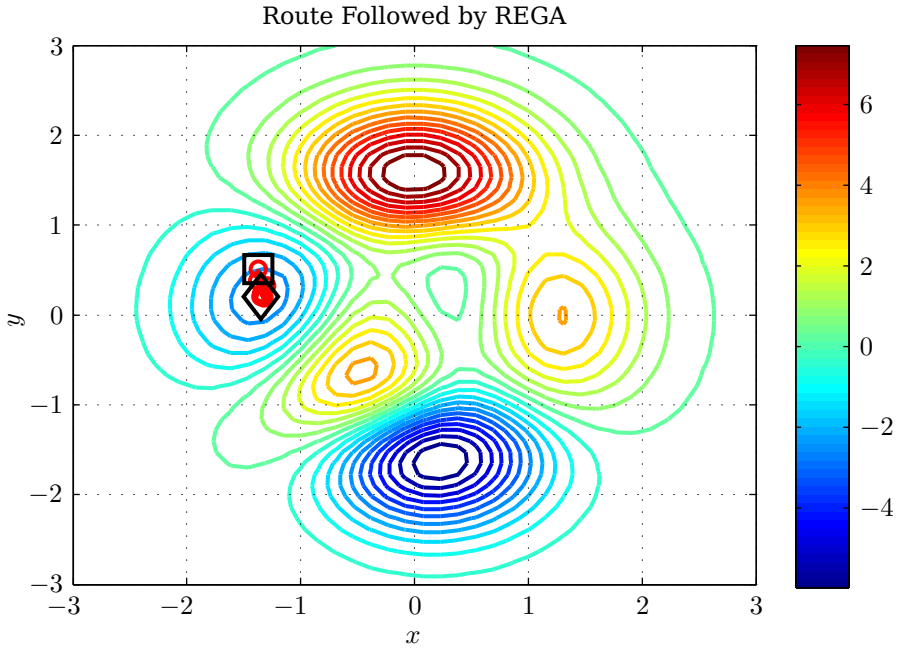


**Figure 4.14** – A local minimum result with the REGA.

It is not *impossible* for the REGA to converge on a *local* minimum, though it is much less likely than for the SQP, and is usually accompanied by a poor choice of optimisation parameters, such as a very small mutation value, $P_M < 0{,}1$, or a very large elitism value, $P_E > 0{,}5$. An example of this is shown in Figure 4.14.

In this case the parameters are

$$\begin{aligned} k_{\max} &= 300 & P_s &= 20 \\ P_E &= 0{,}2 & P_C &= 0{,}2 \\ P_P &= 0{,}45 & \beta_{P_P} &= 0{,}05 \\ P_M &= 0{,}15 & & \\ n_e &= 5 & \beta_{n_e} &= 0{,}0001 \end{aligned}$$

and it required $50$ generations to converge to the local minimum.

Another interesting result is shown in Figure 4.15. In this case the parameters are

$$\begin{aligned} k_{\max} &= 300 & P_s &= 20 \\ P_E &= 0{,}2 & P_C &= 0{,}2 \\ P_P &= 0{,}4 & \beta_{P_P} &= 0{,}05 \\ P_M &= 0{,}2 & & \\ n_e &= 5 & \beta_{n_e} &= 0{,}0001 \end{aligned}$$

and it required $20$ generations to converge to the global minimum. Here it can be seen how *mutation* resulted in a chromosome of higher fitness being selected close to the local minimum, before the optimisation returned to the global minimum region. This shows how mutation can also potentially lead to negative results if, by chance, another mutation did not cause the optimisation to return to the global minimum region.

After experimenting with the REGA, a few remarks regarding the parameters listed in Table 4.5 can be made.

- The population size can affect the rate of convergence. A population that is too large results in very time-consuming operations (though this can be alleviated through the use of distributed processing; see §4.6) where many chromosomes are required to be evaluated. This could result in fewer generations being required to converge, but will not necessarily require fewer function calls or processing hours. Likewise, a population size that is too small will result in insufficient chromosomes to apply

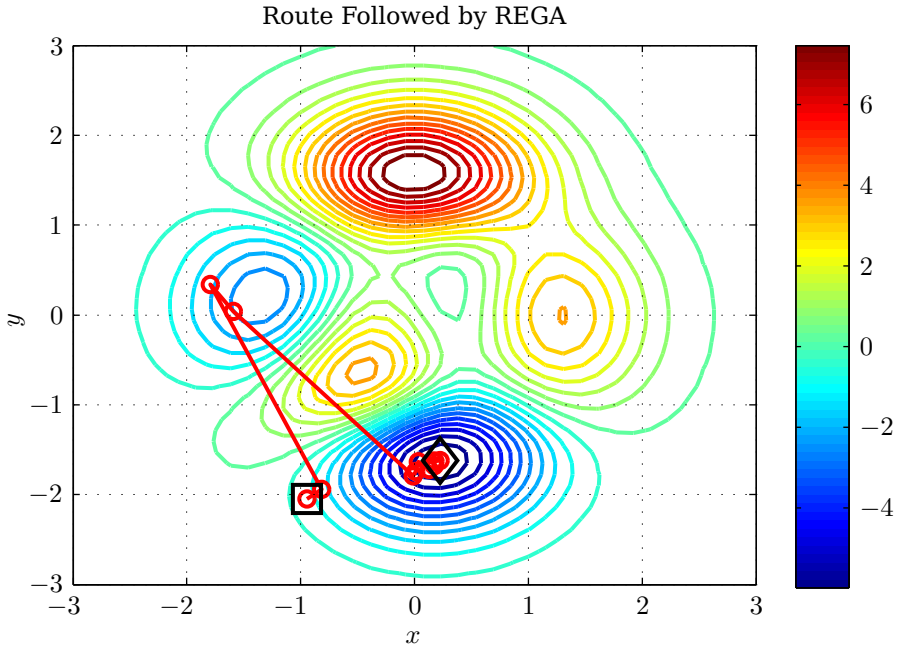


**Figure 4.15** – The effect of mutation during the optimisation.

all the genetic algorithm operators to, resulting in more generations being required to converge, if convergence occurs.

- The number of chromosomes passed through using elitism should not be too large, not more than about $20\,\%$ of the population size. Elitism does not change the chromosomes of the population in any way, and can lead to stagnation, and convergence on local minima. It is possible to pass only the most fit individual through, though this tends to have a negative effect on the perturbation operator, which is exercised on the most fit individuals in the generation.
- The value of the crossover-operator percentage should also not be too large, since, for the REGA, design variables within the design vector are swapped, but no new information is incorporated. Only existing design information is transferred amongst individuals.
- The perturbation mutation operation was found to be a fairly important operator, and thus was typically assigned a fairly high percentage of the next generation. The reasoning behind this can be seen from the clustering nature during evolution. Clusters tend to form around the minima, but none of the chromosomes within the cluster may lie *on* the minimum. By perturbing a sufficient number of these individuals the likelihood of moving closer to the minimum is much larger, which is why the perturbation should be performed on the fittest percentage of the generation.
- Selecting the value of the perturbation deviation variable is also important. This value adjusts the perturbed variable by a particular percentage. Making the value too large could result in the chromosome being perturbed too far from the minimum to be useful. Making the variable too small results in convergence being very slow since the amount by which the variable is perturbed is too small to make a notable change in the fitness.
- The mutation parameter cannot be ignored since it provided entirely new information to the next generation. Making this parameter too small leads to greater chances of converging on a local minimum since the region around the global minimum never gets explored. Making this parameter too large results in very slow convergence since too much new information is introduced and not enough of the new chromosomes are selected by the other operators to result in a suitable convergence rate, and this results in a potential loss of valuable information that may already be in the population.

### 4.5.3 Comparison of Results

Now that both the SQP and REGA have been used for examples, it is possible to highlight some of the advantages and disadvantages of each.

When considering run-time (in terms of the number of generations or iterations) required, it can be seen that the SQP is considerably faster. This has the drawback of requiring the gradient information of the function being optimised, which is not always available. It is possible to work around this problem by using gradient approximation techniques such as finite difference techniques.[2]

It is also possible for the SQP to result in an unbounded answer where this should not be the case. This comes about as a result of numerical inaccuracies due to discretisation and the floating point number representation used by computers. This occurs especially when steps within the simplex method multiply and divide very large and very small numbers with each other.

The population-based REGA has the advantage of being better at converging on the global minimum if one exists, and are typically easier to parallelise than the gradient based methods. They also have the advantage of dealing with problems where the objective function does not have a gradient, such as for discrete variables, and in cases where there are discontinuities in the objective function.

The REGA is also much less susceptible to numerical inaccuracies since complex mathematics are not required as with the SQP.

In both cases the designer is also required to understand the meanings of the various optimisation parameters in relation to the physical design in order to make effective decisions regarding the values of these parameters.

## 4.6 Distributed Processing

Optimisation for engineering design problems often make use of external programs in order to assess the performance of a specific design. For example, flow solvers such as FLUENT are used to evaluate aerofoil designs as well as other computational fluid dynamics (CFD) software. These software packages often have fairly long execution times, which result in the optimisation process taking very long.

As a means to alleviate this problem, the concept of *parallel processing* can be used. To be able to use parallel processing, the problem being solved needs to divisible into a collection of jobs which can be performed simultaneously. The terminology used is as follows: a *task* is the overall problem being solved (say the optimisation) whereas *jobs* are the individual sub-components of the task that can be performed in parallel.

While the SQP optimisation method is not directly capable of being parallelised, the real-encoded genetic algorithm has good parallelisation potential. This can be seen in Step 2 of §4.4.5 where the fitness calculations are performed. In this case none of the chromosomes in the current generation require other information in order to have their fitness calculated. This means that all the chromosomes' fitnesses can be calculated simultaneously.

Since it is this fitness calculation that is typically the most time-consuming part of the optimisation, this provides great time savings during the optimisation process. This can be reasoned as follows: Assume that each fitness calculation takes $x$ seconds to complete. In the current implementation the total time required to evaluate all the chromosomes in the population is $(P_s \times x)$ seconds. If they are calculated in parallel, this reduces simply to $x$ seconds, regardless of the population size. Even if it takes a differing amount of time to calculate each chromosome's fitness, the total fitness calculation time is reduced to the time taken for the slowest fitness calculation, which will always be less than the summation of each individual calculation.

In order to achieve this, a distributed processing framework was developed. The structure consists of a server to coordinate all the tasks, a number of clients which can perform jobs and finally the task executor itself. This is shown graphically in Figure 4.16. This figure also shows the basic work-flow between the individual components in a numbered sequence as described below:

1. Create task and connect to the server.
2. Task requests that a specific job be performed.
3. The server accepts the job and assigns it to a client waiting for a job in the client pool if one is available. If a client is not available, the task must wait until one becomes available.
4. The job is dispatched to the client.

[2]Thanks go to Dr BA Broughton for his inputs in this section.

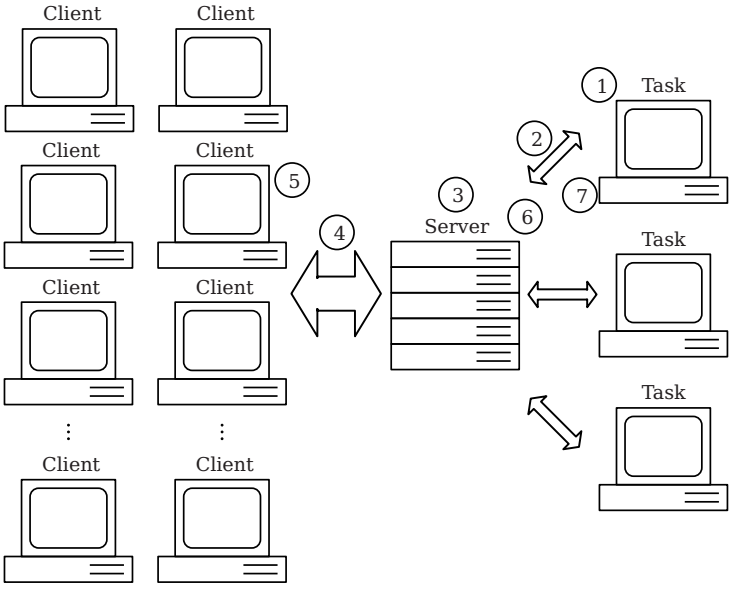


**Figure 4.16** – Distributed processing system structure flow diagram.

5. The client executes the job and collects the results which are sent back to the server, where they are stored until needed.
6. The task now requests the results of individual tasks and the server sends the results to the task.
7. Task continues with its remaining computations using the results obtained from the server (and hence the individual clients).

While the principle is fairly general, this specific implementation was developed with the goal of executing MATLAB code on the clients. It can be generalised to execute any type of external software. The basic infrastructure consists of a number of programs and components, which will be discussed in the paragraphs that follow. The overall system consists of a number of client computers, each running the client software, a server computer to manage the tasks, as well as the task computer (which can be the same computer as the server).

IP addresses are used to distinguish the various clients which are performing specific jobs. At any given time, each client is only capable of performing a single job. This is not very efficient since it does not directly allow multi-core systems to be utilised fully as, theoretically, a job could be scheduled on each core. For the case of this project this was not seen as a limitation since the client computers used were not the latest models available and had various other hardware limitations (specifically memory).

The server computer's primary goal is to manage the clients and tasks. It allows multiple tasks to be executed simultaneously, and allows any number of clients to be in the client pool. Since it is used to temporarily store the results of various jobs until the task can retrieve them, its primary requirement is large amounts of memory and virtual memory (swap space).

### 4.6.1 Some Networking Background

The distributed processing infrastructure makes use of network sockets through the *WinSock2* API (application programming interface). A socket is essentially a connection between two programs (which may or may not be running on the same computer). Two types of socket connections are used, namely UDP (user datagram protocol) and TCP (transmission control protocol), both over an IP (internet protocol) network.

With UDP, data packets are broadcast over the network without specifying a destination. Anyone listening on the correct port will be able to receive the data. This is convenient if the destination is unknown and allows the initiation of a more direct connection. There is also typically a limit on the amount of data that can be transmitted in one datagram, and there is no guarantee that packets sent via UDP will arrive in any specific order [58].

TCP requires a direct connection to the destination and thus the destination must be known. Once a socket has been opened to the destination data can be transmitted to and from the source and destinations

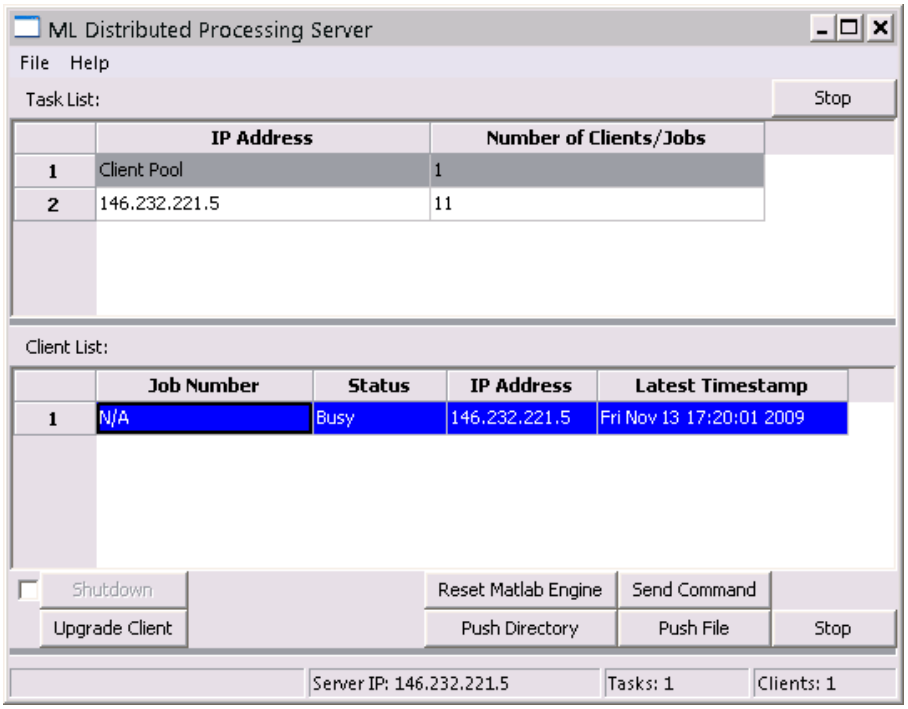


**Figure 4.17** – Screen capture of the server program.

easily since TCP "provides sequenced, reliable, two-way connection-based byte-streams" [58]. There is no specific limit on the amount of data that can be sent over the connection, though sending too much data results in bottlenecks, and a lack of responsiveness while the data is being sent.

### 4.6.2 The Server

The *server* is a single multi-threaded program that is used to establish and maintain connections with the clients. and to keep track of tasks that are currently executing. A screen capture is provided in Figure 4.17. The top portion of the display provides a listing of the tasks that are currently being executed, and the client pool. The client pool is a list of all clients currently connected to the server. Each task has an associated IP address, and the number of jobs (both complete and in progress), currently associated with the task is indicated.

The lower portion of the display lists the jobs currently active for the task currently selected, or provides a listing of the status of the clients in the client pool, if it is selected. If a task is selected the job identifier of each of the jobs is displayed as well as its status (busy, done, etc.) and the IP address of the client that performed, or is performing the job.

The main program flow of the server is provided in Figure 4.18 and is now briefly described. During startup the server sets up its networking and opens a UDP port on which to listen for clients. Clients that are not yet connected to a server periodically send out a packet identifying themselves. These packets are analysed by the server before establishing a connection to the client over a TCP socket. The client is then added to the client pool and a separate thread is created to monitor the client and handle client communications.

Also over UDP the server listens for packets from potential task machines. Once a task has been found that is requesting clients, a connection is also established over TCP and a thread is created to manage the task communication.

Each of the threads is required to facilitate communication between the server and the client or task. Multiple threads are used to prevent the server from not servicing each of the clients or tasks in a timely manner. The server acts a mediator between the tasks which provide jobs and the clients which execute them. A task will request that a job be completed and send the required parameters as a data packet to the server. The server then examines the list of clients in the client pool and attempts to find a client that is not currently busy. If one can be found the client is marked as busy and the necessary parameters are sent to the client which then proceeds to execute the task. The job and associated client information is then added to the task's information list.

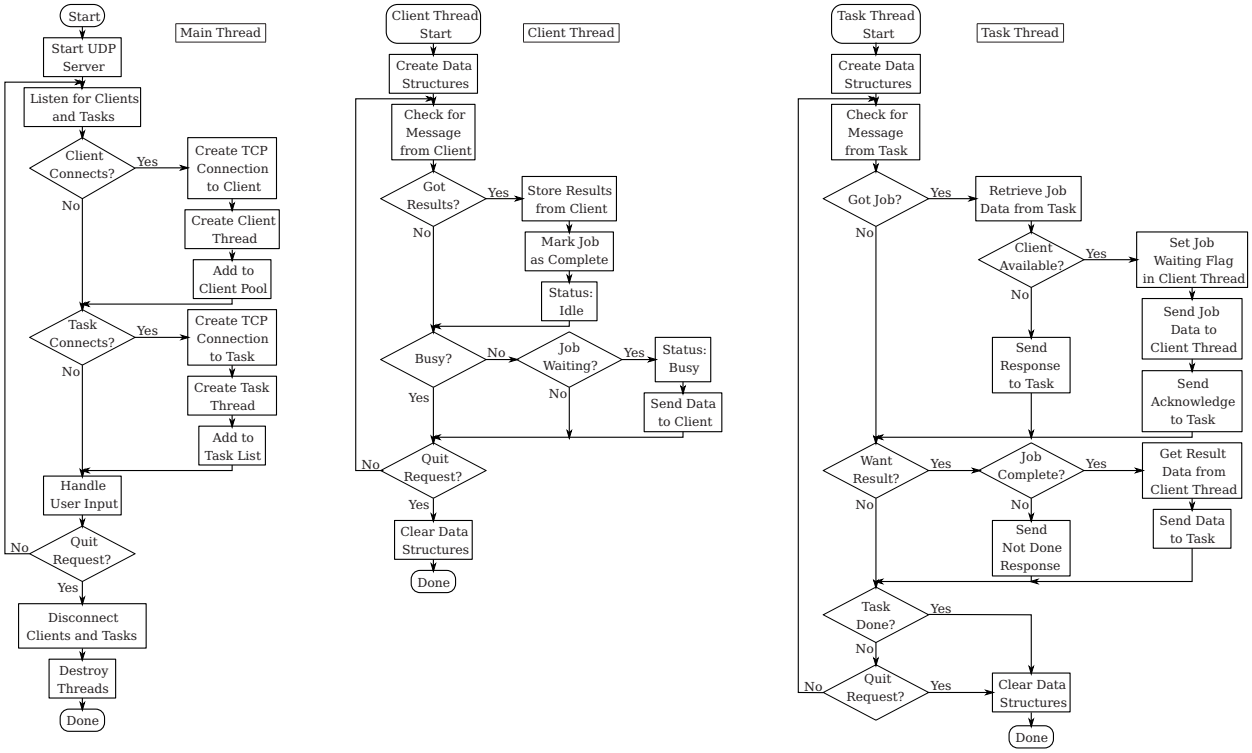


**Figure 4.18** – Basic server program flow diagrams, including the main thread as well as the client and task threads.

Once the job has been completed by the client, the client will send the results to the server. The server then stores the results internally until the task can request the specific job's results. Once the job's results have been sent back to the task, they are erased from memory. A design decision was made not to store the data on the hard-drive since access time became to great. The negative side affect is much greater memory (RAM) usage.

As jobs are completed, clients are marked as idle and become available for further jobs from the same or other tasks. As tasks are completed they are removed from the task list and the socket connection is terminated. The server also provides functionality to send files and folders to a selection of clients in the client pool. Basic commands can also be sent via the server interface, which allows as little interaction with the client as possible since all necessary files can be transferred remotely from the server. It is also possible to upgrade the client program remotely if bugs are found and repaired.

### 4.6.3 The Client

The *client* program is a single-threaded program with relatively little direct functionality. This specific implementation is used to execute jobs in the form of MATLAB scripts. The program flow is provided in Figure 4.19.

The basic operation is as follows: On start-up, the client creates a new MATLAB engine session, which will be used to execute the scripts provided by the server. It also initially creates a UDP socket over which it broadcasts an identifier packet until a server creates a TCP connection to the client. Once the TCP connection has been established, the UDP socket is closed and the client goes to an idle state where it waits for jobs from the server.

Jobs arrive in the form a compressed MATLAB workspace file. This file contains all the necessary parameters to execute the job on the client. If external files are required, it is necessary for the server to upload these files before the job can be executed. The workspace file contains the following parameters:

| | |
|---|---|
| `job_ID` | The job's unique identifier. |
| `main_func` | The function to call to execute the job. |
| `params` | The MATLAB cell array of parameters to pass to the main function. |

A MATLAB helper script is executed by the client (`dp_Execute.m`) which loads the workspace file and restores all the function handles stored in the parameter list before calling the main job function. Once

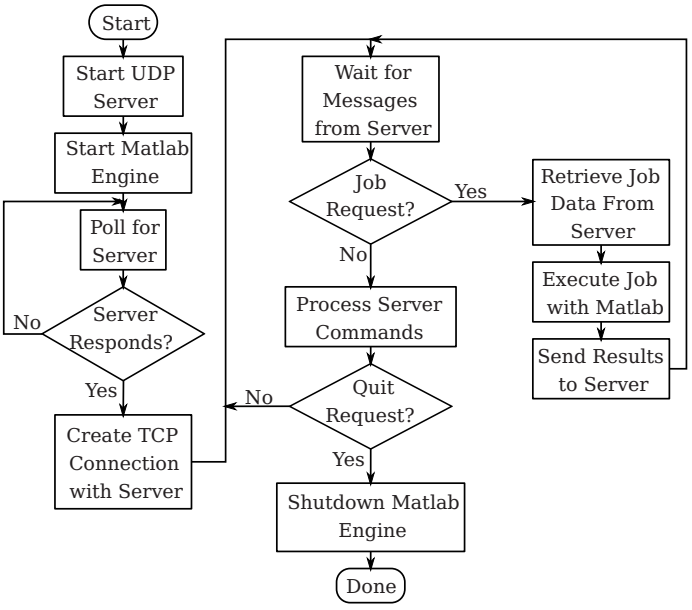


**Figure 4.19** – Client program flow diagram.

the job has been completed the script creates a second workspace file which contains the results of the job function. In order to function correctly it is necessary that the job function return a single MATLAB structure which contains all the required data. It is this structure which is stored in the results workspace file along with the job identifier.

Once the MATLAB session has ended, the file is transferred to the server and deleted locally along with the parameter file. The client now becomes available to receive more jobs.

If at any time connection to the server is lost, the client will revert to its initial state where it broadcasts UDP packets until a server connects again.

### 4.6.4 The Task

The *task* component of the distributed processing does not have a specific program which is called. Typically a program is busy executing (in this case MATLAB) normally up to point where is requires to perform multiple jobs. The typical program flow for the process followed from this point is given in Figure 4.20. There is no fixed structure defined since the distribution code needs to be integrated into the task code, though the order of execution is important. To assist in this, a number of functions have been created that are dynamically linked to the main program.

In the case of MATLAB a number of binary MEX (MATLAB executable) files are used to provide the extensions necessary to facilitate the distributed processing system. MEX files are pre-compiled "dynamically linked subroutines that the MATLAB interpreter loads and executes" [59]. The various MEX files and MATLAB helper scripts are listed below with their purposes:

| | | |
|---|---|---|
| `dp_CreateJob` | script | Used to create a job from a function handle and parameter list to be sent to the server for execution on a client. |
| `dp_Dispatch` | MEX file | Called by `dp_CreateJob` to dispatch the job to the server. |
| `dp_GetJobResult` | MEX file | Called by `dp_GetResult`. Requests the results from server for a specific job if they are available. |
| `dp_GetResult` | script | Retrieves the results for the provided job. Wraps `dp_getJobResult` in order to perform error checking. If a job failed for some reason it is re-dispatched at most three times before an irrecoverable error is returned. |
| `dp_Init` | MEX file | Initialises WinSock2 and establishes a connection to the server. This returns the ip and socket number of the server which are used as parameters for the other scripts. |

| | | |
|---|---|---|
| `dp_Shutdown` | MEX file | Closes the connection to the server cleanly, indicating that a task has been completed successfully. This is required since even if an error occurs, MATLAB will not close the connection to the server until it exits or this function is called with the appropriate parameters. |

From the above list one can derive the necessary steps required during the task execution. Typically the portion of the code that is parallelisable is implemented in some sort of loop structure (`for`, `while`, `do-while`, etc.) where the code would have been executed successively. The structure will not change much except that now there will be two loops – the first to dispatch the jobs, and the second to retrieve the results and process them as normal. A simple example of the type of code that can be converted is given in Appendix B.

### 4.6.5 Adapting the REGA for Distributed Processing

The example described in Appendix B indicates the ease with which existing code can be modified to make use of the distributed processing framework. The pre-requisite is that the code must be parallelisable. As described in the first part of §4.6, the loop in the genetic algorithm which determines the fitness values can be parallelised.

In general, connection to the server should be done before the algorithm is started (during the initialisation stage), and the disconnection once the algorithm is complete. The loop (in Step 2 of the algorithm) where the fitness is calculated is replaced with two loops (as in the example) where the first is used to dispatch the jobs and the second is used to retrieve the results. As mentioned in §4.4.5, only the fitness of chromosomes which do not violate constraints are determined. This needs to be taken into account in *both* the loops.

## 4.7 Summary

This chapter considers several optimisation-related topics. The concept of optimisation is introduced along with various definitions and notations relating to optimisation in general, such as the concepts of feasible design spaces, equality and inequality constraints, global versus local minima and Pareto optimality. The necessary conditions for optimality in the form of the Karush-Kuhn-Tucker conditions are also described as an extension of the Lagrange Multiplier theorem for constrained optimisation problems.

The concepts of multi-objective and multi-point optimisations are discussed before describing in detail the two optimisation techniques that will be used in Chapter 5, namely the sequential quadratic programming algorithm and the real-encoded genetic algorithm. A comparison between the techniques is also provided along with the implementations and explanations relating to each with examples to indicate their operation.

The final topic of this chapter is a discussion on distributed processing and how it can be used by the REGA to increase efficiency.

The optimisation techniques described in this chapter are general enough to be applied to any number of problems, and having now developed the necessary tools to perform the optimisations, Chapter 5 makes use of these tools by applying them to the problem of reducing the aileron hinge moments.

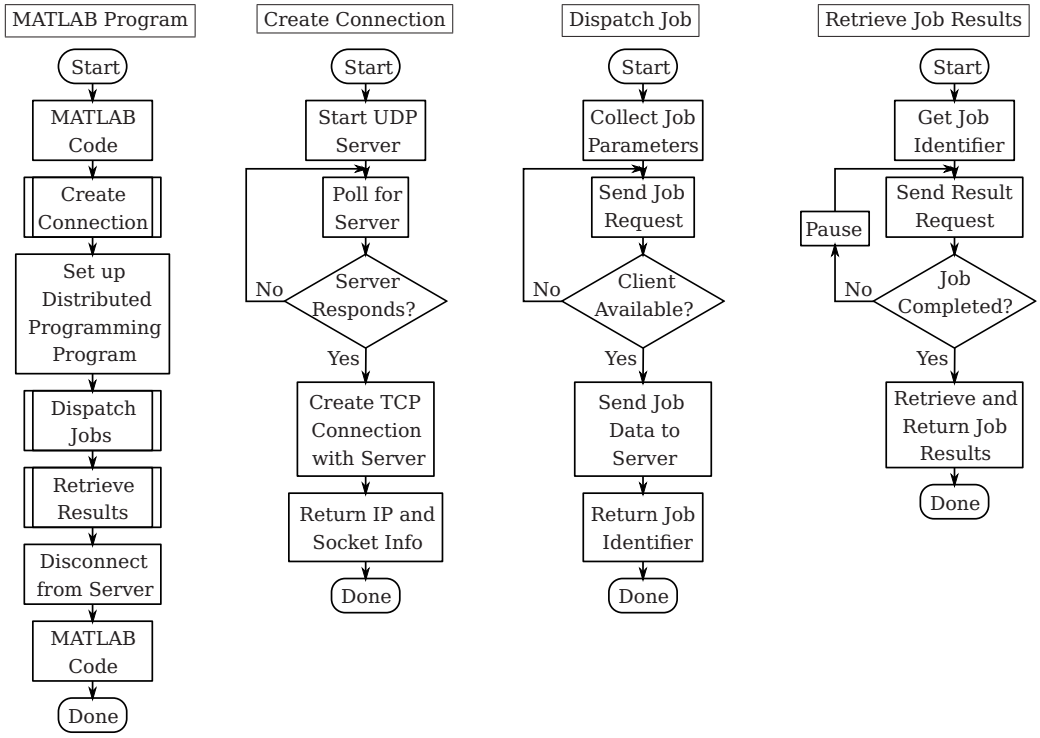


**Figure 4.20** – Task program flow diagrams.

# Chapter 5

# Optimisation – Application and Results

## 5.1 Introduction

In Chapter 4 the concept of optimisation is introduced and discussed. Two optimisation methods are described, viz. the *sequential quadratic programming* algorithm and the *real-encoded genetic algorithm*. The SQP method makes use of gradient information in order to function, while for the REGA gradient information is unnecessary. The reason for developing these two methods will become apparent in this chapter.

The goal of the project is to reduce the aileron actuator size, and the proposed use of a trailing-edge tab resulted in the need to determine the optimum dimensions of the tab. As discussed in §3.8, it is also necessary to determine the optimal tab deflections. These two optimisations lead to the dual-layered optimisation concept. All of these optimisations are discussed in this chapter along with the results obtained by making use of the optimisations.

In order to reduce confusion, the concept of the *operating point* is defined in the context of the optimisation problems of this chapter. Since the aerodynamic equations that were developed in Chapter 3 are those for an infinitely spanned two-dimensional aerofoil, only the parameters that have an effect on the two-dimensional aerofoil are considered. The operating point thus consists of a point in the flight domain with a certain angle of attack and a certain (old) aileron deflection. These all refer to the currently used configuration of the aircraft, which consists of the wing and aileron only.

Since it is desired to make the substitution of the new system invisible to the pilot and currently used fly-by-wire system, an assumption is made at this stage in the development of the overall CoSICS project that only an aileron command signal will be delivered by the control system of the aircraft. This commanded aileron deflection then needs to be converted to a suitable (new) aileron and tab deflection to provide satisfactory performance, thus eliminating the need to modify the existing system directly. This fits in with the modular approach described in Chapter 1.

In short the operating point is defined by the angle of attack and the *old* aileron deflection, both of which have certain ranges over which the new configuration is required to be effective.

## 5.2 Physical Design Variables

In order to perform an optimisation, one of the first steps is to define the design variables. The most obvious variables are those related to the geometry of the aircraft and aerofoil.

As has been previously mentioned, it is desired to reduce the size of the aileron actuator, or eliminate it completely; thus it is necessary to examine the components that will affect the actuator's dimensions. In Chapter 3 equations were developed to determine the hinge moments of the aileron and tab surfaces, and, since it is these hinge moments that must be overcome by the actuator, it is appropriate to make use of the parameters that affect the hinge moments.

These parameters are physical dimensions relating to the construction of the aileron and these are shown in Figure 5.1

The figure shows a planar view of the right wing in the left half of Figure 5.1 and a cross-section in the right half. The parameters that can be varied are listed in Table 5.1.

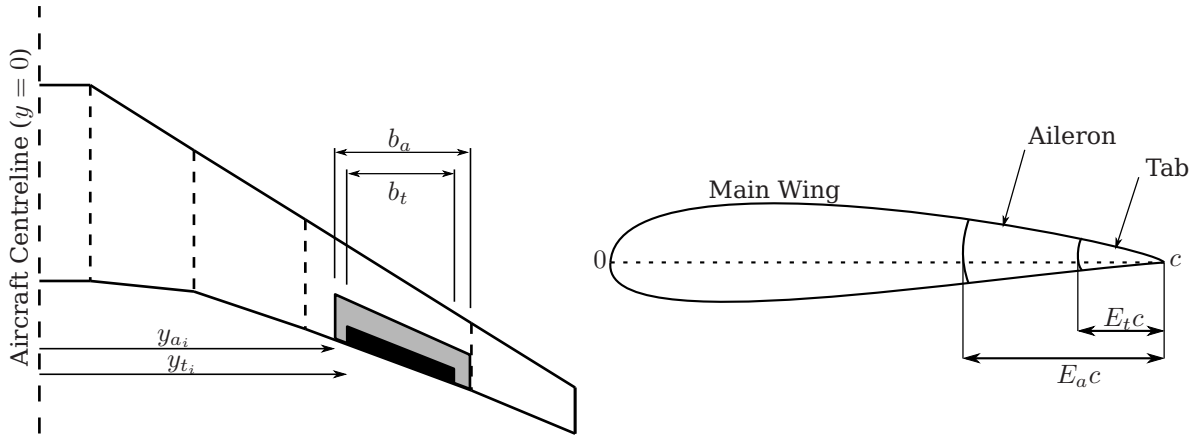


**Figure 5.1** – The physical design parameters that can be varied to affect the aileron hinge moment.

**Table 5.1** – The list of possible design variables.

| Variable | Description |
|---|---|
| $E_a$ | The fraction of the wing chord which is taken up by the aileron/tab combination. |
| $E_t$ | The fraction of the wing chord which is taken up by the tab. |
| $b_a$ | The aileron span. |
| $b_t$ | The tab span. |
| $y_{a_i}$ | The $y$-distance from the aircraft centreline to the inboard side of the aileron. |
| $y_{t_i}$ | The $y$-distance from the aircraft centreline to the inboard side of the tab. |

The variables listed in Table 5.1 assume that the other components of the wing geometry (wing span, shape, sweep-back angles, etc.) remain the same. For the initial optimisation the only design variable is the tab chord length, represented by $E_t$ (§5.7) in accordance with the "crawl-walk-run" approach mentioned previously.

The optimisation process is then be expanded to two design variables where both the tab *and* the aileron chord length, represented by $E_a$, are varied (§5.8). The final optimisation shown in this project also consists of two two design variables and will involve adjusting $E_t$ and $y_{a_i}$ with the added condition that $b_t = b_a$ (thus these parameters will also vary, but do not have a separate degree of freedom) and all other geometry is kept constant (§5.9). Thus three independent optimisations are performed: first $E_t$ only, then both $E_t$ and $E_a$, and finally $E_t$ and $y_{a_i}$.

For this initial study it is desired to lay the framework for the optimisation and provide preliminary observations regarding the effectiveness of using servo tabs; thus only a small subset of the many possible parameters has been used. Other parameters which can be varied include the shape of the wing (both planar and cross-sectional) as well as the shapes of the ailerons and tabs, to name a few.

## 5.3 Dual-Layer Optimisation

Any optimisation requires an objective function which is evaluated for some value of the design vector. Depending on the type of optimisation being performed, this objective function may need to adhere to certain properties, for example, gradient based optimisation techniques (such as SQP) require that the cost function be differentiable (and maybe even twice differentiable). Methods that do not make use derivative information (simulated annealing, genetic algorithms, etc.) can however make use of objective functions that are not merely a mathematical formula.

This allows the calling of external programs in order to evaluate a design vector, such as is done in the aerofoil shape optimisations discussed in Song and Keane [60], Peigin and Epstein [61], Huyse and Padula [45], Nemec, et al [42] and Zingg and Elias [43], where external CFD programs (such as FLUENT and FUN2D) are used to determine drag and lift coefficients which are used in the cost function, usually by solving the Navier-Stokes equations.

This project takes this process one step further by making use of a cost function that is itself an optimisation, resulting in a so-called dual layer optimisation. If a design vector is evaluated during the main (or

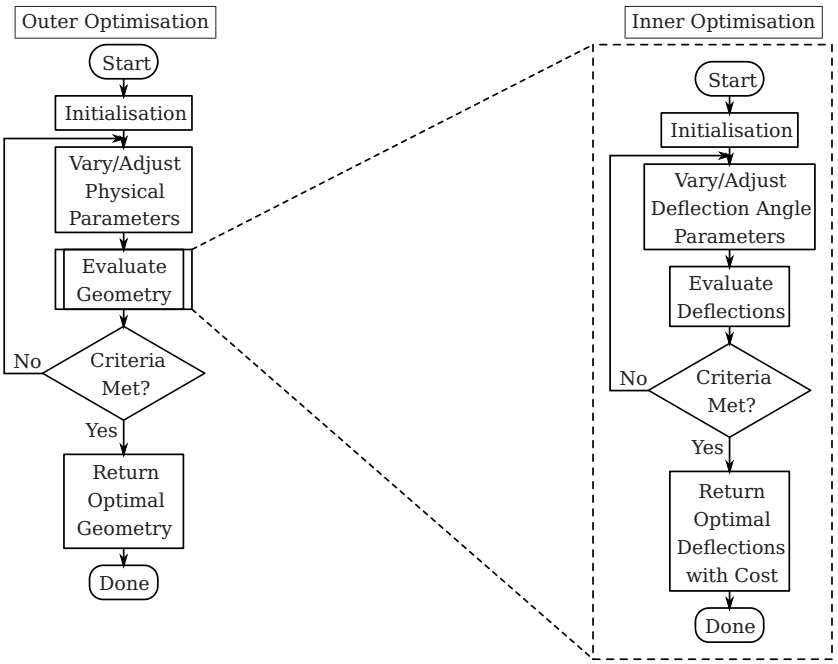


**Figure 5.2** – The main optimisation program flow (left) with the inner optimisation bordered by the dotted line shown on the right. The outer optimisation varies the physical geometry while the inner optimisation determines the optimal deflection angles for an operating point given the current geometry.

outer) optimisation process, a secondary (or inner) optimisation is used to determine the cost associated with this vector. Naturally it is necessary for the inner optimisation to deliver the same result (or at least within some tolerance) each time it is evaluated for a specific design vector.

It should be noted that the inner optimisation may also make use of external programs for evaluation of their cost functions, or even make use of yet another optimisation, and so on. The major drawback of this process is the processing time increases drastically for each additional layer of optimisation.

This optimisation process is shown as a flow diagram in Figure 5.2.

The physical parameters that can be varied were discussed in §5.2; however, as was noted in §3.8, there is also the consideration of both the new aileron deflection angle and the tab deflection angle which need to be calculated. The dual-layer approach discussed thus far is thus applied in such a way that the main optimisation is used to determine the physical geometric parameters, while the inner optimisation is used to determine the tab and aileron deflections for a given operating point.

## 5.4 Multiple Operating Points

The discussion of §4.2.1 regarding multi-point optimisations is now justified. Since the optimisation pertains to aircraft control surfaces, it is logical to assume that any design used needs to be suitable under a variety of operating conditions. As such it is necessary for the optimisation to take these operating points into account.

The description of an operating point in the context of this project is provided in §5.1 as the situation where the angle of attack and the old aileron deflection is held constant. Since an aircraft is expected to function under a range of angles of attack, and be able to deflect the ailerons over a range of deflections, it is possible to set up a two-dimensional range of parameters where each of the possible combinations is discussed.

The angle of attack range is determined by examining the *aerofoil performance characteristics* given by Moran [16], specifically the sectional lift coefficient versus angle of attack graphs provided therein. Most of the aerofoils described there, and especially the NACA 23012 used for the purposes of this project, have a linear relationship from about $-8^\circ$ to approximately $14^\circ$ when considering the aerofoil alone. As such this range was chosen as the angle of attack operating range.

The original documentation provided by Airbus for the project indicated that the maximum deflections for the A320 are $\pm 21^\circ$ [62]. While this range is deemed outside the validity region for the thin aerofoil theory, it does defines the operating range for the old aileron deflection, and is used as is for this initial study.

A discrete grid is now established where points are chosen across both ranges as the operating points at which to perform the multi-point optimisation. This grid need not be uniform, though it is recommended that, where possible, the form of the overall cost function be used to select suitable points. For the purpose of this project a uniform grid was chosen as it was deemed the easiest means to obtain satisfactory results over the entire operating point range.

The weighted sum method of §4.2.2.2 is used to assign specific weightings to the various operating points and combine all the individual points into a single objective function. This initial study assumes that all points are equally important in the operating range; thus all the weightings were given a value of $1$. It may be useful to consider typical mission profiles to examine the most-used ranges of the parameters. For example, if it is seen that aileron used follows a standard deviation of $5^\circ$ about $0^\circ$ for a typical mission profile the weightings can be assigned such a way that those operating points are favoured rather than those which hardly ever occur.

It *is* important to note, however, that in order to be certified for flight, aircraft typically have a series of *sizing manoeuvres* that must be satisfactorily performed. If the weightings are chosen such that excellent performance is delivered in, say, the cruise region, but the design renders the aircraft unable to perform in an emergency manoeuvre, certification will not be given. This is another reason why the initial weightings were chosen to be equal.

Sizing manoeuvres are discussed further in Chapter 6.

## 5.5 Optimal Tab and Aileron Deflection: A Gradient Based Two-Dimensional Optimisation

As stated in the heading, the optimisation discussed in this section is used to determine the optimal tab and aileron deflection, using a gradient-based approach. This optimisation is one of the potential inner optimisations. As described in §3.8 new aileron/tab deflections need to be calculated in order to deliver as close to the original response for a specific old aileron deflection.

To re-iterate: the pilot (or autopilot) gives a roll command (in the form of a commanded roll rate) which must induce a rolling moment. This command is then converted by the Elevator and Aileron Computers (ELACs) into a commanded aileron deflection. Since we are replacing the aileron with the new aileron-tab configuration, this old aileron deflection must now be converted into a new aileron deflection, as well as, a tab deflection.

For each operating point (and for a given set of geometry) it now desired to determine the best new aileron and tab deflections in order to minimise some objective function. In other words, given an angle of attack, $\alpha$, and an old aileron deflection, $\delta_{a_o}$, for some aileron chord length, $E_a$, and tab chord length, $E_t$; we now need a new aileron deflection angle, $\delta_{a_n}$, and a tab deflection angle, $\delta_t$, such that some (as of yet undefined) objective function is minimised.

The objective function mentioned above is a *multi-objective function* which consists of three sub-objectives. These sub-objectives are based on the logical reasoning given in §3.8. When considering aerofoil design the two key considerations are lift and drag, and most optimisations related to aerofoil shape design consider meeting some desired lift value while at the same time reducing the drag as much as possible. Since deflecting the control surfaces changes the effective camber of the aerofoil, it can also be considered a shape optimisation; thus the types of objectives which are to be obtained are similar.

### 5.5.1 Objective Function

The aim in this case is to keep the rolling moment the same between the old and new configurations for a specific angle of attack and old aileron deflection, and with the two-dimensional aerofoil theory used thus far the only way to examine the effect on the rolling moment is to consider the lift coefficient for the two-dimensional aerofoil. In this case we thus desire to minimise the *difference* between the old and new lift coefficients:

$$J_L = (C_{L_o} - C_{L_n})^2 \tag{5.5.1}$$

It is also desired to reduce the aileron hinge moments:

$$J_{H_a} = (C_{H_a})^2 \tag{5.5.2}$$

and finally we do not want a large tab actuator either, so we desire to minimise the tab hinge moment as well:

$$J_{H_t} = (C_{H_t})^2 \tag{5.5.3}$$

The three distinct objectives in Equations 5.5.1 to 5.5.3 are now combined into a single multi-objective function and the optimisation aims to *minimise*:

$$J_{\text{in}} = w_L(C_{L_o} - C_{L_n})^2 + w_{H_a}(C_{H_a})^2 + w_{H_t}(C_{H_t})^2 \tag{5.5.4}$$

where $w_L$, $w_{H_a}$ and $w_{H_t}$ are the weightings of each of the individual objectives relative to each other.

Typically the weightings are used to emphasise the various components of the objective function depending on how important it is to meet the desired goal. For this to work effectively it is necessary that the various sub-objectives provide costs on the same scale (order of magnitude) as the other components.

The method typically used by shape optimisation (Zingg and Elias [43], Zingg, et al [63]) where a specific value is to be achieved (as in Equation 5.5.1) is to rewrite the equation in the format

$$J_L = \left(1 - \frac{C_{L_n}}{C_{L_o}}\right)^2$$

but this is based on the assumption that $C_{L_o}$ is a *non-zero* constant. In the case of this project the value of $C_{L_o}$ is determined based on the current operating point, and it is possible for certain $(\alpha, \delta_{a_o})$ combinations to result in $C_{L_o} = 0$. In order to remedy this the format of Equation 5.5.1 was chosen.

This does have the negative side-effect that the orders of magnitude of the three objective functions are no longer the same, even though all are non-dimensional. The weightings were thus initially adjusted such that the weighed objective functions have the same order of magnitude. This was done primarily through a trial-and-error approach where several simulations were performed at extremities of the operating ranges and the averages were taken.

Once the normalised weightings are calculated it is necessary to decide on the relative weightings between the particular objective functions. Numerical values will be provided in the results part of this section (§5.5.3).

### 5.5.2 Constraints

The aim of this optimisation is to determine a new aileron and tab deflection angle. In order to achieve reasonable answers it is necessary to impose limits on the maximum and minimum deflections which are allowed by the new configuration.

The original system had an aileron deflection range of between $-21\,^\circ$ and $+21\,^\circ$. Based on the discussion in the aerodynamics chapter, specifically §3.8, it is already known that in maintaining these maximum deflections it is unlikely that satisfactory performance will be achieved. In order to reduce this problem the angle constraints have been relaxed to between $-30\,^\circ$ and $+30\,^\circ$ for the aileron and the same for the tab deflection. These limits need to be chosen carefully for a final design since they are determined by the actuation mechanism (hydraulic jack, SMA actuator, etc.).

In equation form the constraints used for the purpose of this optimisation are

$$\begin{array}{rcl} -\delta_{a_{\max}} \leq \delta_{a_n} \leq \delta_{a_{\max}} & \Rightarrow & -\delta_{a_n} - \delta_{a_{\max}} \leq 0 \quad \text{and} \quad \delta_{a_n} - \delta_{a_{\max}} \leq 0 \\ -\delta_{t_{\max}} \leq \delta_t \leq \delta_{t_{\max}} & \Rightarrow & -\delta_t - \delta_{t_{\max}} \leq 0 \quad \text{and} \quad \delta_t - \delta_{t_{\max}} \leq 0 \end{array} \tag{5.5.5}$$

where $\delta_{a_{\max}} = 30\,^\circ$ and $\delta_{t_{\max}} = 30\,^\circ$.

In standard form Equation 5.5.5 becomes

$$\begin{array}{rcl} g_1(\delta_{a_n}, \delta_t) & = & -\delta_{a_n} - \delta_{a_{\max}} \leq 0 \\ g_2(\delta_{a_n}, \delta_t) & = & \delta_{a_n} - \delta_{a_{\max}} \leq 0 \\ g_3(\delta_{a_n}, \delta_t) & = & -\delta_t - \delta_{t_{\max}} \leq 0 \\ g_4(\delta_{a_n}, \delta_t) & = & \delta_t - \delta_{t_{\max}} \leq 0 \end{array} \tag{5.5.6}$$

### 5.5.3 Results

It was found using parameter sweeps that the order of magnitude of the lift coefficient is about $1 \times 10^5$ times that of the aileron hinge moment coefficient for the old system.

It was then decided to choose the following weightings for the normalisation component of the multi-objective function:

$$w_{L_n} = 1 \times 10^{-5} \qquad w_{H_{a_n}} = 1 \qquad w_{H_{t_n}} = 1$$

to bring all the components into same range. The very small weighting on $C_L$ resulted in numerical problems during initial test runs of the simulation and this was remedied by making all the components ten times larger resulting in the normalisation weightings becoming

$$w_{L_n} = 1 \times 10^{-4} \qquad w_{H_{a_n}} = 10 \qquad w_{H_{t_n}} = 10 \tag{5.5.7}$$

Having now settled on the normalisation weightings provided in Equation 5.5.7, it is necessary to assign relative weightings where the importance of each objective is decided. There are no set ways of selecting these weightings, though some adaptive techniques have been developed (see Zing and Elias [43]) where the weightings are adjusted as the optimisation progresses. It was decided to make use of a systematic variation of the weightings until satisfactory performance was achieved for a reduced optimisation.

Since optimisation is an iterative process and the values of the weightings are difficult to determine a priori [33], some test weightings were chosen initially at this point; however, as the optimisation implementation progressed, it became clear that the initially chosen values were inappropriate. The results shown in this section thus make use of the weightings chosen using information that was not available at the time of the implementation of this section. The choice of the weightings simply listed and used here will be discussed in §5.7 when the tab length is optimised as well, and not just the angles.

The weightings used for the purposes of demonstrating the angle optimisations are:

$$w_L = 3 \times 10^{-4} \qquad w_{H_a} = 10 \qquad w_{H_t} = 10 \tag{5.5.8}$$

The optimisation technique used for the purposes of the optimisation is the *sequential quadratic programming method*, and thus relies on gradient information. Taking Equation 5.5.4 and substituting in the linearised equations for the coefficients gives

$$\begin{aligned} J_{\text{in}} &= w_L(C_{L_o} - C_{L_n})^2 + w_{H_a}(C_{H_a})^2 + w_{H_t}(C_{H_t})^2 \\ J_{\text{in}} &= w_L \left[C_{L_o} - (a_0 + a_1\alpha + a_2\delta_{a_n} + a_3\delta_t)\right]^2 \\ &\quad + w_{H_a} \left(b_{0_a} + b_{1_a}\alpha + b_{2_a}\delta_{a_n} + b_{3_a}\delta_t\right)^2 \\ &\quad + w_{H_t} \left(b_{0_t} + b_{1_t}\alpha + b_{2_t}\delta_{a_n} + b_{3_t}\delta_t\right)^2 \end{aligned}$$

and now the partial derivatives with respect to the design variables $\delta_{a_n}$ and $\delta_t$ need to be taken:

$$\begin{aligned} \frac{\partial J_{\text{in}}}{\partial \delta_{a_n}} &= 2w_L \left[C_{L_o} - (a_0 + a_1\alpha + a_2\delta_{a_n} + a_3\delta_t)\right][-a_2] \\ &\quad + 2w_{H_a} \left(b_{0_a} + b_{1_a}\alpha + b_{2_a}\delta_{a_n} + b_{3_a}\delta_t\right)(b_{2_a}) \\ &\quad + 2w_{H_t} \left(b_{0_t} + b_{1_t}\alpha + b_{2_t}\delta_{a_n} + b_{3_t}\delta_t\right)(b_{2_t}) \\ \frac{\partial J_{\text{in}}}{\partial \delta_t} &= 2w_L \left[C_{L_o} - (a_0 + a_1\alpha + a_2\delta_{a_n} + a_3\delta_t)\right][-a_3] \\ &\quad + 2w_{H_a} \left(b_{0_a} + b_{1_a}\alpha + b_{2_a}\delta_{a_n} + b_{3_a}\delta_t\right)(b_{3_a}) \\ &\quad + 2w_{H_t} \left(b_{0_t} + b_{1_t}\alpha + b_{2_t}\delta_{a_n} + b_{3_t}\delta_t\right)(b_{3_t}) \end{aligned}$$

The partial derivatives of the constraints are also taken and provided below:

$$\begin{aligned} \frac{\partial g_1}{\partial \delta_{a_n}} &= -1 & \frac{\partial g_1}{\partial \delta_t} &= 0 \\ \frac{\partial g_2}{\partial \delta_{a_n}} &= 1 & \frac{\partial g_2}{\partial \delta_t} &= 0 \\ \frac{\partial g_3}{\partial \delta_{a_n}} &= 0 & \frac{\partial g_3}{\partial \delta_t} &= -1 \\ \frac{\partial g_4}{\partial \delta_{a_n}} &= 0 & \frac{\partial g_4}{\partial \delta_t} &= 1 \end{aligned}$$

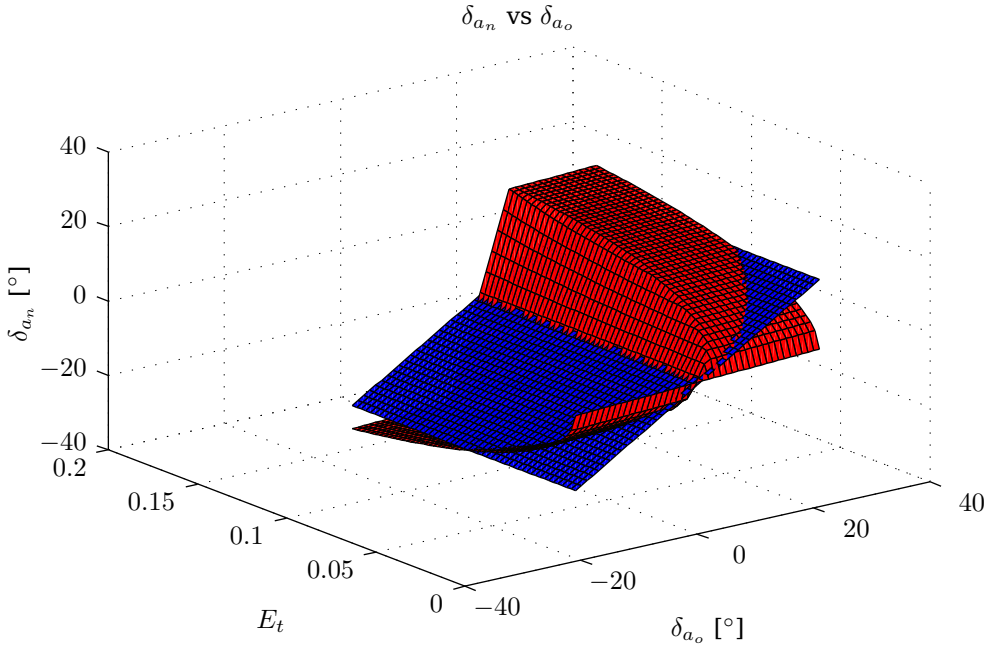


**Figure 5.3** – New aileron deflection angles.

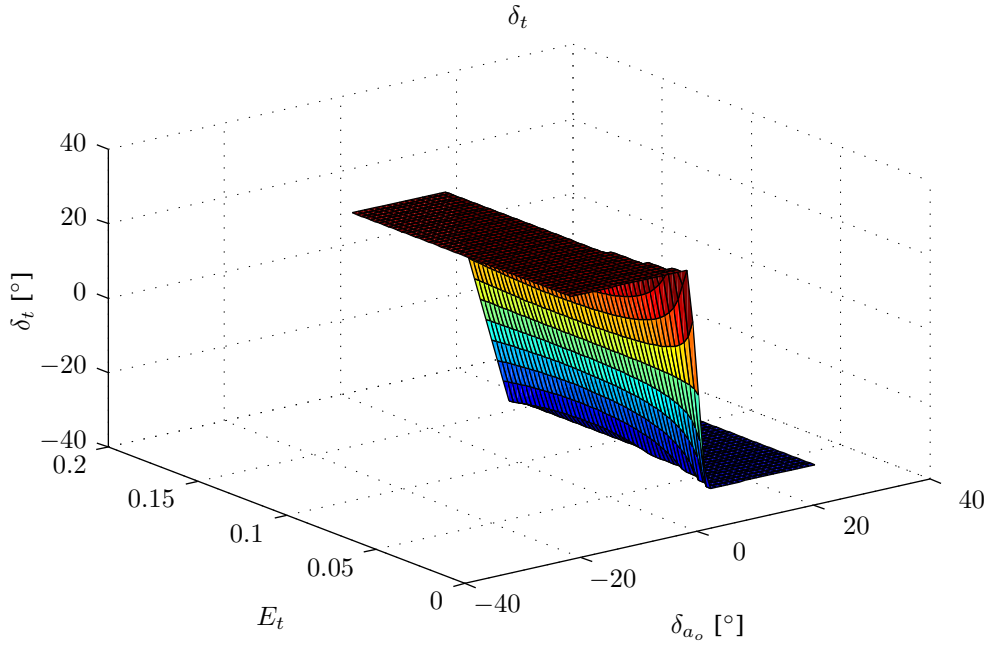


**Figure 5.4** – Tab deflection angles.

These derivatives and those of the cost function are used within the SQP method for the purposes of this optimisation.

The test case for which results are provided is defined by the weighting parameters discussed previously and a specific a specific angle of attack was chosen, in this case $3\,^\circ$. The aileron chord length as $E_a = 0{,}25$. The tab length was swept over the range $0 \leq E_t \leq \frac{1}{2}E_a$ and the operating old aileron deflection $-25\,^\circ \leq \delta_{a_o} \leq 25\,^\circ$.

The results of the optimisation are shown in Figures 5.3 to 5.11, which show the optimal angles, the cost function and how the coefficients are affected. As can be seen in Figure 5.3, Figure 5.7 and Figure 5.9, which compare old (wing-aileron) vales with the new, optimal (wing-aileron-tab) values, there is clearly a difference, indicating that the addition of the tab is capable of influencing these coefficients. On closer inspection, Figure 5.3 shows the new aileron deflection versus the old. It can be seen in this case that for smaller tab lengths at large $\delta_{a_o}$ deflections, the magnitude of $\delta_{a_n}$ is smaller than that of the original $\delta_{a_o}$. At

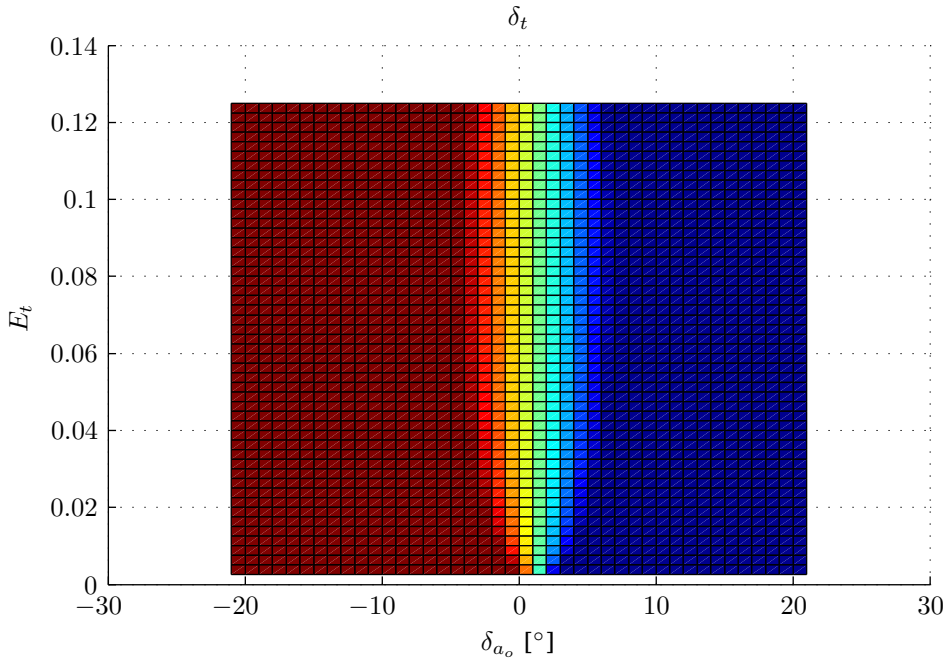


**Figure 5.5** – Tab deflection surface top view. Maroon indicates maximum deflection of $30\,^\circ$ and the dark blue minimum deflection of $-30\,^\circ$. The gradient region indicates values between these two extremes.

larger tab lengths this is no longer the case. Since the tab is now taking up an appreciable fraction of the aileron, the aileron is required to deflect further to achieve the same result (lift).

Examining the tab deflection shown in Figure 5.4, one can see that for the most part the tab is at either of the two tab deflection limits, indicating that in these regions the tab is incapable of resulting in a zero hinge moment and same lift condition. A small region centred about $\delta_{a_o} = 1\,^\circ$ shows differing behaviour. This region is shown from a different perspective in Figure 5.5 one can clearly see a gradient that is centred about $\delta_{a_o} = 1\,^\circ$. This region indicates where both the lift and aileron hinge moment objectives have been achieved. For simplicity this region will be called the *achievement region*.

It may be noted that in Figures 5.4 and 5.5 values for $E_t = 0$ are not shown. For this case where there is no tab it is not possible to have a tab deflection angle. Since the optimisation assumes there is a tab, this results in anomalous results in the form of a series of random, non-zero values of tab deflection for the cases where $E_t = 0$. This anomaly has no effect on the final result since the zero tab length cancels out all these side-effects mathematically, and has been omitted from the graphs in the interest of clarity.

Figure 5.6 shows the cost function and Figures 5.7 to 5.11 show the various coefficients being examined for the purpose of the optimisation. As one can see, the cost function (Figure 5.6) is parabolic for any particular value of $E_t$, except where the graph flattens to the minimum value of zero. This region of zero cost as $E_t$ increases from zero grows from a single point (at $E_t = 0$) to its widest (at $E_t \approx 0.08$) before shrinking again. This can be more easily seen in Figure 5.5.

The effect on the lift coefficient is shown in Figure 5.7, and while it can be seen that the value of the lift coefficient is *not* the same over the entire range, there is a region where old and new lift coefficients are similar.

A “front” view of Figure 5.7 is given in Figure 5.8. In this case it is easy to see the achievement region. The single diagonal line is the old aileron deflection angle, and the achievement region can be found where it intersects with the red surface (new aileron deflection). In this case the values of the old and new lift coefficients are the same, and Equation 5.5.1 is zero.

Similarly, when examining the aileron hinge moment coefficient, as shown in Figure 5.9, and the projection down the $E_t$ axis in Figure 5.10, it is also possible to see the achievement region. Again it is not very clear, but one can see that while the aileron hinge moment coefficient is not precisely zero, its magnitude is substantially smaller than that of the original (shown in blue in Figure 5.9 and the diagonal line in Figure 5.10). The achievement region can be seen more clearly in Figure 5.10, though as the tab chord length changes, it does deviate slightly, as with the lift coefficient. Again the deviation is of the same shape as that shown in Figure 5.5.

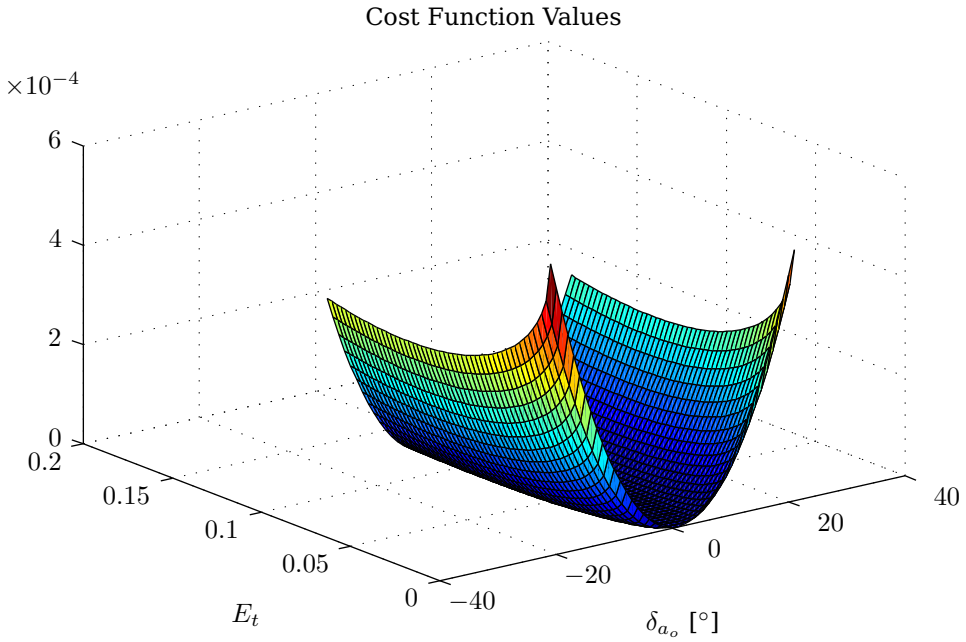


**Figure 5.6** – Minimum cost values for each $\delta_{a_o}$ and $E_t$.

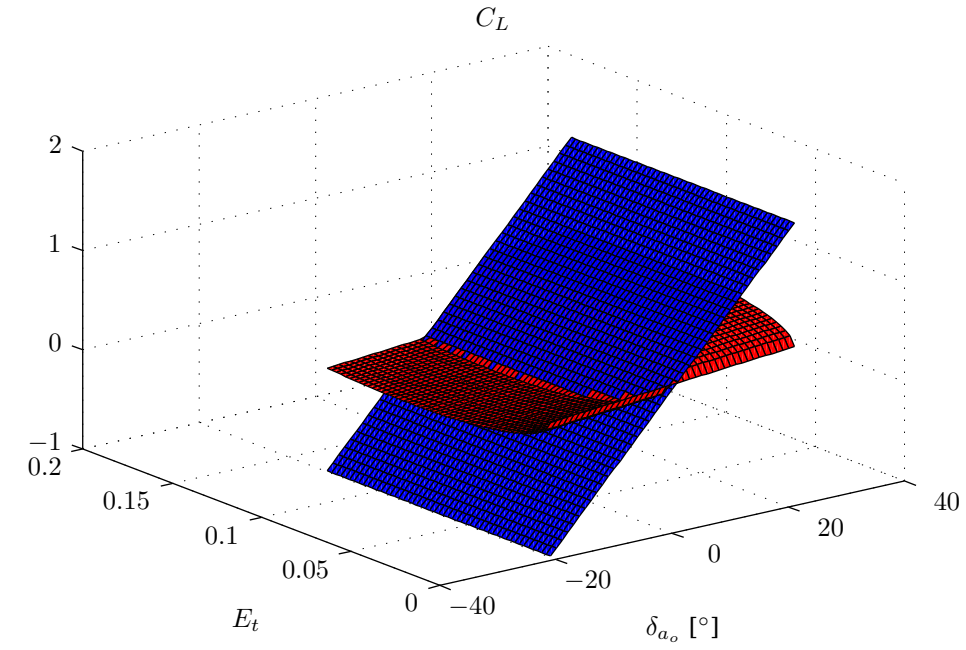


**Figure 5.7** – Lift coefficient.

An important observation at this stage is that it seems the hinge moment coefficient is too heavily weighted when compared with the lift coefficient, thus resulting in less than satisfactory performance regarding the lift, and hence the rolling moment. It should also be mentioned that these results were generated using the same set of weightings in order to be consistent throughout and to allow the comparison of the various techniques, for both the angle optimisations in §5.5 and §5.6.

The final graph, shown in Figure 5.11, is that of the tab hinge moment coefficient. Examining the magnitude of this hinge moment, one can see that there is a large difference between this and the aileron hinge moment coefficient. The maximum value of the tab hinge moment coefficient is about $3 \times 10^{-4}$ for the largest tab size allowed ($E_t = \frac{1}{2}E_a = 0{,}125$).

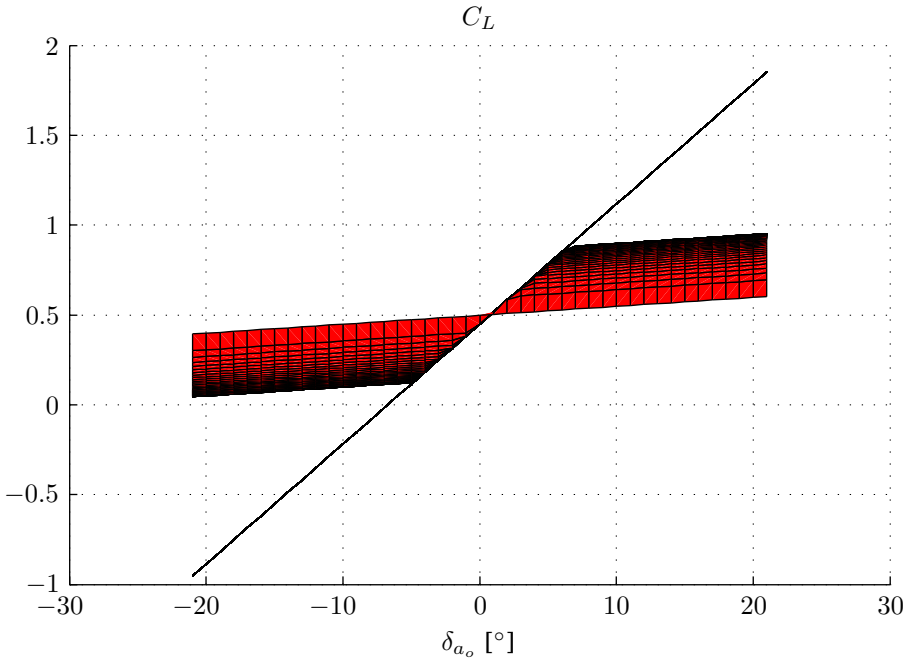


**Figure 5.8** – Lift coefficients of Figure 5.7 viewed down the $E_t$ axis.

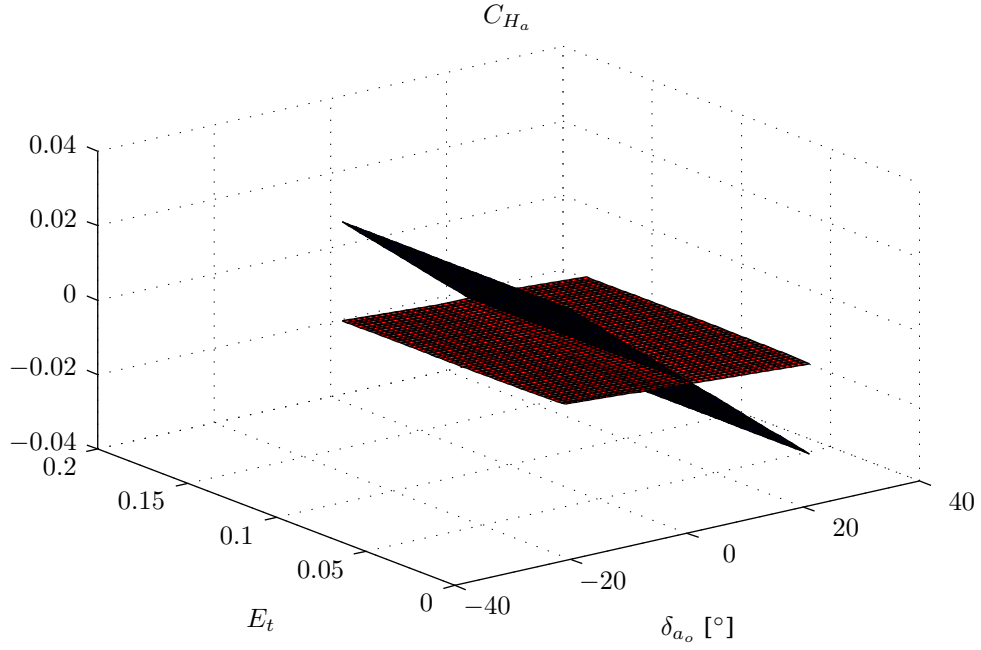


**Figure 5.9** – Aileron hinge moment coefficient.

## 5.6 Optimal Tab and Aileron Deflection: A Non-Gradient-Based Two-Dimensional Optimisation

In §5.5 the gradient-based, *sequential quadratic programming* method of §4.3 is used. As such the linearised thin aerofoil theory was used in order to easily determine the derivatives of the objective function as well as the constraint functions.

This section makes use of the *real-encoded genetic algorithm* approach described in §4.4 which *does not* require gradient information. This section is broken into two components. The first applies to the REGA to the same problem as in §5.5, i.e. it makes use of the linearised thin aerofoil theory which allows the comparison of the REGA to the SQP.

Once it is established that the REGA and SQP solutions are satisfactorily similar, the REGA will be applied to the non-linear thin aerofoil theory, for which gradient information is more complicated to determine.

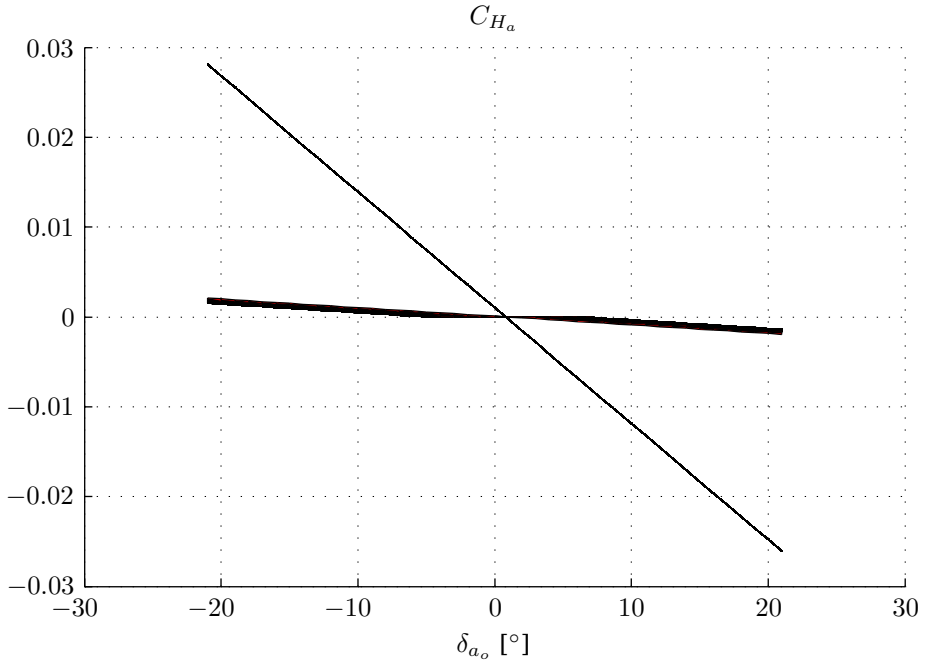


**Figure 5.10** – Aileron hinge moment coefficient viewed down the $E_t$ axis.

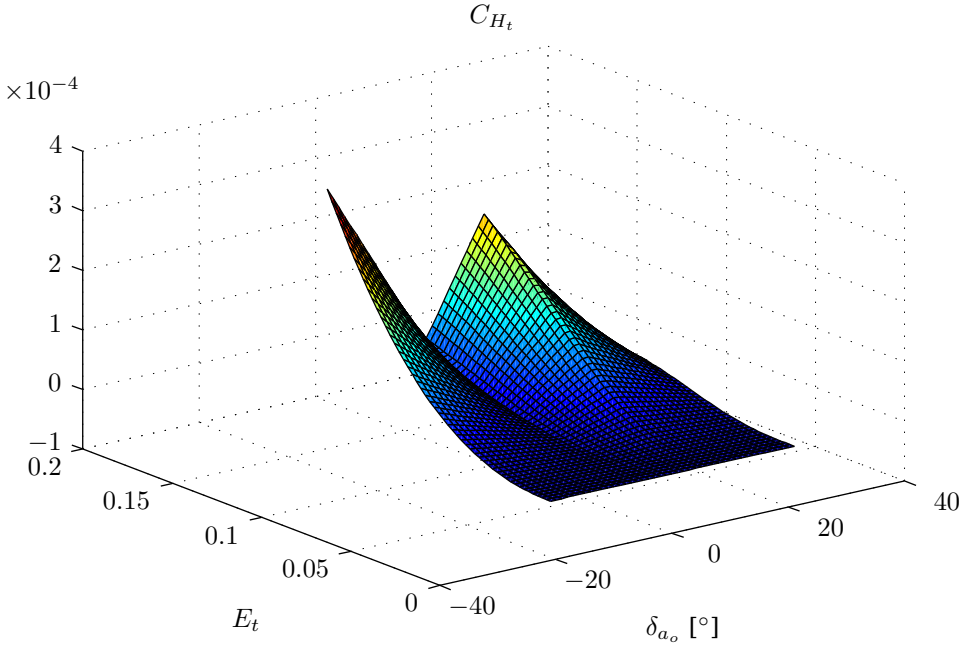


**Figure 5.11** – Tab hinge moment coefficient.

This forms the second part of this section.

### 5.6.1 Linearised Thin Aerofoil Theory with the Real-Encoded Genetic Algorithm

The same equations derived in §5.5 are used here, except that the gradient information (partial derivatives) is ignored. The same set of constraints are also applied.

The equivalent graphs of §5.5, Figures 5.3 to 5.11 are shown in Figures 5.12 to 5.17 and it can be seen immediately that the graphs of §5.5 are almost identical to those in this section.

The same achievement region is visible in Figure 5.14 as in Figure 5.5, indicating that the two optimisation techniques that were described in Chapter 4 are valid. Each technique validates the other since they arrive at the same values for the optimisations. The REGA actually provides one further attribute based on the specific characteristics of the algorithm. By the reasoning of §4.4, the values obtained can be considered

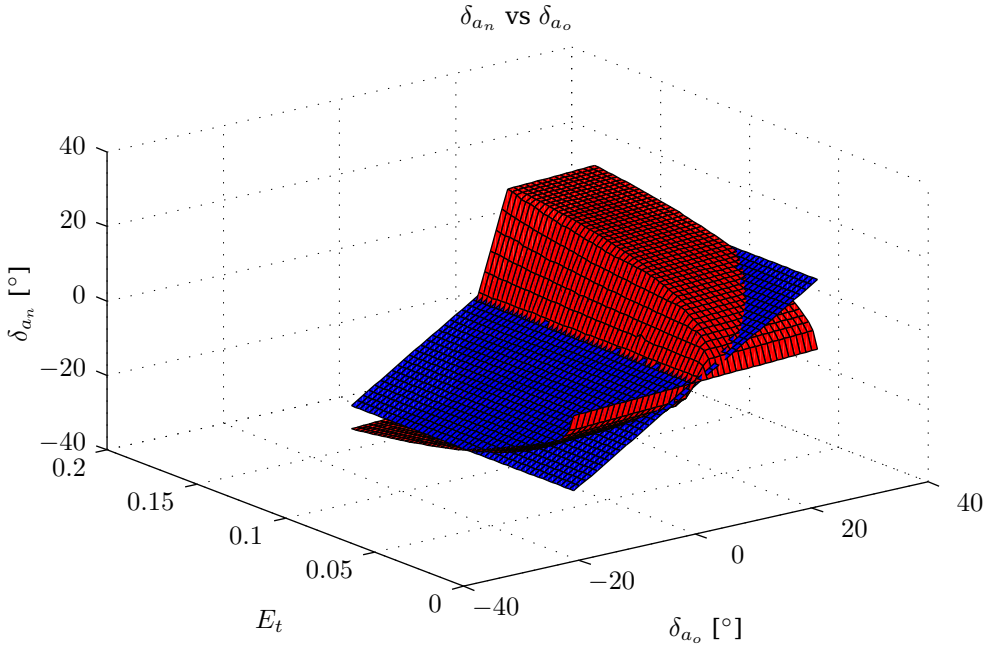


**Figure 5.12** – New aileron deflection angles.

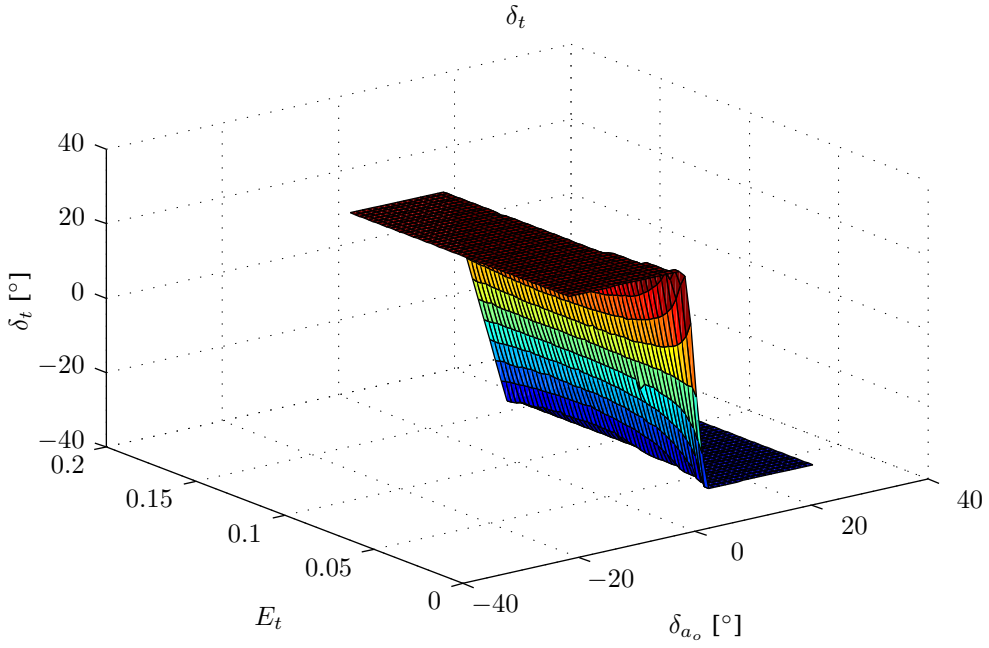


**Figure 5.13** – Tab deflection angles.

global minima. This was ensured by running the optimisation multiple times and comparing the results. In the case of the angle optimisations, each optimisation run that was performed resulted in negligible differences in the results of the design variables, $\delta_{a_n}$ and $\delta_t$.

It seems prudent to make some remarks and observations regarding the deflection angles in both §5.5 and §5.6. When examining the deflection angles, specifically the aileron deflection angles, in both sections it can be seen that as the tab length tends to zero, the aileron deflection angles *do not* revert to their original deflection angles. This seems incorrect at first glance: "if there is no tab then the old and new aileron deflections should be the same".

The results shown in Figures 5.3 and 5.12 *are, however, correct*. While it seems counter intuitive, this is a by-product of the optimisation process. Remembering that the optimisation takes multiple objectives into account, the lift coefficient, the aileron hinge moment and the tab hinge moment, it can be seen through a numerical example why the results differ from the original deflection angles.

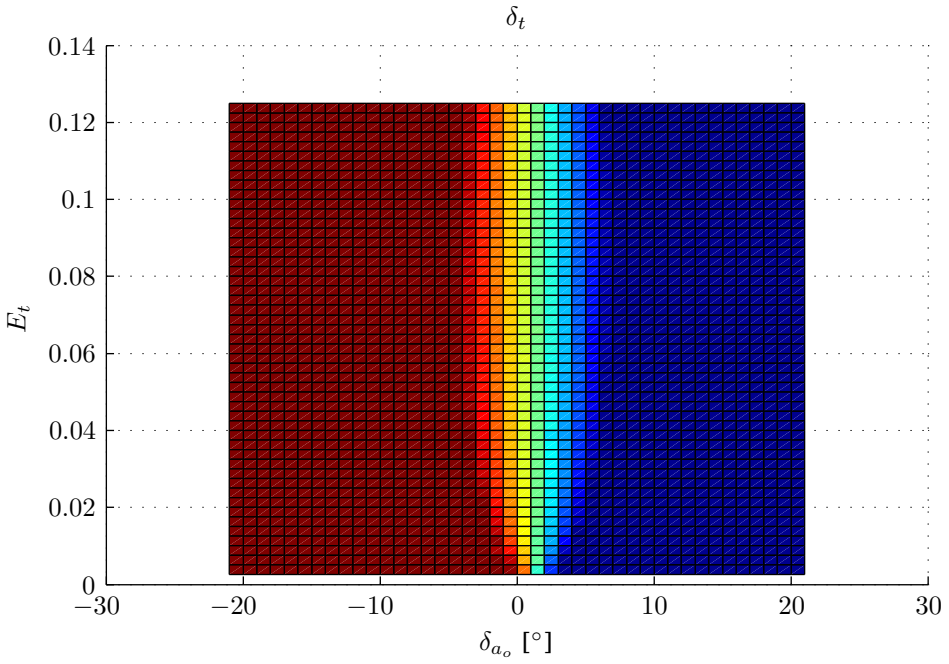


**Figure 5.14** – Tab deflection surface top view. Maroon indicates maximum deflection of $30\,^\circ$ and the dark blue minimum deflection of $-30\,^\circ$. The gradient region indicates values between these two extremes.

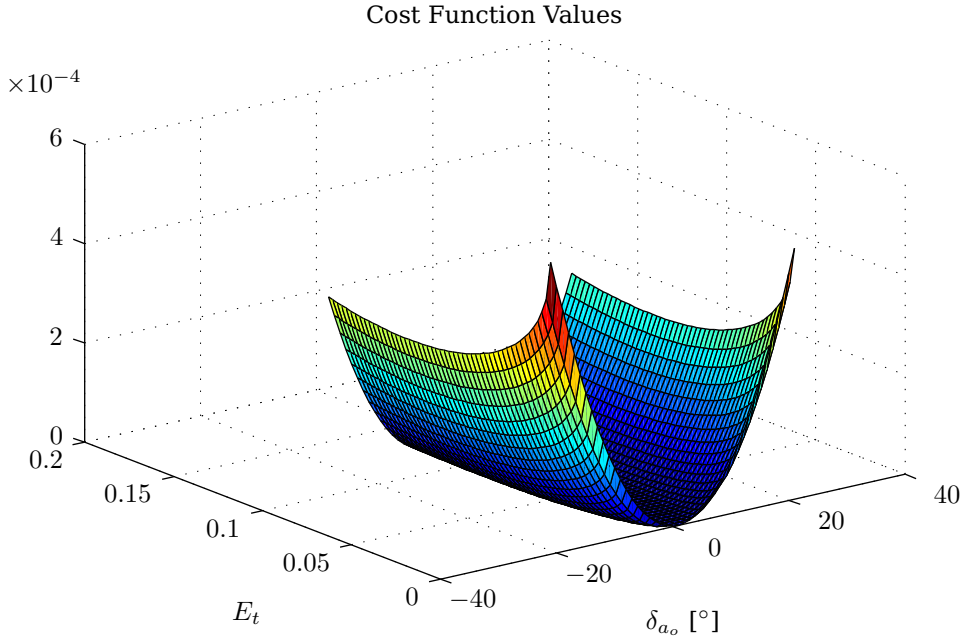


**Figure 5.15** – Minimum cost values for each $\delta_{a_o}$ and $E_t$.

Considering the objective function given in §5.5.1, repeated below,

$$J_{\text{in}} = w_L(C_{L_o} - C_{L_n})^2 + w_{H_a}(C_{H_a})^2 + w_{H_t}(C_{H_t})^2 \qquad [5.5.4]$$

and with the associated associated weightings of

$$w_L = 3 \times 10^{-4} \qquad w_{H_a} = 10 \qquad w_{H_t} = 10 \qquad [5.5.8]$$

it is possible to see that, if there is no tab the $C_{H_t}$ component becomes zero (regardless of calculated deflections), but this still leaves a relative weighting between the lift coefficients and the aileron hinge moment coefficients.

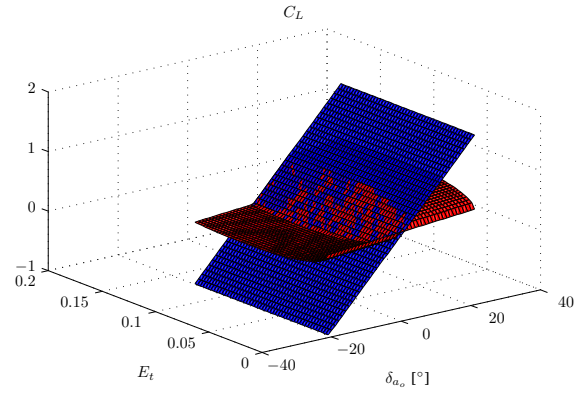


(a) Lift coefficient.

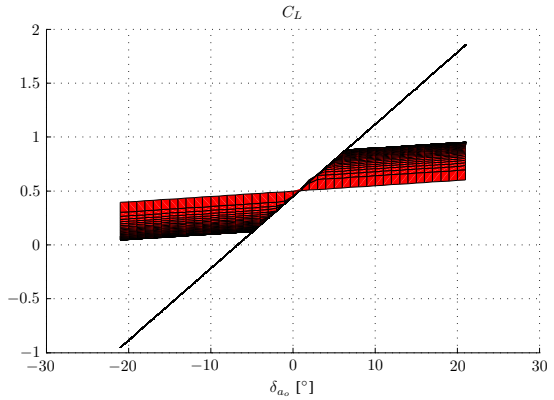


(b) Lift coefficients of Figure 5.16(a) viewed down the $E_t$ axis.

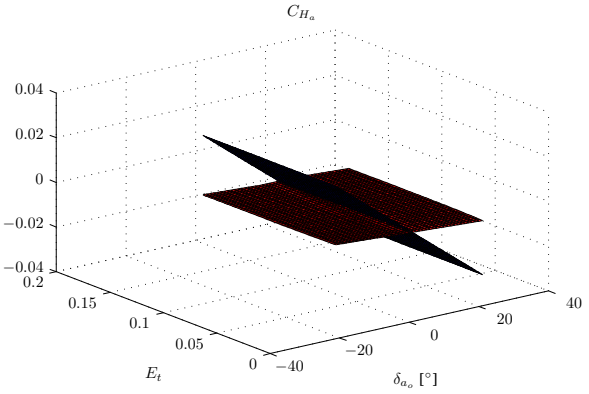


(c) Aileron hinge moment coefficient.

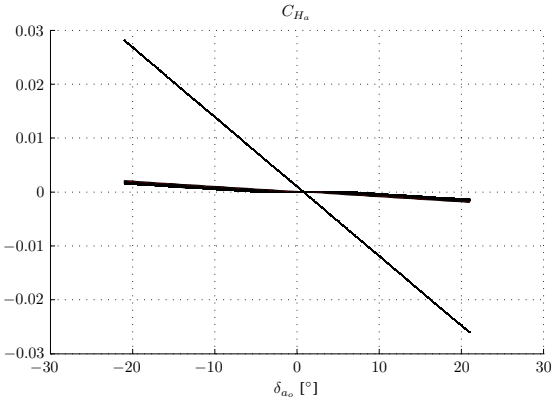


(d) Aileron hinge moment coefficient viewed down the $E_t$ axis.

**Figure 5.16** – Lift and aileron coefficients.

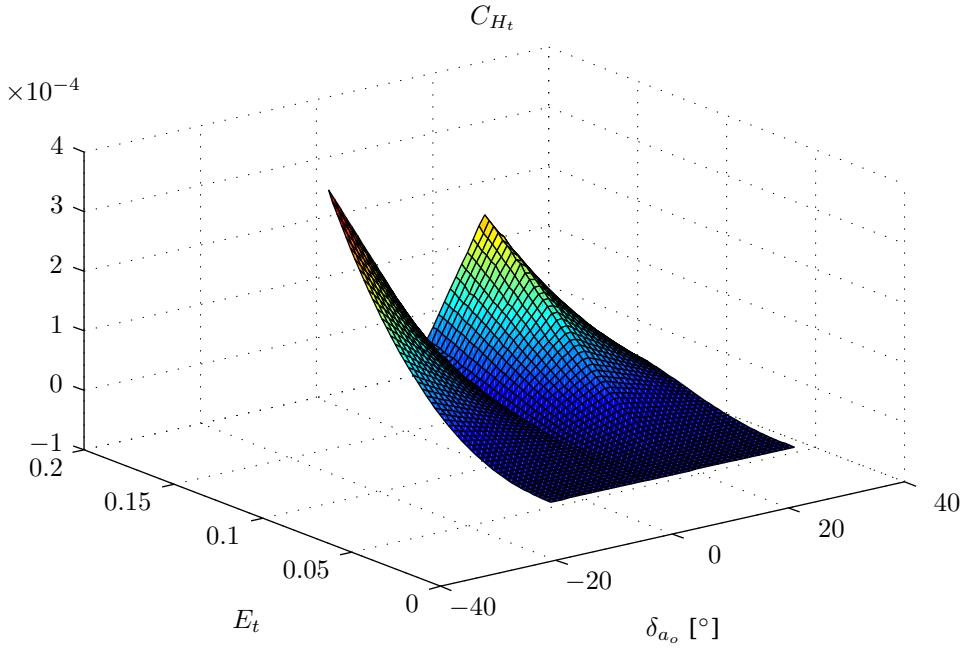


**Figure 5.17** – Tab hinge moment coefficient.

Examining either Figure 5.7 or Figure 5.16(a) it is possible to see the maximum value of the old lift coefficient is about $1{,}5$ and the minimum is about $-1{,}0$, and from either Figure 5.9 or Figure 5.16(c), the maximum magnitudes of the old aileron hinge moment coefficients are approximately $0{,}03$.

When looking at Equation 5.5.4, and setting $C_{H_a}$ to the maximum aileron hinge moment of $0{,}03$, the

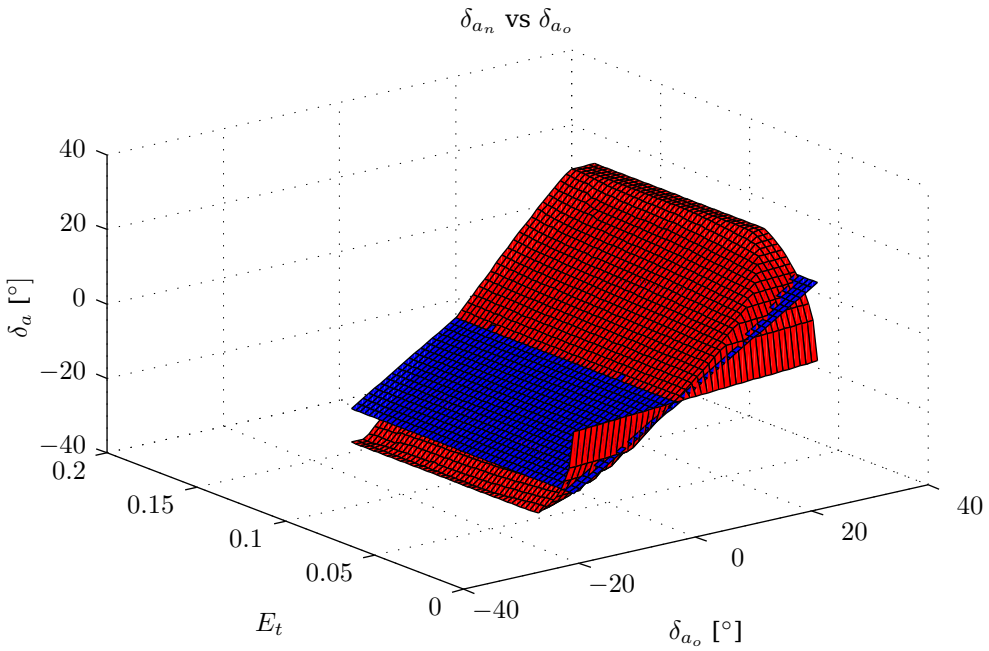


**Figure 5.18** – New aileron deflection angles.

*maximum* cost due to the aileron hinge moment is

$$J_{H_a} = (10)(0{,}03)^2 = 9 \times 10^{-3}$$

and the maximum cost due to the lift (i.e. when new lift is zero) is

$$J_L = (3 \times 10^{-4})(1{,}5 - (-1{,}0))^2 = 1{,}875 \times 10^{-3}$$

thus it becomes apparent that for the case of $E_t = 0$ regardless of the operating point, with the current weightings, the aileron hinge moment coefficient plays a much larger role than that of the lift (at least for the linearised case). The optimisation then endeavours to minimise the aileron hinge moment coefficient, rather than matching the old and new lift coefficients, which results in better aileron hinge moment values, but very poor lift performance.

This highlights one of the particularly difficult aspects of optimisation: selection of suitable weightings. This is an aspect that will require further examination by prospective students involved in the CoSICS project. In the case of this specific iteration of the project, the weightings provide satisfactory results, as will be seen in later sections of this chapter.

### 5.6.2 Non-Linear Thin Aerofoil Theory with the Real-Encoded Genetic Algorithm

Having established that the REGA provides satisfactorily valid optimal solutions, it is applied to the case of *non-linear thin aerofoil theory*. Since the derivatives of this set of equations are difficult to determine, a non-gradient-based optimisation method is required to make use of the mathematical equations derived in Chapter 3.

By using the non-linearised thin aerofoil theory, more accurate results can be achieved, though, as has been previously mentioned, thin aerofoil theory also only provides an approximation of the aerodynamics, and does not take into account viscosity and compressibility effects or corrections. The results of this section (§5.6.2) are compared with the results of §5.5 in order to see the effect the linearisation process had on the results. It needs to be remembered that during the linearisation process, small-angle approximations were made and only the first three terms of the Fourier series expansions were taken.

When examining the new aileron deflection angles in Figure 5.18 it is possible to see that the new aileron deflection angle values are much closer to their original values (of the wing-aileron system), though still larger in magnitude (negative angles have become slightly more negative, and positive angles have become slightly more positive).

This agrees with the reasoning given in §3.8: in order to produce the same lift with the reduced surface area of the aileron, a greater aileron deflection is required. This greater deflection angle can easily be

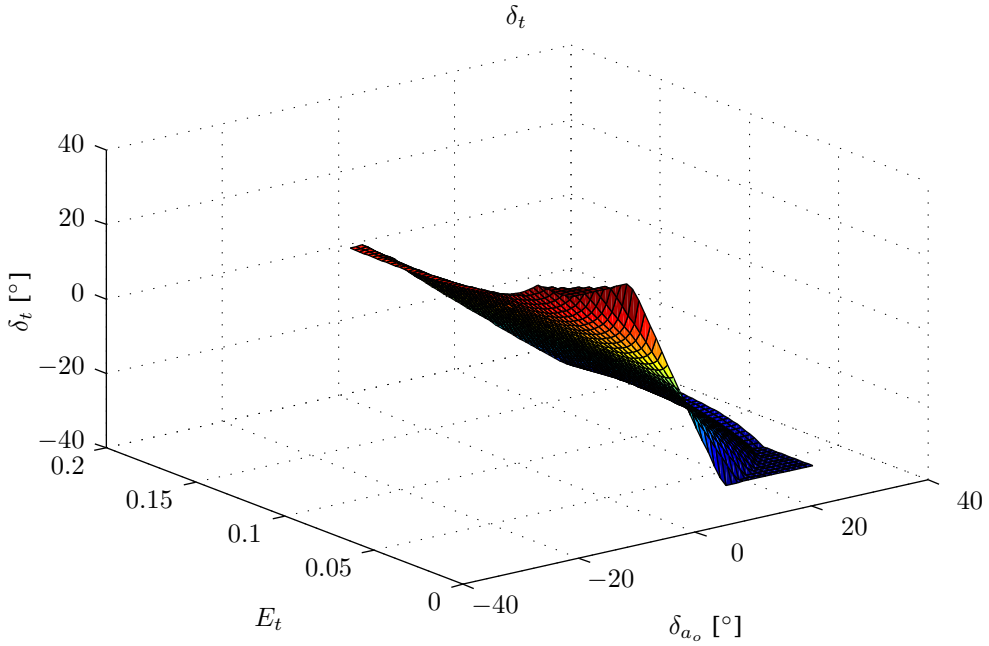


**Figure 5.19** – Tab deflection angles.

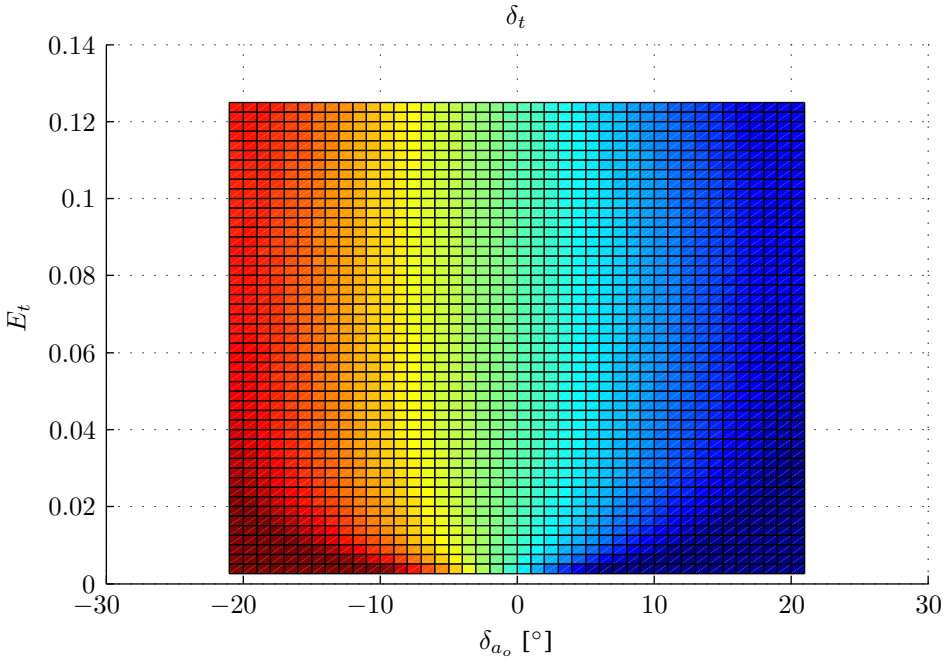


**Figure 5.20** – Tab deflection surface top view. Maroon indicates maximum deflection of $30\,^\circ$ and the dark blue minimum deflection of $-30\,^\circ$. The gradient region indicates values between these two extremes.

seen in the figure. It should be pointed out, however, that there are still areas where the new aileron deflection angle is limited to the maximum allowed values, at high deflection angles.

Examining the tab deflection, as given in Figure 5.19, one can see the almost-linear increase in tab deflection (magnitude) as the old aileron deflection values increase. One still sees very poor performance for very small tabs, for the same reasons as given in §5.6.1. Note that the tab deflection is opposite that of the aileron, as previously surmised.

Typically the region of achievement could easily be determined by examining tab deflections as projected in Figure 5.14, where the tab maximum and minumum deflections could easily be seen. For the case of the non-linear aerofoil theory this is not as easily determined since, as shown in Figure 5.20, there are very few regions where the tab has obtained a maximum deflection angle. The regions where it is visible are for small values of $E_t$, but large positive and negative values of $\delta_{a_o}$, corresponding to the lower left and

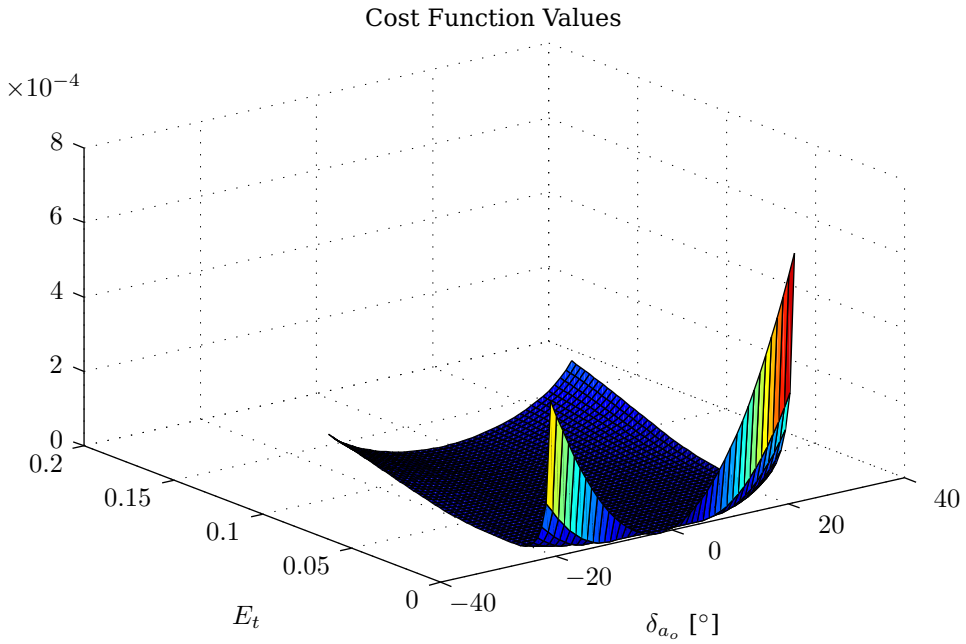


**Figure 5.21** – Minimum cost values for each $\delta_{a_o}$ and $E_t$.

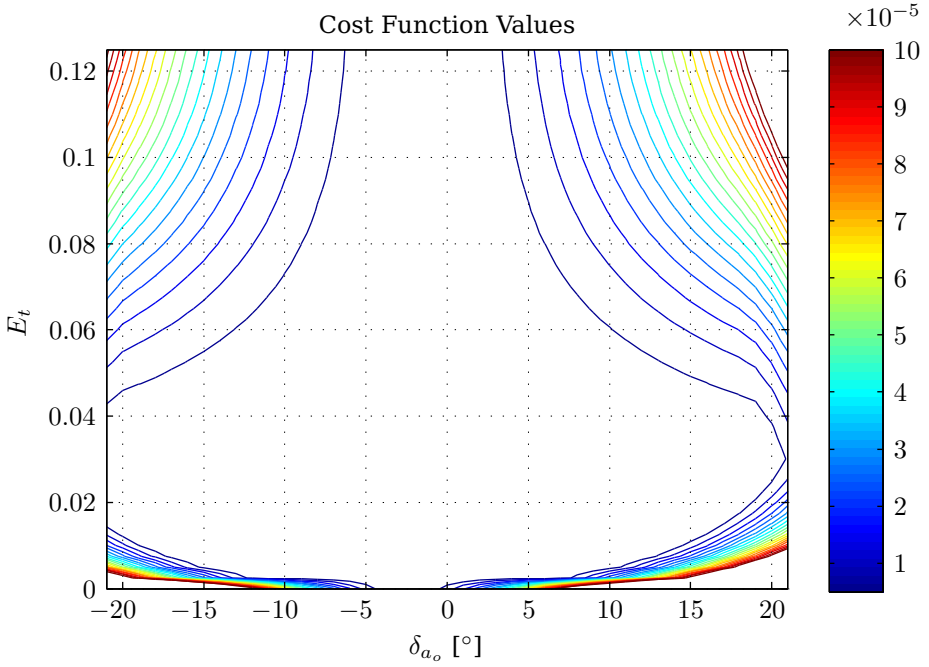


**Figure 5.22** – The graph shown in Figure 5.21 as a contour plot. Note that to provide better resolution for small values, the maximum value seen in the contour is $J = 1 \times 10^{-4}$.

right corners of the graph shown in Figure 5.20.

In order to better view the achievement region, in this case it is more convenient to turn to the graph indicating minimum cost function values for the parameter sweep, Figure 5.21. Comparing this graph to its counterpart for the linearised theory, Figure 5.15, it can immediately be seen that the overall average magnitude of the minimum cost is substantially decreased. The magnitude of the peaks for small values of $E_t$ and $\delta_{a_o}$ deflections are, however, substantially larger. In order to better view this much flatter minimum cost graph, some contours are shown in Figure 5.22. These contours were taken at intervals of $5 \times 10^{-6}$. The innermost contour is the minimum contour, and while not completely zero is close enough for all practical purposes. These graphs indicate that while it is not possible to obtain an *ideal* achievement region, given the weightings used, and the practical system to which the optimisation is being applied, the minimum values obtained within this minimum contour are satisfactorily small enough to be treated as an achievement region.

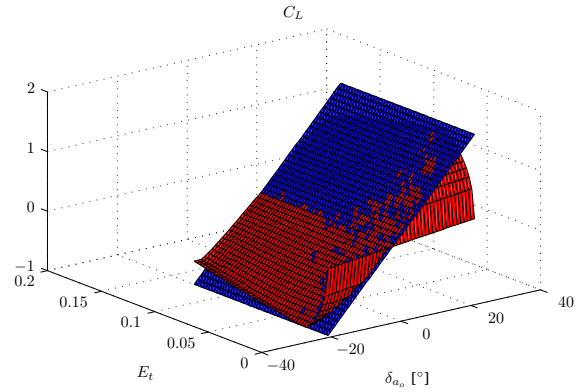


(a) Lift coefficient.

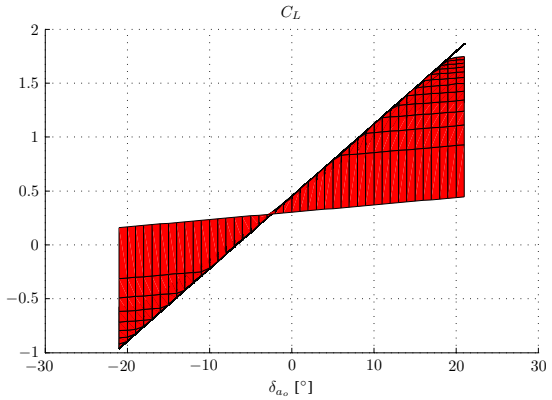


(b) Lift coefficients of Figure 5.23(a) viewed down the $E_t$ axis.

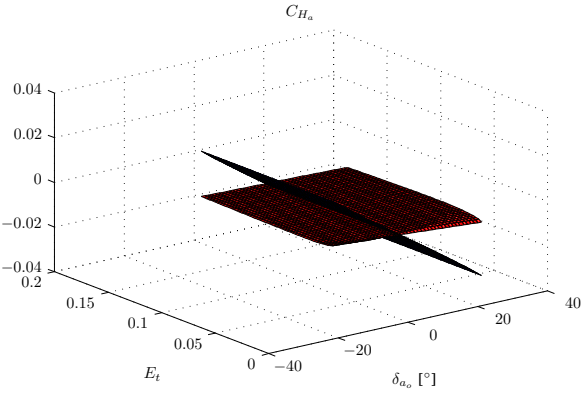


(c) Aileron hinge moment coefficient.

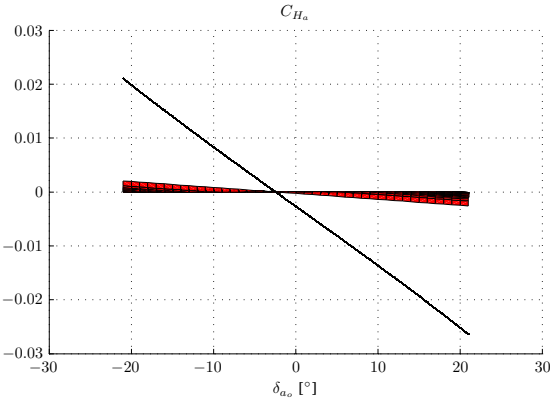


(d) Aileron hinge moment coefficient viewed down the $E_t$ axis.

**Figure 5.23** – Lift and aileron coefficients.

Examining this contour's form more closely, certain observations can be made. The first observation is the symmetry of the region. The symmetry is clearly visible, however, it is not symmetrical about the $\delta_{a_o} = 0$ axis. Unlike the linearised theory, the axis of symmetry is *negative*, at approximately $\delta_{a_o} \approx -1{,}5\,°$. This negative "axis value" will be visible in all the successive graphs of this section.

The second observation that can be made concerns the width of the contour (in the $\delta_{a_o}$ direction). Beginning at $E_t = 0$, it can be seen that the width is very narrow (and can be seen to tend to zero as $E_t$ tends to zero when contours are chosen more finely), before growing rapidly to its maximum width at $E_t \approx 0{,}03$, before rapidly narrowing again. The effect can be seen clearly for small $E_t$ values when examining Figure 5.20, though the narrowing at larger values is unclear. This can be attributed to the significantly larger cost values for the small $E_t$, large $\delta_{a_o}$ regions versus the rest of the graph where the deviation is much smaller.

Comparing the lift and hinge moment coefficient graphs of §5.5.3 against those provided here, it is possible to see *very* different results.

Since the calculated optimal deflection angles are quite different from the non-linear case, it is to be expected that the coefficient graphs will differ. Noting that since the approximations used in linearising the thin aerofoil theory are no longer applicable, the values in the non-linear results are expected to be valid over a larger operating range, and this was seen in Figure 5.22. This also indicates that the results obtained from the linearised theory should be accepted only where the assumptions hold true, i.e. for small deflections.

Considering the lift coefficient in Figure 5.23(a) (and the projection down the $E_t$ axis shown in Figure 5.23(b)) it is possible to see a very satisfactory result. Over large portions of the operating range the old and new lift coefficients are seen to be almost equal. Deviations occur at very large $\delta_{a_o}$ where, as can be seen in Figures 5.18 and 5.19, the actuators hit their maximum allowable deflections. Again for small tab lengths there are large deviations from the optimal where the optimisation favours the aileron hinge moment coefficient over the lift coefficient as discussed previously.

The aileron hinge moment coefficients values have also improved. It is difficult to see on the surface plot

of Figure 5.23(c), but examining the view down the $E_t$ axis in Figure 5.23(d), it is possible to see that there are regions for all values $\delta_{a_o}$ where the hinge moment is zero. From the surface plot it *is* possible to see that the new aileron hinge moment coefficient surface is fairly level, indicating a large region where the hinge moment value is very close to zero. Once again the deviations occur in the small $E_t$, large $\delta_{a_o}$ regions.

The final plot of this section is the tab hinge moment coefficient plot of Figure 5.24. Comparing this figure with its counterpart in §5.5.3, Figure 5.17, it is possible to see very large differences in the forms of the graphs. This is expected since, for the linearised case, the tab reached its maximum positive and negative deflection angles for relatively small values of the old aileron deflection angles. For the non-linear case the maximum deflections were reached only at the extremes of the old aileron deflection angles. The graph

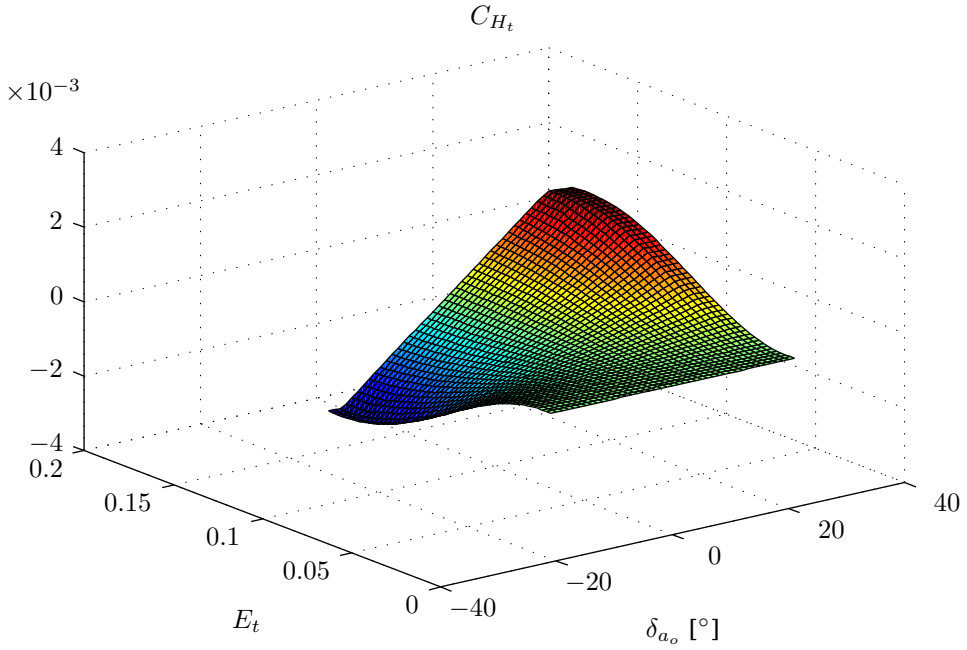


**Figure 5.24** – Tab hinge moment coefficient.

depicts expected tab hinge moment characteristics: as the chord length of the tab increases, the hinge moment associated increases for any given $\delta_{a_o}$ since there is a larger aerodynamic force acting on the tab as the chord increases. Except for the zero tab length case, there is an increase in the magnitude of the tab hinge moment coefficient as the magnitude $\delta_{a_o}$ increases.

## 5.7 Optimal Tab Chord Length: A Non-Gradient-Based One-Dimensional Optimisation

This section discusses the first *geometric* optimisation. The goal of the optimisation of this section is to determine the most suitable tab length that will meet the requirements of the project specifications. As the heading states, this a one-dimensional (only one element in the design vector) optimisation where the two-dimensional thin aerofoil theory is used, as with the previous sections.

Before delving into the optimisation itself and providing some results, the selection of the weightings used in the previous sections is discussed.

### 5.7.1 Weighting the Objective Function Components

Up to now a certain selection of weightings for the various components of the multi-objective objective function has been used without much explanation, but to great effect. The selection of these weightings is now discussed, and continues from where §5.5.1 and §5.5.3 left off.

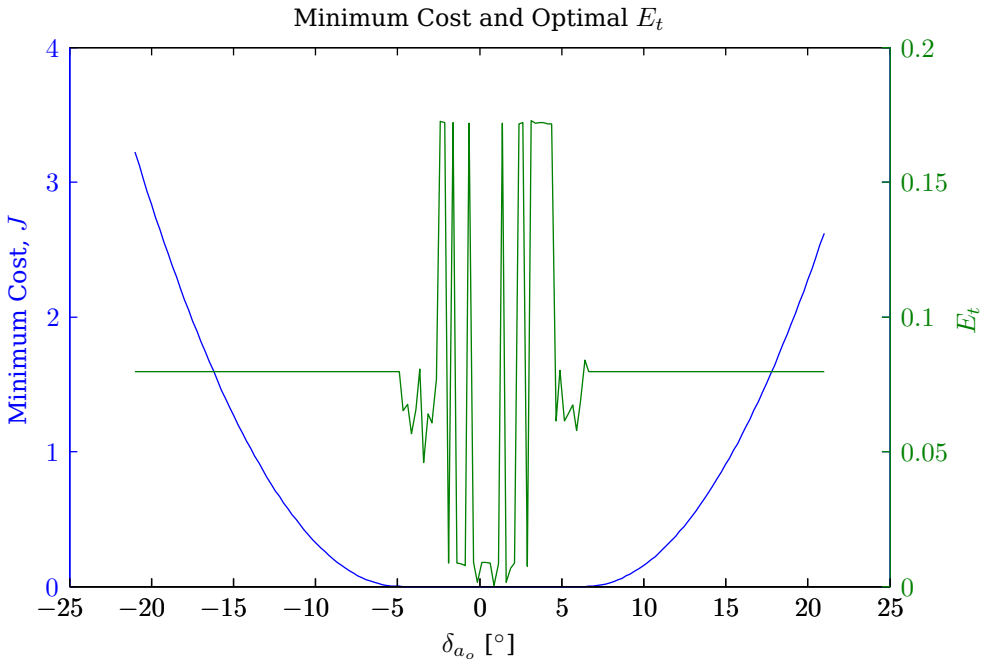


**Figure 5.25** – Minimum cost and optimal $E_t$ obtained for $\alpha = 3\,^\circ$ over the operating range $-21\,^\circ \leq \delta_{a_o} \leq 21\,^\circ$ with *no* tab hinge moment coefficient weighting.

In §5.5.3 the relative normalisation weightings are determined to be those in Equation 5.5.7, repeated below for convenience:

$$w_{L_n} = 1 \times 10^{-4} \qquad w_{H_{a_n}} = 10 \qquad w_{H_{t_n}} = 10 \qquad [5.5.7]$$

These weightings bring the approximate values of each of the components of the multi-objective function into the same range, thus allowing them to be related to each other. A metric that is often used to normalise this type of objective is the *utopia point*, which is the point defined by the minima of each of the objective functions in criterion space, Arora [33] and Marler, et al [40]. This ideal point is obtained by actively determining the minimum of each of the individual objective functions, which is a very time-consuming process and is thus not ideal for this application. It should be noted that the utopia point is typically not within the feasible criterion space, and is thus usually unobtainable.

Considering the performance requirements of the new (wing-aileron-tab) system, it is desired that the new lift be as close as possible to the old lift, even at the expense of some aileron hinge moment, thus initially this component was weighted more heavily ($w_{L_o} = 0{,}9$) than the aileron hinge moment ($w_{H_{a_o}} = 0{,}1$), or a nine-to-one relation, while the tab was not weighted at all. For this case there was no noticeable reduction in the aileron hinge moments, thus the relative weighting of the two components was reduced incrementally until the final weighting was chosen as three to one ($w_{L_o} = 0{,}75$, $w_{H_{a_o}} = 0{,}25$ and $w_{H_{t_o}} = 0$) Again, due to numerical errors, each of the values was scaled, in this case by four to result in better solutions.

This final relative weighting gives the following total weightings:

$$\begin{aligned} w_L &= w_{L_n} \times w_{L_o} \times 4 = 3 \times 10^{-4} \\ w_{H_a} &= w_{H_{a_n}} \times w_{H_{a_o}} \times 4 = 10 \\ w_{H_t} &= w_{H_{a_n}} \times w_{H_{a_o}} \times 4 = 0 \end{aligned}$$

A test case was chosen where the angle of attack was kept constant (at $3\,^\circ$) while sweeping the old aileron deflection from $-21\,^\circ$ to $21\,^\circ$. At each point during the sweep, the best tab chord length (as $E_t$) for that point was determined. The result of this test run is shown in Figure 5.25. As can be seen, the minimum cost in Figure 5.25 is a smooth curve with a region of zero value between approximately $-6\,^\circ$ and $7{,}5\,^\circ$ and a non-zero value elsewhere. The region on the graph where this minimum cost function is zero is the region where both the objectives were satisfied: aileron hinge moment is zero, and the old and new lift values are the same.

A non-zero value indicates that one or more of the objectives could not be satisfied completely, and the tab length obtained results in the minimum possible cost value for that $(\alpha, \delta_{a_o})$ combination.

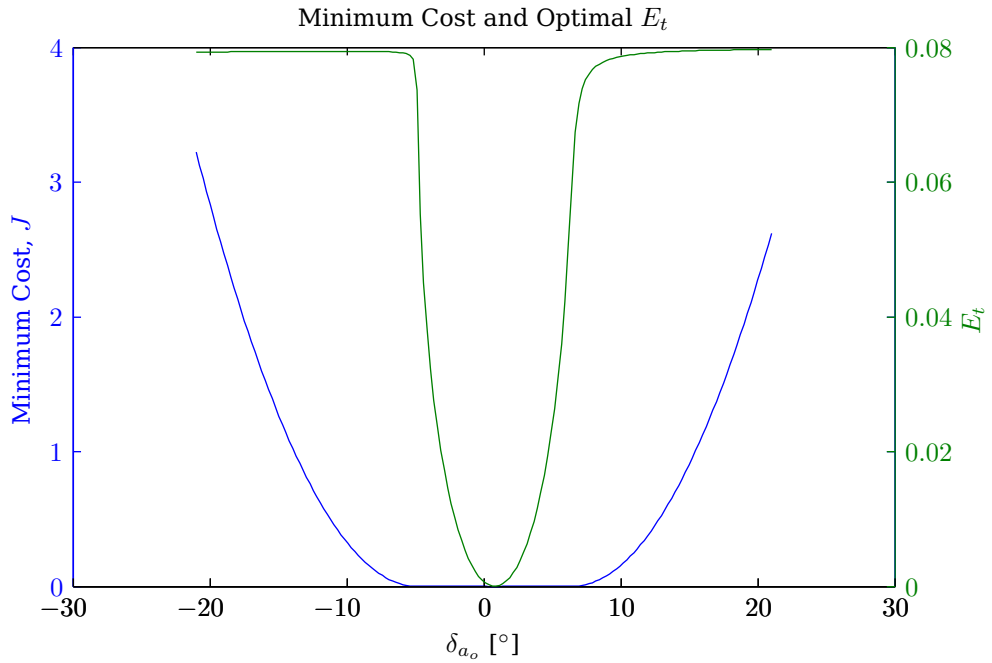


**Figure 5.26** – Minimum cost and optimal $E_t$ obtained for $\alpha = 3\,^\circ$ over the operating range $-21\,^\circ \leq \delta_{a_o} \leq 21\,^\circ$ *with* tab hinge moment coefficient weighting.

Looking at the optimum value of $E_t$ over the $\delta_{a_o}$ sweep, one sees relatively consistent values which correspond to the regions where the cost could not be satisfied, indicating unique solutions to the optimisation problem. The $J = 0$ region shows some strange behaviour where two consecutive values of $E_t$ in the $\delta_{a_o}$ sweep are not similar at all. These jumps in the optimal values indicate that in the region where both the objectives are satisfied there are multiple solutions to the optimisation problem (except at the boundary where a single solution still exists).

The set of optimal solutions in this $J = 0$ region for any $(\alpha, \delta_{a_o})$ combination forms the Pareto front.

In order to coerce the optimisation to present a single solution, an extra objective is added. This is done by making the weight of the tab hinge moment non-zero. In this case the weighting chosen is the same as that of the aileron hinge moment, which results in the final choice of weightings as originally stated in Equation 5.5.8:

$$w_L = 3 \times 10^{-4} \qquad w_{H_a} = 10 \qquad w_{H_t} = 10 \qquad [5.5.8]$$

This combination gives a $3 : 1 : 1$ relation between the various objectives, ignoring the normalisation components of the weightings.

It may seem odd to select the weighting of the aileron actuator and tab actuator to be the same, however, it is justified by the following reasoning. It is desired to reduce the aileron hinge moment but regardless of the configuration chosen a tab hinge moment will be incurred. It is not desired that the tab hinge moment be near in value to the aileron hinge moment, and, as such, it would be expected that the tab hinge moment weighting would be chosen smaller than that of the aileron. This was *not* done since the effect on the aileron hinge moment by the tab is fairly large for small tabs because the tab is located on the trailing edge of the aerofoil.

Since the tab is expected to be much smaller than the aileron the hinge moment on the tab will be also be much smaller, thus allowing the use of equivalent weightings. There are constraints on the maximum size (chord length) of the tab (half that of the aileron) to ensure that this is the case.

The results for the new weightings with a non-zero tab hinge moment coefficient weighting are given in Figure 5.26. It can be seen that by adding this extra objective, the number of solutions become further restricted. As such there are now unique values of the tab length for the entire $\delta_{a_o}$ region, including the $J = 0$ region, thus indicating that the tab hinge moment is now also being minimised. The tab hinge-moment contribution plays an almost negligible role if either of the other two objectives is not satisfied.

This is satisfactory since typically the other two objectives are of greater importance, even though the weightings do not indicate this.

### 5.7.2 Objective Function

The weightings of the inner cost function have now been selected, and all that remains is the creation of the outer optimisation objective function. In §5.4 the concept of a multiple operating point optimisation is discussed in the context of this project and the method that is used to solve this problem is described. The following now provides the actual objective function definition, as well as an explanation.

As was mentioned, the weighted sum method will be used to create the multi-objective objective function. The inner objective function which determines the optimal deflection angles is defined in Equation 5.5.4; however, this objective function assumes a fixed geometry. During the outer optimisation loop the geometry is modified, indicating that the inner optimisation needs to be re-optimised. The result of the inner optimisation is used to determine the minimum cost attainable for the specific geometry ($E_t$) at that specific operating point ($\alpha$, $\delta_{a_o}$). This minimum cost then forms a component of the outer objective function which is summed over the entire operating range at the discrete intervals deemed appropriate:

$$J_{\text{out}} = \sum_{\alpha} \sum_{\delta_{a_o}} w_\alpha w_{\delta_{a_o}} \min J_{\text{in}}(\alpha, \delta_{a_o}) \tag{5.7.1}$$

Where viable the grid used was over the previously mentioned angle of attack range, $-8\,^\circ \leq \alpha \leq 14\,^\circ$, and old aileron deflection, $-21\,^\circ \leq \delta_{a_o} \leq 21\,^\circ$, with $1\,^\circ$ intervals.

Since the inner optimisation needs to be performed for every operating point, it is possible to record the optimal aileron and tab deflections at each point in the operating range. This information can be used to determine if the solutions are viable: a vast change in optimal deflection angles for a small change in the operating range, for example, is not suitable.

As was mentioned in §5.4, it is possible to assign weightings to each operating point in the form of the $w_\alpha w_{\delta_{a_o}}$ multiples in order to give preference to specific areas in the operating region. For the purpose of this project, these weightings are kept at one in order to weighting each point equally and in an attempt to obtain the same response over the entire operating range.

### 5.7.3 Constraints

The inner optimisation's constraints remain the same as described in §5.5.2 for §5.5 and §5.6. The outer optimisation optimises the geometry; thus additional constraints need to be created.

Since only the tab chord length is being varied, the additional constraints are those relating to the expression $E_{t_{\min}} \leq E_t \leq E_{t_{\max}}$ where the tab length range is limited to a value between two constants. This translates to

$$-E_t + E_{t_{\min}} \leq 0 \quad \text{and} \quad E_t - E_{t_{\max}} \leq 0 \tag{5.7.2}$$

and in standard form Equation 5.7.2 becomes

$$\begin{aligned} g_1(E_t) &= -E_t + E_{t_{\min}} \leq 0 \\ g_2(E_t) &= E_t - E_{t_{\max}} \leq 0 \end{aligned} \tag{5.7.3}$$

The constants are chosen to prevent the tab chord length from becoming negative ($E_{t_{\min}} = 0$) and to be a maximum of the constant aileron chord length, in this case $E_{t_{\max}} = \frac{1}{2}E_a$, since it is expected a tab larger than the aileron would have an associated hinge moment that is comparable to the aileron's. This is undesirable since this could result in zero aileron hinge moment, but a very large tab hinge moment, thus negating the purpose of the tab.

The two components of Equation 5.7.3 are then used during the optimisation process.

### 5.7.4 Results

Since the outer optimisation relies on the results of the inner optimisation loop, gradient information is not readily available for use with this objective function. As such, the real-encoded genetic algorithm is used to optimise the funtion.

The results given in this section are for two cases: the first case is where the optimisation has been applied to the *linearised* thin aerofoil theory and the second case makes use of the non-linear thin aerofoil theory.

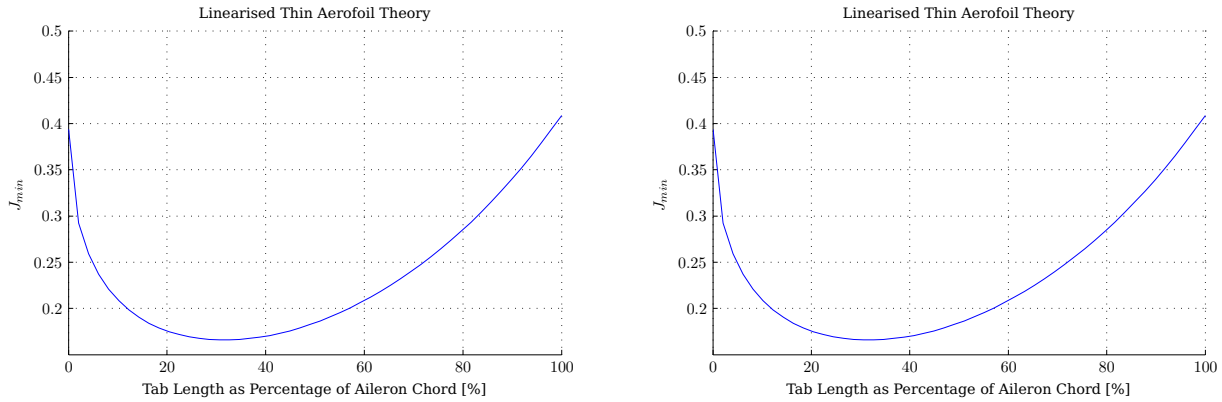


(a) Inner optimisation uses SQP.

(b) Inner optimisation uses REGA.

**Figure 5.27** – Outer cost function value as $E_t$ varies for the linearised thin aerofoil theory case.

#### 5.7.4.1 Linearised Thin Aerofoil Theory – $E_t$ Sweep

The goal of the optimisation is to determine the best choice of tab chord length that will function satisfactorily over the largest operating range. Since this problem is still fairly small, and only consists of a single design variable, it is possible to perform a parameter sweep over the entire range of $E_t$ which allows the visualisation of the objective function. This is shown in Figure 5.27.

The first figure (Figure 5.27(a)) shows the function as determined using the SQP method for the inner optimisation, and the second figure (Figure 5.27(b)) shows the function as determined using the REGA method. In both cases the outer optimisation is a REGA as described previously.

It can be seen that the two graphs are identical, which merely reinforces that both optimisation algorithms provide the same optimal values. The graphs themselves also display a key feature: they have a clear minimum, in this case where the tab chord length is $32{,}6\,\%$ of the aileron chord length, with a minimum cost of $J = 0{,}166$. They are also well behaved, i.e. there are no local minima and the graph is smooth with no discontinuities.

The aileron chord length for these simulations was taken to be $E_a = 0{,}25$, which is $25\,\%$ of the total wing chord length. A normalised chord length is used to allow for scalability (an attribute that is very important for the case of §5.9). This means that the optimal tab chord length, as read off from the graph, is given to be

$$E_t = \left(\frac{32{,}6}{100}\right) E_a = (0{,}326)(0{,}25) = 0{,}0816 \tag{5.7.4}$$

which means that the optimal tab chord length is approximately $7{,}65\,\%$ of the total wing chord length. The fact that the cost is non-zero at the minimum indicates that there is no tab length which can satisfy all the objectives ideally over the whole operating range.

#### 5.7.4.2 Linearised Thin Aerofoil Theory – $E_t$ Optimisation

The objective function for the linearised case has been plotted in Figure 5.27; thus it is known that a minimum exists. The complete dual-layer optimisation is now applied to determine this optimal point without prior knowledge of what the objective function looks like, but under the assumptions that it is well behaved.

Both parts of the optimisation made use of real-encoded genetic algorithms since it has been established that the results of the inner optimisation are the same regardless of whether SQP or REGAs are used, and for the non-linear thin aerofoil theory it is not possible to make use of SQP. The optimisation made use of parameters as follows for both REGAs (refer to §4.5 for descriptions):

$$\begin{aligned} k_{\max} &= 300 & P_s &= 20 \\ P_E &= 15\,\% & P_C &= 25\,\% \\ P_P &= 40\,\% & \beta_{P_P} &= 0{,}1 \\ P_M &= 20\,\% & n_e &= 5 \\ \beta_{n_e} &= 1 \times 10^{-4} \end{aligned}$$

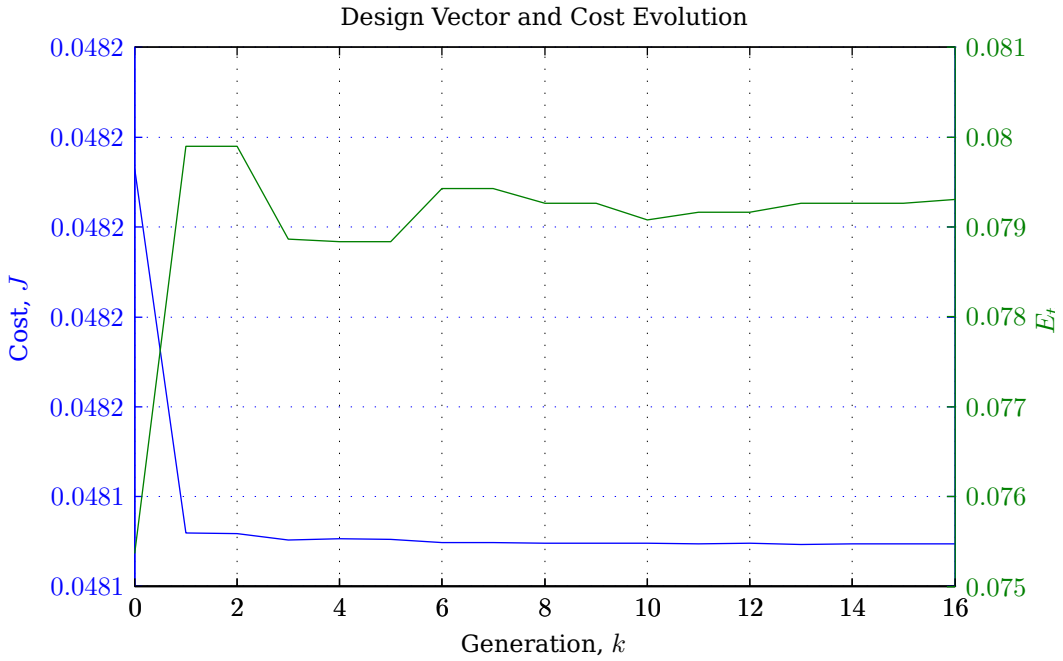


**Figure 5.28** – Graph showing the evolution of the tab chord length and the cost function as the outer optimisation progresses.

The final solution delivered by the optimisation gives $E_t = 0{,}0793$, which is $31{,}72\,\%$ of the aileron chord length. This was obtained after sixteen generations with a total simulation time of 2 hours and 40 minutes. The minimum cost is stated to be $J = 0{,}0481$, which is much lower than that of the parameter sweeps of §5.7.4.1. While this may sound suspect, it is accounted for as follows: With the parameter sweeps the operating region was divided into $1\,^\circ$ intervals along each axis while for the optimisation the aileron deflection interval was reduced to $1{,}87\,^\circ$ (or 23 points).

There is thus a reduction in the total number of operating points evaluated by the inner optimisation and since the overall cost is determined as a *summation* of the minimum costs of each operating point, the reduction in the number of operating points results in an associated reduction in the total cost for any given $E_t$.

The actual value of the cost is not too important, and does not have a large effect on the result of the optimisation, provided that the form, or shape, of the minimum cost surface is maintained. If too few points are selected over the range, the results will be biases towards those specific operating points and this *will* affect the shape of the objective function. Choosing too many points also has a negative side effect in that the time required to perform the optimisation increases greatly.

A history of the optimisation is given in Figure 5.28. The figure shows how the design variable, $E_t$ varies with each generation of the genetic algorithm, and also the cost related to that specific value of the design variable. It can be seen how the cost decreases as the optimisation progresses, until there is no more notable change in cost or design variable, or, in other words, the optimisation has converged.

Comparing the optimum values obtained from reading off the sweep graphs ($E_t = 0{,}0816$) and that obtained from the algorithm ($E_t = 0{,}0793$), it can be seen that the values are very close (a difference of $0{,}0023$ or $0{,}23\,\%$ of the total chord), thus indicating that the minimum was successfully obtained. For a chord length of $3\,\mathrm{m}$ the difference in the optimal tab chord lengths is less than $7\,\mathrm{mm}$.

Now that the optimal tab chord length has been determined, it is desired to examine the performance of this optimal tab over the operating range. To examine this, a similar process is followed as in §5.5 and §5.6 where the coefficients used in the objective function are examined, and compared to the equivalent values of the old system. Also examined are the deflection angles of the tab and aileron in order to achieve these values over the operating range.

A graph indicating the minimum attainable costs associated with each operating point is given in Figure 5.29. It can be seen from the cross-sectional plots (Figure 5.29(b)) that there are clearly regions throughout the operating range where the objective can be satisfied locally, i.e. no aileron hinge moment and the same lift characteristics; however, there is also a large range where it is not possible and either the lift is not the same, the aileron hinge-moment is non-zero, or a compromise between the two is attained.

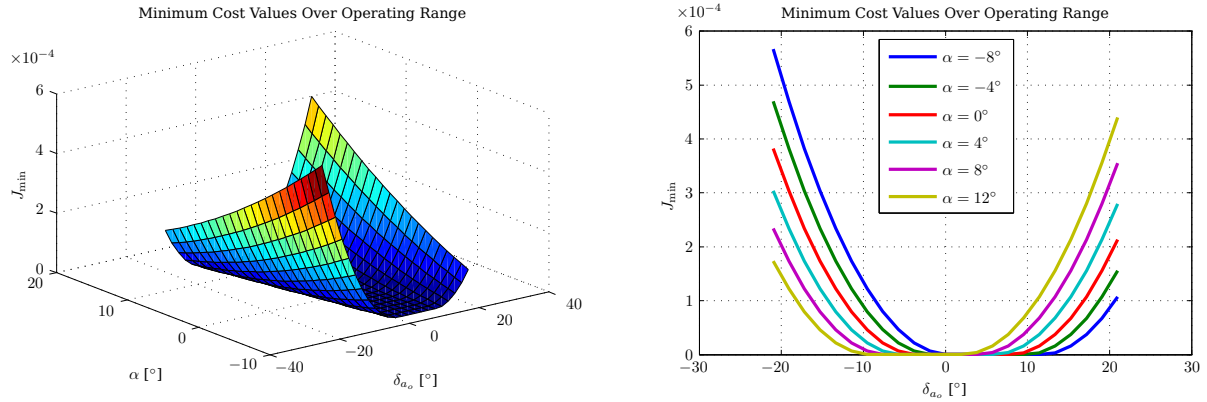


(a) (b)

**Figure 5.29** – The minimum cost attainable over the operating range. The values at each operating point are summed to give the total. Figure 5.29(a) shows a three-dimensional surface view, while Figure 5.29(b) shows cross-sections at regular intervals of $\alpha$.

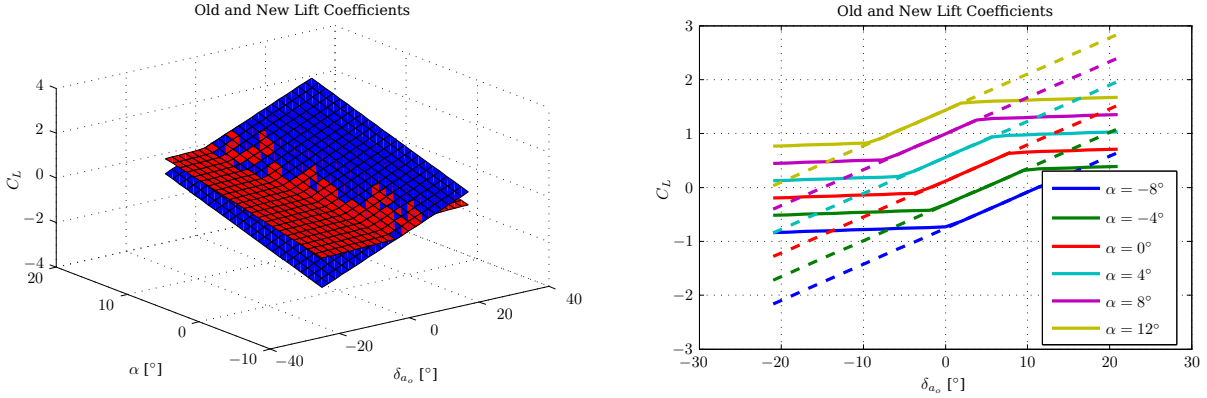


(a) (b)

**Figure 5.30** – A comparison between the old and new lift coefficient values over the operating range. Figure 5.30(a) shows a three-dimensional surface view, while Figure 5.30(b) shows cross-sections at regular intervals of $\alpha$.

The main performance characteristic is determined based on the lift coefficient which is shown in Figure 5.30. The general trends are shown in the surface plot, but are more easily visible when looking at the cross-sectional information. In Figure 5.30(b), and other cross-sectional plots where old and new values are compared, the dashed lines indicate the old (original) values while the solid lines indicate the values obtained using the tab. For surfaces (as shown in Figure 5.30(a)), blue surfaces indicate old values while red or green surfaces indicate new values.

From Figure 5.30 it is possible to clearly see the the region where the lift condition has been satisfied, though it should be noted that according to the linear thin aerofoil theory, performance degrades substantially outside this region. In the region where the lift conditions are satisfied, the difference in old and new lifts over the angle of attack range is bounded by an absolute value of $5 \times 10^{-3}$. The largest deviation outside this region is $1{,}323$ which is more than $250$ times larger.

Examining the aileron hinge moment coefficient in Figure 5.31, it can be seen that the aileron hinge moment *has* been reduced to very close to zero over the entire operating range. The maximum absolute value of the new coefficient is $2{,}042 \times 10^{-3}$, which, when compared to the maximum value of the aileron only configuration of $34{,}89 \times 10^{-3}$, can be seen to be 17 times smaller. This, when compared to the effect on the lift coefficient, leads to the conclusion that the aileron hinge moment objective may have been weighted too heavily.

In order to reduce the aileron hinge moment, the tab now has a hinge moment that needs to be overcome. Figure 5.32 shows the tab hinge moment. Again, the region where the lift and aileron hinge moments are satisfactory can be seen clearly on the graph. The rapid change in the gradients of the cross-sectional graphs can be attributed to both the aileron and tab being deflected to their maxima, as will be seen in

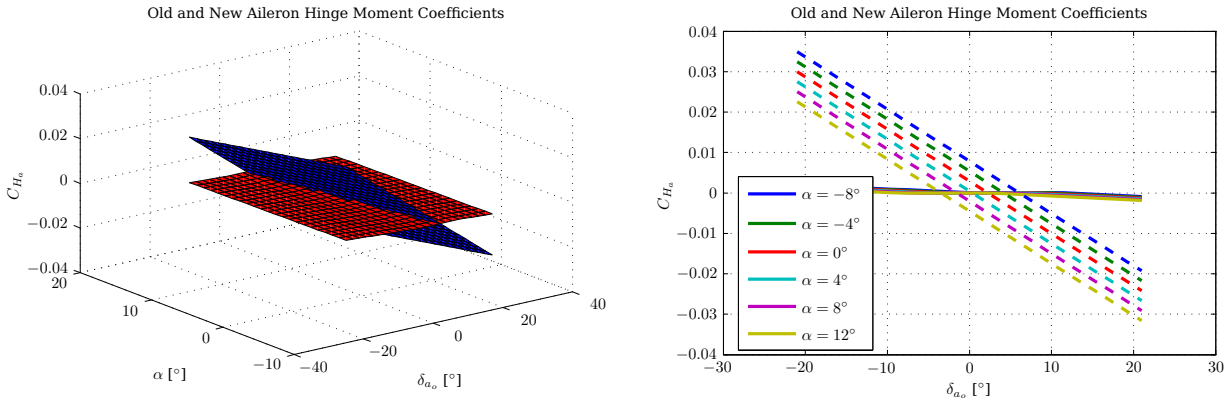


(a) (b)

**Figure 5.31** – A comparison between the old and new aileron hinge moment coefficient values over the operating range. Figure 5.31(a) shows a three-dimensional surface view, while Figure 5.31(b) shows cross-sections at regular intervals of $\alpha$.

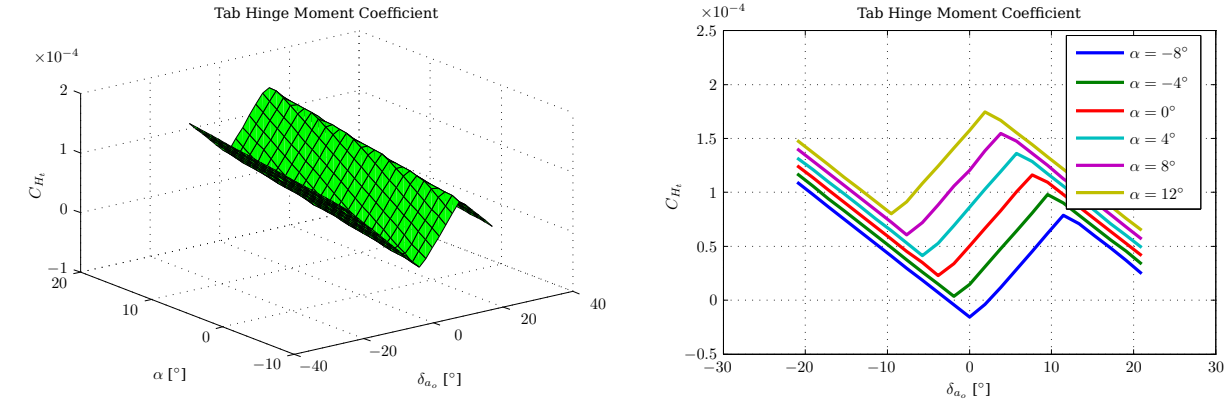


(a) (b)

**Figure 5.32** – The tab hinge moment coefficient values over the operating range. Figure 5.32(a) shows a three-dimensional surface view, while Figure 5.32(b) shows cross-sections at regular intervals of $\alpha$.

Figures 5.33 and 5.34. Examining the magnitudes of the tab hinge moment coefficients, it is possible to see that the values are very similar to those of the new aileron hinge moment coefficient. This indicates that similar "sized" actuators can be used to deflect both, and these actuators will be substantially smaller than those used for the original aileron actuator, especially when considering the reduction of the aileron hinge moment coefficient's maximum values.

Figures 5.33 and 5.34 show the optimal deflection angles of the aileron and tab respectively which result in the lift and aileron hinge moment conditions mentioned above. It can be seen from both graphs that within the region where performance is satisfactory both the tab and the aileron hove non-maximum deflection angles. As soon as either the tab or the aileron is deflected to its limit the lift and hinge moment performance decreases rapidly.

This re-enforces the idea that (according to the linearised thin aerofoil theory) there is only a small region where the use of this optimal tab is suitable; however, it needs to be considered that the deviations from the ideal appear strongly where the small-angle approximations used during the linearisation process no longer hold. This suggests that, while it is possible to obtain a reasonable-looking solution from the linearised theory within a suitable amount of time, this solution may or may not be valid in practice. This suggests that the non-linear theory should be examined, the topic of §5.7.4.3.

### 5.7.4.3 Non-Linear Thin Aerofoil Theory – $E_t$ Sweep

In §5.7.4.1, the linearised thin aerofoil theory is used to arrive at a first attempt at an optimal tab. It was noted that performance is not satisfactory over the entire operating range and it is speculated that the use of the linearised theory outside of its region of validity may have lead to some misleading results. This

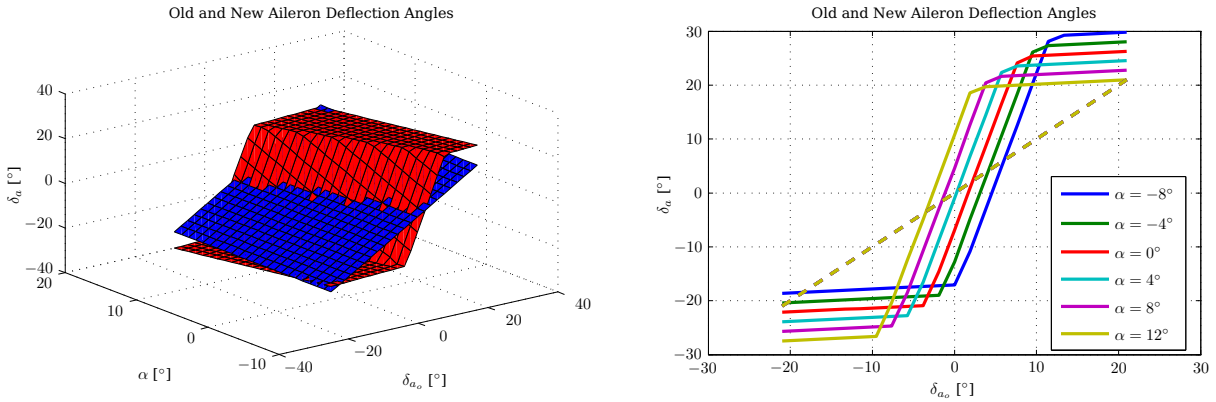


(a) (b)

**Figure 5.33** – A comparison between the old and new aileron deflection angles over the operating range. Figure 5.33(a) shows a three-dimensional surface view, while Figure 5.33(b) shows cross-sections at regular intervals of $\alpha$.

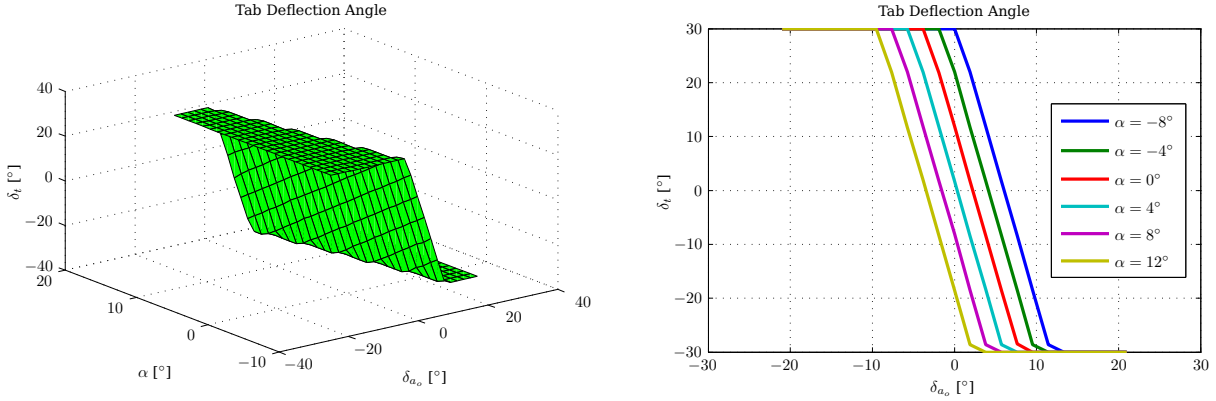


(a) (b)

**Figure 5.34** – The tab deflection angle over the operating range. Figure 5.34(a) shows a three-dimensional surface view, while Figure 5.34(b) shows cross-sections at regular intervals of $\alpha$.

hypothesis is now tested by performing the same optimisation with the same parameters again, but making use of the *non-linear* thin aerofoil theory, i.e. without small-angle approximations, and taking higher order components of the Fourier series into account.

The first step was to once again perform a parameter sweep since this will allow the comparison of the two objective functions. The operating point grid used for this sweep is the same as for the linearised case: with $1\,^\circ$ steps for both the old aileron deflection angle ad the angle of attack. A portion of this sweep is done at a much higher $E_t$ resolution than that of the linear versions for values less than $30\,\%$ of the aileron chord since it was discovered that some of the detail around the minimum was being lost due to step sizes that were too large.

When comparing Figure 5.35 to Figure 5.27 it is immediately apparent that the linearisation does have an effect on the shape of the cost function, especially since large angles are used.

Reading off the graph it is possible to determine the optimal tab chord length based on the non-linear thin aerofoil theory. This is seen to be $12{,}6\,\%$ of the aileron chord length, which translates to $E_t = 0{,}0315$, which is substantially smaller than the tab chord length obtained in §5.7.4.2. The minimum cost associated with this tab chord length is $J = 0{,}001\,25$.

The shape of the outer objective function shown in Figure 5.35 can also be seen to have a clear minimum, as with Figure 5.27, though the general shape is different. There are, however, still no other (local) minima over the range of $E_t$, making this function well-behaved.

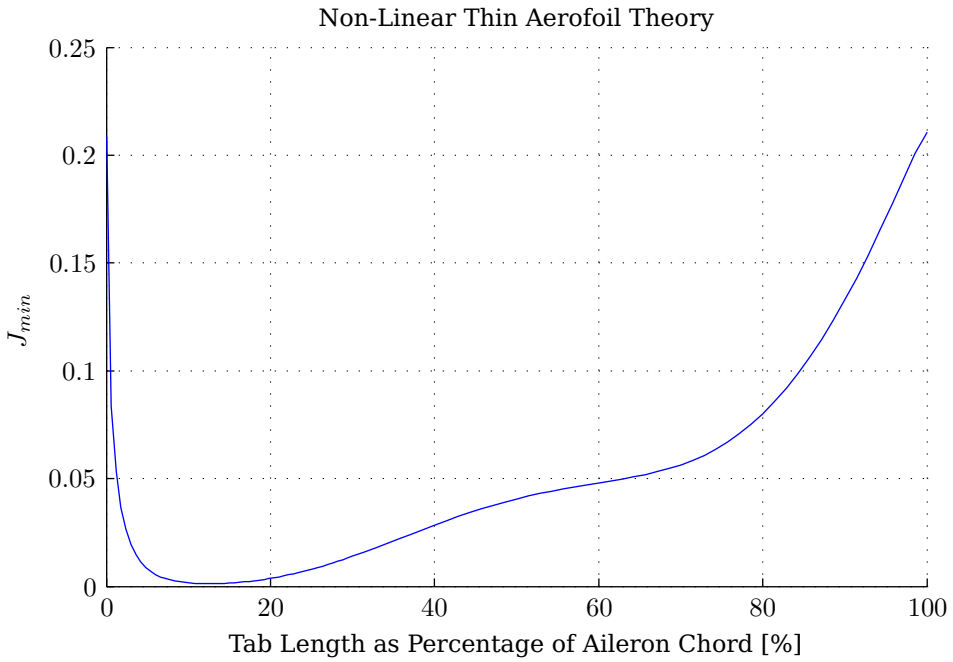


**Figure 5.35** – Outer cost function value as $E_t$ varies for the linearised thin aerofoil theory case.

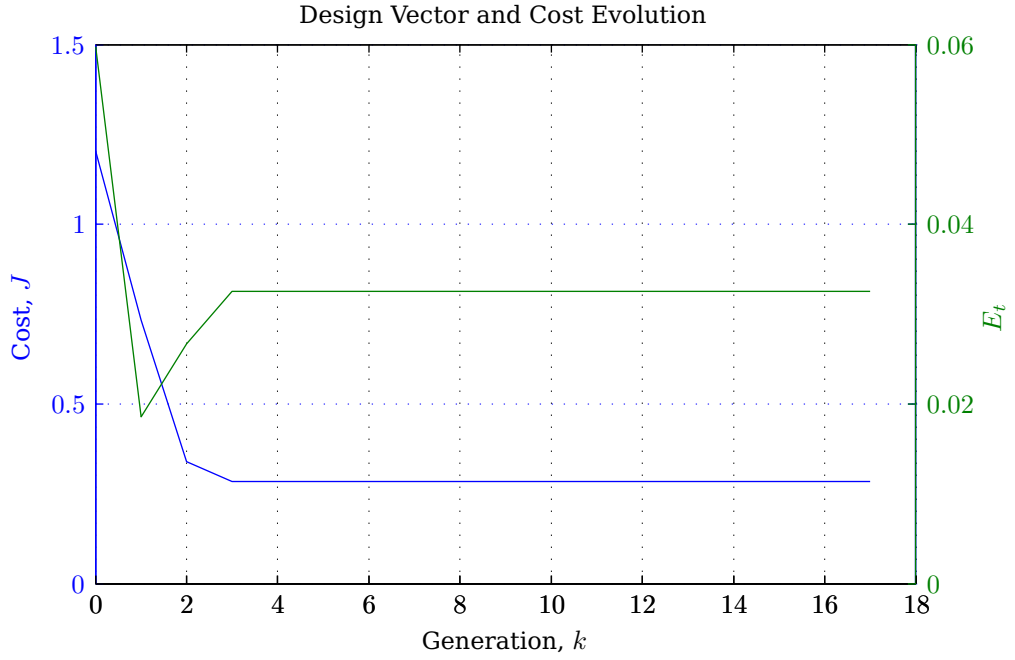


**Figure 5.36** – Graph showing the evolution of the tab chord length and the cost function as the outer optimisation progresses.

#### 5.7.4.4 Non-Linear Thin Aerofoil Theory – $E_t$ Optimisation

Having established that the non-linear thin aerofoil theory can potentially deliver better results, the optimisation is applied to this case. It may be noted that a minimum has already been obtained by examining the parameter sweep of Figure 5.35; however, should results prove favourable in this section, the non-linear thin aerofoil theory will be used in more complex examples where performing the brute-force parameter sweep is not viable.

The optimisation parameters are kept the same as in §5.7.4.2, and a history of the optimisation is given in Figure 5.36. It can be seen that the minimum is obtained very quickly (in terms of the number of generations), but that it still takes several generations further for the convergence criteria to be satisfied (see §4.4.5).

The optimisation process produces an optimal tab chord length: $E_t = 0{,}0325$ after 17 generations with a

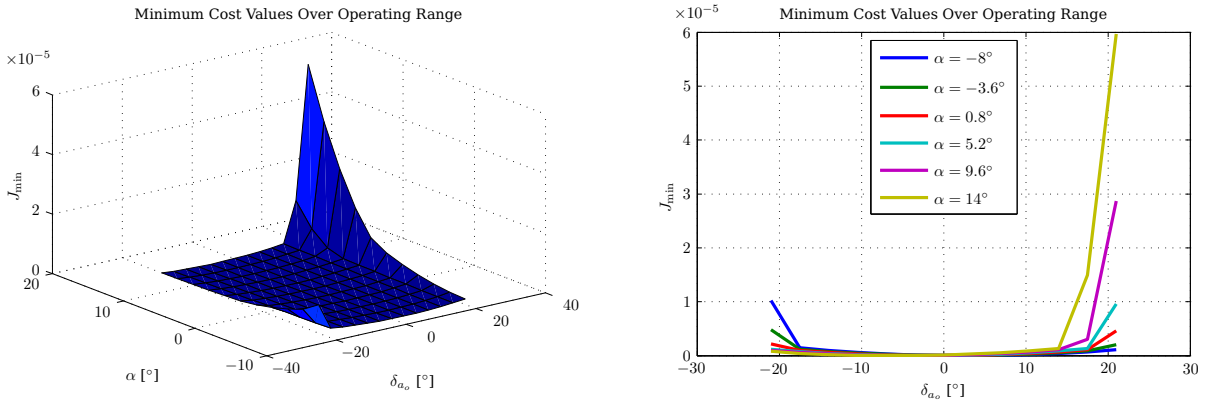


(a) (b)

**Figure 5.37** – The minimum cost attainable over the operating range. The values at each operating point are summed to give the total. Figure 5.37(a) shows a three-dimensional surface view, while Figure 5.37(b) shows cross-sections at regular intervals of $\alpha$.

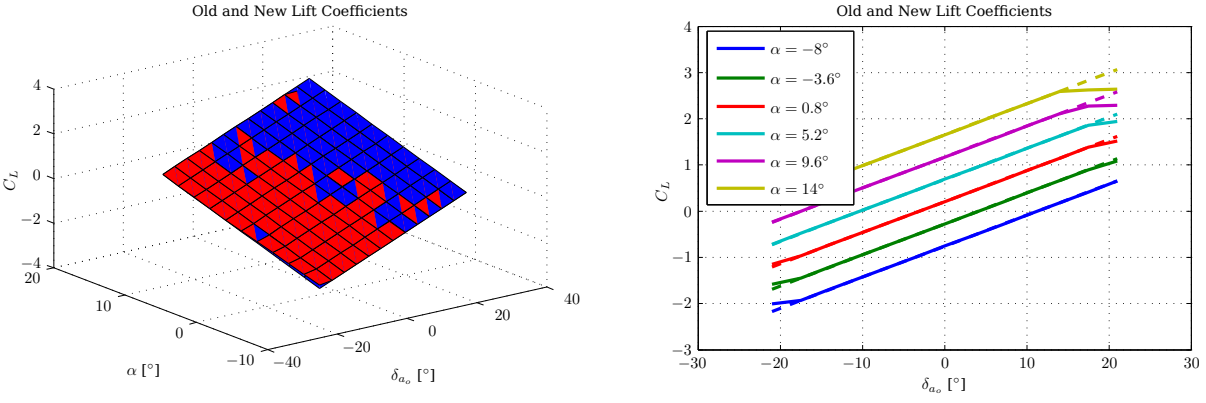


(a) (b)

**Figure 5.38** – A comparison between the old and new lift coefficient values over the operating range. Figure 5.38(a) shows a three-dimensional surface view, while Figure 5.38(b) shows cross-sections at regular intervals of $\alpha$.

minimum cost of $J = 2{,}8337 \times 10^{-4}$. Again the optimisation was done on a less dense operating point grid (11 $\alpha$ steps by 13 $\delta_{a_o}$ steps) in order to obtain a result within a reasonable amount of time (23 hours 27 minutes), and as such the minimum cost is again much smaller than that of parameter sweep.

This is once again due to the summation by the multi-point optimisation of the minimum costs determined by the inner optimisation loop at each of the operating points in the grid. The grid is, however, still dense enough to provide suitable results and it is reinforced that the actual value of the minimum cost is not really relevant, as long as the shape of the objective function is still accurate.

The optimum tab chord length obtained is comparable to that obtained in the sweep with a difference of only $0{,}001$ which is about $0{,}1\,\%$ of the total chord length. For a chord length of $3\,\mathrm{m}$ this equates to a $3\,\mathrm{mm}$ difference between the two values in real-world parameters.

The evaluation of this tab length is provided using Figures 5.37 to 5.42.

Examining the form of the minimum attainable cost graph shown in Figure 5.37 it can be seen that there is a very large area which is very close to flat, indicating similar minimum costs, which can be bounded by a value of $1{,}328 \times 10^{-6}$. This can be seen over a large portion of the operating range, except for the region relating to large positive aileron deflection with large angle of attack, which has a substantially higher minimum cost of $5{,}97 \times 10^{-5}$ which is almost $45$ times larger than the flat region.

When looking at the deflection angles of the tab and aileron, it is possible to see that tab has reached its maximum deflection angle, and is thus not able to deliver enough counter-hinge moment. This then becomes a compromise region where the lift coefficient suffers a reduction, as shown in Figure 5.38. When examining the lift coefficient over the operating range, both as a surface and with the cross-sectional

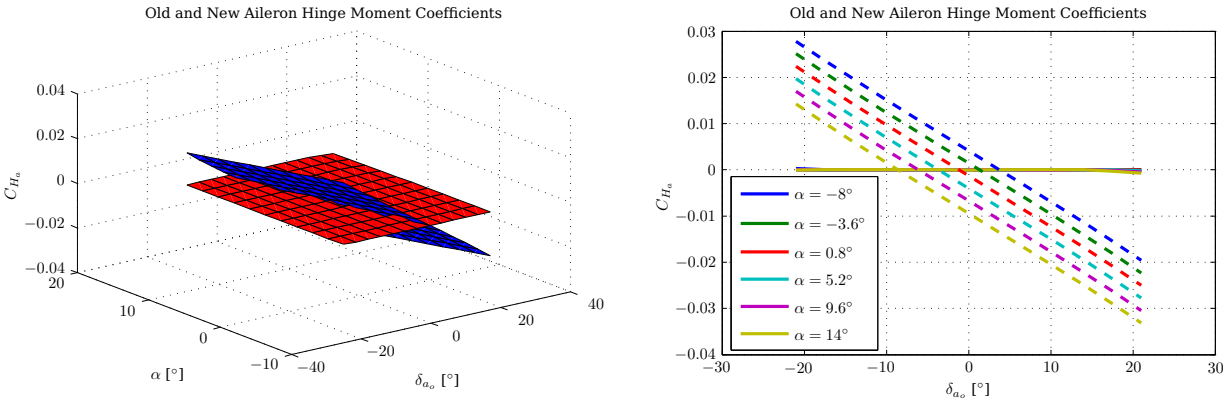


(a) (b)

**Figure 5.39** – A comparison between the old and new aileron hinge moment coefficient values over the operating range. Figure 5.39(a) shows a three-dimensional surface view, while Figure 5.39(b) shows cross-sections at regular intervals of $\alpha$.

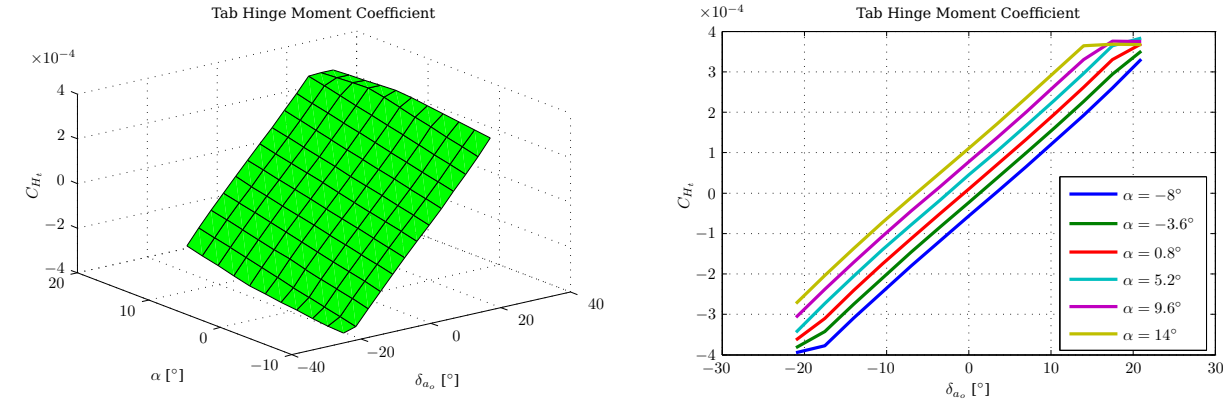


(a) (b)

**Figure 5.40** – The tab hinge moment coefficient values over the operating range. Figure 5.40(a) shows a three-dimensional surface view, while Figure 5.40(b) shows cross-sections at regular intervals of $\alpha$.

views, it can be seen that in most cases the new lift coefficient values are the same as those for the old configuration with a maximum absolute deviation between the old and new values of $6{,}362 \times 10^{-3}$, except for the large $+\delta_{a_o}$ and $+\alpha$, and large $-\delta_{a_o}$ and $-\alpha$ where the deviation is $423{,}1 \times 10^{-3}$, approximately $60$ times larger.

The less satisfactory results of these regions are due to the non-zero camber of the aerofoil. As can be seen by the blue surface in Figure 5.38(a), which represents the old lift coefficient over the operating range, the lift coefficient values are asymmetrical, both as the angle of attack varies, as well as over the old aileron deflection range. In other words, at $\alpha = 0\,°$ and $\delta_{a_o} = 0\,°$, the aerofoil still has non-zero lift, which would not be the case for a symmetrical aerofoil.

Examining the hinge-moment coefficients shows that the new aileron hinge moment coefficients (Figure 5.39) are substantially reduced over the entire operating range as desired and the tab hinge moment coefficient values (Figure 5.40) are also suitably small, indicating that while it may not be possible to eliminate the aileron actuator completely, both aileron and tab actuators can be much smaller than the current aileron actuator.

The maximum absolute new aileron hinge moment coefficient value over the entire operating range is found to be $681{,}2 \times 10^{-6}$ versus the maximum of the old system of $33{,}15 \times 10^{-3}$. The new maximum is $48$ times smaller than that of the old system.

The new aileron deflections (solid lines) shown in Figure 5.41 are shown to be slightly larger in magnitude over the old values (shown by the dashed lines), which is to be expected by the reasoning of §3.8, since the effective aileron chord length has decreased by $12{,}6\,\%$. It can be seen, though, that for the extremes where the tab deflection saturates (Figure 5.42), the difference starts to decrease. This is caused by the

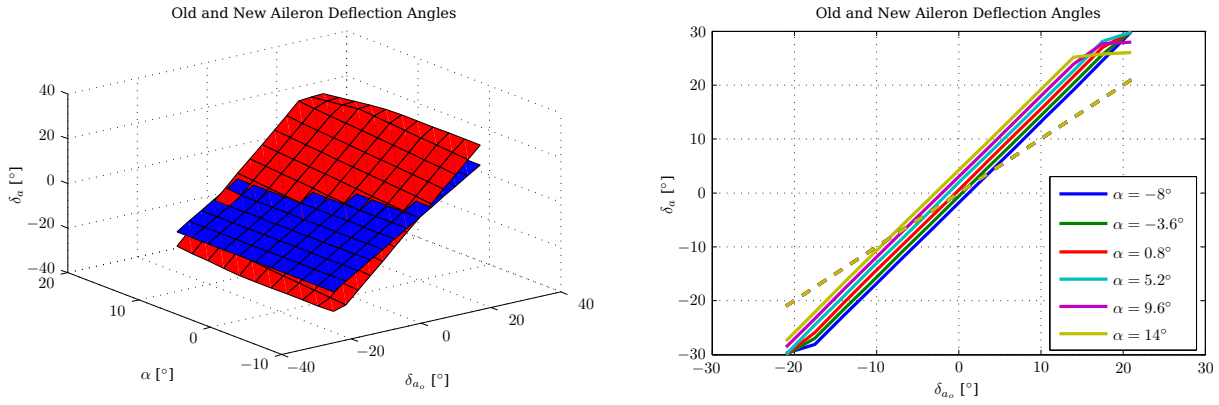


(a) (b)

**Figure 5.41** – A comparison between the old and new aileron deflection angles over the operating range. Figure 5.41(a) shows a three-dimensional surface view, while Figure 5.41(b) shows cross-sections at regular intervals of $\alpha$.

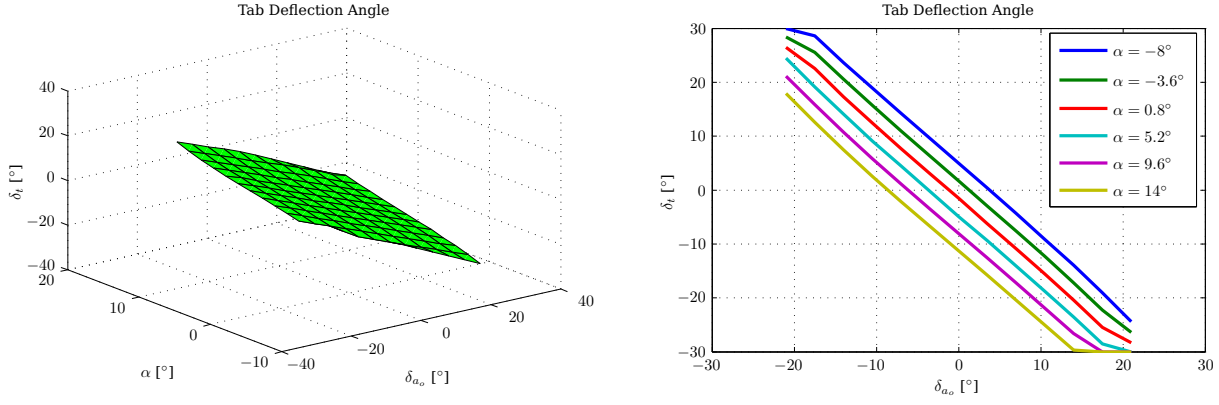


(a) (b)

**Figure 5.42** – The tab deflection angle over the operating range. Figure 5.42(a) shows a three-dimensional surface view, while Figure 5.42(b) shows cross-sections at regular intervals of $\alpha$.

effect the tab has on the aileron hinge moment being less pronounced, and in order to not increase the aileron hinge moment component of the cost too greatly, a smaller deflection of the aileron is used. This has the negative side-effect of reducing the lift, as was seen in Figure 5.38.

## 5.8 Optimal Tab and Aileron Chord Lengths: A Non-Gradient-Based Two-Dimensional Optimisation

In §5.7.4.1 to §5.7.4.4, only the tab chord length was varied as a percentage of the existing aileron chord length since it is desired to maintain the same geometry of the existing wing structure. From the results of these sections it can be seen that by simply replacing the system directly it is not possible to achieve the same performance over the entire operating range.

It is expected, then, that some of these physical constraints need to be relaxed, thus providing extra design variables that can be adjusted in an attempt to expand the operating region in which the new tab/aileron system would be suitable. One possible variation on the previous optimisations, then, is to allow the aileron chord length to be varied as well as the tab chord length, thus providing the new design vector $\mathbf{x} = (E_t, E_a)$. This still allows the two-dimensional thin aerofoil theory used thus far to be applied. Since the design vector contains two elements, this is a two-dimensional optimisation problem.

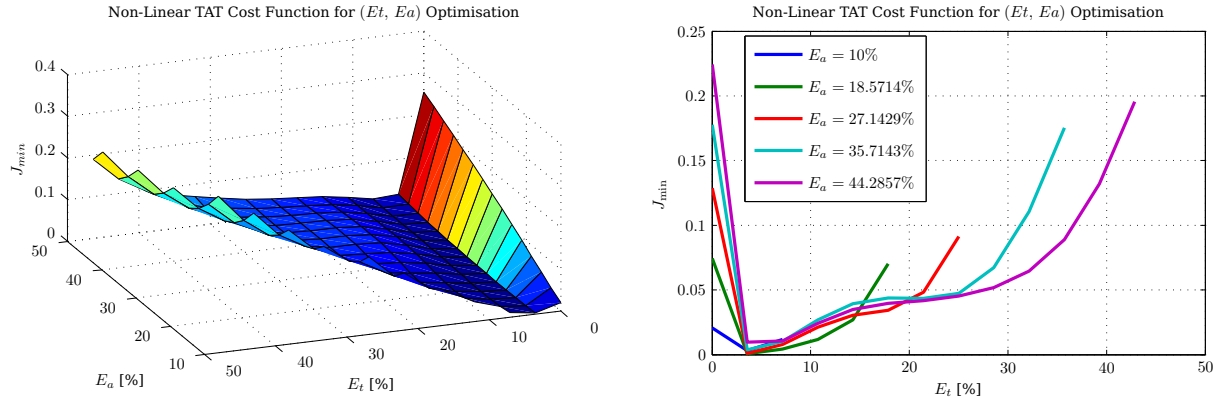


(a) (b)

**Figure 5.43** – Outer cost function value as $E_t$ and $E_a$ vary for the non-linearised thin aerofoil theory case. Figure 5.43(a) shows a three-dimensional surface view, while Figure 5.43(b) shows cross-sections at regular intervals of $E_a$.

### 5.8.1 Objective Function and Constraints

The *objective function* used in the previous section remains the same, except that now both $E_t$ and $E_a$ are varied during the optimisation. The tab constraints were defined in terms of constants determined at the beginning of the optimisation, related to the fixed aileron chord length. Since the tab cannot be larger than the aileron, and the aileron chord length is now allowed to vary, this constraint needs to be modified to "dynamically" take into account the varying aileron chord length. Results from the previous optimisations also suggest that the tab chord length will be much smaller than the aileron chord length, thus validating the previous choice of half the aileron chord length:

$$0 \leq E_t \leq \frac{1}{2} E_a$$

which will replace the previous constraints on $E_t$. Since the aileron chord length has been added to the design problem, constraints need to be applied to $E_a$ as well:

$$E_{a_{\min}} \leq E_a \leq E_{a_{\max}}$$

which results in the following four constraint functions for the outer optimisation, in standard form:

$$\begin{aligned} g_1(E_t, E_a) &= -E_t \leq 0 \\ g_2(E_t, E_a) &= E_t - \tfrac{1}{2} E_a \leq 0 \\ g_3(E_t, E_a) &= -E_a + E_{a_{\min}} \leq 0 \\ g_4(E_t, E_a) &= E_a - E_{a_{\max}} \leq 0 \end{aligned} \tag{5.8.1}$$

The values used for the maximum and minimum allowable aileron chord lengths are $0{,}15 \leq E_a \leq 0{,}5$, or between $15\,\%$ and $50\,\%$ of the total wing chord.

The inner optimisation components remain unchanged.

### 5.8.2 Results

The optimisation makes use of the REGA for both the outer and inner optimisations as before; however, only the non-linear thin aerofoil theory is used since it has already been established that the linearisation is not valid over the entire operating range.

#### 5.8.2.1 $E_t$ and $E_a$ Parameter Sweep

In the spirit of the preceding sections, a parameter sweep is again attempted, though since the optimisation problem has become multi-dimensional, a very low operating point resolution was used to generate results in a reasonable amount of time. The results shown in Figure 5.43 provide an approximation of the actual objective function which will be optimised. Note that only the region where $E_t \leq E_a$ is shown.

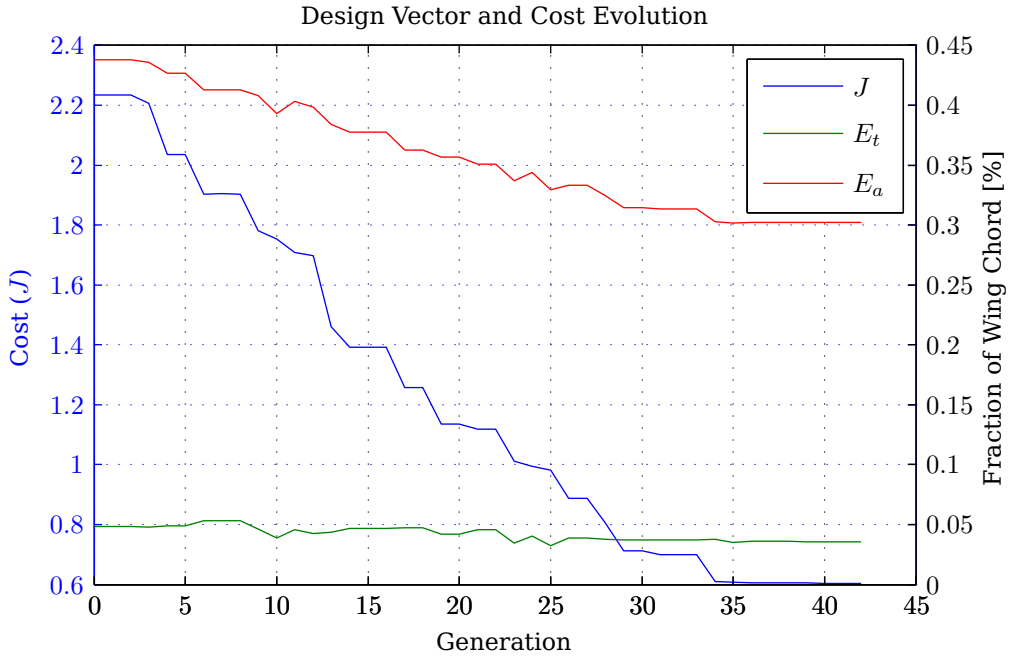


**Figure 5.44** – Graph showing the evolution of the tab chord length and the cost function as the outer optimisation progresses.

Due to the low resolution of the graph the region of interest where the minimum is expected to be found is not accurately represented. This means that while a minimum may be read off the graph, there is no guarantee that the values are valid. For information, the optimum values of the design variables as obtained from Figure 5.43 are $E_t = 0{,}0357$ and $E_a = 0{,}186$ with the associated cost of $J = 6{,}22 \times 10^{-4}$.

#### 5.8.2.2 Optimisation Results

The optimisation converged after $56$ hours and $35$ minutes with the solution: $E_t = 0{,}0358$ and $E_a = 0{,}302$. The optimal tab length appears to correlate well with that obtained in the parameter sweep, though the aileron chord lengths do not match. Since in previous sections the optimisation (which does not rely on only the discrete grid chosen for the sweep) has shown itself to provide accurate minimums, the solution determined by the optimisation is thus chosen as the "correct" optimal solution.

A history of the optimisation evolution is shown in Figure 5.44.Notice the steadily decreasing cost as the optimisation executed, typical of genetic algorithms. Forty-two generations were required for convergence and the final cost was $J = 0{,}0411 \times 10^{-4}$. Since the same operating region grid was used for both the sweep and the optimisation, it is possible to compare the costs. The optimisation converged on a cost $30\,\%$ smaller than that shown in Figure 5.43. This shows how inaccurate results can be obtained from the graph made up of discrete sampling points in the design space.

The minimum cost, aerodynamic coefficients and deflection angles are plotted over the operating range as before, and these are shown in Figures 5.45 to 5.50.

Examining Figure 5.45, which gives the minimum cost for each of the discrete operating points used for the optimisation, once still cannot see a perfect response. The notable deviation is the region of large $+\alpha$ and large $+\delta_{a_o}$, as before. Referring back to Figure 5.37, where only the tab chord length was varied, it is possible to see that the minimum cost graphs have the same form, and in both cases the large $+\alpha$, large $+\delta_{a_o}$ show a peak many times larger than the other regions on the graph. The similarity implies that many of the discussions of §5.7.4.4 are also applicable here.

On careful inspection of the cross-sectional views (Figure 5.45(b)), it is possible to see that the region of similar low minimum cost is slightly smaller in the case of the two-dimensional optimisation. The aileron chord length has increased from $25\,\%$ to $30{,}2\,\%$ of the total wing chord, which means a larger aileron hinge moment is required to deflect the control surface. As such it can be seen that the tab chord length has also increased from $3{,}25\,\%$ to $3{,}58\,\%$ of the total wing chord. Noting, however that the chord now makes up only $11{,}85\,\%$ of the total aileron chord length, versus the $13\,\%$ of the previous case, it is expected that some performance degradation will occur.

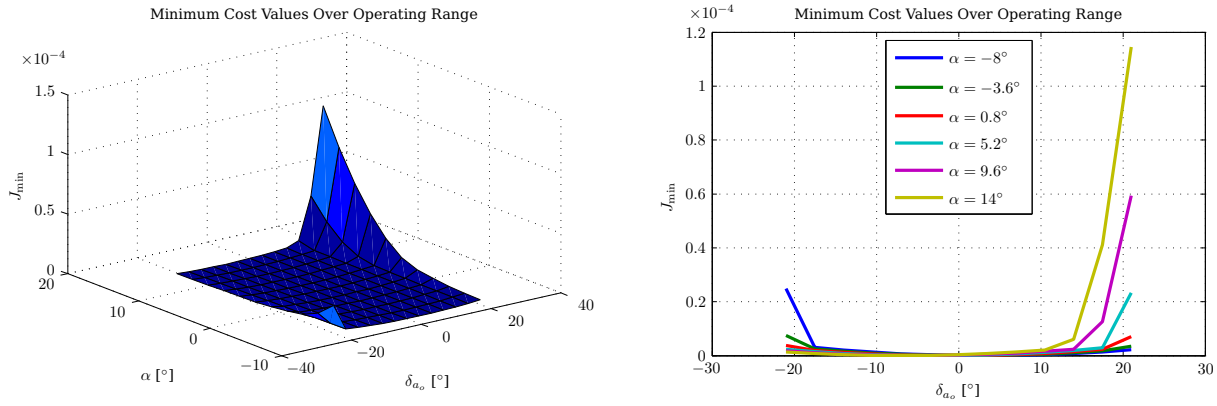


(a) (b)

**Figure 5.45** – The minimum cost attainable over the operating range. The values at each operating point are summed to give the total. Figure 5.45(a) shows a three-dimensional surface view, while Figure 5.45(b) shows cross-sections at regular intervals of $\alpha$.

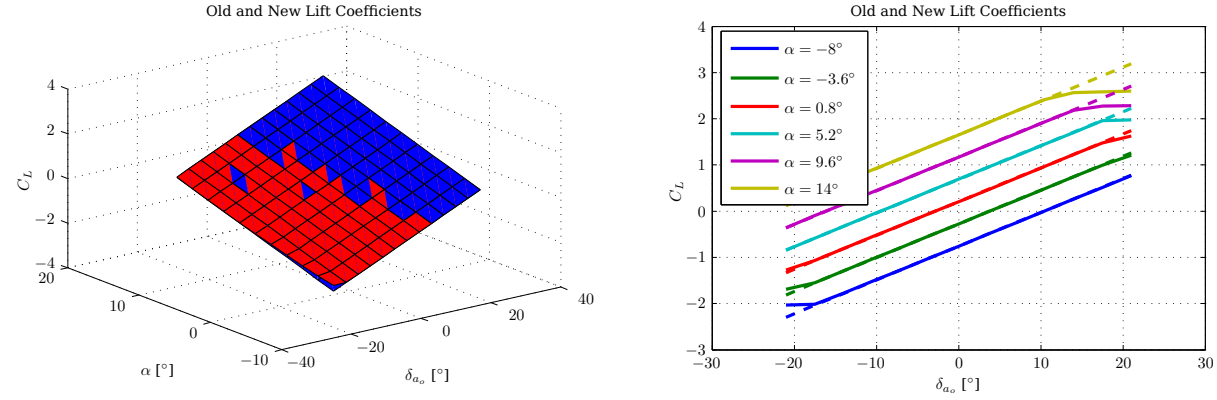


(a) (b)

**Figure 5.46** – A comparison between the old and new lift coefficient values over the operating range. Figure 5.46(a) shows a three-dimensional surface view, while Figure 5.46(b) shows cross-sections at regular intervals of $\alpha$.

This slight degradation can be seen in the lift coefficient which is shown in Figure 5.46, where the flattening of the gradients occurs at lower $\delta_{a_o}$ deflections than for the one-dimensional optimisation. Performance is still very satisfactory within this reduced optimal operating region (a maximum difference of $0{,}1058$ is found) as can be seen from the equivalent old (dashed) and new (solid) values shown in Figure 5.46(b).

The aileron hinge moment coefficient still displays suitable performance over the entire operating range, with a maximum new value of $735{,}3 \times 10^{-6}$ which is $68{,}7$ times smaller than the old maximum value of $50{,}52 \times 10^{-3}$. Since the aileron hinge moment is not much different from that shown in Figure 5.39 it is expected that the tab hinge moment coefficient (Figure 5.48) will have a larger magnitude over the operating range versus that shown in Figure 5.48, which is indeed the case.

Aileron deflection angles have not been affected greatly, though for the large angles of attack the flattening in the gradient has occurred at a lower $\delta_{a_o}$. The gradients of the tab deflection angles shown in Figure 5.50 can be seen to have a steeper gradient in both the $\alpha$ and $\delta_{a_o}$ directions, which is expected since larger counter hinge moments are required than those of Figure 5.42.

This correlates with the tab hinge moment coefficient shown in Figure 5.48.

### 5.8.3 Comparing the $E_t$ and $E_t,\ E_a$ Optimisations

It is expected that with more degrees of freedom ($E_t$ and $E_a$) that a better result would be obtained than where there is only one design variable ($E_t$), as in §5.7. As has just been seen this is not the case, with the

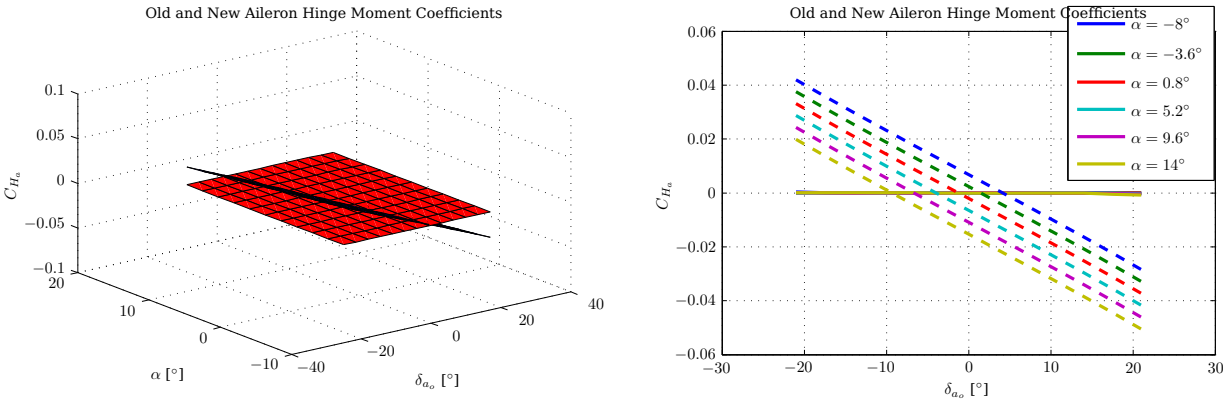


(a) (b)

**Figure 5.47** – A comparison between the old and new aileron hinge moment coefficient values over the operating range. Figure 5.47(a) shows a three-dimensional surface view, while Figure 5.47(b) shows cross-sections at regular intervals of $\alpha$.

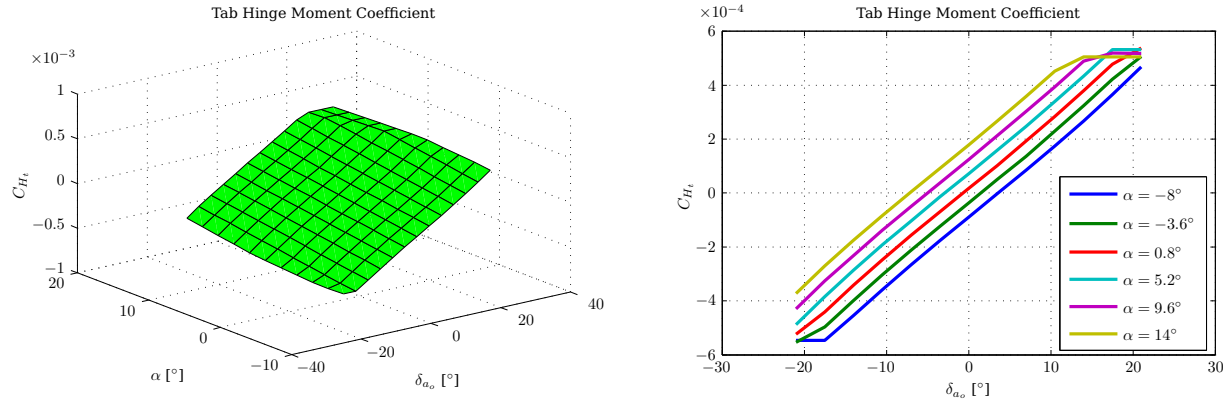


(a) (b)

**Figure 5.48** – The tab hinge moment coefficient values over the operating range. Figure 5.48(a) shows a three-dimensional surface view, while Figure 5.48(b) shows cross-sections at regular intervals of $\alpha$.

($E_t$, $E_a$) optimisation providing a smaller achievement region than the $E_t$ only case.

While there are a number of factors that could have influenced the result, the two primary reasons are: premature convergence and low operating point grid resolution.

As was stated in Chapter 4, the REGA is not absolutely perfect and it is possible that in this case the convergence criteria were met prematurely. The only means to be reasonably certain that the result is correct would be to perform this same optimisation several times, and then comparing the results to ensure the same design vector is obtained.

The low operating grid resolution chosen for the optimisation is expected to play a role, as fewer operating points are evaluated when compared to the previous optimisations. While this was done in order to obtain results timeously, the optimisation should be re-performed at a higher resolution, at the expense of a much greater execution time.

## 5.9 A Two-Dimensional Optimisation Using the Three-Dimensional Aerodynamic Approximations

The final optimisation makes use of the three-dimensional aerodynamic approximation given in §3.7. This approach allows the *rolling moment* to be taken into account, which is desired since this is the primary metric by which the new configuration will be measured.

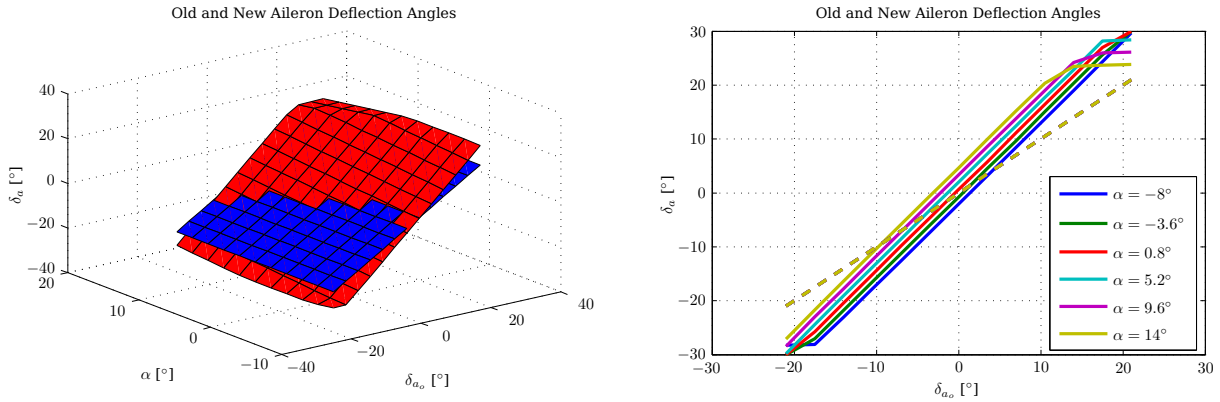


(a) (b)

**Figure 5.49** – A comparison between the old and new aileron deflection angles over the operating range. Figure 5.49(a) shows a three-dimensional surface view, while Figure 5.49(b) shows cross-sections at regular intervals of $\alpha$.

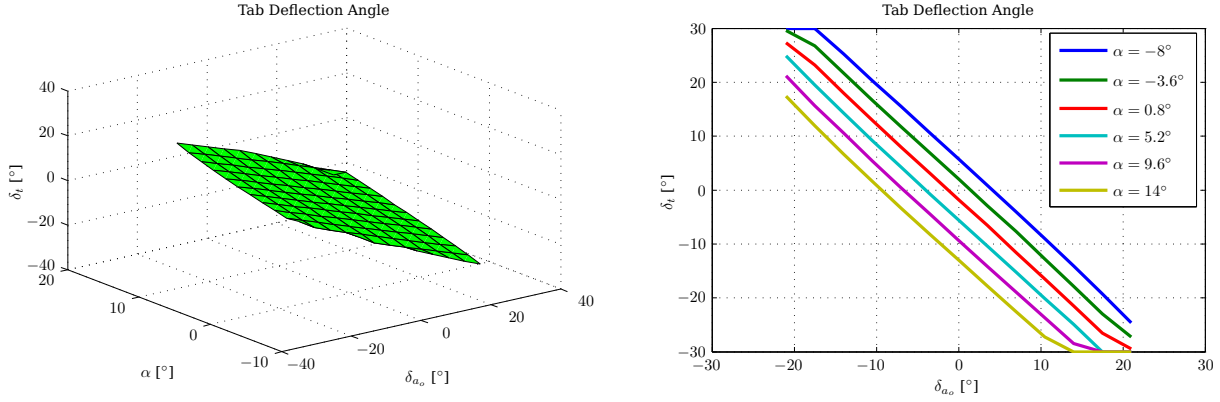


(a) (b)

**Figure 5.50** – The tab deflection angle over the operating range. Figure 5.50(a) shows a three-dimensional surface view, while Figure 5.50(b) shows cross-sections at regular intervals of $\alpha$.

### 5.9.1 Objective Functions

Since the rolling moment coefficient is to be taken into account in the optimisation it needs to be incorporated into the objective functions. This incorporation is done in the *inner* objective function since it will influence the optimal deflection angles, as the lift did previously for the optimisations described thus far.

It should be noted that since the aerodynamics are now being treated as 3D, a single tab and aileron can no longer be considered in isolation. The entire main wing is examined, along with the left and right ailerons as well as the associated tabs on these two ailerons. This results in a *four*-dimensional inner optimisation, where both aileron and both tab deflections need to be determined. The objective function can thus not be completely visualised two- or three-dimensionally.

The inner objective function now has the form

$$J_{\text{in}}\left(\delta_{a_{n_R}}, \delta_{a_{n_L}}, \delta_{t_R}, \delta_{t_L}\right) = w_L(C_{L_o} - C_{L_n})^2 + w_{M_l}(C_{M_{l_o}} - C_{M_{l_n}})^2 + w_{H_a}(C_{H_a})^2 + w_{H_t}(C_{H_t})^2 \qquad (5.9.1)$$

where each of the coefficients in Equation 5.9.1 is no longer the sectional coefficient, but the full non-dimensional coefficient. These coefficients are calculated from the two-dimensional thin aerofoil theory as described in §3.7. Again, drag can be easily added as an additional term once a means to determine the drag becomes available.

The outer cost function remains the the same, except that in this case there are still two design variables. The first parameter is the tab chord length, as normal. The second parameter is chosen to be the inboard location of the aileron with the additional constraints that the tab and aileron have the same span, and that the outboard location of both is still fixed. This effectively results in the span of the aileron-tab ($b_a$

and $b_t$) combination being the design variable, but represented by the inboard location of both, ($y_{a_i}$ or $y_{t_i}$). To emphasise, $y_{a_i} = y_{t_i}$ and $b_a = b_t$ at all times, thus $y_{t_i}$, $b_a$ and $b_t$ are all dependant on the chosen design variable, $y_{a_i}$.

### 5.9.2 Constraints

While the inner cost function has changed, the constraints are still on the deflection angles. The four current constraints are merely duplicated to take into account the additional tab and aileron, thus limiting the maximum and minimums of all four control surface deflections.

One of the outer optimisation design variables has changed from that of §5.8, and the limitation on the tab chord length is again constant since the aileron chord length is fixed again. The new outer optimisation constraints are now described by the equations

$$\begin{aligned} g_1(E_t,\, y_{a_i}) &= -E_t + E_{t_{\min}} \leq 0 \\ g_2(E_t,\, y_{a_i}) &= E_t - E_{t_{\max}} \leq 0 \\ g_3(E_t,\, y_{a_i}) &= -y_{a_i} + y_{a_{i_{\min}}} \leq 0 \\ g_4(E_t,\, y_{a_i}) &= y_{a_i} - y_{a_{i_{\max}}} \leq 0 \end{aligned} \tag{5.9.2}$$

with $g_3$ and $g_4$ describing the relation $y_{a_{i_{\min}}} \leq y_{a_i} \leq y_{a_{i_{\max}}}$, the limitations on the location of the inboard edge of the aileron/tab combination.

### 5.9.3 Optimisation and Results

The real-encoded genetic algorithm is used for both the inner and outer optimisations. Since in total there are six "design" variables that are being considered, the optimisation process is considerably slower than those discussed thus far. Due to time constraints, only preliminary results are shown for this optimisation. The results shown in this section are those obtained for the following weightings:

$$w_{M_l} = 3 \times 10^{-4} \qquad w_L = 3 \times 10^{-4} \qquad w_{H_a} = 10 \qquad w_{H_t} = 10 \tag{5.9.3}$$

which were chosen as a logical extension of the previous weightings. It was found that where the lift weighting was set to zero, very poor results were obtained.

The weightings were originally chosen based on the sectional coefficients for a two-dimensional aerofoil. During the three-dimensional approximation these sectional coefficients were multiplied by $\Delta y$ components of the span during the integration process, and scaled according to the actual chord length of the aerofoil where the $\Delta y$ slice is being evaluated. The spans of the ailerons and tabs are thus not the same as the entire aerofoil, and in order to normalise the coefficients to common values, the pseudo-coefficients were divided by the *mean aerodynamic chord* and the reference area of the aerofoil as described in §3.7.

It should be noted that a potentially better set of weightings can be obtained since the process of re-normalising these actual coefficients was neglected (in error). While the results shown below show excellent performance characteristics (in terms of lift, rolling moment and hinge moment coefficients), it cannot be assumed that the weightings used are the most suitable for the optimisation process.

A history of the optimisation is given in Figure 5.51. The optimisation process was terminated before completion (after four generations) in order to view the preliminary results. The time taken for the above results is approximately $50$ hours given the number of points in the operating region and number of design variables. After the fourth generation the design vector is given as $E_t = 0{,}0302$ and $y_{a_i} = 18{,}29\,\text{m}$. The span of both the aileron and tab has increased from $3{,}505\,\text{m}$ to $5{,}1032\,\text{m}$ (remembering that $b_t = b_a$), which can be seen to be a very large difference and is not necessarily practically realisable given that other control surfaces such as flaps are also located on the wing's trailing edge. This may be remedied if the normalisation of the objective functions is performed correctly.

Using these results, however, it is possible to generate the graphs shown in Figures 5.52 to 5.57.

The primary performance indicator is the rolling moment coefficient and this is shown in Figure 5.52. As can be seen the operating region has been optimised only for the positive deflections of $\delta_{a_o}$. This is due to the symmetry of the main wing which will lead to negative deflections being handled in an identical manner.

The effect of the configuration described by the optimal design vector on the rolling moment coefficient can be seen to be very effective with very little deviation from the old values. The maximum absolute

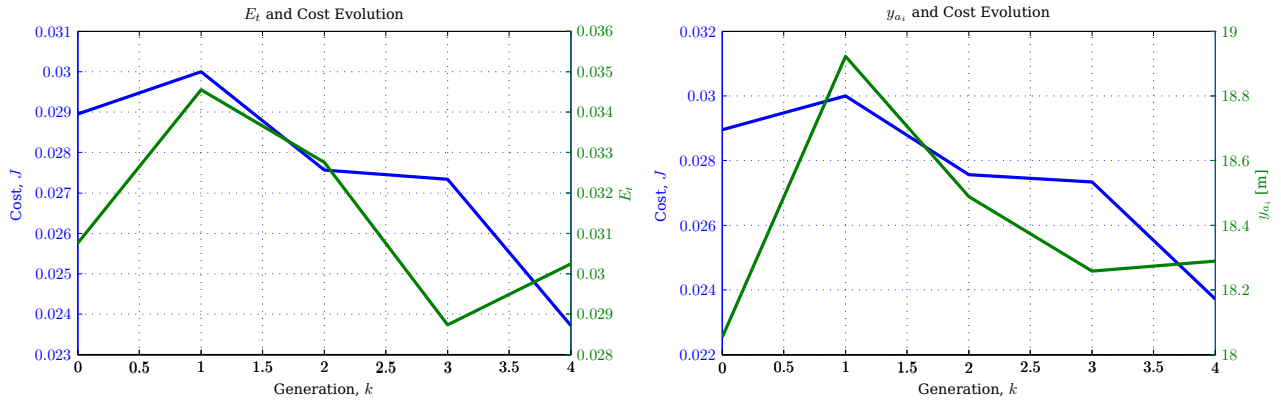


(a) Evolution of $E_t$. (b) Evolution of $y_{a_i}$.

**Figure 5.51** – Graph showing the evolution of the design vector elements and the cost function as the outer optimisation progresses.

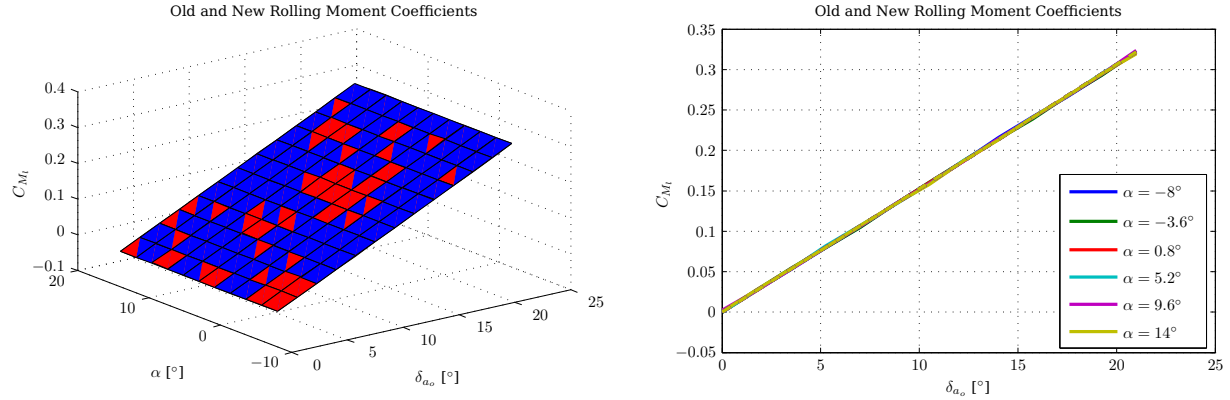


(a) (b)

**Figure 5.52** – A comparison between the old and new rolling moment coefficient values over the operating range. Figure 5.52(a) shows a three-dimensional surface view, while Figure 5.52(b) shows cross-sections at regular intervals of $\alpha$.

deviation over the entire operating range is $2{,}566 \times 10^{-3}$. It can also be seen (as expected) that larger commanded aileron results in larger rolling moment, and that this rolling moment is independent of the angle of attack. This is expected since the angle of attack is taken as the same for both the left and right wings.

The lift component appears to be optimal, resulting in near equal lift characteristics, as shown in Figure 5.53. The maximum absolute deviation in the lift coefficient is $3{,}464 \times 10^{-3}$ over the entire operating range, and for case where this absolute deviation occurs ($\alpha = 14\,°$), this is determined to be a deviation of only $0{,}21\,\%$. While it is viewed as not as important as the rolling moment characteristics, it is encouraging to note that it is possible to achieve the same lift characteristics, while at the same time achieving the same rolling moment characteristics. This is, however, an ideal situation and it may be necessary to sacrifice some of either the lift or rolling moment performance when aspects such as drag are taken into account. By the characteristics of this graph, since the lift characteristics are almost identical, the induced drag is also expected to be very similar to old values. Parasitic drag is expected to play a more prominent role.

The aileron hinge moment coefficients are shown in Figure 5.54 for both the left and right ailerons. For the current weightings and design vector it can be seen that it is possible to reduce the aileron hinge moment coefficients to approximately zero over the entire operating range. A maximum absolute deviation of $20{,}64 \times 10^{-6}$ for the right aileron and $13{,}8 \times 10^{-6}$ for the left can be seen and these values are $35$ and $44$ times smaller than their respective old maximums of $722{,}1 \times 10^{-6}$ and $606{,}2 \times 10^{-6}$, which means at least an overall reduction of $35$ times if both positive and negative old aileron deflections are taken into account.

It can also be seen that for zero old aileron deflection, the values of the left and right hinge moment coefficients are equal for any particular $\alpha$ value. This is also seen to be the case for the tab hinge moment

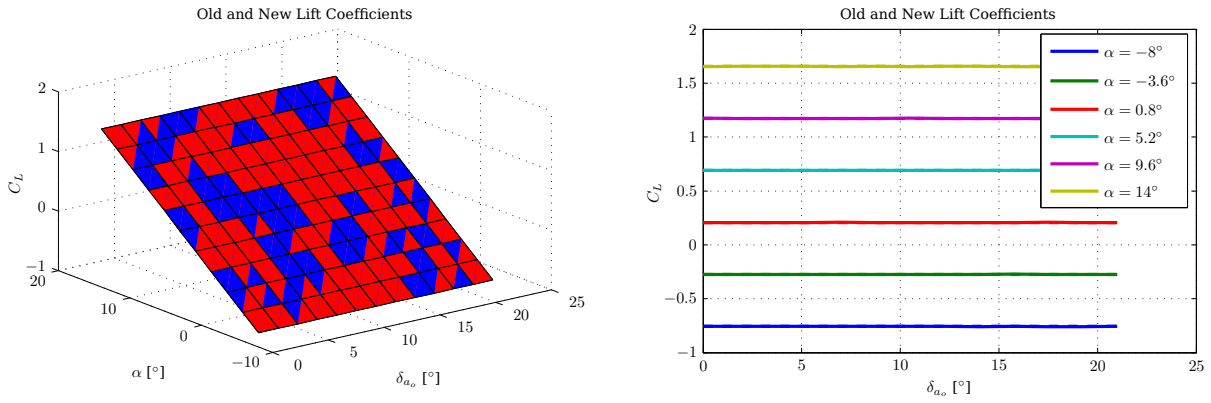


(a) (b)

**Figure 5.53** – A comparison between the old and new lift coefficient values over the operating range. Figure 5.53(a) shows a three-dimensional surface view, while Figure 5.53(b) shows cross-sections at regular intervals of $\alpha$.

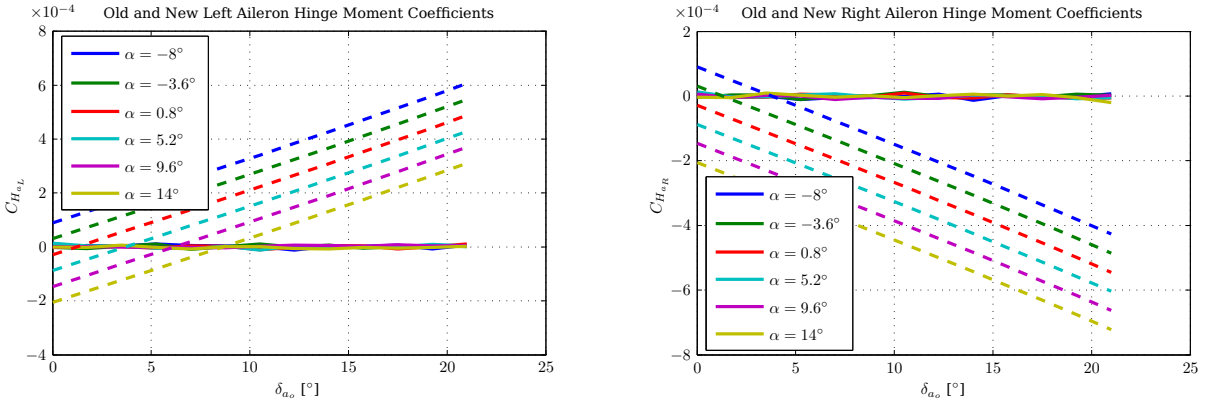


(a) Left (b) Right

**Figure 5.54** – A comparison between the old and new aileron hinge moment coefficient values over the operating range.

coefficients, as well as the control surface deflections.

The tab hinge moment coefficients are shown in Figure 5.55 and it can be seen that the values are of an order a hundred times smaller than the aileron hinge moment coefficients, indicating that the tab still does not require a very large (compared to the old aileron) actuator.

The aileron deflection angles are shown in Figure 5.56. The first remark is that the left and right aileron deflections are no longer odd symmetrical. Typical aileron usage relies on the principle of differential control where one aileron is deflected by an angle of $+\delta_a$ and the other by $-\delta_a$. Since the tab has been added to reduce the aileron hinge moment, this is no longer the case, as can be seen in the figures. It can be seen, as with the previous cases, that a larger deflection is typically required for the aileron-tab combination versus that of the original aileron system.

The tab deflections used to achieve the approximately zero aileron hinge moment coefficients are shown in Figure 5.57. For both the aileron and tab deflections it can be seen that when the aircraft is in wings-level flight, i.e. the commanded aileron is $\delta_{a_o} = 0\,°$, the ailerons are deflected symmetrically by some non-zero value while the tabs are also deflected symmetrically in the opposite direction to the ailerons as they counter the aileron hinge moment.

A final note regarding the above results: while only positive $\delta_{a_o}$ values were shown, the results also hold for negative $\delta_{a_o}$ deflections and these are provided by exchanging the graphs of the left and right values of each component.

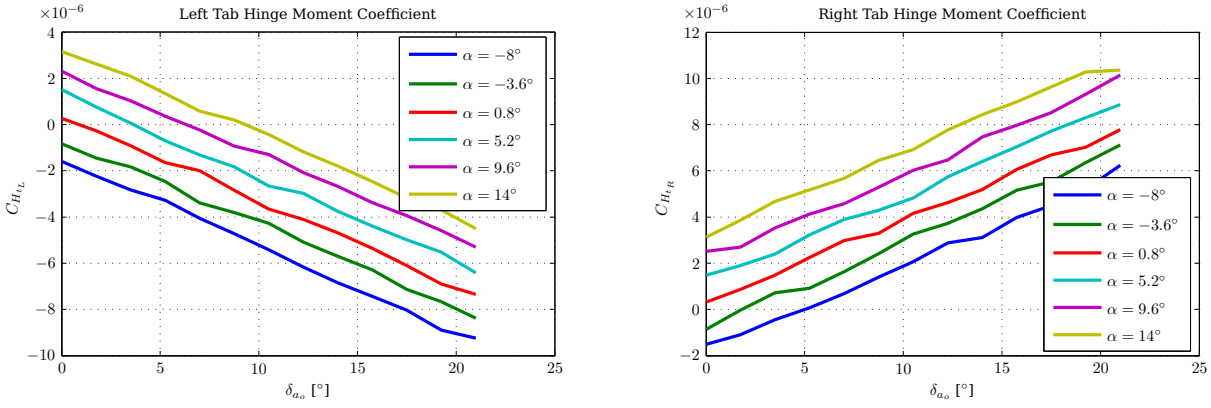


(a) Left (b) Right

**Figure 5.55** – The tab hinge moment coefficient values over the operating range.

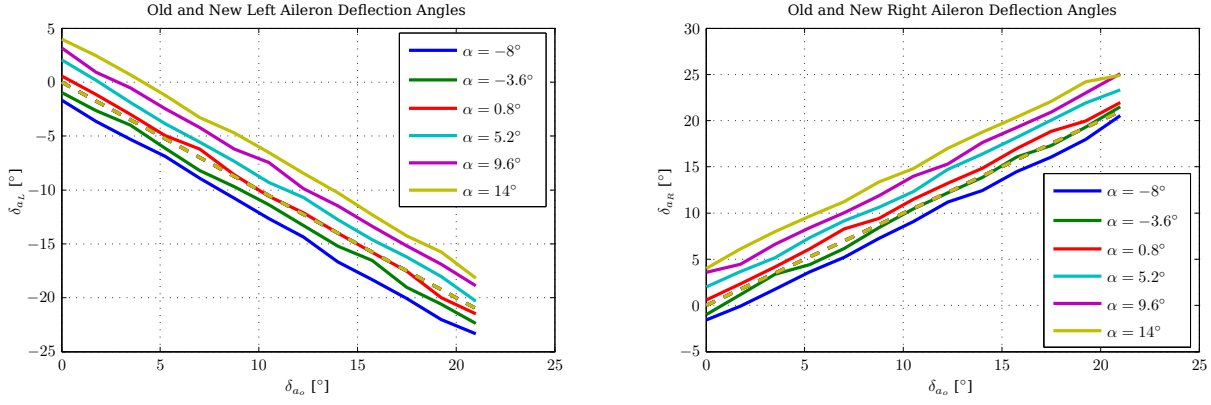


(a) Left (b) Right

**Figure 5.56** – A comparison between the old and new aileron deflection angles over the operating range.

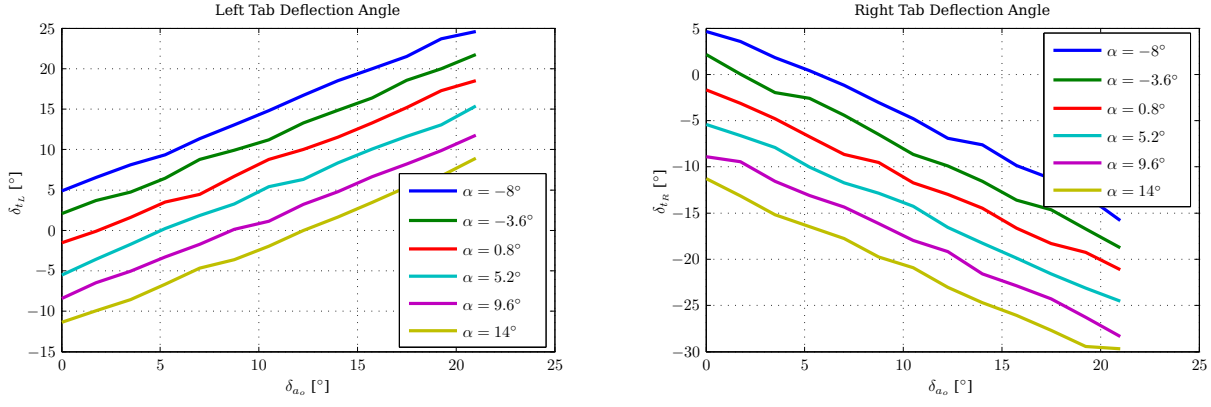


(a) Left (b) Right

**Figure 5.57** – The tab deflection angles over the operating range.

## 5.10 Summary of Results

Three main optimisations were discussed in this chapter, namely the optimisations of $E_t$ only, $E_t$ and $E_a$, and finally $E_t$ and $y_{a_i}$. The $E_t$ optimisation was also performed using both the linear and non-linear thin aerofoil theories.

In all cases it is found that there is a region where the desired objectives can be met, whereby the lift performance is similar between the old and new configurations and the aileron hinge moment has been reduced to near-zero values. In the final optimisation it is also noted that the rolling-moment performance

**Table 5.2** – Table comparing the various optimisation results described in this chapter. The values shown for the lift and rolling moment coefficients correspond to values within the achievement regions, as described in the text of the relevant sections.

| **Optimisation** | **Max** $\Delta C_L$ | **Max** $C_{H_{a_n}}$ | **Max** $C_{H_{a_o}}$ | **Reduction in** $C_{H_a}$ | **Max** $\Delta C_{M_l}$ |
|---|---|---|---|---|---|
| $E_t$ (Linear) | $5 \times 10^{-3}$ | $2042 \times 10^{-6}$ | $34{,}89 \times 10^{-3}$ | 17 times smaller | |
| $E_t$ (Non-Linear) | $6{,}362 \times 10^{-3}$ | $681{,}2 \times 10^{-6}$ | $33{,}15 \times 10^{-3}$ | 48 times smaller | |
| $E_t$ and $E_a$ | $105{,}8 \times 10^{-3}$ | $735{,}3 \times 10^{-6}$ | $50{,}52 \times 10^{-3}$ | 68 times smaller | |
| $E_t$ and $y_{a_i}$ | $3{,}464 \times 10^{-3}$ | $20{,}64 \times 10^{-6}$ | $722{,}1 \times 10^{-6}$ | 35 times smaller | $2{,}566 \times 10^{-3}$ |

| **Optimisation** | **Design Vector** |
|---|---|
| $E_t$ (Linear) | 0,0793 |
| $E_t$ (Non-Linear) | 0,0325 |
| $E_t$ and $E_a$ | (0,0358, 0,302) |
| $E_t$ and $y_{a_i}$ | (0,0302, 18,29 m) |

as well as the lift performance is also very similar to the old system.

A summary of the primary results are now provided in Table 5.2.

From the table it can be seen that there is a reduction in the aileron hinge moment coefficient for each of the cases described, with the largest reduction for the third case. Here, however, there is a much larger deviation in the lift coefficient values than those of the remaining cases, where this deviation is almost 20 times larger. The possible reasons for this deviation were discussed in §5.8.3.

The smallest lift deviation is found for the three-dimensional case (fourth in the table) where $E_t$ and $y_{a_i}$ are varied, and this is also accompanied by a small deviation in the rolling moment coefficient. It is noted that the hinge moment coefficient reduction is the second smallest but still significant when compared to the two-dimensional, non-linear $E_t$ case.

Now that optimal physical parameters have been obtained it is necessary to perform some simulations to evaluate their usefulness during the performance of various manoeuvres. This is the topic of Chapter 6 where the simulation environment is explained and a rolling manoeuvre is performed as example.

# Chapter 6

# Sizing Manoeuvres and Aircraft Simulation

## 6.1 Introduction

In order for an aircraft to obtain certification for use, it needs to be proven that it can perform a series of manoeuvres relating to extreme points in its operating envelope as well as a number of emergency manoeuvres. In order for any modification of the the aircraft to be accepted, it is necessary to prove that the modification will not inhibit the ability of the aircraft to perform these manoeuvres, collectively termed sizing manoeuvres.

This section describes a number of the sizing manoeuvres relating to the roll characteristics of the aircraft and then demonstrates how one such manoeuvre can be used to indicate the performance of the geometric results obtained in Chapter 5.

## 6.2 Description of the Sizing Manoeuvres

*Airbus* provided a list of sizing manoeuvres that need to be performed successfully in order to obtain certification [64]. The manoeuvres relating to the ailerons are described briefly below.

1. **Static Equilibrium at $V_D$/$M_D$** – When diving at very high speed the aileron actuators must be able to prevent the ailerons from being deflected by the aerodynamic forces acting on them. This needs to be achieved at speeds near the structural breaking point of the aircraft.
2. **Roll Manoeuvre at $V_{MO}$/$M_{MO}$** – For typical high speeds the aircraft must be able to roll to an angle of $40\,^\circ$ using maximum commanded roll rate of $15\,^\circ$/s (full stick) and be able to return to wings level conditions safely.
3. **Roll Manoeuvre at high angle of attack** – while in a condition of high angle of attack ($\alpha_{\max} < \alpha_{\text{stall}}$) the aircraft needs to be able to roll to $\pm 50\,^\circ$ at a rate of $15\,^\circ$/s, typically achieved by reducing speed and commanding constant altitude.
4. **Roll at $2\,$g** – Initiated from a bank angle of $60\,^\circ$, the aircraft needs to roll at $15\,^\circ$/s until wings-level is attained ($0\,^\circ$), while at high speed ($V_{FE}$).
5. **Landing with crosswind and turbulence** – During a landing where crosswinds and turbulence is present, the aircraft needs to be able to land successfully, thus the ailerons need to be able to provide satisfactory performance at low speeds in unsteady conditions.

The sizing manoeuvre that is chosen as an initial test case is the second in the list: *Roll manoeuvre at $V_{MO}$*. In order to achieve this a simple "bang-bang" controller is implemented to interface with the simulation model described in §6.3. In this case the controller commands a maximum roll rate from wings-level flight until the aircraft reaches a roll angle of $-40\,^\circ$. Once the desired roll angle is obtained the commanded roll rate is reversed until a roll angle of $0\,^\circ$ is obtained. Once the $0\,^\circ$ mark is reached a simple proportional controller is used to restore wings-level flight. In this case a proportional controller is acceptable since the roll *rate* is controlled, and thus there is a natural integrator present that will eliminate any offsets in the roll angle. The process is then repeated but in the opposite direction.

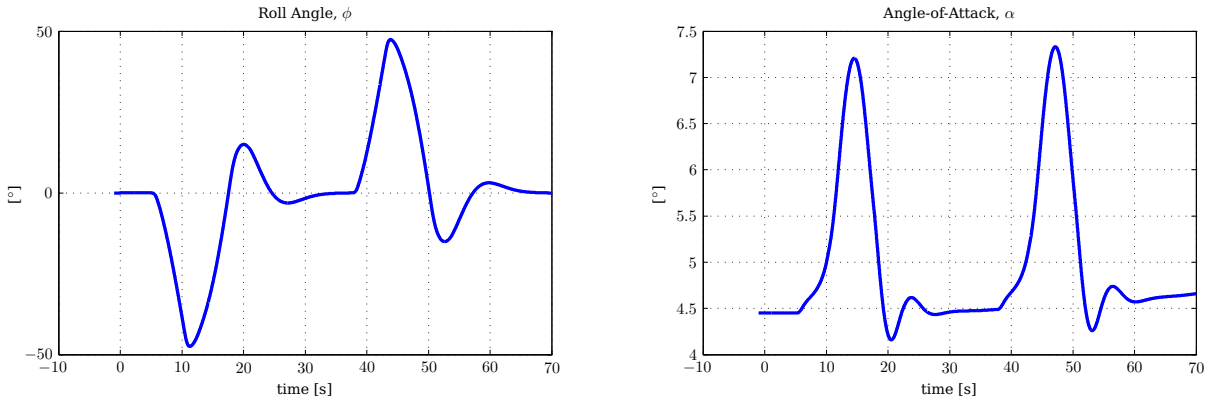


(a) Roll Angle ($\phi$) (b) angle of attack

**Figure 6.1** – Important angles during the roll manoeuvre.

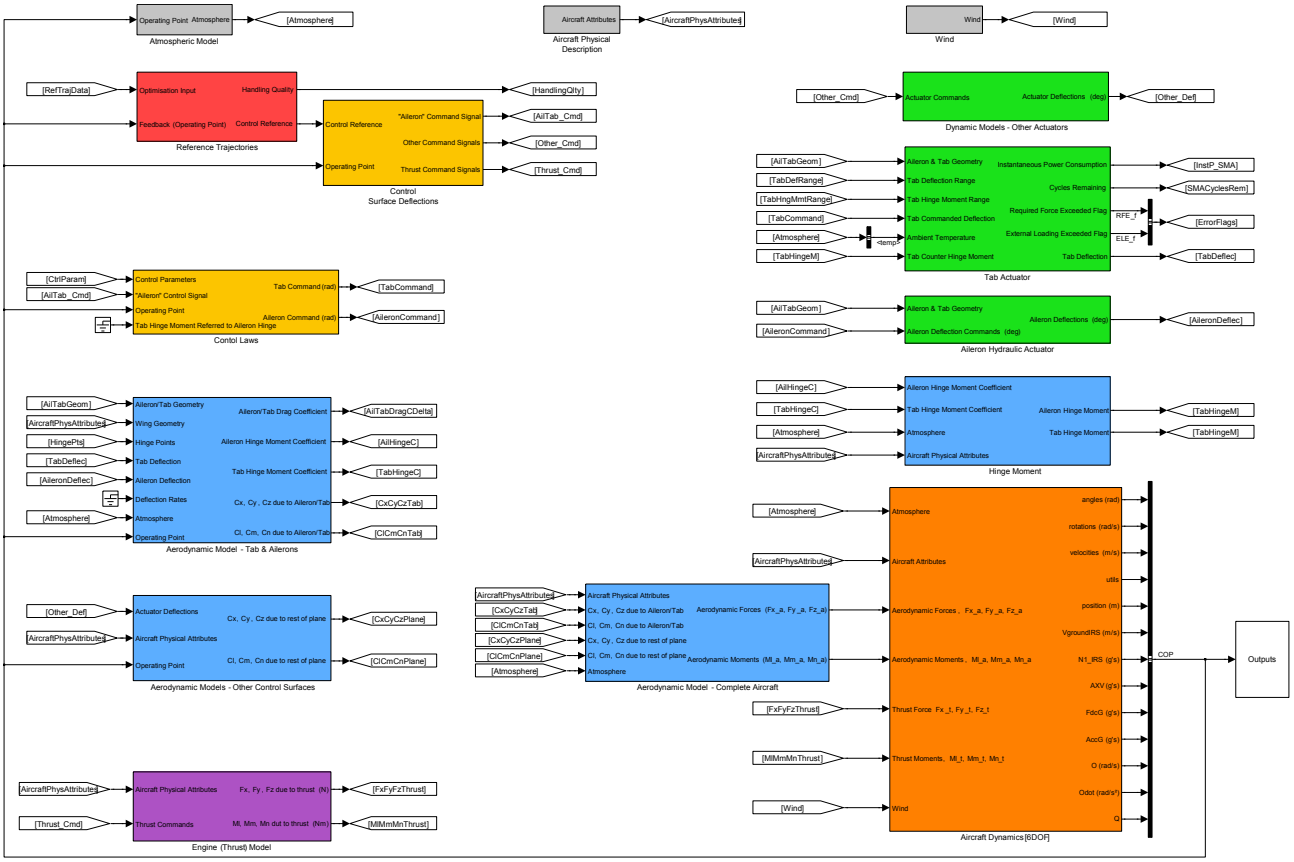


**Figure 6.2** – The complete simulation block diagram used to perform the sizing manoeuvres. A larger version can be found in Appendix C.

The roll angle and associated angle of attack are shown in Figure 6.1. The angle of attack and roll angle are identical for all (design) cases since the dynamics of the new configuration have not been used in the closed loop system directly. Rather, the original aerodynamic coefficients are used to provide aircraft behaviour, and a parallel system containing the aileron-tab system is used to gather data. From Figure 6.1 it can be seen that there is a large amount of overshoot during the manoeuvre as expected of the bang-bang control. The manoeuvre is initiated at $5\,\mathrm{s}$ for the $-40\,^\circ$ roll and $38\,\mathrm{s}$ for the $+40\,^\circ$ roll.

## 6.3 Simulink Simulation Model

In order to perform the roll manoeuvre discussed in §6.1, a Simulink simulation model was developed based on one provided by Airbus. The model was created using the modular approach described in Chapter 2

such that the various modules (aileron actuator, tab actuator, aileron and tab aerodynamics, etc.) could easily be exchanged with alternative, higher fidelity components.

The interfaces and each of the components of the block diagram are described in Appendix C with an overview of the block diagram is shown in Figure 6.2. The key components of the block diagram are listed below, with brief descriptions:

- The *controllers* are shown in yellow blocks with the guidance controller in the red *reference trajectory* block. This block includes components such as the pilot inputs, as well as the control system used to perform the sizing manoeuvres, which is implemented as a pre-compiled MEX file. This block provides control references in the form of commanded rates to the successive block labelled *Control Surface Deflections*. This block makes use of Airbus' fly-by-wire system to convert the rates into commanded control surface deflections and thrust commands. It also serves to separate the commanded aileron deflections from those of the other control surface. In the case of the A330, only the inner ailerons are separated.
- The block labelled *Control Laws*, is used to convert the old aileron deflections for the left and right ailerons into suitable new aileron and tab deflections.
- The outputs of the controller blocks are fed to the green blocks used to provide actuator dynamics. The *Tab Actuator* and *Aileron Hydraulic Actuator* blocks provide the dynamics of the tab and aileron actuators respectively and are intended to be replaced as various alternatives are tested.
- The other actuator dynamics are the same as those used by the original Airbus model and are contained in the block labelled *Dynamic Models – Other Actuators*, with
- The thrust dynamics are encapsulated in the purple *Engine (Thrust) Model* block.
- The blue blocks convert the actual control surface deflections into force and moment coefficients in the case of the *Aerodynamic Model – Tab and Ailerons*, and *Aerodynamic Models – Other Control Surfaces*; and into forces and moments in the case of the *Aerodynamic Model – Complete Aircraft* and *Hinge Moment* blocks.
- The orange block, *Aircraft Dynamics (6DOF)*, converts all the forces and moments into kinematics using a six-degree-of-freedom model. This block is based around one developed in the ESL, and augmented with components required for the Airbus fly-by-wire system.
- The grey blocks provide atmospheric conditions, physical aircraft dimensions and wind disturbances.

For the results provided in §6.5, the original aileron dynamics are used while the effects on the new aileron-tab system are merely recorded for analysis, and do not affect the kinematics directly. This is done since aerodynamic models of a sufficient fidelity to perform suitably in the model do not exist at the time of writing. Actuator dynamics are also not currently available, thus the original aileron actuators have been duplicated for the tab actuators in order to prevent instantaneous deflections during the simulation.

## 6.4 Deflection Angles

Since a suitable controller has at this stage not been designed for the aileron-tab system it is necessary to calculate the deflection angles required using some other means.

It is very time-consuming to pre-determine the optimal values for every possible combination of aileron deflection and angle of attack, and, while it is possible, to perform the optimisation once the operating point is known is not an efficient means of determining the deflection angles. This is mainly due to the time required to perform the optimisation making it unsuitable for a real-time application. Fortunately the optimisation process provides an intermediate solution.

During the optimisation, at each of the ($\alpha$, $\delta_{a_o}$) operating points, the inner optimisation was used to determine the optimal deflection angles of both the tab and the aileron to minimise the cost of this point. These values were recorded during the optimisation process, and can now be used as part of the solution.

The results were obtained only for a small number of the possible operating points, but a sufficient number were considered in all the optimisations of Chapter 5 to develop a trend that is useful. Referring to Figure 5.42 in this chapter it can be seen that in the region where neither the aileron or tab is deflected to its

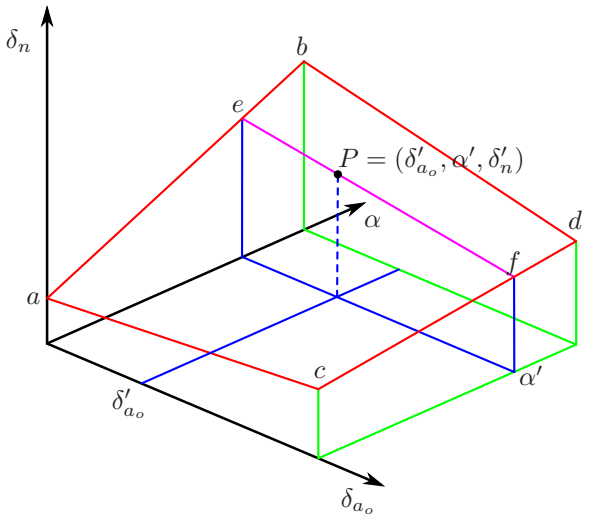


**Figure 6.3** – This figure shows the means used to determine the required tab and aileron deflection angle based on the sparse information generated during the optimisation process.

maximum extent that the relation for a given angle of attack between the new deflection (both tab and aileron) and the old aileron deflection is fairly linear.

This linearity suggests that a plane can be extrapolated relating the required deflection angle to the two parameters of $\alpha$ and $\delta_{a_o}$. It was decided not to follow this route, however, since a relatively straight-forward method was developed which could be used to determine the parameters over the surface regardless of the form. While the method is still an approximation, it is simple to implement and provides suitable deflections based on the predetermined values (from the optimisation) around the actual operating point.

The method is described using Figure 6.3 as a reference. The process used to determine the deflection angles considers the already existing data points obtained in the optimisation, then uses three linear equations to determine the deflections. Each deflection is calculated independently for each aileron and tab as follows:

1. Considering the grid of discrete operating points used in the optimisation, the four points surrounding the desired operating point are found. These four points are designated $a$, $b$, $c$ and $d$ as shown in the figure.
2. The first linear equation is used to define the line $\overline{ab}$, with the second line used to define the line $\overline{cd}$. Both of these lines are for constant $\delta_{a_o}$ and thus provide deflection angle versus $\alpha$.
3. Substituting the operating angle of attack into the two equations provides two deflections at points $e$ and $f$.
4. Points $e$ and $f$ are used to obtain the third linear equation representing a line of constant $\alpha$ passing through these points, providing deflection angle as a function of old aileron deflection.
5. Using the third equation the deflection angle can be obtained by substituting in the operating $\delta_{a_o}$.

The process is repeated for each deflection required, and is considerably faster than performing the optimisation repeatedly.

## 6.5 Results

The results of two of the optimisations are shown, namely the one-dimensional optimisation where the optimal tab chord length, $E_t$, is obtained maintaining all other geometry, and the two-dimensional optimisation where the tab chord length, $E_t$, and the aileron inboard position, $y_{a_i}$, is obtained.

### 6.5.1 Tab Chord Length Using the Two-Dimensional Thin Aerofoil Theory

The first case considers the optimisation result of §5.7.4.4. The non-linear thin aerofoil theory is used during the simulation to determine the parameters shown in the graphs of Figures 6.4 to 6.9.

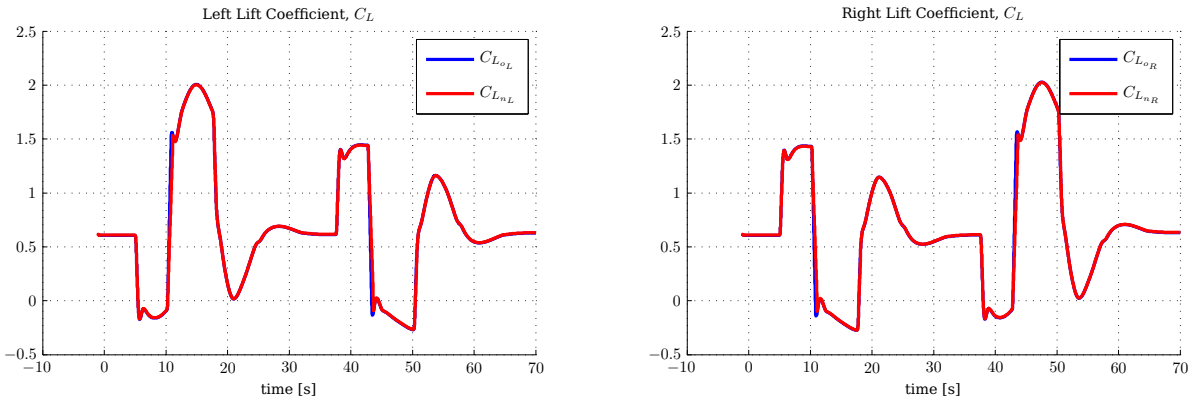


(a) Left Wing (b) Right Wing

**Figure 6.4** – Sectional lift coefficients.

In summary, the tab chord length parameter is $E_t = 0{,}0325$ which is $3{,}25\,\%$ of the total wing chord, taken in this case as the mean aerodynamic chord of the Airbus A330, $c_{\text{mac}} = 7{,}27\,\text{m}$, [64]. The aileron chord length parameter is $E_a = 0{,}25$, thus the physical dimensions of the tab and aileron are treated as $c_t = 0{,}2363\,\text{m}$ and $c_a = 1{,}8175\,\text{m}$.

Though these are not accurate dimensions in terms of the three-dimensional model (the wing is tapered for example), they provide representative results for comparison. It must also be remembered that the two-dimensional thin aerofoil theory is used which provides sectional values. In order to obtain the hinge moments provided in this section, these sectional coefficients are multiplied with the span of the aileron, as well as the square of $c_{\text{mac}}$ and the dynamic pressure. While the actual hinge moments are not obtained, this provides useful values for comparisons. The tab and aileron spans are assumed equal and are set to the aileron span length of $3{,}505\,\text{m}$.

For the purpose of comparison, a simulation was performed for the case of only the aileron with the chord and span as described above, and no tab. These results are shown as the *blue* graphs in the figures. The graphs in *red* are the results of the simulation with the aileron and tab.

The sectional lift coefficients are provided in Figure 6.4 for the left and right wings. It can be seen initially that in both the old and new cases the wings generate lift initially, corresponding to zero old aileron deflection as can be seen in Figure 6.9. This is due to the camber of the wing, as well as the non-zero angle of attack which can be seen in Figure 6.1(b). From Figure 6.4 it can be seen that the goal of similar lift coefficient values have been attained throughout the manoeuvre, for both positive and negative roll angles, except around points where there is rapid deflection of the control surfaces. These points can be seen as peaks in Figure 6.5, and will be explained in successive paragraphs.

Examining the sectional hinge moment coefficients of the aileron, it is possible to see a very large difference between the old and new configurations for both wings. As expected, the original aileron-only system has a non-zero hinge moment, even when the old aileron deflection is zero (due to the angle of attack and non-zero camber), and during the execution of the manoeuvre the aileron hinges experience widely varying hinge moments, depending on the deflection of the aileron, as well as the current attitude of the aircraft. As can be seen from the red graphs in Figure 6.5, it is possible to reduce the aileron hinge moment coefficient to almost zero over the entire manoeuvre. There are, however, peaks in the graphs where the hinge moment is non-zero.

These peaks are attributed to the hydraulic actuator dynamics used for the tab. As previously stated, the hydraulic actuators for original ailerons are duplicated for the tab. Since the tab is not able to deflect instantaneously, there is a period of time while the tab and aileron are both in motion as they move to the commanded deflections. During this time the aileron hinge moment is non-zero.

It is expected that this non-zero aileron hinge moment can be eliminated by making use of an “intelligent” controller. Currently the deflections of the tab and aileron are determined based on the static analyses performed thus far. No dynamics (of the air or actuator) have been taken into account, thus it is expected that if a predictive controller is used, the tab can be deflected pre-emptively in order to reduce the magnitude of the peaks in aileron hinge moment coefficient during rapid deflections of the tab and aileron.

The tab hinge moment coefficient is shown in Figure 6.6. While the tab hinge moment is decidedly non-zero, it is should be noted that the magnitude of the coefficient is almost seventy times smaller at the

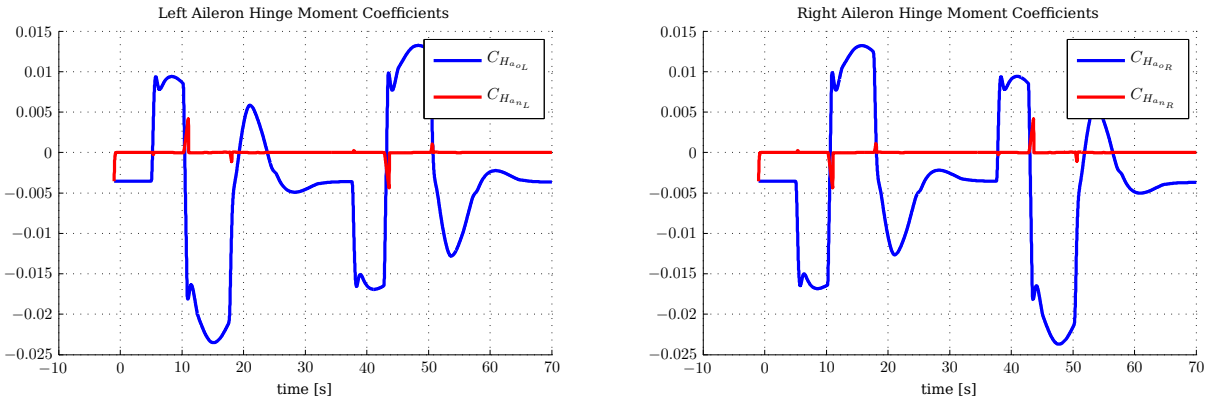


(a) Left Wing (b) Right Wing

**Figure 6.5** – Aileron hinge moment coefficients.

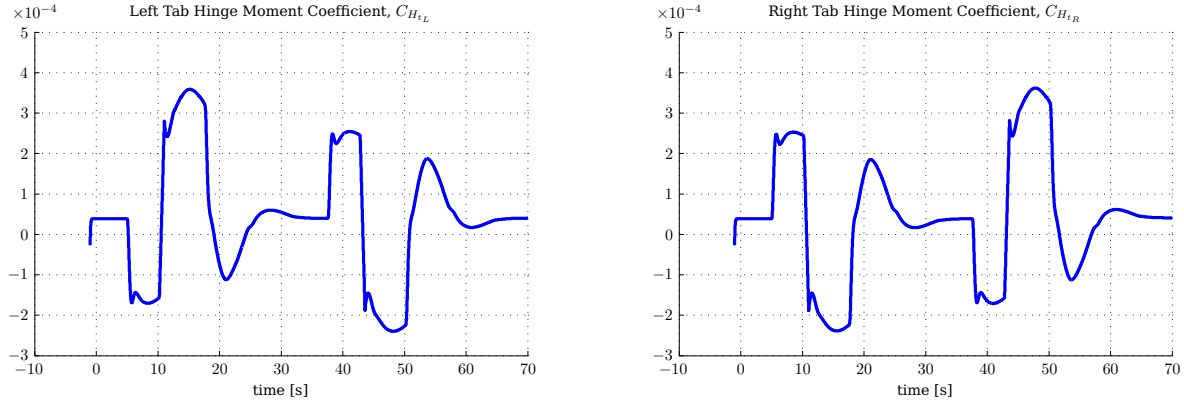


(a) Left Wing (b) Right Wing

**Figure 6.6** – Tab hinge moment coefficients.

peak old aileron hinge moment. This indicates that a much smaller actuator can be used to deflect the tab versus that of the old aileron.

Representative values of the aileron and tab hinge moments can be seen in Figures 6.7 and 6.8. It must not be forgotten that these values are based on the two-dimensional theory and do not take the wing taper into account, and are thus not directly comparable to the original hinge moments provided by Airbus. The results provided in §6.5.2 provide more accurate values.

The control surface deflections are provided in Figure 6.9, with the old aileron deflection ($\delta_{a_o}$) for the ori-

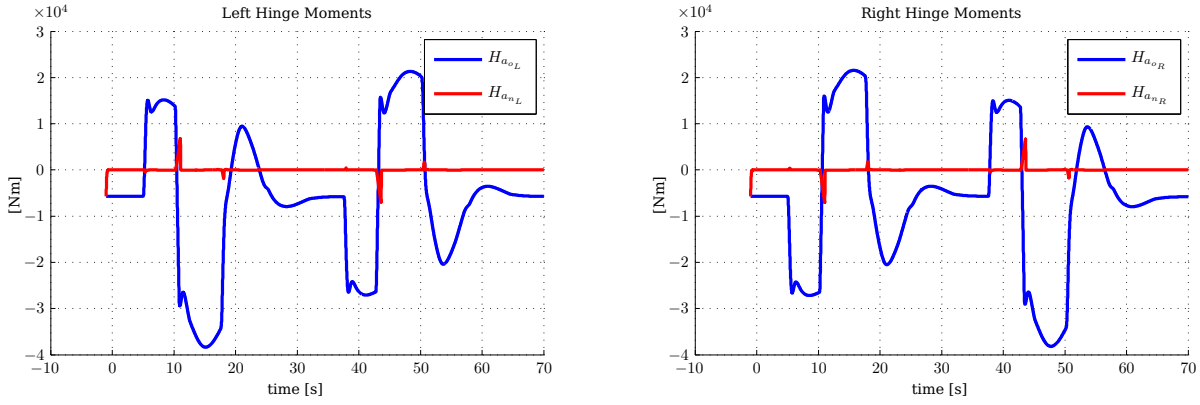


(a) Left Wing (b) Right Wing

**Figure 6.7** – Aileron hinge moments.

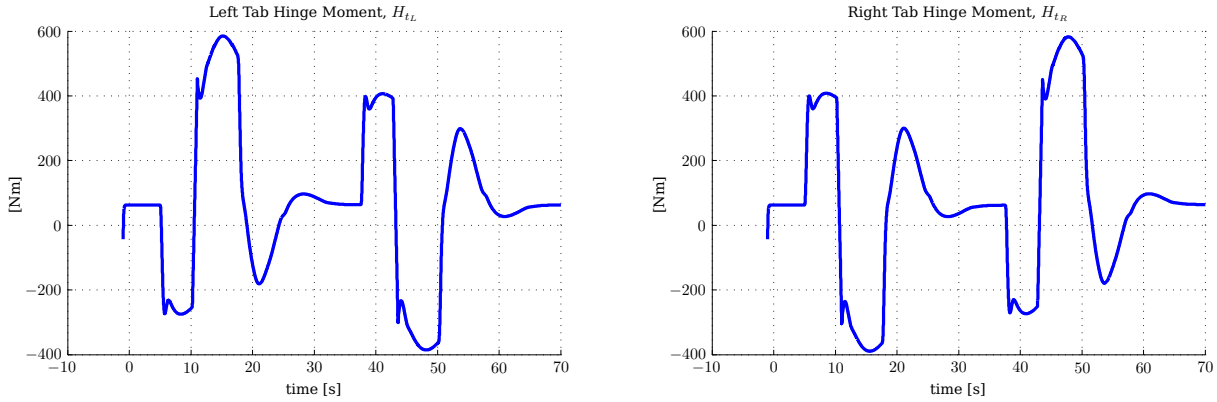


(a) Left Wing (b) Right Wing

**Figure 6.8** – Tab hinge moments.

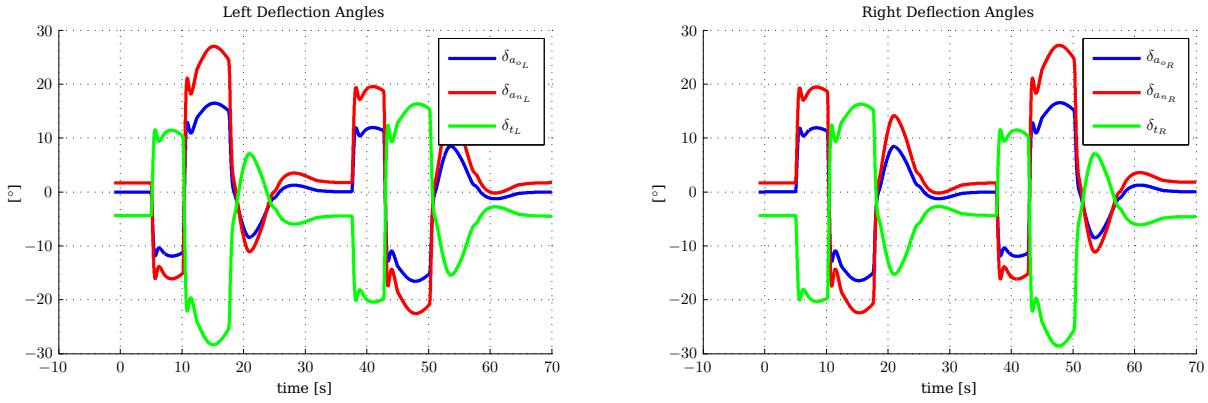


(a) Left Wing (b) Right Wing

**Figure 6.9** – Aileron and tab deflections.

ginal system shown in blue, the new aileron deflection ($\delta_{a_n}$) shown in red and the tab deflection ($\delta_t$) shown in green. There is a noticeable increase in the magnitude of the aileron deflections since the effective area of the aileron is smaller for the new system than for the original system, and the tab deflection is in the opposite direction to the aileron deflection. It can be seen that for the roll manoeuvres that the deflection angles do not reach their limits (of $30\,°$) at any point in the manoeuvre. This is one of the reasons that the lift coefficients match, and aileron coefficients are zero for the aileron-tab system during most of the manoeuvre.

### 6.5.2 Tab Chord Length and Span Using the Three-Dimensional Aerodynamic Approximation

This section provides the results of a simulation using the optimal tab obtained in §5.9. In this case the three-dimensional approximation based on the thin aerofoil theory described in §3.7 is used to determine the total lift of the main wing, as well as the rolling moment induced when the control surfaces are deflected.

The tab and aileron specifications of §5.9.3 are repeated here for convenience. The tab chord length parameter is $E_t = 0{,}0302$, or $3{,}02\,\%$ of the wing chord with the aileron chord length being $25\,\%$ of the wing chord length. This chord length varies over the span of the wing, and it is assumed that the thickness of the wing varies by the same proportion, though in practice this is not the case. The span of the aileron-tab combination was determined to be $5{,}1032\,\text{m}$ with the inboard edge located at $y_{a_i} = 18{,}29\,\text{m}$.

The rolling moment coefficients generated during the manoeuvre are shown in Figure 6.10, with the associated total lift shown in Figure 6.10(b). Again, the results of the the original aileron-only system are shown in blue while those of the new system are shown in red. As was seen in §5.9.3, both the rolling moment and the lift coefficients are almost the same for the new system as for the old system.

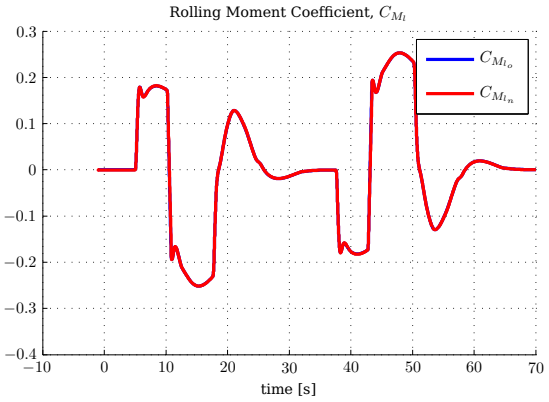


(a) Rolling moment coefficient.

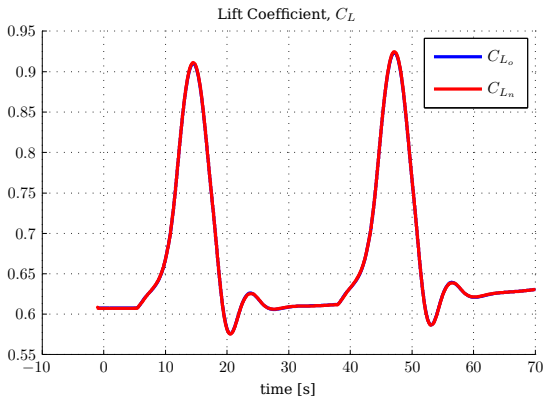


(b) Lift coefficient

**Figure 6.10** – Rolling moment and lift coefficients.

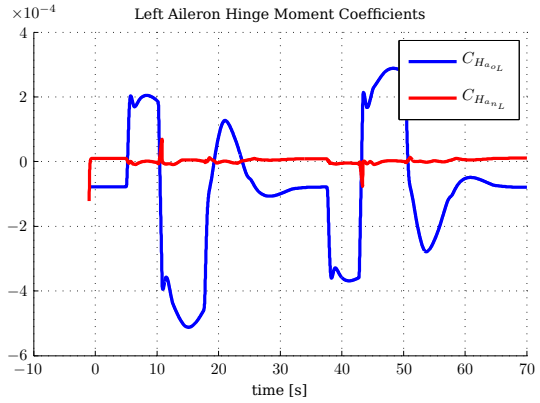


(a) Left Wing

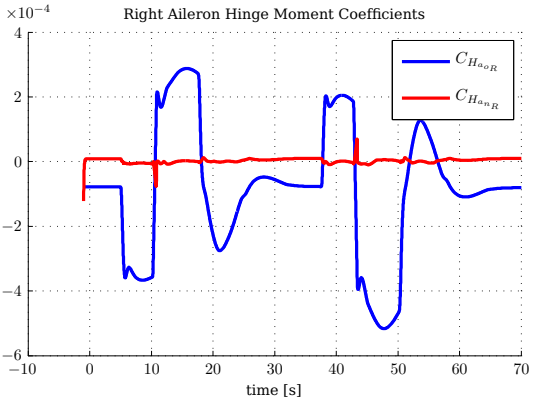


(b) Right Wing

**Figure 6.11** – Aileron hinge moment coefficients.

When correlated with the control surface deflections of Figure 6.15 and the hinge moment coefficients of Figure 6.11, it can be seen that the deviation is slightly larger when the control surfaces are being rapidly deflected.

Examining the hinge moment coefficients for the ailerons (Figure 6.11) one can see a substantial reduction in the new system versus that of the old system, although the coefficients are not exactly zero. Bearing in mind that the optimisation was terminated prematurely, it is possible that the final result of the optimisation could result in more optimal tab and aileron geometries which would allow the aileron hinge moments to be eliminated completely. The substantial reduction in the coefficient values already suggests that smaller aileron actuators can be used, though the dynamic responses of the actuators still need to be taken into account.

The tab hinge moment coefficients are seen to be almost a hundred times smaller than the original aileron hinge moment coefficients, as was seen in §6.5.1. This re-enforces the consideration that a smaller actuator is needed to deflect the tab than the current aileron actuator.

The approximated aileron hinge moment in newton metres is given in Figure 6.13, with a peak magnitude of $12\,000\,\mathrm{N \cdot m}$ for the old aileron-only system. For the new aileron-tab system, it is possible to see a reduction where the average hinge moment required is at most a few hundred newton metres. There are peaks (which can also be seen in the hinge moment coefficients graphs) which are attributed to the rapid deflections commanded and the finite times required for the tabs to be deflected to counteract the aileron hinge moments as described in §6.5.1. As stated previously, it is expected that a good control system will be able to eliminate these spikes. The magnitude of these peaks can be seen to be approximately $200\,\mathrm{N \cdot m}$, which is about five times larger than the the non-peak regions. It is thus highly desirable to eliminate these peaks, else a larger actuator would be required simply to deliver the hinge moments required during these peak values.

Since a three dimensional aerodynamic approximation is used where the taper of the wing is taken into

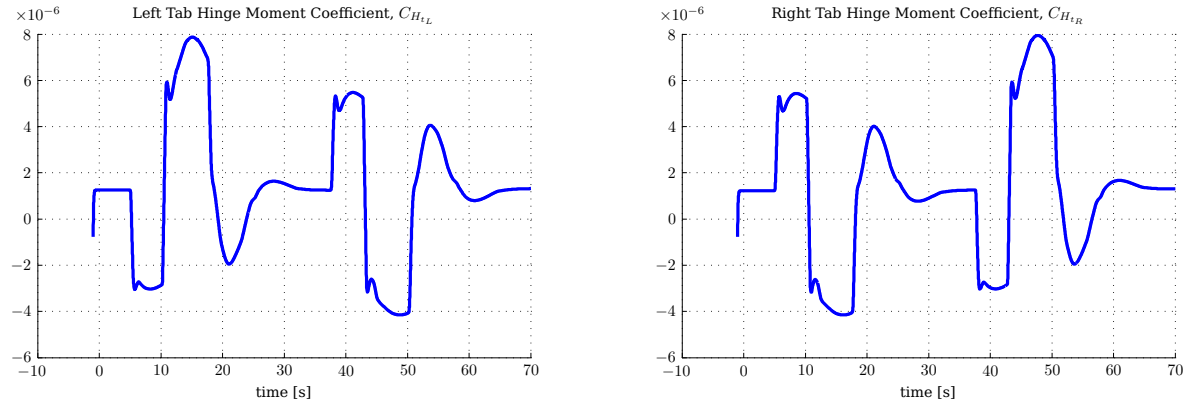


(a) Left Wing (b) Right Wing

**Figure 6.12** – Tab hinge moment coefficients.

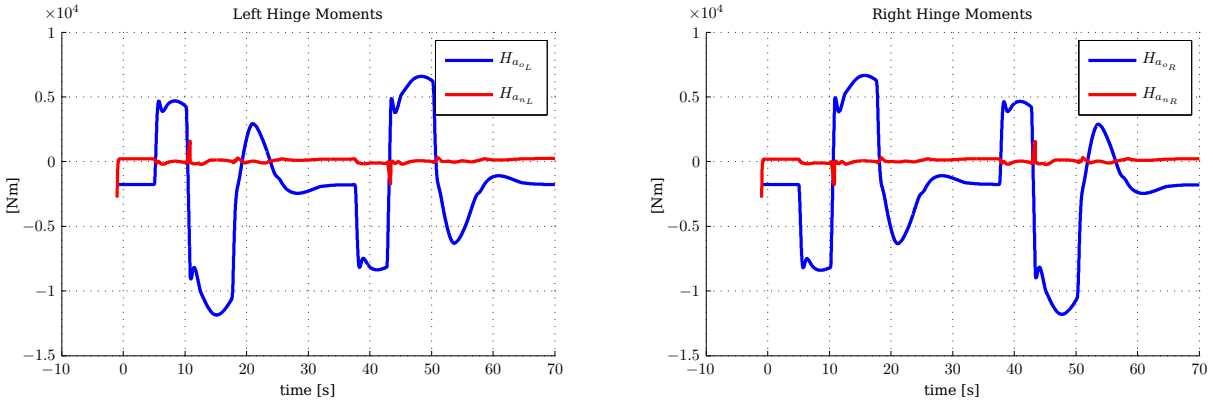


(a) Left Wing (b) Right Wing

**Figure 6.13** – Aileron hinge moments.

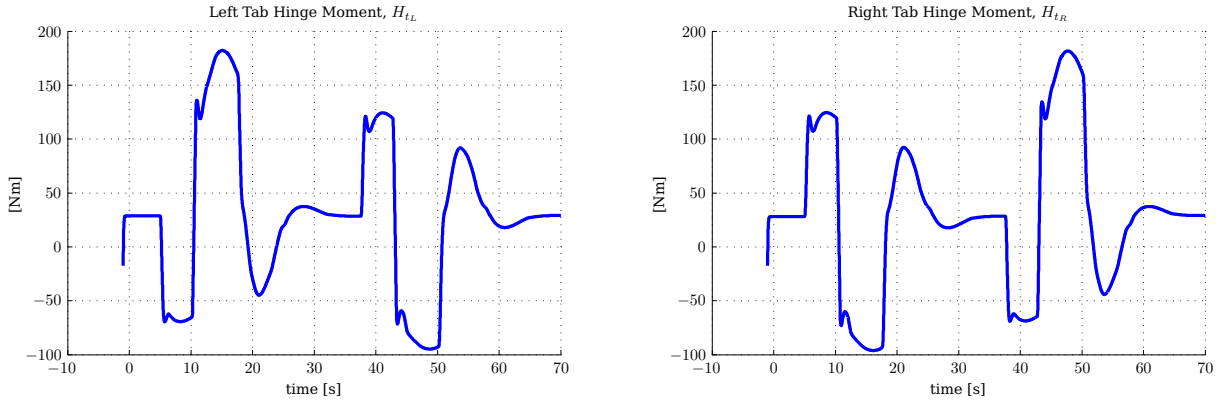


(a) Left Wing (b) Right Wing

**Figure 6.14** – Tab hinge moments.

account, the results of the hinge moments can be considered more accurate and representative of an actual manoeuvre than those for the two-dimensional approximation provided in §6.5.1.

The tab hinge moment is shown in Figure 6.14 and is seen to be at most $200\,\mathrm{N}\cdot\mathrm{m}$ in value. This brings the (new) aileron and tab hinge moments into the same order of magnitude suggesting that actuators of similar capabilities could be used to deflect the control surfaces.

The deflection angles of the new and old configurations are provided for each wing in Figure 6.15. A similar increase in magnitude of the aileron deflections can be seen as noted in §6.5.1, for the same reasons. The

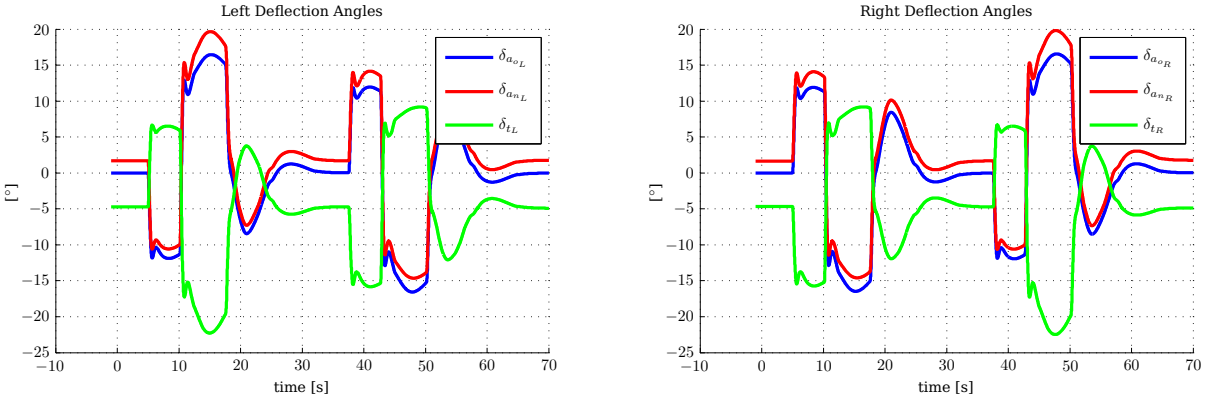


(a) Left Wing (b) Right Wing

**Figure 6.15** – Aileron and tab deflection angles.

graphs also show the non-zero deflections of the new ailerons and tabs for old aileron deflections of $0\,°$. When compared to the results of §6.5.1, it should be pointed out that the maximum deflections of the new ailerons and tabs are much smaller for equivalent portions of the manoeuvre, suggesting that the two-dimensional theory provides very conservative results. This will have to be verified with more accurate aerodynamic models.

# Chapter 7

# Conclusions and Recommendations

This final chapter aims to close off this project with conclusions drawn up based on the results obtained, as well as certain remarks regarding the project in general that may be of benefit. The second part of the chapter provides suggestions regarding potential topics for future research, as well as suggestions on how to improve this results obtained in this project.

## 7.1 Conclusions and Deductions

The first conclusion that can be drawn relates to the overall goal of the entire CoSICS project, namely: Is it possible to reduce the size of actuators of control surfaces in such a way that they can be used in confined spaces? In short, from the results shown in this project, it is promising that there are potential solutions available which make use of aerodynamic effects to decrease the size of necessary actuators, and it is worth spending further time and resources in future research concerning this topic.

Regarding the goals of this project specifically, as defined in §1.6, the following conclusions can be drawn.

1. The task of creating a simulation framework to use throughout the project has been completed. Through consultation with CPUT and UCT the interfaces between the various components have been defined allowing the development of these components within the framework in such a way that they can be easily removed and replaced without affecting other components directly. Minor changes may need to be made to support unforeseen developments within the framework, though these are not expected to be extensive, and will merely entail the addition or removal of parameters required for specific implementations.

2. The two optimisation techniques developed and implemented during the course of the project have also been done in such a way that the objective and constraint functions can be easily modified without affecting the inner workings of the optimisation algorithms. All necessary parameters for the algorithms are easily set during the initialisation of the optimisation and have been grouped for convenient use as part of the optimisation infrastructure. Due to the nature of the implementation, these algorithms and codes can be used for tasks other than those described in this project, with little, if any, modifications being required.

3. The aerodynamic models developed for use in the project provide sufficient insight into the nature of hinge moments and the effects of tab deflections in attempts to reduce hinge moments to indicate that the initial idea is viable. The variation between the linearised and non-linear thin aerofoil theory do, however, highlight the dependence of the research on accurate aerodynamic information, and indicate that depending on this information, the achievement region (in terms of being able to achieve similar rolling moment and lift coefficients, as well as the small aileron hinge moment coefficients) varies greatly. This also imports the need to adhere to any assumptions made during the development of any simplified theory.

4. The results of the optimisations performed using the developed algorithms and aerodynamic theory indicate a good possibility of tab-like structures being useful in the endeavour to reduce primary control surface (such as aileron) hinge moments. It is noted that while in many cases it is possible to reduce the aileron hinge moment to zero, this does not apply over the entire flight domain. This indicates that while it is unlikely that the aileron actuator can be eliminated completely, it is possible to make use of smaller actuators instead of large hydraulic actuators.

5. The tab hinge moment is also suitably small enough that large actuators will not be necessary to deflect the ailerons. Coupled with the previous paragraph, this suggests that alternative means of actuation, such as the smart material actuators or pure electric actuators can be considered instead of the currently used hydraulic systems.

An important remark regarding the optimisation. During the execution of this project, wherein simplified mathematical models are used for aspects such as the aerodynamics, it is noted that making use of the genetic algorithm method is very time consuming. While it is preferred to use the REGA since it has a better guarantee of providing a global optimisation, it is necessary to consider methods that reduce the need to simulate as many potential solutions as was performed during this project. Without the use (on fifty computers) of the parallel processing system developed, it would not have been possible to perform the optimisations required within the time available for the project.

Overall this project can be considered a success in that it achieved a first order solution to the optimisation problem using the simplified aerodynamics, as well as simulating one of the sizing manoeuvres successfully. This indicates that the infrastructure laid down is suitable for the desired application, and it is in a position to be developed and used further as the CoSICS project progresses.

## 7.2 Future Work and Recommendations

While it is felt that a wide variety of different topics were covered during the course of the project there are still many considerations that can be taken into account in future work. Some of these considerations are now listed and described.

1. The first, and most important aspect that needs to be taken into account is that regarding the premise on which this project was performed. This project made use of some first order approximations regarding aspects such as the aerodynamics, ignoring aspects such as drag due to the mathematical complexity of developing suitable models, which are beyond the scope of this project. It has already been mentioned how pivotal the aerodynamics are to the successful evaluation of various designs, thus it is necessary that much higher fidelity models be produced in order to obtain accurate results.

2. This project made use of two-dimensional thin aerofoil theory, then used this theory to approximate some of the three dimensional aerodynamics. It is thus necessary to build accurate three-dimensional aerodynamic models, since the problem is to be applied to full six-degree-of-freedom model. It is also pivotal that *drag* be taken into account as the addition of the additional flap is expected to have a negative influence on drag. Once it is possible to determine the drag component, a drag term can be easily added to the cost function, thus allowing the effect of drag to be taken into account appropriately.

3. The simulations performed thus far are also performed at sub-sonic speeds. Since the cruise velocity of most commercial airliners is in the transonic region, it needs to be possible to simulate within these regions, as well as obtain the necessary lift, drag and rolling moment values. An additional consideration is that of boundary layer separation. Since the tab is located at the trailing edge of another deflected control surface, the airflow over the aerofoil is not expected to be smooth, and it could happen that boundary layer separation occurs, thus rendering the tab less-effective in certain conditions. The same effect could occur as a result of turbulent flow.

4. As of yet, only static analyses have been performed. It is thus necessary to take into account dynamic effects of the tab, and eventually all the potential actuators. It would not be satisfactory to have an actuator that is capable of producing the hinge moment required, but is unable to perform quickly enough (has insufficient bandwidth) to act as an aileron or tab actuator. Both the actuator and tab dynamics need to be incorporated in their relevant portions of the simulation model.

5. Once the dynamics are known, control strategies can be considered, implemented and tested. Initially it is recommended to create a separate controller from the fly-by-wire system which accepts the original aileron deflection command as input and translates it to suitable tab and new aileron deflections. The controller will also need to take into account aspects such as potential instabilities. A suitable controller would be able to eliminate the spikes noted in the simulation results of Chapter 5.

6. Noting that all the provided graphs and surfaces from the optimisation results are smooth curves, it may be possible to fit these curves to known analytical functions, or at least approximated mathematical functions that can be used in the optimisation process. If these surfaces can be parameterised according to the design variables being considered, the efficiency of the optimisation process could be dramatically improved. Potential closed-form solutions may then be obtained, eliminating the need for the optimisation component altogether.

7. A greater study into the effects of the weightings used by the optimisation process should be considered. While the results provided are satisfactory for the given desires, these design parameters may not be the best for overall efficiency. Consider the case where the aileron hinge moments are much smaller than the tab hinge moments. Theoretically a smaller aileron actuator could then be used, though the aileron may still need to house the tab actuator, which in this case would be larger. It would be more economical to adjust the optimisation weightings in such a way that the aileron and tab hinge moment values are more-or-less equal, thus requiring the same size actuators to be used. Only one actuator type would then need to be designed.

8. During the course of this project only one sizing manoeuvre was performed indicating the ability of the new configuration to perform this manoeuvre, as well as providing an example of how the simulation model can be used to demonstrate it. For the final project, it is necessary that all the sizing manoeuvres be demonstrated, thus those remaining should also be implemented. There is also currently insufficient information available from Airbus to demonstrate the effectiveness of a design at low speeds since the flap configuration is not taken into account. The model should thus be expanded to allow this.

9. As noted in §7.1, the optimisation process is not a fast process, even using the reduced order aerodynamic models in this project. This indicates that better techniques should to be used to reduce the number of data points that need to be simulated. One potential method that could aid in this regard is the concept of design of experiments, where only a few data points are simulated, providing a general idea of the behaviour of the system, thus allowing decisions to be made that will reduce the design space of the system, which reduce the number of simulation points required. A technique that can be considered is that of response surface models.

10. In addition to the previous point, an examination should be performed to determine if it is possible to make use of the gradient methods in all cases. It is possible that finite difference methods can be used to determine local gradients about the current point being evaluated. This seems plausible since the results, as mentioned in the preceding point, are all smooth curves which do not suggest any “strange” behaviour to invalidate the approximate gradients.

11. It has also been suggested that some of the optimisation objectives be converted to constraints. An example of this is to set the constraint of the new and old lift coefficient or moment coefficient values to be equal. Care must be taken, however, to ensure that the base case of an aileron-only configuration does not result. Other goals may also be converted to constraints in this manner, simplifying the objective function being optimised.

12. An examination should also be performed to determine if it is possible to eliminate the dual-layer optimisation process entirely, and to rather combine the objectives in such a way that a single optimisation can be performed.

13. During the implementation of future projects, the methodologies used should take into account considerations which would allow the use of parallel computing systems, rather than being limited to sequential operations only. If this is possible, the time required for optimisations could be drastically reduced.

## 7.3 Closing

After spending two years consulting with an assortment of professionals from other universities in South Africa, as well as those from the NACoE and Airbus, it is believed that with the conclusion of this project that the information provided in this thesis will be useful to promote further research in the topic of Control Surfaces in Confined Spaces, and will even benefit research outside this main focus area.

# Appendix A

# Linearisation of the Thin Aerofoil Theory

The appendix provides the detailed linearisation of the thin aerofoil theory described in §3.5.

The equations developed in §3.4.2, specifically Equations 3.4.39 to 3.4.41, provide a non-linear approximation of the lift and control surface hinge moments. Many stability and control texts (Etkin and Reid [7], and Cook [6]) regarding aerodynamic flight use linearised equations of the form

$$C_x = C_{x_0} + C_{x_\alpha}\alpha + C_{x_{\delta_a}}\delta_a + C_{x_{\delta_t}}\delta_t \qquad [3.5.1]$$

where $C_x$ is any of $C_L$, $C_{H_a}$ and $C_{H_t}$. $C_{x_0}$ is the constant contribution due to the shape (camber and thickness) of the aerofoil, $C_{x_\alpha} = \frac{\partial C_x}{\partial \alpha}$ is a derivative providing the contribution to $C_x$ due to angle-of-attack, $C_{x_{\delta_a}} = \frac{\partial C_x}{\partial \delta_a}$ is the derivative providing the contribution due to aileron deflection and $C_{x_{\delta_t}} = \frac{\partial C_x}{\partial \delta_t}$ is the derivative providing the contribution due to tab deflection.

Since this is a convenient form with which to work, Equations 3.4.39 to 3.4.41 will be linearised in this section. Texts discussing thin aerofoil theory (Anderson [28], Kueth and Chow [15], and Moran [16]) simplify the analysis by ignoring the higher order components ($n > 2$) in the Fourier series expansions. Following the same route here, and with some small angle approximations, it is possible to re-write Equations 3.4.39 to 3.4.41 in the form of Equation 3.5.1, where the dependencies on $\alpha$, $\delta_a$ and $\delta_t$ are separated.

## A.1 Sectional Aileron Hinge Moment Coefficient

Starting with the sectional aileron hinge moment coefficient equation of Equation 3.4.40:

$$
\begin{aligned}
C_{H_a} &= -\int_{\theta_{h_a}}^{\pi} \left(A_{0_u} + A_{0_a} + A_{0_t}\right)(1 + cos\theta)\left((2E_a - 1) - \cos\theta\right) + \sum_{n=1}^{\infty}\left(A_{n_u} + A_{n_a} + A_{n_t}\right)\sin n\theta \sin\theta\left((2E_a - 1) - \cos\theta\right)\ \mathrm{d}\theta \\
&= -\int_{\theta_{h_a}}^{\pi}\left\{\alpha - \frac{1}{\pi}\int_0^{\pi}\frac{\mathrm{d}z}{\mathrm{d}x}\,\mathrm{d}\theta\right\}(1 + cos\theta)\left((2E_a - 1) - \cos\theta\right) + \left\{\alpha_a - \frac{1}{\pi}\left(m_{1_a}\theta'_{h_a} + m_{2_a}\left(\pi - \theta'_{h_a}\right)\right)\right\}(1 + cos\theta)\left((2E_a - 1) - \cos\theta\right) \\
&\quad + \left\{\alpha_t - \frac{1}{\pi}\left(m_{1_t}\theta'_{h_t} + m_{2_t}\left(\pi - \theta'_{h_t}\right)\right)\right\}(1 + cos\theta)\left((2E_a - 1) - \cos\theta\right) \\
&\quad + \sum_{n=1}^{\infty}\left\{\frac{2}{\pi}\int_0^{\pi}\frac{\mathrm{d}z}{\mathrm{d}x}\cos\left(n\theta\right)\ \mathrm{d}\theta\right\}\sin n\theta\sin\theta\left((2E_a - 1) - \cos\theta\right) + \left\{\frac{2}{n\pi}\sin\left(n\theta'_{h_a}\right)\left(m_{1_a} - m_{2_a}\right)\right\}\sin n\theta\sin\theta\left((2E_a - 1) - \cos\theta\right) \\
&\quad + \left\{\frac{2}{n\pi}\sin\left(n\theta'_{h_t}\right)\left(m_{1_t} - m_{2_t}\right)\right\}\sin n\theta\sin\theta\left((2E_a - 1) - \cos\theta\right)\ \mathrm{d}\theta
\end{aligned}
$$

and expanding leads to

$$
\begin{aligned}
C_{H_a} &= -\int_{\arccos(2E_a - 1)}^{\pi}\left\{\alpha - \frac{1}{\pi}\int_0^{\pi}\frac{\mathrm{d}z}{\mathrm{d}x}\,\mathrm{d}\theta\right\}(1 + cos\theta)\left((2E_a - 1) - \cos\theta\right) \\
&\quad + \left\{\alpha_a - \frac{1}{\pi}\left(\tan\alpha_a \arccos\left(1 - 2\frac{(1 - E_a)\cos\alpha_a}{\sqrt{(1 - E_a)^2 + E_a^2 + 2E_a(1 - E_a)\cos\delta_a}}\right) + \tan\left(\alpha_a - \delta_a\right)\left(\pi - \arccos\left(1 - 2\frac{(1 - E_a)\cos\alpha_a}{\sqrt{(1 - E_a)^2 + E_a^2 + 2E_a(1 - E_a)\cos\delta_a}}\right)\right)\right)\right\} \\
&\quad \times (1 + cos\theta)\left((2E_a - 1) - \cos\theta\right) \\
&\quad + \left\{\alpha_t - \frac{1}{\pi}\left(\tan\alpha_t \arccos\left(1 - 2\frac{(1 - E_t)\cos\alpha_t}{\sqrt{(1 - E_t)^2 + E_t^2 + 2E_t(1 - E_t)\cos\delta_t}}\right) + \tan\left(\alpha_t - \delta_t\right)\left(\pi - \arccos\left(1 - 2\frac{(1 - E_t)\cos\alpha_t}{\sqrt{(1 - E_t)^2 + E_t^2 + 2E_t(1 - E_t)\cos\delta_t}}\right)\right)\right)\right\} \\
&\quad \times (1 + cos\theta)\left((2E_a - 1) - \cos\theta\right) \\
&\quad + \sum_{n=1}^{\infty}\left\{\frac{2}{\pi}\int_0^{\pi}\frac{\mathrm{d}z}{\mathrm{d}x}\cos\left(n\theta\right)\ \mathrm{d}\theta\right\}\sin n\theta\sin\theta\left((2E_a - 1) - \cos\theta\right)\ \mathrm{d}\theta + \left\{\frac{2}{n\pi}\sin\left(n\arccos\left(1 - 2\frac{(1 - E_a)\cos\alpha_a}{\sqrt{(1 - E_a)^2 + E_a^2 + 2E_a(1 - E_a)\cos\delta_a}}\right)\right)\left(\tan\alpha_a - \tan\left(\alpha_a - \delta_a\right)\right)\right\} \\
&\quad \times \sin n\theta\sin\theta\left((2E_a - 1) - \cos\theta\right)\ \mathrm{d}\theta \\
&\quad + \left\{\frac{2}{n\pi}\sin\left(n\arccos\left(1 - 2\frac{(1 - E_t)\cos\alpha_t}{\sqrt{(1 - E_t)^2 + E_t^2 + 2E_t(1 - E_t)\cos\delta_t}}\right)\right)\left(\tan\alpha_t - \tan\left(\alpha_t - \delta_t\right)\right)\right\}\sin n\theta\sin\theta\left((2E_a - 1) - \cos\theta\right)\ \mathrm{d}\theta
\end{aligned}
\tag{A.1.1}
$$

If we assume operation about the cruise trim point, then $\delta_a$ and $\delta_t$ are small, and thus $\alpha_a$ and $\alpha_t$ are small. Thus, with the previous statement in mind, the following small angle approximations are used:

$$\cos x \approx 1 \qquad \sin x \approx x \qquad \tan x \approx x \qquad \tan\left(A \pm B\right) \approx \left(A \pm B\right)$$

which results in Equation A.1.1 becoming

$$\begin{aligned}
C_{H_a} \quad = \quad & -\int_{\arccos(2E_a-1)}^{\pi} \left\{\alpha - \frac{1}{\pi}\int_0^{\pi} \frac{\mathrm{d}z}{\mathrm{d}x}\,\mathrm{d}\theta\right\}(1+cos\theta)\left((2E_a-1)-\cos\theta\right) \\
& + \left\{\alpha_a - \frac{1}{\pi}\left(\alpha_a \arccos\left(2E_a-1\right) + \left(\alpha_a-\delta_a\right)\left(\pi - \arccos\left(2E_a-1\right)\right)\right)\right\}(1+cos\theta)\left((2E_a-1)-\cos\theta\right) \\
& + \left\{\alpha_t - \frac{1}{\pi}\left(\alpha_t \arccos\left(2E_t-1\right) + \left(\alpha_t-\delta_t\right)\left(\pi - \arccos\left(2E_t-1\right)\right)\right)\right\}(1+cos\theta)\left((2E_a-1)-\cos\theta\right) \\
& + \sum_{n=1}^{\infty}\left\{\frac{2}{\pi}\int_0^{\pi}\frac{\mathrm{d}z}{\mathrm{d}x}\cos\left(n\theta\right)\,\mathrm{d}\theta\right\}\sin n\theta\sin\theta\left((2E_a-1)-\cos\theta\right) \\
& + \left\{\frac{2}{n\pi}\sin\left(n\arccos\left(2E_a-1\right)\right)\left(\alpha_a-\left(\alpha_a-\delta_a\right)\right)\right\}\sin n\theta\sin\theta\left((2E_a-1)-\cos\theta\right) \\
& + \left\{\frac{2}{n\pi}\sin\left(n\arccos\left(2E_t-1\right)\right)\left(\alpha_t-\left(\alpha_t-\delta_t\right)\right)\right\}\sin n\theta\sin\theta\left((2E_a-1)-\cos\theta\right)\,\mathrm{d}\theta
\end{aligned} \tag{A.1.2}$$

Taking note that the only difference between Equations 3.4.40 and 3.4.41 is the change in the integration boundary and the moment arm, it is possible to generalise the derivation by replacing these differing values with the generalising parameter $\Psi$. For the aileron hinge moment coefficient:

$$\Psi = (2E_a - 1)$$

and for the tab hinge moment coefficient

$$\Psi = (2E_t - 1)$$

The generalised form of Equation A.1.2 is given below

$$\begin{aligned}
C_H \quad = \quad & -\int_{\arccos\Psi}^{\pi} \left\{\alpha - \frac{1}{\pi}\int_0^{\pi} \frac{\mathrm{d}z}{\mathrm{d}x}\,\mathrm{d}\theta\right\}(1+cos\theta)\left(\Psi-\cos\theta\right) \\
& + \left\{\alpha_a - \frac{1}{\pi}\left(\alpha_a \arccos\left(2E_a-1\right) + \left(\alpha_a-\delta_a\right)\left(\pi - \arccos\left(2E_a-1\right)\right)\right)\right\}(1+cos\theta)\left(\Psi-\cos\theta\right) \\
& + \left\{\alpha_t - \frac{1}{\pi}\left(\alpha_t \arccos\left(2E_t-1\right) + \left(\alpha_t-\delta_t\right)\left(\pi - \arccos\left(2E_t-1\right)\right)\right)\right\}(1+cos\theta)\left(\Psi-\cos\theta\right) \\
& + \sum_{n=1}^{\infty}\left\{\frac{2}{\pi}\int_0^{\pi}\frac{\mathrm{d}z}{\mathrm{d}x}\cos\left(n\theta\right)\,\mathrm{d}\theta\right\}\sin n\theta\sin\theta\left(\Psi-\cos\theta\right) \\
& + \left\{\frac{2\delta_a}{n\pi}\sin\left(n\arccos\left(2E_a-1\right)\right)\right\}\sin n\theta\sin\theta\left(\Psi-\cos\theta\right) \\
& + \left\{\frac{2\delta_t}{n\pi}\sin\left(n\arccos\left(2E_t-1\right)\right)\right\}\sin n\theta\sin\theta\left(\Psi-\cos\theta\right)\,\mathrm{d}\theta
\end{aligned}$$

which can be reduced to the form

$$C_H = b_0 + b_1\alpha + b_2\delta_a + b_3\delta_t \tag{3.5.2}$$

After limiting the number of Fourier coefficients to three ($A_0$, $A_1$ and $A_2$), the *functions* $b_0$, $b_1$, $b_2$ and $b_3$ are determined to be

$$\begin{aligned}
b_0 = C_{H_0} = & \left[\left(A-B\right)\Psi + \frac{1}{2}\left(D-A\right)\right]\left(1-\frac{\arccos\Psi}{\pi}\right) - \frac{1}{\pi}\left(\left(A-D\right)\Psi - A + \frac{B}{2}\right)\sin\left(\arccos\Psi\right) \\
& - \frac{1}{2\pi}\left(B\Psi - \frac{A}{2}\right)\sin\left(2\arccos\Psi\right) - \frac{1}{3\pi}\left(D\Psi - \frac{B}{2}\right)\sin\left(3\arccos\Psi\right) \\
& + \frac{D}{8\pi}\sin\left(4\arccos\Psi\right)
\end{aligned} \tag{A.1.3}$$

where

$$A = \int_0^{\pi}\frac{\mathrm{d}z}{\mathrm{d}x}\,\mathrm{d}\theta \qquad B = \int_0^{\pi}\frac{\mathrm{d}z}{\mathrm{d}x}\cos\theta\,\mathrm{d}\theta \qquad D = \int_0^{\pi}\frac{\mathrm{d}z}{\mathrm{d}x}\cos 2\theta\,\mathrm{d}\theta$$

and

$$b_1 = C_{H_\alpha} = \left(\Psi - \frac{1}{2}\right)(\arccos\Psi - \pi) + (\Psi - 1)\sin(\arccos\Psi) - \frac{1}{4}\sin(2\arccos\Psi) \tag{A.1.4}$$

Also

$$b_2 = C_{H_{\delta_a}} = K(\pi - \arccos\Psi) - L\sin(\arccos\Psi) - \frac{M}{2}\sin(2\arccos\Psi) - \frac{N}{3}\sin(3\arccos\Psi) + \frac{H}{16\pi}\sin(4\arccos\Psi) \tag{A.1.5}$$

where

$$G = \sin(\arccos(2E_a - 1)) \qquad L = \left[I(1-\Psi) + \frac{1}{2\pi}(G - H\Psi)\right]$$

$$H = \sin(2\arccos(2E_a - 1)) \qquad M = \left[\frac{I}{2} + \frac{G\Psi}{\pi}\right]$$

$$I = \left(1 - \frac{1}{\pi}\arccos(2E_a - 1)\right) \qquad N = \left[\frac{H\Psi}{2\pi} - \frac{G}{2\pi}\right]$$

$$K = \left[I\left(\frac{1}{2} - \Psi\right) - \frac{G\Psi}{\pi} + \frac{H}{4\pi}\right]$$

and finally

$$b_3 = C_{H_{\delta_t}} = T(\pi - \arccos\Psi) - U\sin(\arccos\Psi) - \frac{V}{2}\sin(2\arccos\Psi) - \frac{W}{3}\sin(3\arccos\Psi) + \frac{Q}{16\pi}\sin(4\arccos\Psi) \tag{A.1.6}$$

where

$$P = \sin(\arccos(2E_t - 1)) \qquad U = \left[R(1-\Psi) + \frac{1}{2\pi}(P - Q\Psi)\right]$$

$$Q = \sin(2\arccos(2E_t - 1)) \qquad V = \left[\frac{R}{2} + \frac{P\Psi}{\pi}\right]$$

$$R = \left(1 - \frac{1}{\pi}\arccos(2E_t - 1)\right) \qquad W = \left[\frac{Q\Psi}{2\pi} - \frac{P}{2\pi}\right]$$

$$T = \left[R\left(\frac{1}{2} - \Psi\right) - \frac{P\Psi}{\pi} + \frac{Q}{4\pi}\right]$$

By setting the parameter $\Psi$ appropriately, the above coefficients can be used to determine either the tab, or the aileron sectional hinge moment coefficient.

## A.2 Sectional Aileron Lift Coefficient

A similar process is followed for the sectional lift coefficient, starting with Equation 3.4.39:

$$
\begin{aligned}
C_L &= 2\int_0^\pi \left[ \left(A_{0_u} + A_{0_a} + A_{0_t}\right) \left(\frac{1+cos\theta}{\sin\theta}\right) + \sum_{n=1}^{\infty} \left(A_{n_u} + A_{n_a} + A_{n_t}\right) \sin n\theta \right] \sin\theta \, \mathrm{d}\theta \\
&= 2\int_0^\pi \left(\alpha - \frac{1}{\pi}\int_0^\pi \frac{\mathrm{d}z}{\mathrm{d}x}\, \mathrm{d}\theta\right)(1+cos\theta) + \left(\alpha_a - \frac{1}{\pi}\left(m_{1_a}\theta'_{h_a} + m_{2_a}\left(\pi - \theta'_{h_a}\right)\right)\right)(1+cos\theta) + \left(\alpha_t - \frac{1}{\pi}\left(m_{1_t}\theta'_{h_t} + m_{2_t}\left(\pi - \theta'_{h_t}\right)\right)\right)(1+cos\theta) \\
&= +\sum_{n=1}^{\infty}\left(\frac{2}{\pi}\int_0^\pi \frac{\mathrm{d}z}{\mathrm{d}x}\cos\left(n\theta\right)\, \mathrm{d}\theta\right)\sin\theta\sin n\theta + \left(\frac{2}{n\pi}\sin\left(n\theta'_{h_a}\right)\left(m_{1_a} - m_{2_a}\right)\right)\sin\theta\sin n\theta + \left(\frac{2}{n\pi}\sin\left(n\theta'_{h_t}\right)\left(m_{1_t} - m_{2_t}\right)\right)\sin\theta\sin n\theta \, \mathrm{d}\theta
\end{aligned}
$$

which is expanded to obtain

$$
\begin{aligned}
C_L &= 2\int_0^\pi \left(\alpha - \frac{1}{\pi}\int_0^\pi \frac{\mathrm{d}z}{\mathrm{d}x}\, \mathrm{d}\theta\right)(1+cos\theta) \\
&= +\left(\alpha_a - \frac{1}{\pi}\left(\tan\alpha_a \arccos\left(1 - 2\frac{(1-E_a)\cos\alpha_a}{\sqrt{(1-E_a)^2 + E_a^2 + 2E_a\left(1-E_a\right)\cos\delta_a}}\right) + \tan\left(\alpha_a - \delta_a\right)\left(\pi - \arccos\left(1 - 2\frac{(1-E_a)\cos\alpha_a}{\sqrt{(1-E_a)^2 + E_a^2 + 2E_a\left(1-E_a\right)\cos\delta_a}}\right)\right)\right)\right)(1+cos\theta) \\
&= +\left(\alpha_t - \frac{1}{\pi}\left(\tan\alpha_t \arccos\left(1 - 2\frac{(1-E_t)\cos\alpha_t}{\sqrt{(1-E_t)^2 + E_t^2 + 2E_t\left(1-E_t\right)\cos\delta_t}}\right) + \tan\left(\alpha_t - \delta_t\right)\left(\pi - \arccos\left(1 - 2\frac{(1-E_t)\cos\alpha_t}{\sqrt{(1-E_t)^2 + E_t^2 + 2E_t\left(1-E_t\right)\cos\delta_t}}\right)\right)\right)\right)(1+cos\theta) \\
&= +\sum_{n=1}^{\infty}\left(\frac{2}{\pi}\int_0^\pi \frac{\mathrm{d}z}{\mathrm{d}x}\cos\left(n\theta\right)\, \mathrm{d}\theta\right)\sin\theta\sin n\theta \\
&= +\left(\frac{2}{n\pi}\sin\left(n\arccos\left(1 - 2\frac{(1-E_a)\cos\alpha_a}{\sqrt{(1-E_a)^2 + E_a^2 + 2E_a\left(1-E_a\right)\cos\delta_a}}\right)\right)\left(\tan\alpha_a - \tan\left(\alpha_a - \delta_a\right)\right)\right)\sin\theta\sin n\theta \\
&= +\left(\frac{2}{n\pi}\sin\left(n\arccos\left(1 - 2\frac{(1-E_t)\cos\alpha_t}{\sqrt{(1-E_t)^2 + E_t^2 + 2E_t\left(1-E_t\right)\cos\delta_t}}\right)\right)\left(\tan\alpha_t - \tan\left(\alpha_t - \delta_t\right)\right)\right)\sin\theta\sin n\theta \, \mathrm{d}\theta
\end{aligned}
$$

Using the previously defined small angle approximations the above equation is reduced to

$$
\begin{aligned}
C_L = 2\int_0^\pi \alpha\left(1+cos\theta\right) - \left(\frac{1}{\pi}\int_0^\pi \frac{\mathrm{d}z}{\mathrm{d}x}\, \mathrm{d}\theta\right)(1+cos\theta) + \delta_a\left(1 - \frac{1}{\pi}\arccos\left(2E_a - 1\right)\right)(1+cos\theta) + \delta_t\left(1 - \frac{1}{\pi}\arccos\left(2E_t - 1\right)\right)(1+cos\theta) \\
+\sum_{n=1}^{\infty}\left(\frac{2}{\pi}\int_0^\pi \frac{\mathrm{d}z}{\mathrm{d}x}\cos\left(n\theta\right)\, \mathrm{d}\theta\right)\sin\theta\sin n\theta + \left(\frac{2\delta_a}{n\pi}\right)\sin\left(n\arccos\left(2E_a - 1\right)\right)\sin\theta\sin n\theta + \left(\frac{2\delta_t}{n\pi}\right)\sin\left(n\arccos\left(2E_t - 1\right)\right)\sin\theta\sin n\theta \, \mathrm{d}\theta \quad \text{(A.2.1)}
\end{aligned}
$$

This now simplifies to Equation 3.5.3 as described in §3.5.

# Appendix B

# Distributed Processing Code Conversion Example

This appendix provides a simple example of the way in which a sequential program which is parallelisable can be converted to make use of the distributed processing system described in §4.6.

The original code segment is shown in Listing B.1,

**Listing B.1** – A simple example of code implemented *sequentially*.

```
% The sequential loop
J = zeros(Ps, 1);
total_cost = 0;
for i=1:1:Ps
    J(i) = cost(x(:, i), false, n, m, p, OtherInfo);
    total_cost = total_cost + J(i);
end

% Print the result
disp('Costs are:');
disp(J);
fprintf('The Total Cost is: %g\n', total_cost);
```

with the converted distributed processing equivalent in Listing B.2.

**Listing B.2** – The code of Listing B.1 after conversion to the distributed processing equivalent.

```
% Connect to  the distributed processing server
[socket ipadr] = dp_Init();
socket = uint32(socket);

% Dispatch all the jobs
jobs = cell(Ps, 1);
for i=1:1:Ps
    cost_params = {x(:, i), false, n, m, p, OtherInfo};
    jobs{i} = dp_CreateJob(@cost, cost_params, ipadr, socket);
end

% Now we must wait for the jobs to be done to get the results
J = zeros(Ps, 1);
total_cost = 0;
for i=1:1:Ps
    [status dp_val] = dp_GetResult(jobs{i}, ipadr, socket);
    if(~strcmp(status, 'DP_SUCCESS'))
        dp_Shutdown(ipadr, socket);
        error('Unable to retreive result of job ', jobs{i});
    end
```

```
    % normal calculations
23  J(i) = dp_val;
    total_cost = total_cost + J(i);
end

% Disconnect from the distributed processing server
28 dp_Shutdown(ipadr, socket);

% Print the result
disp('Costs are:');
disp(J);
33 fprintf('The Total Cost is: %g\n', total_cost);
```

It can be seen that lines 2 to 3 in Listing B.1 are found in Listing B.2 at lines 13 to 14, and lines 9 to 12 are now at lines 30 to 33.

The actual work that is being done (lines 5 and 6) is now broken into two parts in Listing B.2: at lines 8 and 9, where the job is created and dispatched to the server, and 16 to 24 where the result is retrieved, some error checking is done and the calculations continue.

# Appendix C

# Block Diagram

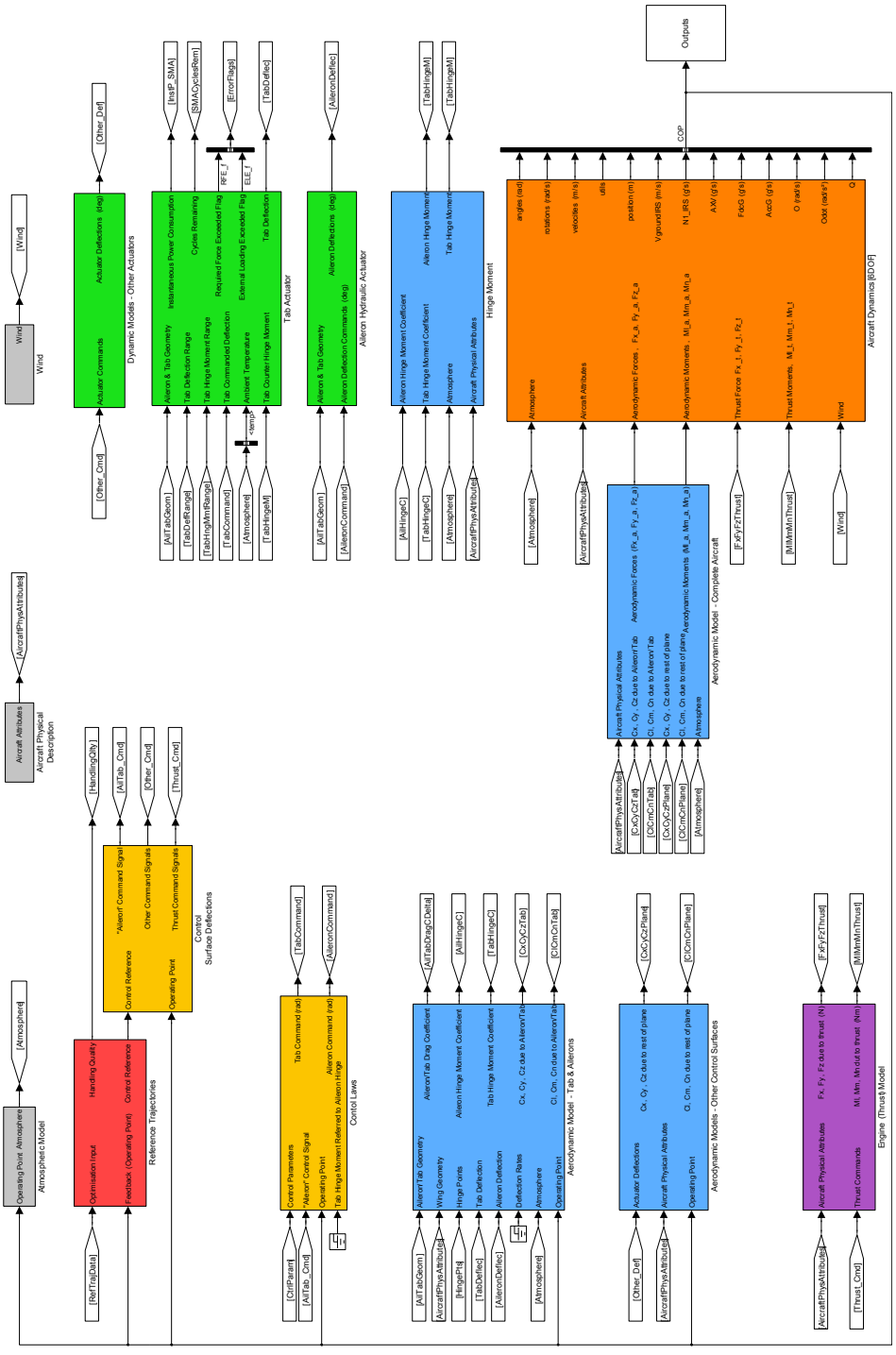


**Figure C.1** – An enlarged version of the complete simulation block diagram first shown in Figure 6.2.

## C.1 Introduction

This appendix intends to explain the components that make up the simulation block diagram first discussed in Chapter 6 and shown in Figures 6.2 and C.1. As stated previously, this Simulink simulation model is used as a means to test the various configurations, and provide performance related data as the various higher fidelity components are implemented and incorporated.

As such it is necessary to define the necessary interfaces between all these components such that each individual component may be developed in isolation, in that the rest of model will only require minor adjustments, if any, during incorporation of the module developed within the necessary infrastructure described here.

Each component of the block diagram is discussed in detail explaining the purpose of the component and its inputs and output. Design considerations will also be discussed where applicable.

The first implementation of this simulation environment, as used by this project, makes use of low order models in order to demonstrate the viability and usefulness of the simulation environment.

Since the interfaces are well-defined, a plug-and-play approach can be used where the various components are replaced with more complex and/or accurate versions allowing the simulation to be re-run to generate new (more accurate) results.

## C.2 Components

This section lists all the main components of the block diagram and how they link to each other. The entire simulation is driven from a Matlab script in which initial parameters are configured for the model.

### C.2.1 Reference Trajectories

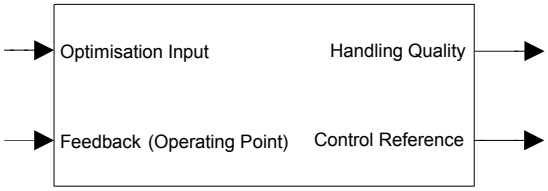


This simulates the pilot input for the model. Here the particular manoeuvres to be tested are implemented and recorded, in the form of a Matlab script, or MEX file.

| **Inputs** | |
|---|---|
| Optimisation Input | This is information provided by the optimisation algorithm to aid in calculating the *Handling Quality* and to ensure the reference trajectories are still valid. |
| Feedback (Operating Point) | The current operating point and associated values are provided in order to evaluate the manoeuvre currently being performed. The operating point consists of angle of attack ($\alpha$), side-slip angle ($\beta$), Airspeed ($V$), the Euler angles ($\phi$, $\theta$ and $\psi$), position ($x$, $y$, and $z$) and angular rates ($p$, $q$ and $r$) |
| **Outputs** | |
| Handling Quality | Information regarding deviation from the desired trajectories is converted to a *Handling Quality* value for the particular instance of the simulation run. |
| Control Reference [°] | These are the signals (essentially pilot commands) based on the current *Operating Point* and reference trajectories which will be sent to the control systems involved. |

### C.2.2 Control Surface Deflections

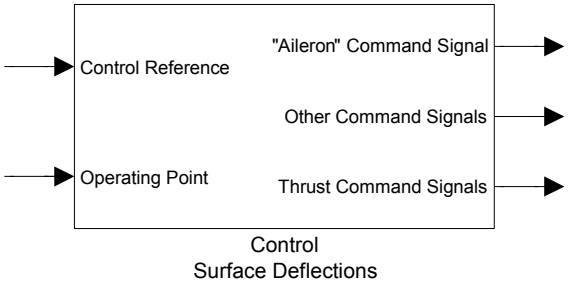


Determines the control surface deflection command signals based on the current system of control computers implemented by Airbus. These computers include the Pilot Inputs, Autopilot Inputs, ELACS, SECs, FACs and SFCCs; essentially the Fly-by-Wire system.

The block then separates the outputs into signals relating to the ailerons and those of the other control surfaces (flaps, elevator, rudder, spoilers, slats, etc.) as well as the thrust commands.

| **Inputs** | |
|---|---|
| Control Reference [°] | The control reference signals as sent by the Reference Trajectory block. |
| Operating Point | The current operating point and associated values are provided in order to evaluate the manoeuvre currently being performed. The operating point is discussed in detail in §C.2.12.1. |

| **Outputs** | |
|---|---|
| “Aileron” Command Signal [°] | The command signal that would normally be sent to the aileron actuator as if there was only an aileron present ($\delta_{ao}$). |
| Other Command Signals [°] | The command signals for all other control surfaces, which are not expected to have changed. |
| Thrust Command Signals [°] | The thrust commands. |

### C.2.3 Control Laws

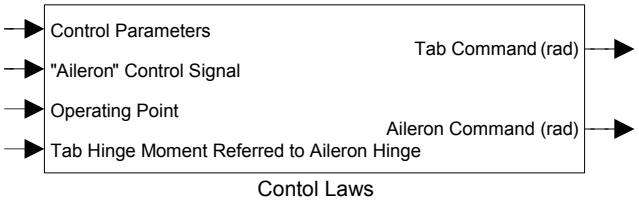


The control laws aim to convert the traditional aileron command signal into a signal for the aileron jack and one for the servo tab. It takes into account where in the flight domain the aircraft currently is and adapts the control as necessary for the operating point.

| **Inputs** | |
|---|---|
| Control Parameters | These are inputs from the optimisation algorithm which will adjust the “weighting” of how the tab will be actuated versus the aileron. |
| “Aileron” Command Signal [°] | The signal to convert to an Aileron and Tab control signal. |
| Operating Point | Refer to §C.2.12.1. |
| Tab Hinge Moment Referred to Aileron Hinge [N m] | This is the hinge moment about the aileron hinge that is due to the aerodynamic forces on the tab, i.e. the “helping” moment of the tab in order to position the aileron. |

| **Outputs** | |
|---|---|
| Tab Command [rad] | The tab command signal sent to the tab actuator. (This is independent of the way the tab is actuated.) |
| Aileron Command [rad] | The actual aileron actuator control signal which is to be fed to the aileron actuator. |

### C.2.4 Dynamic Models – Other Actuators

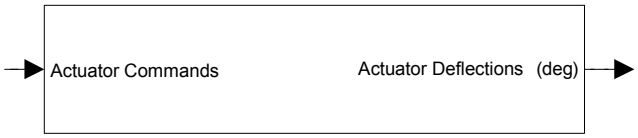

Dynamic Models - Other Actuators

The dynamics associated with the actuators for all the aerodynamic control surfaces are encapsulated in this block. Typically this is a first order approximation with saturation and rate limits. The models are provided by Airbus.

| **Inputs** | |
|---|---|
| Actuator Commands [°] | The command signals for the actuators. |

| **Outputs** | |
|---|---|
| Actuator Deflections [°] | The actual deflections of the relevant control surface. |

### C.2.5 Tab Actuator

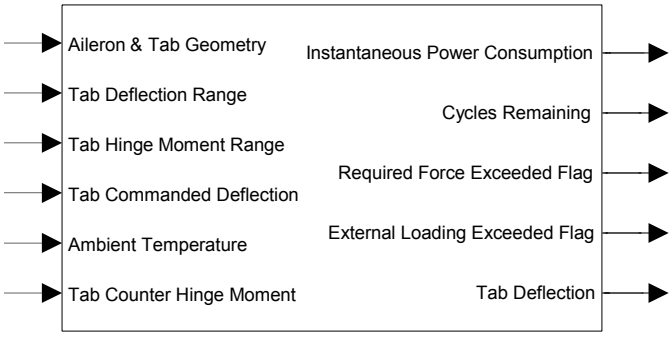

Tab Actuator

The tab actuator encompasses all the mechanisms required to enable, for example, the SMA or Piezoelectric material to result in a deflection of the tab. The actuator's specifications are derived from the input parameters and are hidden from the rest of the block diagram. This aids the implementation of the modular approach.

| **Inputs** | |
|---|---|
| Aileron and Tab Geometry | The tab chord length, span and maximum thickness as well as the aileron chord length. |
| Tab Deflection Range | The desired range over which the tab must be able to deflect. |
| Tab Hinge Moment Range | The range of hinge moments the actuator will have to work against/provide. |
| Tab Commanded Deflection | The currently commanded tab deflection angle. |
| Ambient Temperature | The current ambient temperature (around the actuator). |
| Tab Counter-Hinge Moment | The current aerodynamically induced hinge-moment the tab actuator has to work against. |

| **Outputs** | |
|---|---|
| Instantaneous Power Consumption | The current power required to maintain or effect the deflection. |
| Cycles Remaining | The number of expected cycles before actuator failure. |
| Required Force Exceeded Flag | (Boolean) The commanded force required exceeds that which can be produced by the actuator. |
| External Loading Exceeded Flag | (Boolean) The external loading has now resulted in a force which the actuator cannot work against resulting in damage to the actuator. |
| Tab Deflection [rad] | The actual deflection of the tab. |

### C.2.6 Aileron Hydraulic Actuator

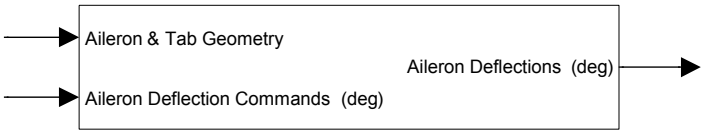

Aileron Hydraulic Actuator

The aileron actuator is a currently a standard hydraulic actuator, though his will not necessarily remain the case. At this stage it is assumed the actuator will always be able to produce the required deflection, i.e. the actuator is large enough to perform all the desired motions. At a later stage (once a suitable model has been obtained) this can be adjusted to be a component similar to the tab.

| **Inputs** | |
|---|---|
| Aileron and Tab Geometry | The geometry of the aileron and tab used to determine the actuator specifications. |
| Aileron Deflection Command [rad] | The command signal to the hydraulic actuator. |

| **Outputs** | |
|---|---|
| Aileron Deflection [rad] | The actual aileron deflection effected. |

### C.2.7 Aerodynamic Model – Tab and Aileron

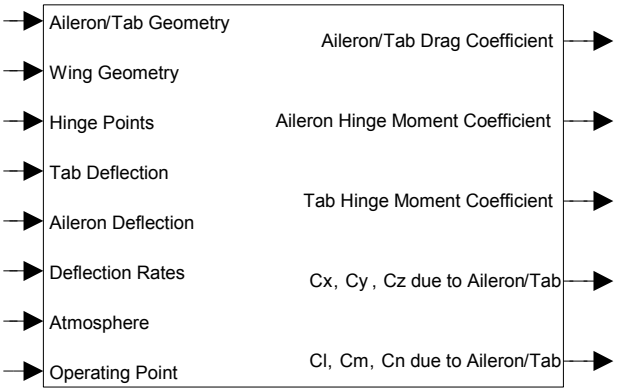

Aerodynamic Model - Tab & Ailerons

Here the various coefficients are calculated for the aileron and tab combination. These are also based on the geometry of the tab, as well as the rest of the aircraft.

The moment and force coefficients will be fed to the overall aerodynamic model whereas the hinge moment and drag coefficients will typically be used for analysis and adjusting optimisation parameters. The tab hinge moment coefficient will also be used to determine the counter hinge moment on the tab which the tab actuator has to work against.

Many of the geometric parameters will be passed by Matlab internally due to the number and variety of the parameters, but are listed as inputs to these blocks to indicate the need for these parameters.

| **Inputs** | |
|---|---|
| Aileron/Tab Geometry | The aileron and tab geometry including the chord and span lengths, as well as the profiles of the surfaces (Mean camber line and thickness distribution). |
| Wing Geometry | The planar geometry of the wing, as its profile. The positions of all the control surfaces are also required. |
| Hinge Points | The position along the tab/aileron profiles where the hinges are located. |
| Tab Deflection [rad] | The actual deflections of the tab and the aileron. |
| Aileron Deflection [rad] | The actual deflections of the tab and the aileron. |
| Deflection Rates [rad/s] | The rates of deflection of the tab and the aileron. |

| | |
|---|---|
| Atmosphere | The current atmospheric conditions. |
| Operating Point | Refer to §C.2.12.1. |

| **Outputs** | |
|---|---|
| Aileron/Tab Drag Coefficient | The change in drag coefficient as a result of the current deflections and operating points. |
| Aileron Hinge Moment Coefficient | The hinge moment about the aileron hinge, $C_{H_a}$. |
| Tab Hinge Moment Coefficient | The hinge moment about the tab hinge, $C_{H_t}$. |
| $C_x$,$C_y$,$C_z$ due to Aileron/Tab | The force coefficients as a result of the current deflections of the tab and aileron. |
| $C_l$,$C_m$,$C_n$ due to Aileron/Tab | The moment coefficients as a result of the current deflections of the tab and aileron, with symbols $C_{M_l}$,$C_{M_m}$ and $C_{M_n}$ used in the text. |

*Note that the coefficients are provided in the aircraft's body axes, and are non-dimensional.*

### C.2.8 Other Actuator Models

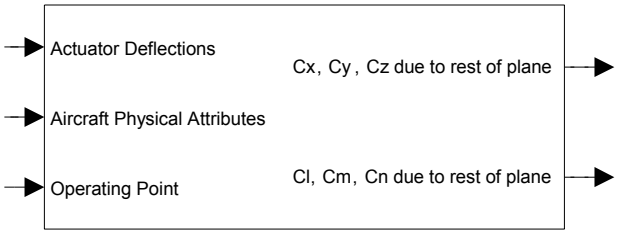

Aerodynamic Models - Other Control Surfaces

The aerodynamic models of the other control surfaces themselves are encapsulated within this block. These are provided by Airbus and provide the moment and force coefficients of all the control surfaces, except those of the ailerons (and tabs) which are calculated elsewhere.

Although two versions of this block exist: the first making use of the Neural Networks used to calculate the (non-linear) coefficients, and the second a linearised module where the coefficients are calculated about the trim value, more accurate results are provided by the non-linear module and thus it is used for simulations.

| **Inputs** | |
|---|---|
| Actuator Deflections [°] | The command signals for all the actuators except the ailerons. |
| Aircraft Physical Attributes | The physical parameters of the aircraft. |
| Operating Point | Refer to §C.2.12.1. |

| **Outputs** | |
|---|---|
| $C_x$,$C_y$,$C_z$ | The force coefficients as a result of the current deflections of the *other* control surfaces. |
| $C_l$,$C_m$,$C_n$ | The moment coefficients as a result of the current deflections of the *other* control surfaces, with symbols $C_{M_l}$,$C_{M_m}$ and $C_{M_n}$ used in the text. |

*Note that the coefficients are provided in the aircraft's body axes, and are non-dimensional.*

### C.2.9 Aerodynamic Model – Complete Aircraft

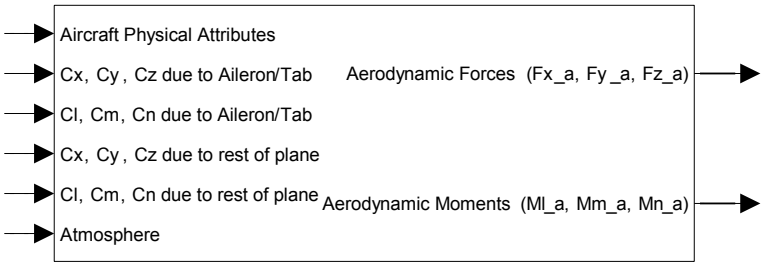


This block takes the force and moment coefficients and calculates the actual aircraft forces and moments based on the current operating point and the current atmospheric conditions (dynamic pressure).

| **Inputs** | |
|---|---|
| Aircraft Physical Attributes | The physical attributes (area's etc) required to perform the calculations |
| $C_x$,$C_y$,$C_z$ due to Aileron/ Tab | The force coefficients as a result of the Tab and Aileron combination. |
| $C_l$,$C_m$,$C_n$ due to Aileron/ Tab | The moment coefficients as a result of the Tab and Aileron combination. |
| $C_x$,$C_y$,$C_z$ due to rest of Plane | The force coefficients as a result of the other control surfaces. |
| $C_l$,$C_m$,$C_n$ due to rest of Plane | The moment coefficients as a result of the other control surfaces. |
| Atmosphere | The current atmospheric conditions, especially the dynamic pressure. |
| **Outputs** | |
| Aerodynamic Forces [N] | The aircraft forces in body axes |
| Aerodynamic Moments [N m] | The aircraft moments in body axes |

*Note that the coefficients and hence the Forces and Moments are provided in the aircraft's body axes, and that in the text the moment symbols used are $C_{M_l}$,$C_{M_m}$ and $C_{M_n}$.*

### C.2.10 Engine (Thrust) Model

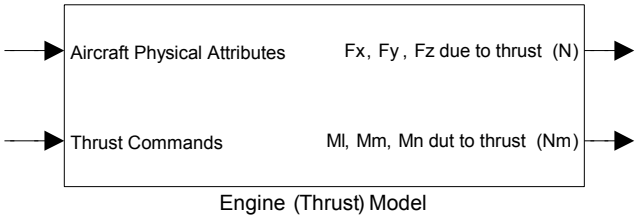


The engine dynamics are encapsulated here. This block takes the reference input and converts it to the current Force and Moment contributions due to thrust produced by the aircraft. These are provided by Airbus.

| **Inputs** | |
|---|---|
| Aircraft Physical Attributes | The physical attributes required to perform the calculations |
| Thrust Commands [°] | The commanded thrust (obtained from the Fly-by-Wire system). |
| **Outputs** | |
| $F_x$, $F_y$, $F_z$ due to thrust [N] | The force contribution due to thrust. |
| $M_m$, $M_n$, $M_l$ due to thrust [N m] | The moment contribution due to thrust. |

*Note that the Forces and Moments are provided in the aircraft's body axes.*

### C.2.11 Hinge Moment

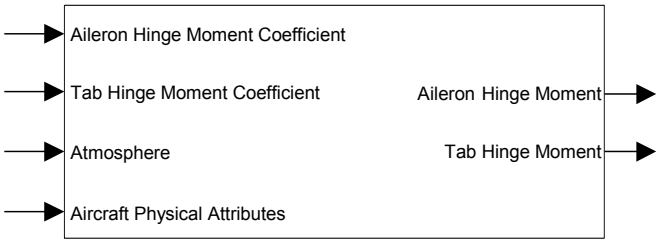


Simply calculates the hinge moments of the aileron and tab based on the hinge moment coefficients. This block may be modified as some designs may not include a tab.

| **Inputs** | |
|---|---|
| Aileron Hinge Moment Coefficient | The aileron hinge moment coefficient. |
| Tab Hinge Moment Coefficient | The tab hinge moment coefficient. |
| Atmosphere | The current atmospheric conditions, especially the dynamic pressure. |
| Aircraft Physical Attributes | The physical attributes required to perform the calculations. |

| **Outputs** | |
|---|---|
| Aileron Hinge Moment | The aerodynamic hinge moment of the tab. |
| Tab Hinge Moment | The aerodynamic hinge moment of the tab. |

### C.2.12 Aircraft Dynamics [6DOF]

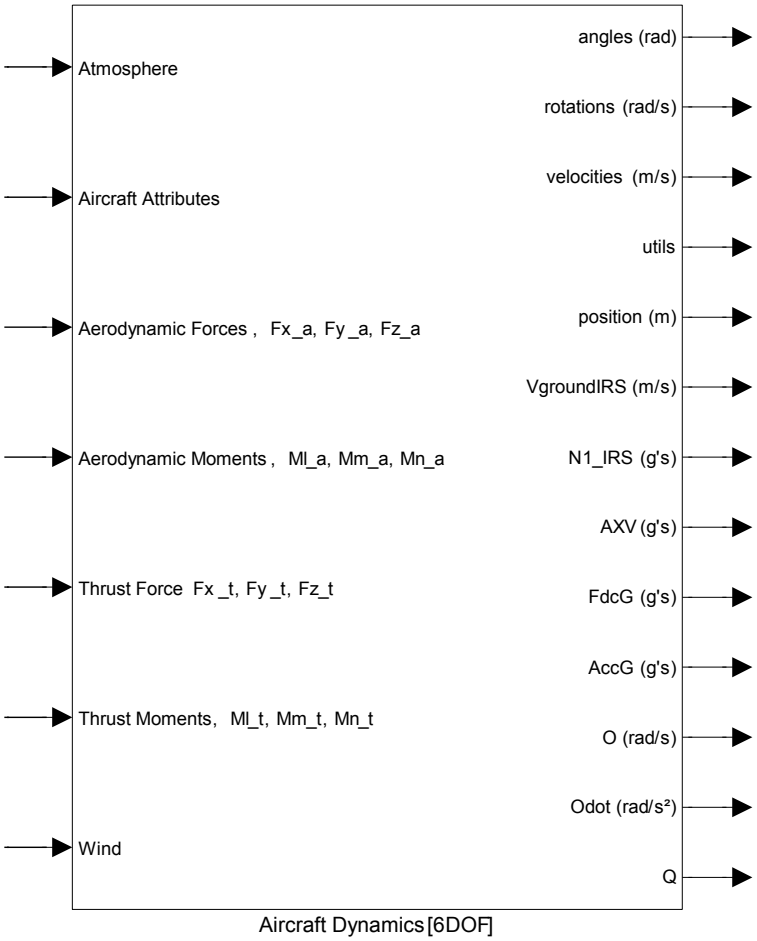

The Aircraft Dynamics block accepts the current atmospheric conditions as well as all the forces and moments acting on the aircraft (in body axes) at and around the Centre-of-Gravity and converts the inputs into the kinematic outputs for the aircraft. These include, but are not limited to the orientation, position and velocities of the aircraft for the current instance in time. The initial values for these outputs are set in the Matlab script run prior to the simulation.

| **Inputs** | |
|---|---|
| Atmosphere | The current atmospheric-related conditions. |
| Aircraft Attributes | The aircraft's physical attributes (e.g. the moment of inertia). |
| Aerodynamic Forces [N] | The aerodynamic forces acting on the aircraft. |
| Aerodynamic Moments [N m] | The aerodynamic moments acting on the aircraft. |
| Thrust Forces [N] | The forces acting on the aircraft due to the thrust. |
| Thrust Moments [N m] | The moments acting on the aircraft due to the thrust. |
| Wind | Prevailing wind velocities. |

#### C.2.12.1 The Operating Point

The outputs of the Aircraft Dynamics block provide what is collectively known as the operating point of the aircraft – its orientation, velocity, position at any point in time. The components of the operating point data bus are described below:

| **angles [**rad**]** | |
|---|---|
| psi | Heading angle, $\psi$ |
| theta | Pitch angle, $\theta$ |
| phi | Roll angle, $\phi$ |
| alpha | Angle of attack, $\alpha$ |
| beta | Side-slip angle, $\beta$ |
| gamma_ground | Flight path angle, $\gamma_{\text{ground}}$ |

| **rotations [**rad/s**]** | |
|---|---|
| psi_dot | Heading angle rate of change, $\dot{\psi}$ |
| theta_dot | Pitch angle rate of change, $\dot{\theta}$ |
| phi_dot | Roll angle rate of change, $\dot{\phi}$ |
| p | Roll rate, $p$ |
| q | Pitch rate, $q$ |
| r | Yaw rate, $r$ |

| **velocities** | |
|---|---|
| V_groundCG [m/s] | Ground speed. |
| Vtas [m/s] | True airspeed. |
| Vcas [m/s] | Conventional (calibrated) airspeed. |
| Mach | Mach number of the aircraft. |

| **utils** | |
|---|---|
| emax [°] | A value used by the propulsion block provided by Airbus. |

| **Others** | |
|---|---|
| position [m] | Position in Earth axes ($N$, $E$, $D$) or ($x$, $y$, $z$). |
| VgroundIRS [m/s] | Ground velocity as measured by the IRS system ($V_x$, $V_y$, $V_z$). |
| N1_IRS [g's] | Load factor at IRS in aircraft axes. |
| AXV [g's] | Acceleration along the flight path in runway axes. |
| FdcG [g's] | Load Factor at CG in body axes. |
| AccG [m/s$^2$] | Acceleration of CG in body axes. |
| O [rad/s] | $\Omega$, the vector consisting of ($p$, $q$, $r$). |

| | |
|---|---|
| Odot [rad/s$^2$] | $\dot{\Omega}$, the vector consisting of ($\dot{p}$, $\dot{q}$, $\dot{r}$). |
| Q | Quaternion describing the orientation of the aircraft. |

Many of these outputs are required by the Airbus Fly-by-Wire system used to determine the control signals.

### C.2.13 Atmospheric Model

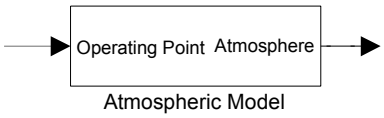


The atmospheric model merely adapts atmospheric conditions based on current location and altitude.

| **Inputs** | |
|---|---|
| Operating Point | Refer to §C.2.12.1. |
| **Outputs** | |
| Atmosphere | Current atmospheric conditions. |

*Atmosphere:*

| **Variable** | **Symbol** | **Units** | **Description** |
|---|---|---|---|
| density | $\rho$ | kg/m$^3$ | Current Air Density $\rho = \frac{P_s}{287{,}053\,T}$ |
| pres | $P_s$ | Pa | Static Pressure $P_s = P_o \left(\frac{T}{T_o}\right)^{-\frac{RL}{gM}} = 101\,325 \left(\frac{T}{288{,}15}\right)^{5{,}255\,877\,4}$ |
| dynpre | $\overline{q}$ | Pa | Dynamic Pressure $\overline{q} = \frac{1}{2}\rho V^2$ |
| temp | $T$ | K | Air temperature $T = T_n + (h - h_n)\lambda_n = 288{,}15 - 0{,}0065h$ |
| spdsnd | $a$ | m/s | Speed of Sound $a = \sqrt{\gamma RT} = \sqrt{1.4 \times 287.053 \times T}$ |

### C.2.14 Wind

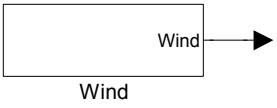


This block is used to input the prevailing wind conditions and gust model during the simulations.

| **Outputs** | |
|---|---|
| Wind | The wind velocity vector ($V_{w_x}$, $V_{w_y}$, $V_{w_z}$) |

### C.2.15 Aircraft Attributes

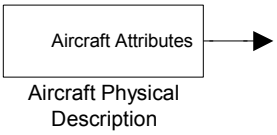


The block describes the physical aspects of the aircraft. This includes, but is not limited to, the mass, fuselage dimensions, landing gear positions and dimensions, control surface locations, dimensions and limits, as well as wing and stabiliser sweep angles and profiles.

| **Outputs** | |
|---|---|
| Aircraft Attributes | The aircraft's physical attributes as described above and below. |

*Aircraft Attributes:*

| Variable | Symbol | Units | Description |
|---|---|---|---|
| mass | $m$ | kg | The mass of the aircraft |
| MOI | $\mathrm{MOI}$ | $\mathrm{kg} \cdot \mathrm{m}^2$ | Mass moment of inertia of the aircraft. $$\mathrm{MOI} = \begin{bmatrix} I_{xx} & I_{xy} & I_{xz} \\ I_{yx} & I_{yy} & I_{yz} \\ I_{zx} & I_{zy} & I_{zz} \end{bmatrix}$$ where $I_{ii}$ are the principle moments of inertia and $I_{ij}$ are the products of inertia of the aircraft. |
| refArea | $S$ | $\mathrm{m}^2$ | The reference area of the aircraft. |
| span | $b$ | m | The span of the main wing. |
| mac | $c$ | m | The mean aerodynamic chord. |
| AR | $\mathcal{AR}$ | m | Aspect ratio. |
| e | $e$ | | Span efficiency factor. |
| coefs | | | Aerodynamic coefficients for linear model. See below. |
| irsPos | | m | IRS position. |
| cgPos | | % of mac | CG position as a percentage of the MAC. |

# Appendix D

# Data Tables

This appendix lists a number of tables consisting of tabularised data that can be used to gain greater insight to statements made in the main text body.

**Table D.1** – A comparison between the thin aerofoil theory (NL), the linearised theory (Lin) and *X-Foil* (XF). Angles are in degrees and coefficients are per unit length. $E_a = 0{,}25$ and $E_t = 0.075$.

| $\alpha$ | $\delta_a$ | $\delta_t$ | $C_L$ | $C_{H_a}$ | $C_{H_t}$ | **Method** |
|---|---|---|---|---|---|---|
| | | | 0,138 948 | −0,000 427 1 | $1{,}258 \times 10^{-5}$ | **XF** |
| 0° | 0° | 0° | 0,119 925 | −0,000 812 349 | $-6{,}902\,71 \times 10^{-5}$ | **NL** |
| | | | 0,119 925 | 0,002 870 23 | 0,000 218 239 | **Lin** |
| | | | 0,348 239 | −0,007 771 49 | −0,000 467 45 | **XF** |
| 0° | 0° | 5° | 0,308 802 | −0,008 293 42 | −0,000 629 682 | **NL** |
| | | | 0,308 699 | −0,001 990 04 | $-5{,}267\,52 \times 10^{-5}$ | **Lin** |
| | | | −0,071 216 4 | 0,006 841 25 | 0,000 459 06 | **XF** |
| 0° | 0° | −5° | −0,068 952 7 | 0,006 668 72 | 0,000 491 631 | **NL** |
| | | | −0,068 848 5 | 0,007 730 5 | 0,000 489 154 | **Lin** |
| | | | 0,884 778 | −0,011 907 | −0,000 513 09 | **XF** |
| 0° | 10° | 0° | 0,788 841 | −0,011 791 2 | −0,000 374 129 | **NL** |
| | | | 0,787 766 | −0,010 027 1 | −0,000 481 225 | **Lin** |
| | | | 1,093 45 | −0,019 989 3 | −0,001 165 38 | **XF** |
| 0° | 10° | 5° | 0,977 718 | −0,019 272 | −0,000 934 76 | **NL** |
| | | | 0,976 54 | −0,014 887 4 | −0,000 752 14 | **Lin** |
| | | | 0,675 795 | −0,004 145 97 | $9{,}012 \times 10^{-5}$ | **XF** |
| 0° | 10° | −5° | 0,599 963 | −0,004 310 41 | 0,000 186 553 | **NL** |
| | | | 0,598 992 | −0,005 166 83 | −0,000 210 311 | **Lin** |
| | | | −0,608 447 | 0,010 191 9 | 0,000 356 72 | **XF** |
| 0° | −10° | 0° | −0,548 991 | 0,010 166 7 | 0,000 236 075 | **NL** |
| | | | −0,547 916 | 0,015 767 6 | 0,000 917 704 | **Lin** |
| | | | −0,399 991 | 0,003 051 72 | $-2{,}975 \times 10^{-5}$ | **XF** |
| 0° | −10° | 5° | −0,360 113 | 0,002 685 88 | −0,000 324 603 | **NL** |
| | | | −0,359 142 | 0,010 907 3 | 0,000 646 789 | **Lin** |
| | | | −0,819 803 | 0,017 503 8 | 0,000 766 41 | **XF** |
| 0° | −10° | −5° | −0,737 868 | 0,017 647 5 | 0,000 796 71 | **NL** |
| | | | −0,736 689 | 0,020 627 8 | 0,001 188 62 | **Lin** |
| | | | 0,862 485 | −0,003 832 43 | −0,000 133 72 | **XF** |
| 6° | 0° | 0° | 0,777 899 | −0,004 512 53 | −0,000 243 951 | **NL** |
| | | | 0,777 899 | −0,000 829 958 | $4{,}331\,16 \times 10^{-5}$ | **Lin** |
| | | | 1,070 49 | −0,011 074 8 | −0,000 611 22 | **XF** |
| 6° | 0° | 5° | 0,966 776 | −0,011 993 6 | −0,000 804 598 | **NL** |
| | | | 0,966 673 | −0,005 690 23 | −0,000 227 603 | **Lin** |
| | | | 0,6537 | 0,003 342 68 | 0,000 307 55 | **XF** |
| 6° | 0° | −5° | 0,589 021 | 0,002 968 54 | 0,000 316 715 | **NL** |
| | | | 0,589 125 | 0,004 030 31 | 0,000 314 226 | **Lin** |

Continued on next page

Table D.1 – continued from previous page

| $\alpha$ | $\delta_a$ | $\delta_t$ | $C_L$ | $C_{H_a}$ | $C_{H_t}$ | **Method** |
|---|---|---|---|---|---|---|
| | | | 1,601 69 | −0,015 161 9 | −0,000 693 02 | **XF** |
| 6° | 10° | 0° | 1,446 81 | −0,015 491 | −0,000 549 054 | **NL** |
| | | | 1,445 74 | −0,013 727 3 | −0,000 656 153 | **Lin** |
| | | | 1,807 28 | −0,023 025 1 | −0,001 325 88 | **XF** |
| 6° | 10° | 5° | 1,635 69 | −0,022 971 8 | −0,001 109 68 | **NL** |
| | | | 1,634 51 | −0,018 587 6 | −0,000 927 067 | **Lin** |
| | | | 1,395 65 | −0,007 605 41 | −0,000 105 64 | **XF** |
| 6° | 10° | −5° | 1,257 94 | −0,008 010 22 | $1{,}163\,65 \times 10^{-5}$ | **NL** |
| | | | 1,256 97 | −0,008 867 02 | −0,000 385 238 | **Lin** |
| | | | 0,117 624 | 0,006 737 1 | 0,000 222 89 | **XF** |
| 6° | −10° | 0° | 0,108 983 | 0,006 466 88 | $6{,}115\,09 \times 10^{-5}$ | **NL** |
| | | | 0,110 058 | 0,012 067 4 | 0,000 742 776 | **Lin** |
| | | | 0,326 39 | −0,000 415 75 | −0,000 168 17 | **XF** |
| 6° | −10° | 5° | 0,297 86 | −0,001 013 93 | −0,000 499 519 | **NL** |
| | | | 0,298 832 | 0,007 207 1 | 0,000 471 862 | **Lin** |
| | | | −0,093 767 5 | 0,014 048 7 | 0,000 633 16 | **XF** |
| 6° | −10° | −5° | −0,079 894 7 | 0,013 947 7 | 0,000 621 794 | **NL** |
| | | | −0,078 715 7 | 0,016 927 6 | 0,001 013 69 | **Lin** |
| | | | −0,223 88 | 0,001 297 88 | $8{,}65 \times 10^{-5}$ | **XF** |
| −3° | 0° | 0° | −0,209 062 | 0,001 037 74 | $1{,}843\,51 \times 10^{-5}$ | **NL** |
| | | | −0,209 062 | 0,004 720 33 | 0,000 305 703 | **Lin** |
| | | | −0,014 801 5 | −0,006 037 56 | −0,000 390 83 | **XF** |
| −3° | 0° | 5° | −0,020 184 3 | −0,006 443 33 | −0,000 542 224 | **NL** |
| | | | −0,020 287 9 | −0,000 139 945 | $3{,}478\,86 \times 10^{-5}$ | **Lin** |
| | | | −0,433 875 | 0,008 552 78 | 0,000 531 9 | **XF** |
| −3° | 0° | −5° | −0,397 939 | 0,008 518 81 | 0,000 579 089 | **NL** |
| | | | −0,397 835 | 0,009 580 6 | 0,000 576 617 | **Lin** |
| | | | 0,522 21 | −0,010 145 5 | −0,000 416 73 | **XF** |
| −3° | 10° | 0° | 0,459 854 | −0,009 941 31 | −0,000 286 667 | **NL** |
| | | | 0,458 779 | −0,008 177 01 | −0,000 393 761 | **Lin** |
| | | | 0,731 572 | −0,018 271 5 | −0,001 072 8 | **XF** |
| −3° | 10° | 5° | 0,648 731 | −0,017 422 1 | −0,000 847 302 | **NL** |
| | | | 0,647 553 | −0,013 037 3 | −0,000 664 676 | **Lin** |
| | | | 0,312 606 | −0,002 345 69 | 0,000 189 25 | **XF** |
| −3° | 10° | −5° | 0,270 976 | −0,002 460 51 | 0,000 274 011 | **NL** |
| | | | 0,270 005 | −0,003 316 74 | −0,000 122 847 | **Lin** |
| | | | −0,969 483 | 0,011 836 2 | 0,000 420 8 | **XF** |
| −3° | −10° | 0° | −0,877 978 | 0,012 016 6 | 0,000 323 537 | **NL** |
| | | | −0,876 902 | 0,017 617 7 | 0,001 005 17 | **Lin** |
| | | | −0,762 035 | 0,004 761 4 | $3{,}989 \times 10^{-5}$ | **XF** |
| −3° | −10° | 5° | −0,6891 | 0,004 535 79 | −0,000 237 145 | **NL** |
| | | | −0,688 129 | 0,012 757 4 | 0,000 734 253 | **Lin** |
| | | | −1,179 96 | 0,019 087 7 | 0,000 826 5 | **XF** |
| −3° | −10° | −5° | −1,066 86 | 0,019 497 4 | 0,000 884 168 | **NL** |
| | | | −1,065 68 | 0,022 477 9 | 0,001 276 08 | **Lin** |

**Table D.2** – A comparison between the thin aerofoil theory (NL), the linearised theory (Lin) and *X-Foil* (XF). The data is the same as in Table D.1, except that the values shown for the linear and non-linear theories are the percentage deviations between the thin aerofoil values and *X-Foil*.

| $\alpha$ | $\delta_a$ | $\delta_t$ | $C_L$ | $C_{H_a}$ | $C_{H_t}$ | **Method** |
|---|---|---|---|---|---|---|
| | | | 0,138 948 | −0,000 427 1 | $1{,}258 \times 10^{-5}$ | **XF** |
| 0° | 0° | 0° | 13,691 | −90,2012 | 648,705 | **NL (% Δ)** |
| | | | 13,6908 | 772,028 | −1634,81 | **Lin (% Δ)** |
| | | | 0,348 239 | −0,007 771 49 | −0,000 467 45 | **XF** |
| 0° | 0° | 5° | 11,3246 | −6,715 92 | −34,7057 | **NL (% Δ)** |
| | | | 11,3544 | 74,3931 | 88,7314 | **Lin (% Δ)** |
| | | | −0,071 216 4 | 0,006 841 25 | 0,000 459 06 | **XF** |
| 0° | 0° | −5° | 3,178 71 | 2,521 93 | −7,095 18 | **NL (% Δ)** |
| | | | 3,324 98 | −12,9984 | −6,555 49 | **Lin (% Δ)** |
| | | | 0,884 778 | −0,011 907 | −0,000 513 09 | **XF** |
| 0° | 10° | 0° | 10,8431 | 0,972 428 | 27,0831 | **NL (% Δ)** |
| | | | 10,9645 | 15,7882 | 6,210 39 | **Lin (% Δ)** |
| | | | 1,093 45 | −0,019 989 3 | −0,001 165 38 | **XF** |
| 0° | 10° | 5° | 10,5841 | 3,588 48 | 19,7892 | **NL (% Δ)** |
| | | | 10,6919 | 25,5234 | 35,4597 | **Lin (% Δ)** |
| | | | 0,675 795 | −0,004 145 97 | $9{,}012 \times 10^{-5}$ | **XF** |
| 0° | 10° | −5° | 11,2211 | −3,966 24 | −107,005 | **NL (% Δ)** |
| | | | 11,3648 | −24,6229 | 333,367 | **Lin (% Δ)** |
| | | | −0,608 447 | 0,010 191 9 | 0,000 356 72 | **XF** |
| 0° | −10° | 0° | 9,771 81 | 0,247 202 | 33,8206 | **NL (% Δ)** |
| | | | 9,948 52 | −54,7071 | −157,262 | **Lin (% Δ)** |
| | | | −0,399 991 | 0,003 051 72 | $-2{,}975 \times 10^{-5}$ | **XF** |
| 0° | −10° | 5° | 9,969 68 | 11,9879 | −991,104 | **NL (% Δ)** |
| | | | 10,2125 | −257,415 | 2274,08 | **Lin (% Δ)** |
| | | | −0,819 803 | 0,017 503 8 | 0,000 766 41 | **XF** |
| 0° | −10° | −5° | 9,994 44 | −0,820 673 | −3,953 46 | **NL (% Δ)** |
| | | | 10,1383 | −17,8475 | −55,0891 | **Lin (% Δ)** |
| | | | 0,862 485 | −0,003 832 43 | −0,000 133 72 | **XF** |
| 6° | 0° | 0° | 9,807 27 | −17,7459 | −82,4346 | **NL (% Δ)** |
| | | | 9,807 24 | 78,3438 | 132,39 | **Lin (% Δ)** |
| | | | 1,070 49 | −0,011 074 8 | −0,000 611 22 | **XF** |
| 6° | 0° | 5° | 9,688 45 | −8,296 57 | −31,638 | **NL (% Δ)** |
| | | | 9,698 12 | 48,6199 | 62,7625 | **Lin (% Δ)** |
| | | | 0,6537 | 0,003 342 68 | 0,000 307 55 | **XF** |
| 6° | 0° | −5° | 9,894 23 | 11,1928 | −2,980 03 | **NL (% Δ)** |
| | | | 9,8783 | −20,5713 | −2,170 72 | **Lin (% Δ)** |
| | | | 1,601 69 | −0,015 161 9 | −0,000 693 02 | **XF** |
| 6° | 10° | 0° | 9,669 54 | −2,170 58 | 20,7737 | **NL (% Δ)** |
| | | | 9,736 63 | 9,462 06 | 5,3198 | **Lin (% Δ)** |
| | | | 1,807 28 | −0,023 025 1 | −0,001 325 88 | **XF** |
| 6° | 10° | 5° | 9,494 13 | 0,231 205 | 16,3064 | **NL (% Δ)** |
| | | | 9,559 34 | 19,2725 | 30,0791 | **Lin (% Δ)** |
| | | | 1,395 65 | −0,007 605 41 | −0,000 105 64 | **XF** |
| 6° | 10° | −5° | 9,8676 | −5,322 62 | 111,015 | **NL (% Δ)** |
| | | | 9,937 15 | −16,5883 | −264,671 | **Lin (% Δ)** |
| | | | 0,117 624 | 0,006 737 1 | 0,000 222 89 | **XF** |
| 6° | −10° | 0° | 7,3464 | 4,010 96 | 72,5646 | **NL (% Δ)** |
| | | | 6,4323 | −79,1182 | −233,248 | **Lin (% Δ)** |
| | | | 0,326 39 | −0,000 415 75 | −0,000 168 17 | **XF** |
| 6° | −10° | 5° | 8,741 01 | −143,879 | −197,032 | **NL (% Δ)** |
| | | | 8,443 41 | 1833,52 | 380,586 | **Lin (% Δ)** |
| | | | −0,093 767 5 | 0,014 048 7 | 0,000 633 16 | **XF** |

Continued on next page

Table D.2 – continued from previous page

| $\alpha$ | $\delta_a$ | $\delta_t$ | $C_L$ | $C_{H_a}$ | $C_{H_t}$ | **Method** |
|---|---|---|---|---|---|---|
| 6 ° | −10 ° | −5 ° | 14,7948 | 0,718 991 | 1,795 17 | **NL (% Δ)** |
| | | | 16,0523 | −20,4927 | −60,1002 | **Lin (% Δ)** |
| −3 ° | 0 ° | 0 ° | −0,223 88 | 0,001 297 88 | $8{,}65 \times 10^{-5}$ | **XF** |
| | | | 6,618 65 | 20,0434 | 78,6878 | **NL (% Δ)** |
| | | | 6,618 78 | −263,695 | −253,414 | **Lin (% Δ)** |
| −3 ° | 0 ° | 5 ° | −0,014 801 5 | −0,006 037 56 | −0,000 390 83 | **XF** |
| | | | −36,3668 | −6,720 72 | −38,7365 | **NL (% Δ)** |
| | | | −37,0665 | 97,6821 | 108,901 | **Lin (% Δ)** |
| −3 ° | 0 ° | −5 ° | −0,433 875 | 0,008 552 78 | 0,000 531 9 | **XF** |
| | | | 8,282 36 | 0,397 202 | −8,871 81 | **NL (% Δ)** |
| | | | 8,306 37 | −12,0173 | −8,407 11 | **Lin (% Δ)** |
| −3 ° | 10 ° | 0 ° | 0,522 21 | −0,010 145 5 | −0,000 416 73 | **XF** |
| | | | 11,9408 | 2,012 82 | 31,2103 | **NL (% Δ)** |
| | | | 12,1465 | 19,4028 | 5,511 64 | **Lin (% Δ)** |
| −3 ° | 10 ° | 5 ° | 0,731 572 | −0,018 271 5 | −0,001 072 8 | **XF** |
| | | | 11,3237 | 4,648 91 | 21,0195 | **NL (% Δ)** |
| | | | 11,4848 | 28,6471 | 38,0429 | **Lin (% Δ)** |
| −3 ° | 10 ° | −5 ° | 0,312 606 | −0,002 345 69 | 0,000 189 25 | **XF** |
| | | | 13,317 | −4,894 73 | −44,7876 | **NL (% Δ)** |
| | | | 13,6275 | −41,397 | 164,913 | **Lin (% Δ)** |
| −3 ° | −10 ° | 0 ° | −0,969 483 | 0,011 836 2 | 0,000 420 8 | **XF** |
| | | | 9,4386 | −1,524 39 | 23,1137 | **NL (% Δ)** |
| | | | 9,5495 | −48,8461 | −138,871 | **Lin (% Δ)** |
| −3 ° | −10 ° | 5 ° | −0,762 035 | 0,004 761 4 | $3{,}989 \times 10^{-5}$ | **XF** |
| | | | 9,571 03 | 4,7384 | 694,498 | **NL (% Δ)** |
| | | | 9,6985 | −167,934 | −1740,69 | **Lin (% Δ)** |
| −3 ° | −10 ° | −5 ° | −1,179 96 | 0,019 087 7 | 0,000 826 5 | **XF** |
| | | | 9,585 12 | −2,146 16 | −6,977 34 | **NL (% Δ)** |
| | | | 9,685 05 | −17,7611 | −54,3959 | **Lin (% Δ)** |

**Table D.3** – Numerical values of the design vector shown in Figures 4.5 and 4.6.

| $k$ | 0 | 1 | 2 | 3 | 4 | 5 | 6 | 7 |
|---|---|---|---|---|---|---|---|---|
| $x$ | 2,5153 | 2,7801 | 2,9499 | 2,9912 | 2,9977 | 3 | 3 | 3 |
| $y$ | −0,1045 | −0,1162 | −0,1228 | −0,1243 | −0,1245 | −0,1313 | −0,179 94 | −0,5213 |
| $k$ | 8 | 9 | 10 | 11 | 12 | 13 | 14 | 15 |
| $x$ | 3 | 2,9998 | 2,9989 | 2,9944 | 2,9707 | 2,826 | 0,561 83 | −0,360 05 |
| $y$ | −2,6358 | −2,6359 | −2,636 | −2,6366 | −2,6382 | −2,6409 | −2,5917 | −2,5229 |
| $k$ | 16 | 17 | 18 | 19 | 20 | 21 | 22 | 23 |
| $x$ | −0,3648 | −0,318 67 | −0,110 99 | 0,298 13 | 0,216 26 | 0,227 39 | 0,228 42 | 0,228 28 |
| $y$ | −1,858 | −1,6312 | −1,6306 | −1,5756 | −1,6434 | −1,625 | −1,6256 | −1,6255 |
| $k$ | 24 | | | | | | | |
| $x$ | 0,228 28 | | | | | | | |
| $y$ | −1,6255 | | | | | | | |

**Table D.4** – Values of the direction vector and step size for Figure 4.5.

| $k$ | $d_x$ | $d_y$ | $\alpha$ |
|---|---|---|---|
| 0 | N/A | N/A | N/A |
| 1 | 1,0595 | −0,047 091 | 0,25 |
| 2 | 0,169 76 | −0,006 483 | 1 |
| 3 | 0,165 41 | −0,005 902 3 | 0,25 |
| 4 | 0,205 02 | −0,007 063 9 | 0,031 25 |
| 5 | 0,002 348 | −0,006 864 8 | 1 |
| 6 | $7{,}3726 \times 10^{-18}$ | −0,048 609 | 1 |
| 7 | $6{,}0715 \times 10^{-18}$ | −0,341 38 | 1 |
| 8 | 0 | −4,229 | 0,5 |
| 9 | −0,000 181 32 | $-45{,}198 \times 10^{-6}$ | 1 |
| 10 | −0,000 905 44 | −0,000 168 87 | 1 |
| 11 | −0,004 550 2 | −0,000 575 79 | 1 |
| 12 | −0,023 614 | −0,001 647 5 | 1 |
| 13 | −0,144 74 | −0,002 631 5 | 1 |
| 14 | −2,2642 | 0,049 148 | 1 |
| 15 | −30 208 | 2256,3 | $30{,}518 \times 10^{-6}$ |
| 16 | −1,2169 | 170,21 | 0,003 906 3 |
| 17 | 5,9055 | 29,033 | 0,007 812 5 |
| 18 | 0,207 68 | 0,000 568 | 1 |
| 19 | 0,818 24 | 0,110 03 | 0,5 |
| 20 | −0,081 869 | −0,067 859 | 1 |
| 21 | 0,011 121 | 0,018 378 | 1 |
| 22 | 0,001 036 1 | −0,000 532 22 | 1 |
| 23 | −0,000 143 27 | $44{,}715 \times 10^{-6}$ | 1 |
| 24 | $128{,}47 \times 10^{-9}$ | $245{,}25 \times 10^{-9}$ | 1 |

**Table D.5** – Values of the design vector shown in Figures 4.9 and 4.10.

| $k$ | 0 | 1 | 2 | 3 | 4 |
|---|---|---|---|---|---|
| $x$ | −1,2762 | 0,240 48 | 0,300 82 | 0,248 99 | 0,217 25 |
| $y$ | 0,589 75 | −1,7167 | −1,5677 | −1,6148 | −1,6212 |

| $k$ | 5 | 6 | 7 | 8 |
|---|---|---|---|---|
| $x$ | 0,2165 | 0,232 75 | 0,235 62 | 0,235 62 |
| $y$ | −1,6227 | −1,6187 | −1,623 | −1,623 |

# Appendix E

# Patents Relating to Trailing Edge Tabs

This appendix lists a number of patents that relate to trailing edge tabs, and includes the the abstract of the patent and the year it was issued. The general trend was that most of the patents were issued between 1940 and 1960. The list below also only contains patents from the United States of America. Patents have been referred to by some of the documentation that are from other foreign companies, however information regarding these are not freely available, or easily accessible.

**US2045667** June 1936 – *Trimming and Balancing Flap for Aircraft*

The present invention relates to airplane control surfaces such as the rudder, elevators and ailerons. Considerable force is met with in swinging the control surfaces of a large airplane to any considerable angular extent from a neutral position. It is desirable to provide means to counteract this force to some degree and to assist the pilot in swinging the control surfaces, and it is also desirable that the pilot be provided with means whereby he can trim the airplane, in case of necessity, by displacing one of the control surfaces from its neutral position to counteract an unbalanced thrust.

**US2252284** August 1941 – *Control Surface Tab Mechanism*

This invention relates to aircraft control systems and is particularly concerned with improvements in control mechanisms for auxiliary aerofoils on movable control surfaces, commonly known as trim tabs.

**US2325548** July 1943 – *Control Means for Rudders and the Flaps Thereon*

This invention relates to improvements in control means for rudders and the flaps thereon, and refers to an arrangement whereby a rudder and its flap may be operated through a single actuating rod.

**US2357465** September 1944 – *Automatic Balance Tab*

This invention relates to control devices for aircraft and in particular provides means for automatically differentially controlling a trailing edge tab or flap with respect to a movable control surface upon which the tab is mounted.

**US2370844** March 1945 – *Airplane Control Mechanism of the Boost Tab Type*

The present invention relates generally to control mechanisms for airplanes. More particularly the invention relates to that type of airplane control mechanism which comprises a pivotally mounted basic or primary control surface, such as an elevator, rudder or aileron, a hinged boost tab on the trailing portion of the control surface, an actuating lever in the pilot's compartment, and an operating connection for causing the control surface to swing into different angular positions in response to control movements of the actuating lever.

**US2431529** November 1947 – *Elevator and Tab Control Mechanism*

The present invention relates to means for controlling aircraft and more particularly to means for actuating elevators or similar control surfaces.

In heavy aircraft, the static loads and air loads on control surfaces are frequently of such magnitude that it is desirable to provide auxiliary surfaces which can be operated easily by the pilot and which function to move the primary control surfaces or to aid the pilot in moving them.

**US2435922** February 1948 – *Tab Control Mechanism*

This invention relates to aircraft of the type characterised by control surfaces which carry auxiliary aerofoils for balancing and trimming purposes and more particularly the invention is concerned with improvements in control mechanisms for such auxiliary aerofoils.

**US2556353** June 1951 – *Aircraft Control System*

This invention relates to an improvement in aircraft controls to provide increased stability and controllability.

It is known that various means may be employed to increase the stability of an airplane. For example it is known that a vane movable in response to changes of angle of attack may be connected to a tab on an elevator in such a manner that when the angle of attack of the airplane is increased, the tab is caused to pivot upwardly. This will result in downward movement of the elevator causing the airplane's angle of attack to be reduced and its airspeed increased.

Similarly an increase in airspeed or decrease in angle of attack may be corrected automatically by the vane swinging the tab downwardly, resulting in the elevator being moved upwardly.

**US2557426** June 1951 – *Tab Actuating Mechanism*

This invention relates to aircraft control devices and relates more particularly to tab actuating mechanisms for automatically differentially controlling a trailing tab or flap with respect to a movable control surface element with which it is associated.

Various systems and mechanisms have been introduced for operating and controlling the flaps or tabs mounted at the rear edges of control aerofoils such as rudders, elevators and ailerons. The prior mechanisms have been such that the tabs may be set or operated by the pilot during flight and in other devices the tab has been actuated to act either as a servo means to assist in the control of the principal control aerofoil or as an anti-servo means. However, so far as I am aware such earlier tab actuating mechanisms have not provided for automatic anti-servo tab motion throughout the neutral range of movement of the control surface or aerofoil and for automatic servo motion of the tab throughout the larger control surface angles or movements.

**US2568719** September 1951 – *Control System for Aircraft Control Surface and Tab*

This invention relates generally to control systems and more particularly to automatic pilots for air-borne or other craft with a main operating surface and an auxiliary or trim tab operating surface.

Primarily, the object of the invention is to minimise any sustained cable loading on the control surfaces of the craft to permit the human pilot to assume control of the craft from the automatic pilot without undue exertion and to secure a minimum resistance. While such systems have heretofore been used in connection where hydraulic servomotors, as shown in the prior patents to B.G. Carlson, 2045579 and 2183932 dated June 20, 1936 and December 19, 1937 respectively, my invention relates to an improved means for accomplishing the stated purpose in an electrical servo-system.

**US2577439** December 1951 – *Differential Spring Balance Tab*

This invention relates to airplane control means of the type wherein a tab is hinged to the trailing edge of a control aerofoil for providing aerodynamic balance.

Usually tabs of this kind are geared to the airplane structure in such a manner that deflection of the tab relative to the control aerofoil is approximately proportional to the control aerofoil's deflection. In some instances means have been provided whereby this proportion, or balance ration, may be adjusted to different values by the pilot so that more or less aerodynamic balance may be provided.

**US2623717** December 1952 – *Control System for Controlled Aerofoils of Aircraft*

This invention relates to control systems for controlled aerofoils, such as ailerons, elevators or rudders, of aircraft and has for its main object to provide an improved power-assisted control system which may be conveniently combined with a form of spring-tab aerodynamic control system that may be alternatively employed with safety in the event, for example, of the failure of the power supply that provides for power assistance. The main objects of the invention therefore are the provision of a composite aerodynamically and power assisted control system of considerable flexibility that is derived from certain novel features and arrangements that will be particularised below.

**US2640665** June 1953 – *Aircraft Trim Tab Control*

The present invention relates to the control of aircraft in flight and more particularly to improvements in trim tab control mechanisms.

In normal course of flight of a conventionally controlled airplane, it is necessary to constantly and frequently adjust the controls in order that the airplane is balanced properly or properly trimmed such that it will maintain a desired attitude of flight. There are a number of methods of accomplishing the balancing or trim of an aircraft in flight and the most common is by the use and adjustment of the trim tabs which are usually located at the trailing edges of the control surfaces. THese trim tabs are operated by various types of mechanisms and may either be hand operated worm and gear devices, a cable drum with attached cables extending and connected to the trim tabs, or other mechanical, hydraulic or electrical mechanisms and systems.

**US2668028** February 1954 – *Aircraft Tab Control Mechanism*

This present invention relates to aircraft controls and more particularly to improvements in control mechanism for control surface tabs and the like.

In the control of modern aircraft, particularly large aircraft or those which operate at higher speeds, it is frequently desirable that the control surfaces be provided with tabs in the region of the surface trailing edge. These control tabs may either be of the trim type in which they assist the pilot in trimming the airplane, or they may be of the servo type in which they assist the pilot in displacing the control surface upon which the tab is mounted.

the present invention is directed to improved irreversible control mechanism in what may be preferably be a gear-driven dual lead screw arrangement which completely eliminates backlash or play within the mechanism in such a manner that it is not subject to fluttering or other undesirable vibration. The improved mechanism also provides the additional advantage of reducing the weight of the installation previously required by irreversible tab control devices and is such that the portion of its greatest weight may be installed ahead of the hinge centreline of the control surface whereby the weight of the unit may be used to advantage to provide a static balance for the control surface.

**US2669401** February 1954 – *Tab Control*

This invention relates to improvements in control means for rudders and other control surfaces and the tabs thereon, and more particularly concerns a control system employing a tab which alternatively serves as a direct action tab when the power boost is available, or as an aerodynamic servo tab when the power boost is not available.

This invention comprises modifications to standard controls of surfaces by including additional linkages that serve a dual purpose either (1) to convey pilot-created motion to a tab hinged to a surface while the boost system valve temporarily remains at dead centre thus acquiring an immediate aerodynamic action equivalent to the action of a small surface, or (2) to convey the pilot-created motion to the same tab in such a direction that the tab will assist the turning of the surface upon failure of the power boost.

**US2696956** December 1954 – *Safety Mechanism for Operating Control Surfaces*

This invention relates to mechanism for operating airplane control surfaces of the type characterised by cooperating main and auxiliary aerofoils and more particularly to a secondary control system for causing movement of a main aerofoil and simultaneous differential movement of an auxiliary aerofoil in order to trim the aircraft in flight or to control it in the event that the primary system is rendered inoperative.

**US2813689** November 1957 – *Convolving Aircraft Control Surfaces and Articulated Tabs*

The present invention involves the combination of an articulated tab and control surface interconnected so that the articulated parts of the tab are deflected relative to each other in the same direction as they are deflected relative to the aircraft control surface which carries them.

Particlulary at high speeds, it has been found that an aircraft control surface, when swung through a large angle from neutral position, tends to blanket a tab which affects swinging of such a control surface relative to a horizontally stationary aerofoil carrying the control surface. As a result, at larger angles of control surface deflection resistance to further deflection of the tab relative to the control surface decreases progressively with increased deflection of the control surface. Eventually a point may be reached at high aircraft speeds where, without the application of any further effort by the pilot, the tab tends to be deflected farther relative to the control surface producing a reversed control force. The large control surface deflection at high speeds which occurs under such circumstances creates undesirably great air loads on the control surface and part of the aircraft associated with it, and also ht pilot tends to manoeuvre the airplane more than he desires because of the reduced or reversed control forces. In large, high-speed airplanes, the controls usually are too large for the pilot to manipulate without the assistance of some power or servomechanism; however, the control forces resulting from use of such assisting devices must not be too light or undesirably high deflections of the main control surface may occur.

A convenient aerodynamic servomechanism for assisting movement of a control surface is the control tab.

**US2817483** December 1957 – *Aircraft control Force Modifier*

This invention relates to aircraft and more specifically to an arrangement for modifying the control forces required to manoeuvre such craft.

It has always been a difficult design problem to obtain the proper control forces thought the speed range of an aircraft. This is particularly true of the high-speed types since the force applied to the control surface for a given deflection varies directly with the dynamic pressure of the airspeed squared. Obviously then, the control force variations may be quite large unless modified in the actuating system. If the control forces are too great the pilot will be unable to control the aircraft and if the control forces are too low excessive control surface deflections may be produced which will overload the control surface and cause it to fail. The forces should be such that a given force will produce a given rate of change of position of the aircraft.

The conventional devices such as tabs used to modify control forces in aircraft are generally no capable, by themselves, of properly modifying the control forces for all the required surface deflections and speed ranges.

With this invention, ram air pressure developed by the forward motion of the aircraft is employed advantageously to either reduce or increase the control forces by an amount varying as a function of airspeed, through the use of a cam in the actuating linkage as hereinafter described in detail in this specification.

**US2843344** July 1958 – *Aircraft Trim Tab Control*

This present invention relates to the control of aircraft in flight and more particularly to improvements in trim tab control mechanisms.

In the normal course of flight of a conventionally controlled airplane, it is necessary to constantly and frequently adjust the controls in order that the airplane is balanced or properly trimmed such that it will maintain a desired attitude of flight. There are a number of methods of accomplishing the balancing or trim of an aircraft in flight and the most common is by the use and adjustment of the trim tabs which are usually located at the trailing edges of the control surfaces. These trim tabs are operated by various types of mechanisms and may either be hand operated worm and gear devices, a cable drum with attached cables extending and connected to the trim tabs, or other mechanisms and systems. In order to relieve the load on the control stick, when the attitude of the airplane is changed for any reason during flight, in the conventional manually operated worm and gear mechanism referred to, it is necessary for the pilot to crank the tab control mechanism to the pint at which the load on the stick is at a minimum. This procedure is more or less continuous in the normal operation of the airplanes, especially those of the larger passenger or transport type wherein the centre of gravity is continually shifting due to movements of the passengers about the airplane.

**US3000595** September 1961 – *Elevator Tab Convertible from an Anti-balance Tab to an Assist Tab*

This invention refers to the aerodynamic control surfaces of aircraft, and more particularly to the horizontal stabiliser and an elevator equipped with tabs for control, anti-balance and assist purposes.

This invention comprises such horizontal tail surfaces including tabs, the function of which depends upon the requirements of flight which are indicated by the positions of the movable horizontal stabiliser. As the stabiliser is moved, either from its cruise and/or somewhat normal deflected positions to a nose fawn landing condition and/or to any appreciable nose down setting, the tab is moved to function respectively and alternately either as an anti-balance tab or as an assist tab.

**US4431149** February 1984 – *Geared Tab*

An improved geared tab configuration for a moveable aerofoil, such as an elevator of an aircraft, is provided which comprises a tab pivotally connected to the aerofoil, and linkage connecting the aerofoil to the tab for simultaneous opposing pivotal movement of the tab relative to the aerofoil to a maximum tab deflection at a determinable intermediate upward aerofoil deflection beyond which the relative tab deflection reverses and fairs to the aerofoil at a determinable maximum upward aerofoil deflection.

**US4479620** October 1984 – *Wing Load Alleviation System Using Tabbed Ailerons*

A wing load alleviation system for redistributing aircraft loads encountered during flight by symmetrically deflecting the outboard ailerons of the aircraft includes a trailing edge tab pivotally supported on each outboard aileron. As each outboard aileron is deflected by the wing load alleviation system to reduce wing bending moments, the corresponding tab is deflected in aerodynamic opposition thereto so as to reduce wing torsional loads caused by the deflection of its associated outboard aileron. The span of each tab is equal to or less than that of its associated outboard aileron, and the chord of each tab is a predetermined fraction of that of its associated outboard aileron. Each tab may be mechanically linked to its associated outboard aileron so that deflection of the outboard aileron causes a proportional but opposite deflection of the tab.

**US4765572** August 1988 – *System for Controlling a Mobile Aerodynamic Surface of an Aircraft*

This invention relates to a system for controlling an aerodynamic surface mounted mobile on an aircraft to as to be able to pivot freely about a fixed axis and provided with a tab itself articulated on the trialling edge of the aerodynamic surface, the system being such that elastic connecting devices are provided with a tab itself articulated on the trailing edge of the aerodynamic surface and the tab can be directly actuated by the pilot, via a voluntary actuating member and a mechanical linkage. According to the invention, this system comprises: an actuator interposed between the elastic connecting device and the aerodynamic surface; a device for controlling the actuator; and a clutch connecting the structure of the aircraft to the mechanical linkage; and the device for controlling he actuator also controls the clutch, so that the latter is in disengaged position when the actuator is active and in engaged position when the actuator is inactive.

**US5366176** November 1994 – *Feedback-Stabilised Aerodynamically Overbalanced Lifting/Control Surface for Aircraft*

An aerofoil of an aircraft is provided with one or more control flaps which are pivotally mounted on the aerofoil in an aeromechanically unstable manner. The trailing edges of the control flops are provided with one or more control tab zones which include trailing portions that deform in response to application of electrical current, heat or pressure thereto. The pitch of the aerofoil is constantly controlled by selectively deforming the control tab zones in response to measured signals indicative of variations in fluid pressure acting upon, or motion of the unstable control flaps. The impetus for moving the control system is thus derived from the air-stream through which the aircraft moves. The control system can also be utilised in watercraft, with the operating impetus being derived from the water stream through which the craft moves.

**US5913492** June 1999 – *System for Controlling an Aircraft Control Surface Tab*

A system for controlling the tab of an aircraft control surface having a pair of position sensors that supply information regarding the turning of the control surface and the position of a jack, respectively, on the

basis of signals generated by the sensors as well as possibly on the basis of at least one parameter originating from the aircraft, such as airspeed, positions of lift-augmenting devices, forces exerted by the pilot on a control, etc, and which formulates a command for the jack.

**US6257528** July 2001 – *Vehicle Control System and Method Employing Control Surface and Geared Tab*

Control systems and methods for a vehicle such as an aircraft or watercraft employ a trailing edge control surface that is pivotal about a pivot axis fixed relative to the vehicle and is deflected to create control forces, and a tab pivotally mounted to an aft end on the control surface. An aft end of a linkage is connected to the tab spaced from the tab pivot axis, and the linkage extends forward to a forward end that is coupled to fixed vehicle structure, such that deflection of the control surface causes a deflection of the tab as long as the forward end of the linkage does not lie in line with the control surface pivot axis, the in-line position defining a neutral position of the linkage. A gearing control actuator is coupled to the linkage and is operable to position the forward end of the linkage at selectively variable distances on one or the other side of the neutral position, thus providing variable gearing ratios between the control surface and the tab. Tab gearing ratio can be varied as a function of vehicle operating condition. An alternative control system includes a backup tab actuator for providing tab deflection upon failure of the actuator system that deflects the control surface. The tab can be used as a control tab for providing the motive force for moving the control surface, or the tab can be used as a mini-control surface by locking the control surface in a fixed position.

# Bibliography


[1] Boye, S.: Technical data for “Control Surfaces in Confined Spaces” project. Tech. Rep. PR0915089, Airbus UK Ltd., October 2009.

[2] Stinton, D.: *The Anatomy of the Aeroplane*. 2nd edn. American Institute of Aeronautics and Astronautics, Inc, 1998.

[3] Stinton, D.: *The Design of the Airplane*. 2nd edn. American Institute of Aeronautics and Astronautics, Inc, 2001.

[4] Phillips, W.H.: *Journey in Aeronautical Research - A Career at NASA Langley Research Center*. No. 12 in Monographs in Aerospace History. NASA History Office, November 1998.

[5] Briere, D., Favre, C. and Traverse, P.: *The Avionics Handbook*, chap. 12: Electrical Flight Controls, From Airbus A320/330/340 to Future Military Transport Aircraft: A Family of Fault-Tolerant Systems, pp. 12.1–12.15. The Electrical Engineering Handbook Series. CRC Press LLC, 2001. Editor: Cary R. Spitzer.

[6] Cook, M.V.: *Flight Dynamics Principles*. Elsevier Aerospace Engineering Series, 2nd edn. Elsevier Ltd., 2007.

[7] Etkin, B. and Reid, L.D.: *Dynamics of Flight: Stability and Control*. 3rd edn. John Wiley & Sons, Inc, 1996.

[8] Harris, T.A.: Reduction of hinge moments of airplane control surfaces. Technical Report 528, National Advisory Committee for Aeronautics, February 1935.

[9] Mungall, R.G.: Flight investigation of a combined geared unbalancing-tab and servotab control system used with an all-movable horizontal tail. Technical Note 1763, National Advisory Committee for Aeronautics, December 1948.

[10] Bland, Jr., W.M. and Marley, E.T.: A free-flight investigation at zero lift in the mach number range between 0.7 and 1.4 to determine the effectiveness of an inset tab as a means of aerodynamically relieving aileron hinge moments. Research Memorandum L52K07, National Advisory Committee for Aeronautics, January 1953.

[11] Wight, K.C.: Measurements of two-dimensional derivatived on a wing-aileron-tab system with a 1541 section aerofoil: Part 1 – direct aileron derivatives. ARC Technical Report 2934, Aeronautical Research Council, October 1952.

[12] Wight, K.C.: Measurements of two-dimensional derivatived on a wing-aileron-tab system with a 1541 section aerofoil: Part ii – direct tab and cross aileron-tab derivatives. ARC Technical Report 3029, Aeronautical Research Council, March 1955.

[13] Trebble, W.J.G. and Holford, J.: Low speed womd tunnel investigation of tab hinge moment characteristics. Technical Note 2130, Aeronautical Research Council, November 1951. CP 112.

[14] Perring, W.G.A.: The theoretical relationships for an aerofoil with a multiply hinged flap system. Technical Report 1171, Aeronautical Research Council, April 1928.

[15] Keuthe, A.M. and Chow, C.-Y.: *Foundations of Aerodynamics: Bases of Aerodynamic Design*. 3rd edn. John Wiley & Sons, Inc, 1976.

[16] Moran, J.: *An Introduction To Theoretical and Computational Aerodynamics*. John Wiley & Sons, Inc, 1984.

[17] Allen, H.: Calculation of the chordwise load distribution over airfoil sections with plain, split or serially hinged trailing-edge flaps. Report 634, National Advisory Committee for Aeronautics, Langley Field, Va., April 1938.

[18] Purser, P.E. and Cook, C.B.: Collection and analysis of hinge-moment data on control-surface tabs. Technical Note 1113, National Advisory Committee for Aeronautics, April 1947.

[19] Crandall, S.M. and Murray, H.E.: Analysis of available data on the effects of tabs on control-surface hinge moments. Technical Note 1049, National Advisory Committee for Aeronautics, May 1946.

[20] White, R.J. and Klampe, D.G.: Force and moment coefficients for a thin airfoil with flap and tab in a form useful for stability and control calculations. Technical Note 960, National Advisory Committee for Aeronautics, January 1945.

[21] Soinne, E.: *Aerodynamic and Flight Dynamic Simulations of Aileron Characteristics*. Dissertation for the degree of Doctor of Technology, Royal Institute of Technology, Stockholm, Sweden, Department of Aeronautics, Royal Institute of Technology, SE-100 44 Stockholm, Sweden, December 2000.

[22] Soinne, E.: Aerodynamically balanced ailerons for a commuter aircraft. *Progress in Aerospace Sciences*, vol. 37, pp. 497–550, 2001.

[23] Iosilevskii, G.: Control with trim tabs and history-dependant aerodynamic forces. *Journal of Fluids and Structures*, vol. 23, pp. 365–389, 2007.

[24] Kostić, I.: Numerical evaluation of the aerodynamic influence of the helicopter composite blade trailing edge tabs. *Archive of Applied Mechanics*, vol. 77, pp. 893–909, 2007.

[25] Prechtl, E.F.: *Development of a Piezoelectric Servo-Flap Actuator for Helicopter Rotor Control*. Master's thesis, Massachusetts Institute of Technology, 1994.

[26] Katz, J. and Plotkin, A.: *Low-Speed Aerodynamics*. 2nd edn. Cambridge University Press, 2001.

[27] McCormick, B.W.: *Aerodynamics, Aeronautics, and Flight Mechanics*. 2nd edn. John Wiley & Sons, Inc, 1995.

[28] Anderson, J.D.: *Fundamentals of Aerodynamics*. 4th edn. McGraw-Hill Higher Education, 2005.

[29] Meriam, J.L. and Kraige, L.G.: *Statics*. Engineering Mechanics, 5th edn. John Wiley & Sons, Inc, 2003. SI Version.

[30] Dommasch, D.O., Sherby, S.S. and Connolly, T.F.: *Airplane Aerodynamics*. 4th edn. Pitman Publishing Corporation, 1967.

[31] Koen, M.C.: *Modelling and Simulation of an RPV for Flight Control System Design Purposes*. University of Pretoria, 2006.

[32] Walsh, G.: *Methods of Optimisaton*. John Wiley & Sons, Inc, 1975.

[33] Arora, J.S.: *Introduction to Optimal Design*. 2nd edn. Elsevier Academic Press, 2004.

[34] Seireg, A.A. and Rodriguez, J.: *Optimising the Shape of Mechanical Elements and Structures*. Marcel Dekker, Inc, 1997.

[35] Pardalos, P.M. and Romeijn, H.E. (eds.): *Handbook of Global Optimization*, vol. 2 of *Nonconvex Optimization and Its Applications v. 62*. Kluwer Academic Publishers, 2002.

[36] Horst, R. and Pardalos, P.M. (eds.): *Handbook of Global Optimization*, vol. 2 of *Nonconvex Optimization and Its Applications v. 62*. Kluwer Academic Publishers, 2002.

[37] Wilde, D.J.: *Globally Optimal Design*. John Wiley & Sons, Inc, 1978.

[38] Haug, E.J. and Arora, J.S.: *Applied Optimal Design: Mechanical and Structural Systems*. John Wiley & Sons, Inc, 1979.

[39] Stewart, J.: *Calculus*. Thomson - Brooks/Cole, 2003.

[40] Marler, R. and Arora, J.: Survey of multi-objective optimization methods for engineering. *Structural and Multidisciplinary Optimization*, vol. 26, no. 6, pp. 369–395, April 2004.

[41] Weisstein, E.W.: Stationary point. From MathWorld–A Wolfram Web Resource, 2009. Accessed on 2009-10-30.
Available at: `http://mathworld.wolfram.com/StationaryPoint.html`

[42] Nemec, M., Zingg, D.W. and Pulliam, T.: Multi-point and multi-objective aerodynamic shape optimization. In: *9th AIAA/ISSMO Symposium on Multidisciplinary Analysis and Optimization*. September 2002.

[43] Zingg, D.W. and Elias, S.: On aerodynamic optimization under a range of operating conditions. *AIAA journal*, vol. 44, no. 11, pp. 2787–2792, 2006.

[44] Huyse, L. and Lewis, R.M.: Aerodynamic shape optimization of two-dimensional airfoild under uncertain conditions. Tech. Rep., ICASE, 2001. ICASE Report No. 2001-1.

[45] Li, W., Huyse, L. and Padula, S.: Robust airfoil optimization to achieve drag reduction over a range of mach numbers. *Structural and Multidisciplinary Optimization*, vol. 24, pp. 38–50, 2002.

[46] Boggs, P.T. and Tolle, J.W.: Sequential quadratic programming. *Acta Numerica*, vol. 4, no. -1, pp. 1–51, 1995. `http://journals.cambridge.org/article_S0962492900002518`.
Available at: `http://journals.cambridge.org/action/displayAbstract?fromPage=online&aid=1771148&fulltextType=RA&fileId=S0962492900002518`

[47] Lay, D.C.: *Linear Algebra and Its Applications*. 3rd edn. Addison Wesley, 2003.

[48] Lemke, C.: A method of solution for quadratic programs. *Management Science*, vol. 8, no. 4, pp. 442–453, July 1962.
Available at: `http://www.jstor.org/stable/2627246`

[49] Rusin, M.: A revised simplex methd for quadratic programming. *SIAM Journal of Applied Mathematics*, vol. 20, no. 2, pp. 143–160, March 1971.

[50] Wolfe, P.: The simplex method for quadratic programming. *Econometrica*, vol. 27, no. 3, pp. 382–398, July 1959.

[51] Wolfe, P.: Some simplex-like nonlinear programming procedures. *Operations Research*, vol. 10, no. 4, pp. 438–447, July – August 1962.

[52] Schutte, J.: Derivative free global optimisation. Electronic Class Notes, November 2004. Experimental Optimum Engineering Design - EML6934, University of Florida.

[53] Smith, J.E.: Genetic algorithms. In: Pardalos, P.M. and Romeijn, H.E. (eds.), *Handbook of Global Optimization*, vol. 2 of *Nonconvex Optimization and Its Applications*, chap. 9, pp. 275–362. Kluwer Academic Publishers, 2002.

[54] Pearson, H.: Genetics: What is a gene? *Nature*, vol. 441, pp. 398–401, May 2006.

[55] Holst, T.L. and Pulliam, T.H.: Aerodynamic shape optimization using a real-number-encoded genetic algorithm. In: *9th AIAA Applied Aerodynamics Conference*, AIAA-2001-2473. American Institute of Aeronautics and Astronautics, June 11-14 2001. AIAA-2001-2473.

[56] Herrera, F., Lozano, M. and Verdegay, J.L.: Tackling real-coded genetic algorithms: Operators and tools for behavioural analysis. *Artificial Intelligence Review*, vol. 12, pp. 265–319, 1998.

[57] Fonseca, C.M. and Fleming, P.J.: An overview of evolutionary algorithms in multiobjective optimization: Formulation, discussion and generalization. *Evolutionary Computation*, vol. 3, pp. 1–16, 1995.

[58] Microsoft Developer Network: *Windows Sockets 2 API Documentation*. Microsoft Corporation, March 2008. MSDN Documentation for Visual Studio 2008.

[59] The MathWorks: *Using MEX-Files to Call C and Fortran Programs*. The MathWorks Inc., 2008. MATLAB Product Help.

[60] Song, W. and Keane, A.J.: A study of shape parameterisation methods for airfoil optimisation. In: *10th AIAA/ISSMO Multidisciplinary Analysis and Optimization Conference*. American Institute of Aeronautics and Astronautics, 2004.
Available at: `http://citeseerx.ist.psu.edu/viewdoc/summary?doi=10.1.1.113.6596`

[61] Peigin, S. and Epstein, B.: Robust optimization of 2D airfoils driven by full Navier-Stokes computations. *Computers and Fluids*, vol. 33, pp. 1175–1200, 2004.

[62] Boye, S.: Initial technical data for "Control Surfaces in Confined Spaces" project. Tech. Rep., Airbus UK Ltd., April 2008. Release 1.0.

[63] Zingg, D.W., Nemec, M. and Pulliam, T.: A comparative evaluation of genetic and gradient based algorithms applied to aerodynamic optimization. *Shape design in aerodynamics*, vol. 17, pp. 103–126, 2008.

[64] Boissenin, S.: Generalities about flight domain in the frame of "Control Surfaces In Confined Spaces" project. Tech. Rep., Airbus France S.A.S., 2009.